Structural elucidation, control and transformation of poly(glycerol) functionalized nanodiamond, and its application to boron neutron capture therapy

Masahiro Nishikawa

論 文 要 旨

論文題目　Structural elucidation, control and transformation of poly(glycerol) functionalized nanodiamond, and its application to boron neutron capture therapy（ポリグリセロール修飾ナノダイヤモンドの構造解析、反応制御および化学変換、ならびにホウ素中性子捕捉療法への応用）

申 請 者　西川　正浩

論文要旨

ナノダイヤモンド（ND）は、高い生体適合性、表面官能基への化学修飾可能性、色中心含有NDにおける蛍光特性などから、バイオ・医療分野への応用に関する研究が多く行われている。一方、種々ナノ粒子を生理的条件下で安定に分散させるために、ポリグリセロール（PG）による修飾が用いられている。PG修飾は、豊富に存在する水酸基により高い親水性をナノ粒子に付与し、また更なる化学修飾を可能にするほか、ナノ粒子の体内での免疫応答を回避させることが知られている。本研究では爆轟法ND（DND）を中心に、PG修飾ND（ND-PG, DND-PG）の構造解析とPG修飾反応の定量的制御に関して検討し、またDND-PGへのホウ素源担持によるホウ素中性子捕捉療法（BNCT）薬剤の合成とその評価を行った。

本論文は6つの章より構成される。第1章は序論であり、ND, PG修飾およびBNCTに関する一般的知識を開示する。第2章ではグリシドールの開環重合を安全に行うために溶媒を用いるPG修飾反応条件を示し、またPG修飾量が反応条件およびND粒子の性状により理論的に制御可能であることを明らかにした。ND-PGのNMR分析からは、PG鎖中での置換様式が異なるモノマー単位の存在比と1級水酸基の量を求めた。更に動的光散乱（DLS）分析からPG鎖の長さを求め、特にDND-PGにおいてPG鎖は柔軟でありPG層内部に多くの水を含むことが可能であると推定した。第3章ではニトロキシルラジカル触媒によりND-PGの1級水酸基をカルボキシ基（COOH）に変換する方法について述べる。酸化剤の使用量に対する反応挙動を検討し、COOH含量が約1 mmol/g以下の範囲では酸化剤の量に対してほぼ定量的にCOOHが生成することがわかった。第4章ではDND-PGにフェニルボロン酸（PBA）を担持したBNCT薬剤の合成とマウスによる評価を行った。DND-PGのOH基をアミノ基に変換し、PBAのアルデヒド体との還元アミノ化によりPBAを導入、血液中で分散させるためにアミノ基の保護を行った。ナノ薬剤は、担がんマウスへの投与において腫瘍に蓄積され、また中性子照射により腫瘍の増大を有意に抑制することを確認した。第5章ではホウ素-10クラスターを担持したナノ薬剤を合成した。第3章で示したCOOH変換体から出発し、ホウ素-10クラスターをクリック反応で導入し、COOH基には能動的ターゲティング部位としてPBAまたはRGDペプチドを結合した。細胞毒性試験、BNCT評価および透過型電子顕微鏡（TEM）による細胞導入の観

察を行い、ホウ素-10クラスター担持ナノ薬剤は細胞内に導入され、中性子照射によりBNCT効果を示すことを確認した。能動的ターゲティング部位の有無による差異はわずかであり、負電荷を持つホウ素-10クラスターの細胞導入への関与が示唆された。第6章は結語であり、本論文におけるND-PGに関する詳細かつ定量的な検討が、バイオ・医療分野でのND-PGの応用に対して、ラボスケールから臨床・工業化段階にわたり重要な知見を与えると期待されること、またDND-PGによるBNCT薬剤が、今後の薬剤開発でのリード物質となり得ると結論した。

Table of contents

Chapter 1: General introduction

1-1. Nanodiamonds

Nanodiamonds (NDs) are nanometer-sized (< 100 nm) diamond particles which have attracted great attention for two decades or more. They are expected to have superior physical and chemical properties of bulk diamond with the features of nanoparticles like dispersibility in various media or versatility of surface chemistry brought by the large surface area and abundant surface functional groups. At present, the following four practical (industrial) synthetic methods of diamond or NDs are known; i) high-pressure high-temperature (HPHT), ii) shock-wave compaction, iii) chemical vapor deposition (CVD) and iv) detonation methods as shown in Table 1-1 [1, 2]. Different method gives NDs of different characteristics especially in size and shape, and also chemical composition or impurity and defect contents. Break-down and classification processes are established in i), ii) and iii) to obtain nanometer-sized particles.

NDs from detonation synthesis designated as detonation NDs (DNDs) are produced by the "detonation" of oxygen-deficient explosives such as the mixture of 2,4,6-trinitrotoluene (TNT) and hexahydro-1,3,5-trinitro-1,3,5-triazine (RDX) in a closed chamber (Figure 1-1) [2–5]. TNT is thought to serve as carbon source while RDX is to provide energy to make high temperature and pressure (3000 K, 20 GPa) for diamond synthesis. Upon the ignition, the explosive charge burns at the combustion speed of ~ 8000 m/s, depending on the type of explosive material, to generate the shock-wave. Diamond structure is formed just behind the shock-wave front at the time-scale of ≤ 1 μs for its formation and growth. Accordingly, the primary particle size of DNDs is uniform in 4–6 nm with spherical or truncated shape, which is the smallest among NDs from the above methods (Figure 1-2).

Table 1-1. Four major synthetic methods of artificial (nano)diamonds.

Synthetic method (Discovery)	Raw materials	Shape and size of ND particles	Description of method
Hydrostatic high-pressure high-temperature (HPHT) (GE, 1955)	Graphite + ferrous metal (Fe, Co, Ni)	Single crystalline particle of truncated shape, 50 µm ~ mm	Graphite is dissolved in melted metal catalyst at high pressure and high temperature (5 GPa, 1500 °C), from which diamond particles are deposited.
Shock-wave compaction (DuPont method) (DeCarli-Jamieson, 1961)	Graphite + Cu powder + explosive (TNT)	Polycrystalline particle, 50 µm	Graphite powder is charged in a sealed metal tube and set in an explosive chamber. Explosion initiates the phase transition to diamond structure at high pressure and high temperature.
Chemical vapor deposition (CVD) (Eversole, 1950)	Methane (CH_4) + hydrogen (H_2)	Polycrystalline film, in the order of µm	Plasma (radical) is generated from raw materials by the microwave or hot filament. Diamond is deposited and grown on the substrate at ~ 800 °C under the pressure of < 27 kPa.
Detonation (Danilenko-Volkov-Elin, 1963)	Explosive (TNT + RDX)	Single crystalline nanoparticles, 4–6 nm	Oxygen-deficient explosives are detonated in a closed chamber. Carbons in explosive molecules come into the plasma state, and then condensed to give diamond at high pressure and high temperature.

Resulting detonation product (soot) is collected from the chamber and purified through oxidation by the mixture of H_2SO_4 and HNO_3 to remove sp^2 amorphous and graphitic carbons. As the purified DNDs are usually aggregation form (cluster DNDs), mechanical or chemical disintegration process is conducted to prepare appropriate dispersion in various media (Figure 1-1) [6, 7]. As necessary, prior to the disintegration, surface chemistry is homogenized by the gas phase reactions with hydrogen, and oxygen or ozone for ζ(zeta)-positive and negative DNDs, respectively, liquid phase treatment at higher temperature or longer time with H_2SO_4/HNO_3 or supercritical condition with HNO_3 for ζ-negative DNDs, or hydrogen plasma treatment for ζ-positive DNDs and so on (Figure 1-1).

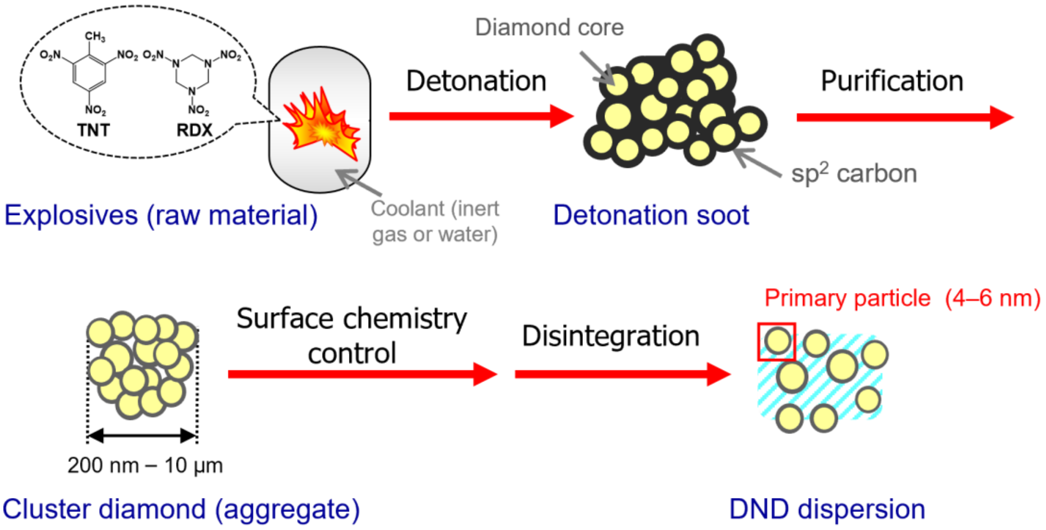

Figure 1-1. Manufacturing process of DNDs.

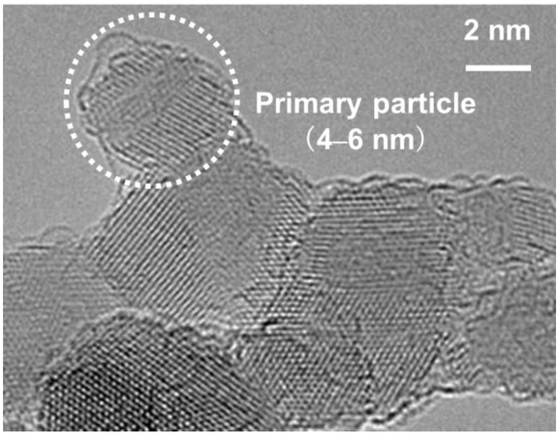

Figure 1-2. Transmission electron microscopy (TEM) image of DNDs (cluster diamond).

(Courtesy of Prof. T. Hayashi, Shinshu University)

DNDs were discovered in 1963 in the former USSR. Since its existence came to be known worldwide after the end of the Cold War in the 1990s, a lot of developmental works have been conducted in various application fields to expect improvement in mechanical strength, thermal conductivity, optical properties, frictional properties of matrices and so on. Among various fields explored so far, biomedical application has been most intensely investigated due to the following advantages [2, 8, 9]. Firstly, DNDs are chemically and biologically inert to exhibit low toxicity or high biocompatibility as with bulk diamond [10–13]. Secondly, DNDs do not interfere the function of biomolecules because the size of 4–6 nm is comparable to the size of typical biomolecules like proteins [14–16]. Thirdly, the physicochemical properties or functionalities are controllable through surface chemical modifications covalently or non-covalently [14, 17, 18]. Based on these features, a lot of investigations have been made for drug delivery system (DDS) with DNDs, in which active pharmaceutical ingredients such as anticancer drug, DNA, siRNA, and antibiotics are adsorbed on the surface of bare (unmodified), surface-modified and polymer coated DNDs by π-stacking or electrostatic interaction as illustrated in Figure 1-3 [19–25]. In most of the works, the resulting complex particles form aggregates (“supraparticle” by “self-assembly") having 50–100 nm-size appropriate for efficient delivery to cancer tissues known as EPR (enhanced permeability and retention) effect. Although a number of profits can be expected by this approach for active pharmaceutical ingredients (APIs) of small molecule, there may be some limitations due to the non-covalent formulation; uniformity or stability of particulate assembly may be largely dependent on the process especially in large scale preparation. In addition, the composition of complex particles may sometimes be intricate with additional component to ensure the appropriate dispersibility especially with insoluble API.

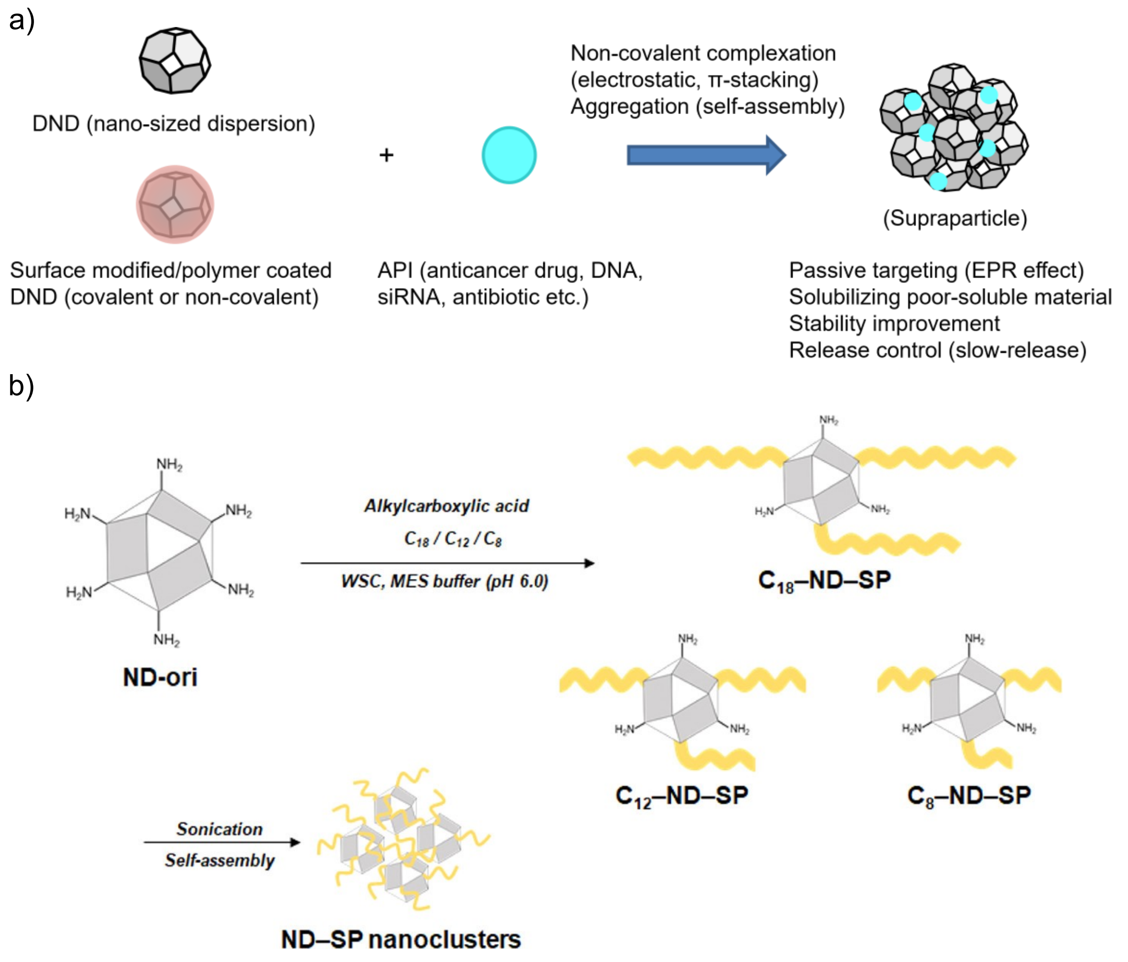

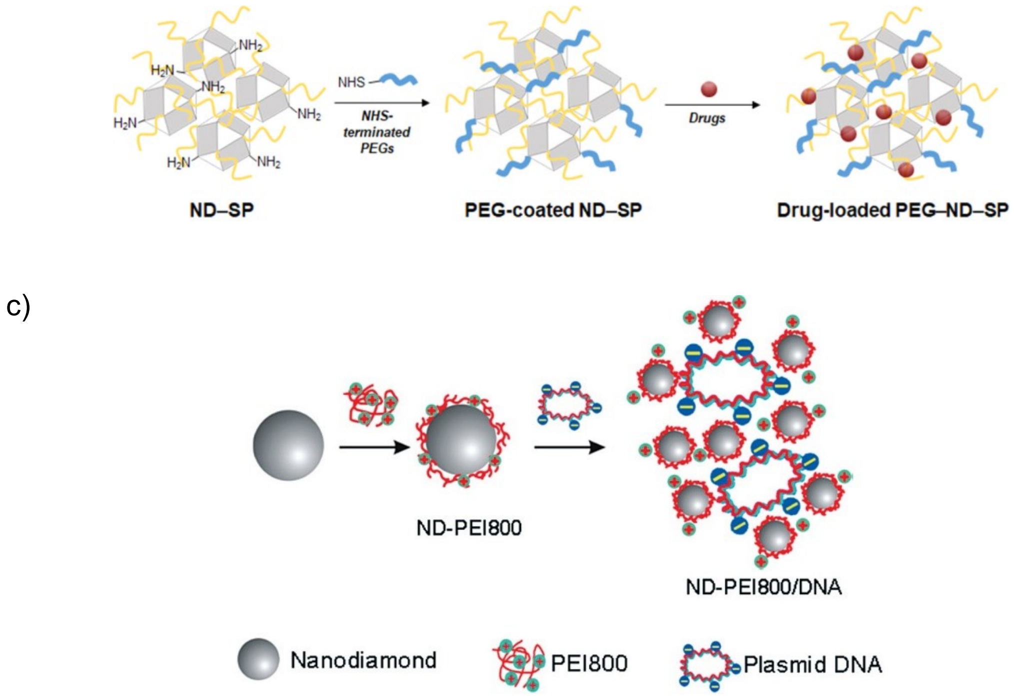

Figure 1-3. DDS applications of DNDs. a) Concept of the approach by the non-covalent complex particle formation, b) Fabrication of supraparticle (SP) from DNDs via surface modification and aggregation (self-assembly) with (anticancer)drug [21] (adapted with permission from *ACS Appl. Mater. Interfaces* **2019**, *11*, 18978–18987. Copyright 2019 American Chemical Society), c) Complexation with DNA (plasmid) on polymer coated DNDs for DNA delivery agent [25] (adapted with permission from *ACS Nano* **2009**, *3*, 2609–2616. Copyright 2009 American Chemical Society).

Besides the use for drug-carriers in chemotherapies mentioned above, DND itself exerts remarkable functions in advanced applications. For example, DNDs may work as API for radio- and photo-sensitizers in radiation and photodynamic therapies, respectively (Figure 1-4) [26–28]. In addition, DNDs are also expected to serve as imaging or sensing agent working in a microenvironment like inside of a cell. The fluorescence from color centers such as nitrogen vacancy (NV) [15, 29–34], silicon vacancy (SiV) and germanium vacancy (GeV) centers (Figure 1-5) [35–38] is applied to diagnostic and "theranostic" purposes. NV center in DNDs has been investigated for long time since DNDs intrinsically contain nitrogen atoms (~ 2%) originated from nitro groups (–NO_2) in the explosives (Figure 1-1). In recent years, SiV or GeV containing DNDs were successfully produced by the detonation of explosive charge with Si or Ge-containing organic compound [36, 38].

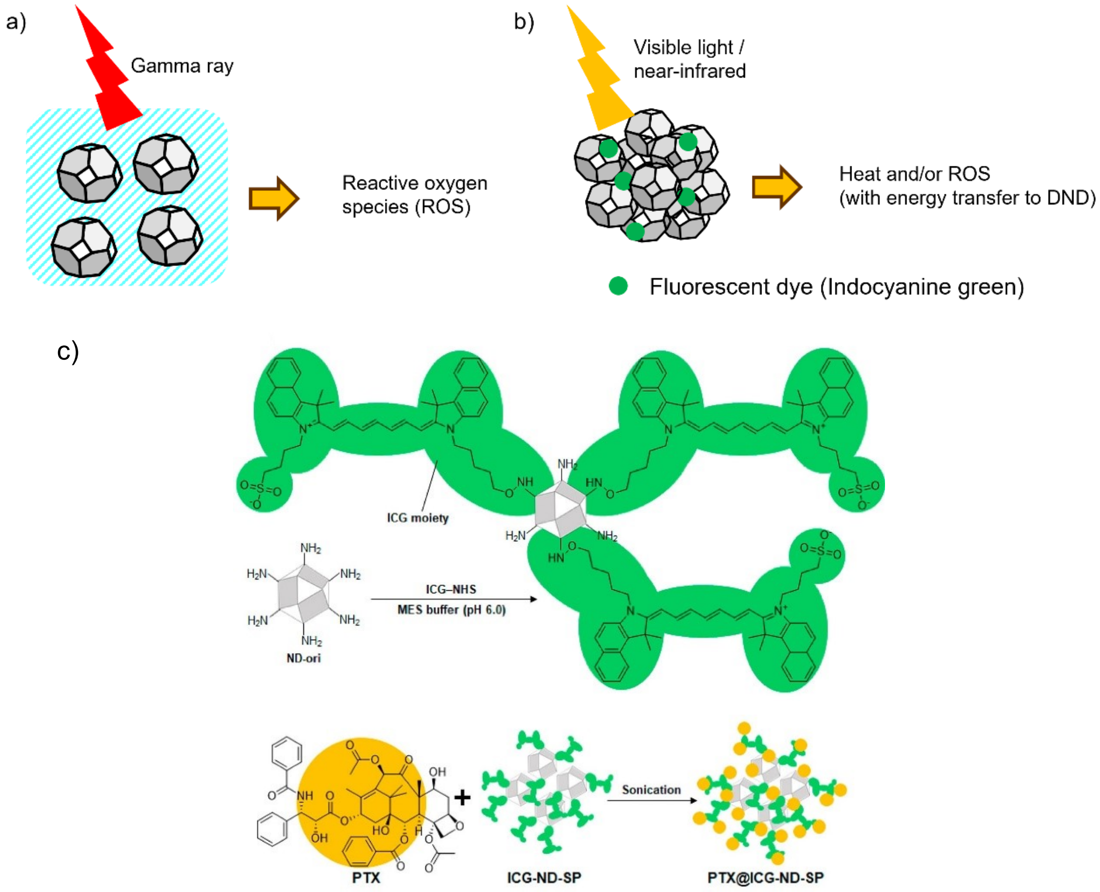

Figure 1-4. DNDs as a) radio- and b) photo-sensitizers. c) Example of radio-sensitizer with fluorescent dye for photodynamic and photothermal therapies [26] (adapted with permission from *ACS Appl. Bio Mater.* **2019**, *2*, 3693–3705. Copyright 2019 American Chemical Society).

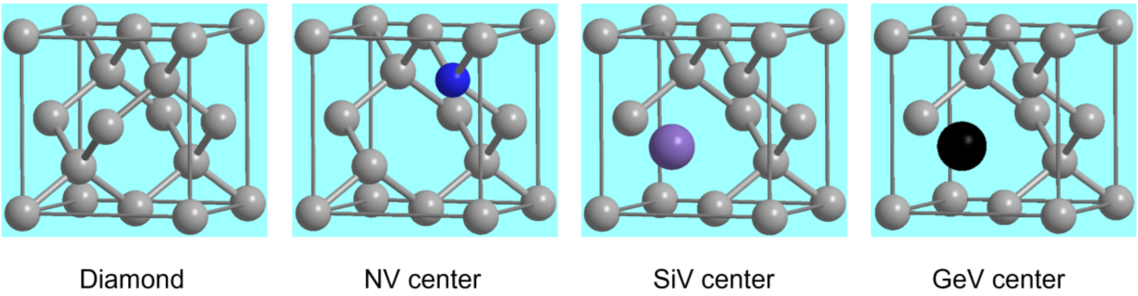

Figure 1-5. Diamond color centers.

1-2. Poly(glycerol) (PG) functionalization

For practical use of nanoparticles (NPs) like *in vivo* applications, the dispersibility of NPs in an aqueous environment such as a physiological one is essential. Bare (unmodified) DNDs are dispersed in water up to 10^{-2} M of ionic strength by electrostatic repulsion between the electric double layers surrounding the surface, known as DLVO theory [39–41]. The potentials of ζ-positive and negative DNDs in pure water are higher and lower than about 35 mV and –35 mV, respectively, and the energy barrier exists where the potential energy of electrostatic repulsion is larger than van der Waals attraction. However, when the ionic strength increases, the energy barrier and the thickness of electrical double layer (Debye length) become lower, and DNDs are getting aggregated and precipitated [39–41]. In addition, electrostatic interaction with proteins or other materials with electric charges would induce aggregation and/or adsorption of DND particles.

Poly (glycerol) (PG) functionalization is one of the most promising solutions to both of above problems for a variety of NPs as hydrophilic polymer coating (Figure 1-6) [42]. The PG coating proceeds through the ring-opening polymerization of glycidol (GD) initiated from the surface of NPs directly, or sometimes the precoated linker molecules [43–45]. Especially, the direct "grafting-from" process without any precoating, under neutral conditions without any additive nor catalyst makes the reaction process simpler and gives denser PG layer than other conditions [46]. While this process is found to apply to various NPs such as superparamagnetic iron oxide (SPION), boron carbide (B_4C) and titanium oxide (TiO_2) NPs [47–49], NDs including DNDs and HPHT-ND have been investigated most intensively for their *in vivo* applications for sensing, imaging [14, 50–60], and treatment [61–63]. Actually, several reviews including PG functionalized NDs (ND-PG) have been published for the recent years [64–70].

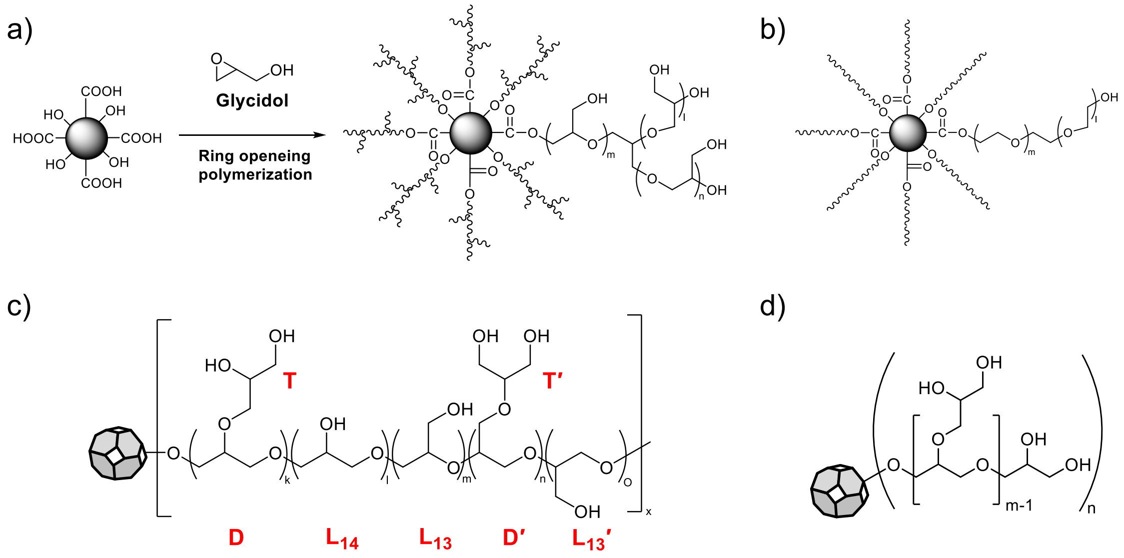

Figure 1-6. a) Synthetic scheme and structure formula representing hyperbranched structure [42]. b) Structure formula of poly(ethylene glycol) (PEG) functionalized NDs (ND-PEG). c) Structure representing various substructures of glycerol unit as discussed in Chapters 2 and 3. d) Simplified structure of ND-PG used in Chapters 4 and 5, although the PG is not complete dendritic structure, as described in Chapter 3 in detail.

For the bifunctionality of glycidol, the resulting PG layer has a hyperbranched structure with numerous hydroxy (–OH) groups. One –OH group is derived from each GD molecule, giving advantageous features to NPs; the high aqueous dispersibility by steric repulsion of hydrophilic polymer layer with higher energy barrier than the electrostatic repulsion [39] and high extensibility for further functionalization through –OH groups as scaffolds [64]. In addition, the PG coating evades the immune response like macrophage uptake by preventing the adsorption of serum proteins, or protein corona formation. The effect of the PG coating is greater than poly(ethylene glycol) (PEG) coated NPs (Figure 1-6b and 1-7a) [71, 72]. This, so-called "stealth effect", would help NPs reach target organ or cells more efficiently for *in vivo* applications [56, 63, 64, 72]. As well, PG functionalization is also applied for *in vitro* application to eliminate non-specific adsorption of NPs to the device (Figure 1-7b) [50].

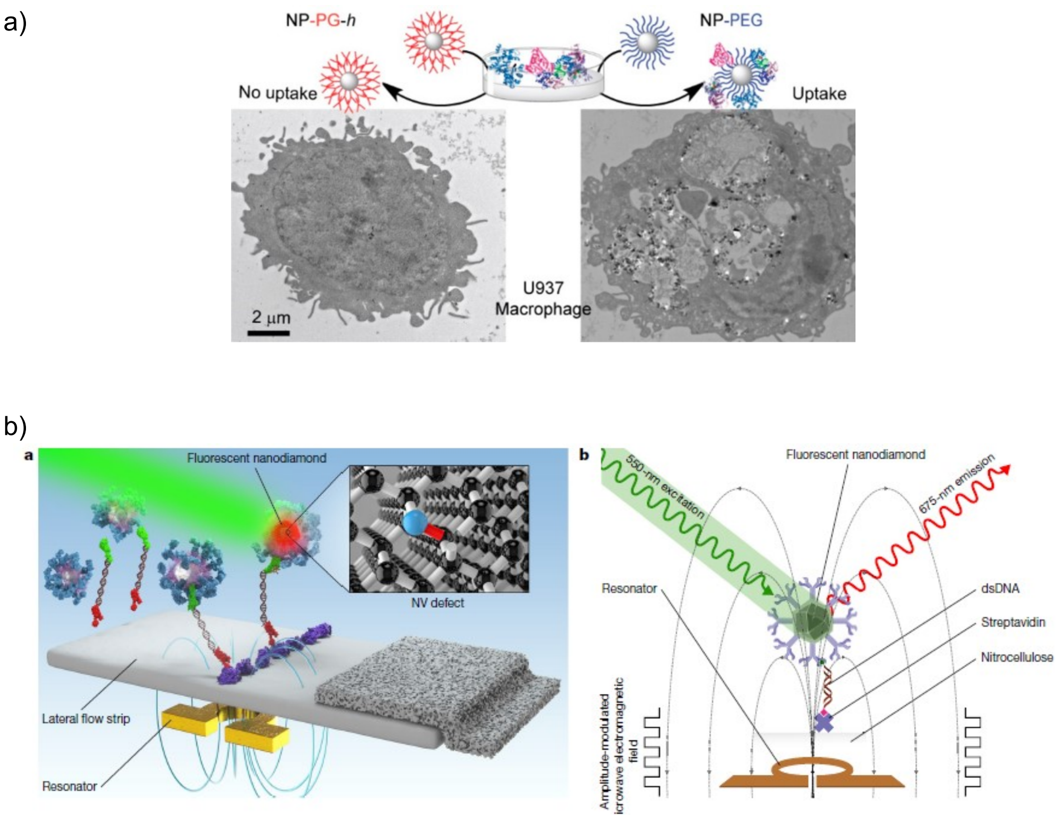

Figure 1-7. Avoiding the immune response and unspecific adsorption of NDs. a) ND-PG prevents protein adsorption on the surface and avoid the macrophage uptake while ND-PEG particles are taken up by the macrophage after the protein adsorption [72] (adapted with permission from *ACS Nano* **2020**, *14*, 7216–7226. Copyright 2020 American Chemical Society). b) Fluorescent NDs are functionalized with PG to avoid nonspecific adsorption to the lateral flow slip in the device. On PG layer, antibody is attached to interact with the target [50] (adapted with permission from B. S. Miller et al, Spin-enhanced nanodiamond biosensing for ultrasensitive diagnostics, *Nature* **2020**, *587*, 588–593. Copyright 2020 Springer Nature).

Further functionalization with biologically active component, active targeting moiety etc. can be achieved via various reactions as exemplified in Figure 1-8. Introduction of another common functional group in the PG layer is meaningful a scaffold to conjugate another functionality [64]. Among the functional groups, amino (–NH_2, DND-PG-NH_2) and carboxylic ones (–COOH, DND-PG-COOH) are useful to covalently bind various functional moieties such as peptides, proteins including antibodies and small molecules like anticancer drugs [53, 60, 61, 63, 71, 73]. Amino group can be introduced via the reduction of azide group (–N_3) by triphenylphosphine (Staudinger reaction). Carboxy groups have been introduced by the reaction of –OH with succinic anhydride in pyridine (Figure 1-8). Azide group is used for the click reaction which also can be a common intermediate [47, 62, 74, 75].

To perform these reactions, it should be important to know the configuration and environment of –OH groups in PG layer. For example, the reactivities of leaving groups from primary and secondary alcohols in substitution (S_N2) reaction are different, and other reactions may also be influenced by the steric hindrance. Information about the proportion between primary and secondary –OH groups is useful especially for quantitative control in the further functionalization. Precise control of the amount of PG layer should also be meaningful. The thickness of PG layer would affect the amounts of attached functional moieties per particle which correlate with dispersibility and performance of the resulting materials.

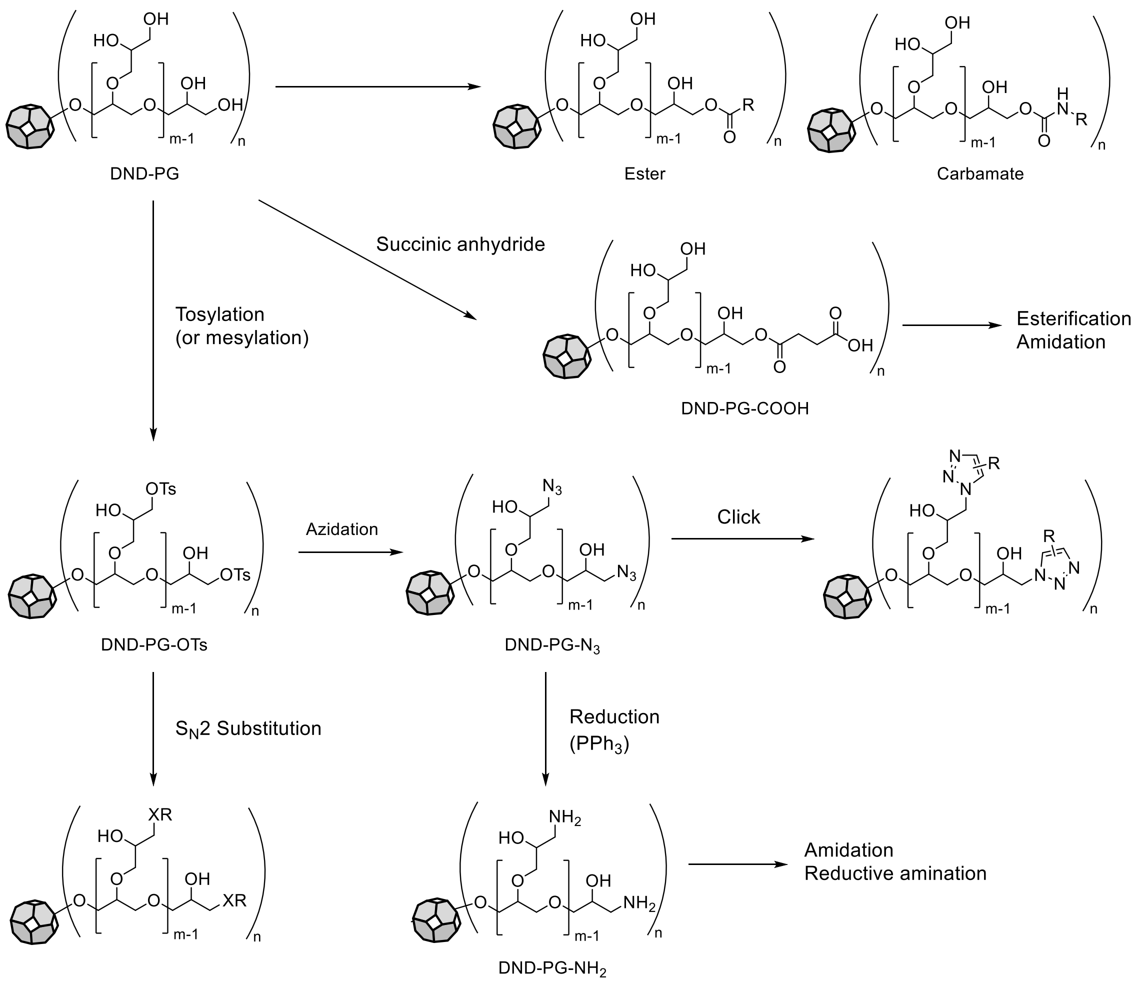

Figure 1-8. Further transformations of DND-PG by various conventional reactions.

1-3. Boron neutron capture therapy (BNCT)

Boron neutron capture therapy (BNCT) is an advanced cancer therapy based on the nuclear fission reaction of ^{10}B(n,α,γ)^{7}Li, in which ^{10}B is advantageous because of its large neutron capture cross-section [76–79]. As the generated α particle (^{4}He) and ^{7}Li nuclei can travel several microns within the cell dimensions, they can selectively kill cancer cells by the selective boron accumulation (Figure 1-9). BNCT is attracting much more attentions in recent years since the accelerator-based cancer treatment has obtained regulatory approval for head and neck cancer in Japan [80–82].

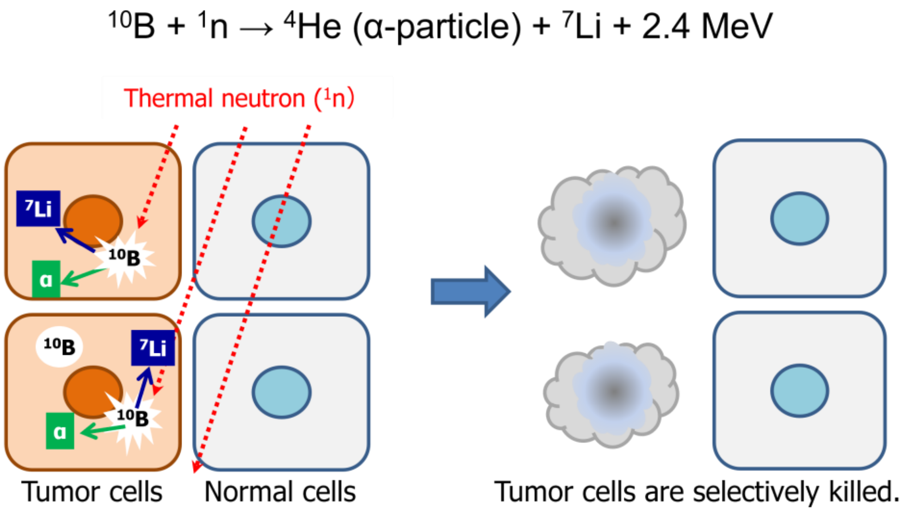

Figure 1-9. Principle of boron neutron capture therapy (BNCT).

As a boron drug, 4-^{10}B-borono-L-phenylalanine (L-BPA) is clinically approved and used at present (Figure 1-10) [83]. It is revealed that L-BPA is selectively internalized by cancer cells through the L-amino acid transporter (LAT1) which is expressed on the cancer cell membrane [84]. L-BPA has an additional advantage that the positron-emission tomography (PET) with ^{18}F-labelled L-BPA (L-FBPA) enables to visualize where L-BPA will be distributed [85]. However, since the penetration of L-BPA through the cell membrane via LAT1 is reversible, L-BPA concentration outside the cell should be high to keep the proper concentration in the cancer cells during neutron irradiation, meaning that the dosage of L-BPA needs to be very high. The ^{10}B concentration in cancer cell is required to be ≥ 25 ppm, which is much higher than anticancer agent in usual chemotherapies. Improvement of the retentivity of ^{10}B drug along with the selective delivery is desired.

On the other hand, ^{10}B-enriched sodium borocaptate, or mercaptoundecahydro-*closo*-dodecaborate (^{10}BSH) (Figure 1-10), a compound of icosahedral boron cluster containing 12 boron atoms, is another compound which has also been used in BNCT clinical study since early times especially for brain cancer [86, 87]. Although ^{10}BSH has high density of boron atoms and hydrophilicity due to the dianion form, the selectivity and retentivity in the tumor are low due to its small molecular size.

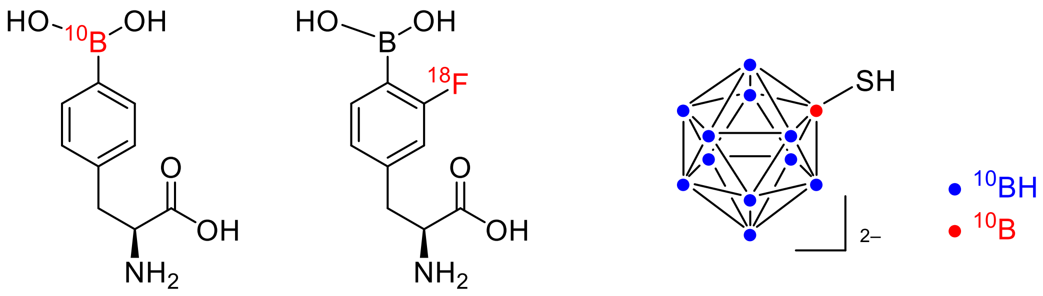

L-BPA L-FBPA ^{10}BSH

Figure 1-10. Structures of L-BPA, L-FBPA and ^{10}BSH.

To solve these intrinsic problems of L-BPA and ^{10}BSH, nanomaterial-based drugs (nanodrugs) including nanoparticles, polymers (as well as oligomers), biopolymers, and micelles have been investigated to improve the retentivity and the selectivity of ^{10}B drugs in and to the tumor tissues and cells [88–91 for review articles]. Conjugation of L-BPA [92], ^{10}BSH [93–101], and other boron containing molecules such as phenylboronic acid with above materials are explored [102, 103]. In addition, a few kinds of boron-containing inorganic NPs such as elemental boron, boron nitride or boron carbide have been reported [49, 104–106]. Combination of BNCT agents with fluorescent or magnetic resonance imaging property would be preferable to establish "theranostic" system as an ultimate goal.

1-4. Scope of the thesis

Final goal of the research regarding this thesis is to demonstrate and discuss the possibility of biomedical application of DNDs to BNCT as one of the promising examples through chemical modification on PG functionalized DNDs (DND-PG). For that, precise and quantitative structural elucidation of DND-PG was explored along with the development of the process enabling precise control of the PG functionalization ratio (PG/DND ratio). Based on these results, BNCT agents (nanodrugs) was designed, prepared by the conjugation of ^{10}B containing moiety, and characterized quantitatively. BNCT efficacies of the nanodrugs were evaluated *in vivo* and *in vitro* by the thermal neutron irradiation experiments.

In the first project described in Chapter 2, precise control of PG content (PG/ND ratio) in ND-PG, including DND and HPHT NDs, was investigated by controlling the amount of GD and solvent (ethylene glycol). The relationship of the PG content to the surface functional group content and particle size was also discussed. In addition, thorough structural elucidation in terms of the proportion in the substructures of glycidol unit and the size of PG layer was analyzed by ^{13}C nuclear magnetic resonance spectroscopy (NMR) and dynamic light scattering (DLS), respectively. In the second project (Chapter 3), conversion of primary alcohol in PG layer into –COOH group via the oxidation using nitroxyl radical catalyst and quantitative analysis of the reaction were conducted. The resulting –COOH containing DND-PG (DND-PG-COOH) can serve for further modification. In the third project (Chapter 4), BNCT agent with ^{10}B enriched phenylboronic acid (PBA) was designed and prepared via amino (–NH$_2$) group containing DND-PG (DND-PG-NH$_2$). The pharmacokinetics study and *in vivo* BNCT efficacy evaluation were performed to observe significant difference with and without ^{10}B nanodrug on thermal neutron irradiation. In the fourth project (Chapter 5) using DND-PG-COOH, another BNCT nanodrugs were designed by the conjugation of ^{10}B enriched boron cluster ($^{10}B_{12}H_{11}^{2-}$) and active targeting moiety such as PBA and RGD peptide. Resulting nanodrugs exhibited high BNCT efficacy by *in* *vitro* thermal neutron irradiation although targeting efficiency by PBA and RGD peptide was not significant. Behaviors in cellular uptake were observed and discussed by transmission electron microscopy (TEM) analysis.

Chapter 2: Thorough elucidation of synthesis and structure of poly(glycerol) functionalized nanodiamonds

2-1. Introduction

Despite the wide-spread use of the simple process, the “grafting from” methodology to obtain ND-PG has not been extended to be scalable and controllable. In addition, the detailed molecular structure of PG on the ND surface is elusive, though the polymer structure and polymerization mechanism were reported for the PG without any core materials, namely free PG [107–110]. The recent investigation on the colloidal stability of DND-PG also motivated us to elucidate the chemical structure of PG on the surface of NDs [39].

In this work, we developed a PG functionalization process through dropwise addition of GD to ND suspension in ethylene glycol (EG), making the process safer and scalable by keeping the concentration of GD much lower than the previous conditions without solvent during the reaction. The thorough elucidation of the reactions enabled us to control the PG amount for NDs theoretically by the properties of ND (diameter and oxygen content) and the reaction conditions (weights of GD, ND and EG). The chemical structures of these ND-PG were elucidated by ^{13}C NMR measurements using inverse gated decoupling and dynamic light scattering (DLS) measurements in various media with different ionic strength. These elucidations should give us an insight for structural design of PG functionalized NPs (NP-PGs) for advanced applications and fundamental understanding of various phenomena of NP-PGs.

2-2. Results and discussion

2-2-1. Elucidation of the scalable and controllable synthesis of ND-PG

PG functionalization was employed for four kinds of NDs; DNDs of 4 – 6 nm in their primary particle sizes with positive and negative ζ-potentials (DND(+) and DND(–), respectively), and HPHT-ND of 50 nm-size (ND50) with and without acid treatment (ND50(A) and ND50(N), respectively). DND(+) and DND(–) were prepared by annealing of DND with hydrogen and oxygen, respectively (see details in 2-4. Experimental) [28, 111]. ND50(A) and ND50(N) were prepared from as-received ND50 by treating with a mixture of H_2SO_4 and HNO_3 and by drying to remove adsorbed moisture, respectively. The oxygen contents in these NDs (O_{ND}) were determined by elemental analysis to estimate the number of oxygen-containing functional groups on the surface (Table 2-1).

In the case of free PG without ND core, it is known that the degree of polymerization is controlled by the ratio between GD and a substrate (alcohol, acid or alkoxide) under homogeneous conditions [107–110]. Although the PG/ND ratio is reported to be controlled in the PG functionalization of ND by the reaction temperature and time [71], the reaction should not be controlled appropriately, as the scale increases, due to the large heat generation by GD (92 – 109 kJ/mol for a similar epoxy compound [112]). To make the reaction much safer, more scalable and more controllable, we added GD dropwise into DND suspension in EG [113]. EG was used as a solvent because of the high boiling point (197 °C) above the reaction temperature of the PG functionalization and high polarity to dissolve GD and disperse ND-PG (Figure 2-1), though the starting materials, DND and ND50, were not fully dispersed.

Under the conditions to add GD dropwise to the ND suspension in EG, the PG content was controlled by changing the amounts of GD and EG, and the reaction temperatures to give ten kinds of ND-PG in addition to DND(+) with extra-high PG content (DND(+)-PG(xh)) prepared under the previous conditions without solvent [62]; DND(+)-PG(xl), -PG(l), -PG(m), -PG(h), DND(–)-PG(l), -PG(m), -PG(h), ND50(N)-PG(l), -PG(m), and ND50(A)-PG where xl, l, m and h denote the extra-low, low, medium and high PG contents, respectively (Table 2-1). For DND-PGs, the amount of EG (W_{EG}) as a solvent was determined so that the final concentration of DND is 1.6 – 2 wt%. The final weight of GD over ND weight (W_{GD}/W_{ND}) was adjusted according to the PG content from 0.324 (xl) to 0.833 (xh). The PG/ND weight ratios (W_{PG}/W_{ND}) and PG contents ($W_{PG}/(W_{PG}+W_{ND})$) were determined by thermogravimetric analysis (TGA) shown in Table 2-1 and 2-2, and Figures 2-2 and 2-3. The PG contents are also calculated based on the results of elemental analysis shown in Tables 2-3 and 2-4, giving consistent results with those determined by TGA.

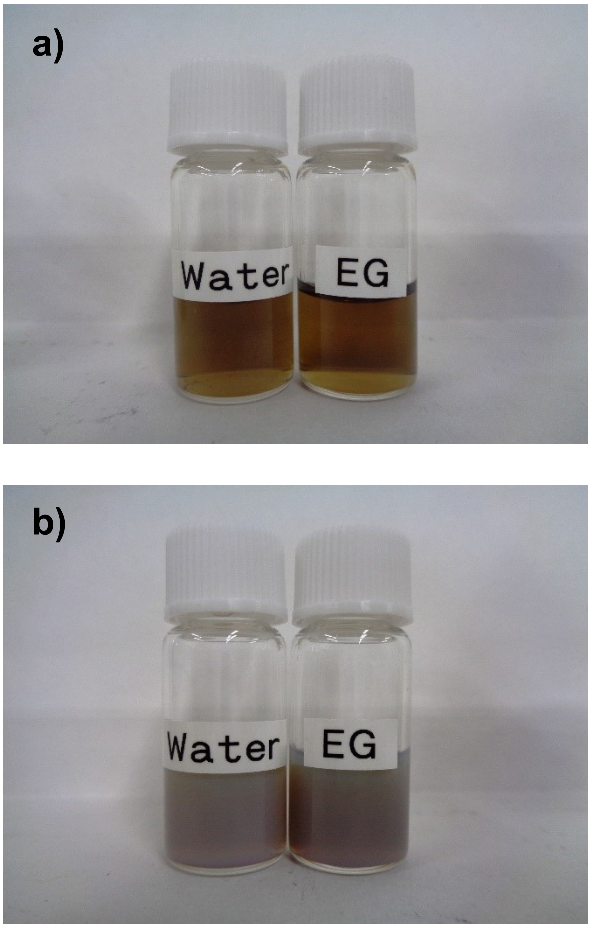

Figure 2-1. Appearance of dispersions in water and ethylene glycol (EG) of (a) DND(+)-PG(m), and (b) ND50(N)-PG(m). Concentration of all dispersions is 0.5 wt% as ND core.

Table 2-1. Summary of ND property, reaction conditions and results in PG functionalization of NDs. See Table 2-2 for detailed TGA results.

	DND(+)-PG(xl)	DND(+)-PG(l)	DND(+)-PG(m)	DND(+)-PG(h)	DND(+)-PG(xh)	DND(–)-PG(l)	DND(–)-PG(m)	DND(–)-PG(h)
ND (raw material)								
Oxygen content (O_{ND}, × 10^{-2}) *	5.14	5.14	4.84	4.84	4.84	9.51	9.51	9.51
Reaction condition								
Ethylene glycol (EG) ($W_{\mathrm{EG}}/W_{\mathrm{ND}}$)	30.0	30.0	15.0	7.50	---	30.0	30.0	15.0
Glycidol (GD) ($W_{\mathrm{GD}}/W_{\mathrm{ND}}$)	22.4	30.0	45.0	52.7	65.7	22.5	30.0	45.0
Temperature (°C)	100	100	100	100	140	100	100	100
Results								
PG/ND ratio by TGA ($W_{\mathrm{PG}}/W_{\mathrm{ND}}$)	0.48	0.99	2.29	2.80	4.99	1.43	1.84	3.62
PG content ($W_{\mathrm{PG}}/(W_{\mathrm{PG}}+W_{\mathrm{ND}})$)	0.324	0.498	0.696	0.737	0.833	0.588	0.648	0.784
Consumption of GD ($W_{\mathrm{PG}}/W_{\mathrm{GD}}$)	0.0214	0.0330	0.0509	0.0531	0.0760	0.0635	0.0613	0.0804

Table 2-1 (continued).

	ND50(N)-PG(l)	ND50(N)-PG(m)	ND50(A)-PG
ND (raw material)			
Oxygen content (O_{ND}, × 10^{-2}) *	2.69	2.69	2.92
Reaction condition			
Ethylene glycol (EG) ($W_{\mathrm{EG}}/W_{\mathrm{ND}}$)	6.50	6.50	6.84
Glycidol (GD) ($W_{\mathrm{GD}}/W_{\mathrm{ND}}$)	80	108	107
Temperature (°C)	140	140	140
Results			
PG/ND ratio by TGA ($W_{\mathrm{PG}}/W_{\mathrm{ND}}$)	0.69	0.85	1.19
PG content ($W_{\mathrm{PG}}/(W_{\mathrm{PG}}+W_{\mathrm{ND}})$)	0.408	0.458	0.542
Consumption of GD ($W_{\mathrm{PG}}/W_{\mathrm{GD}}$)	0.00861	0.00787	0.0111

* Determined by elemental analysis.

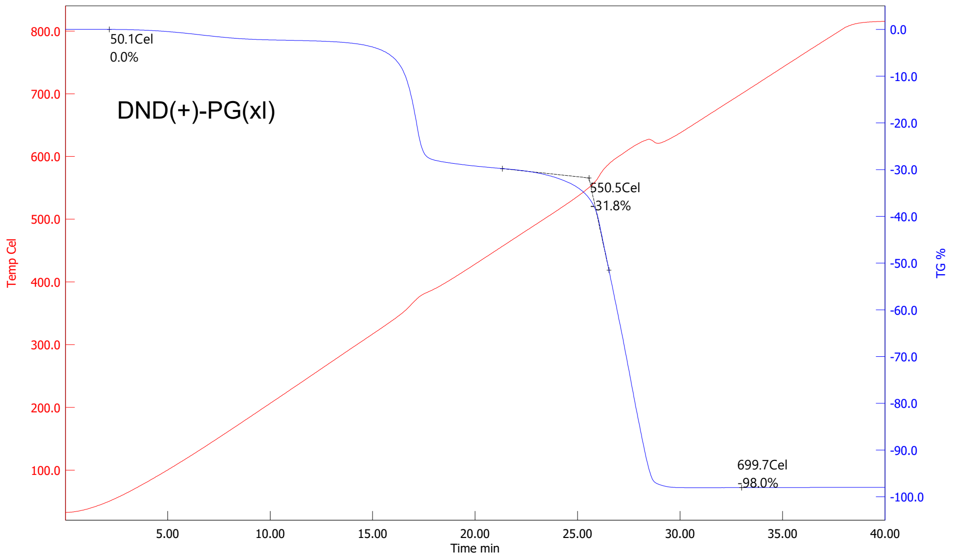
DND(+)-PG(xl)
50.1Cel
0.0%
550.5Cel
-31.8%
699.7Cel
-98.0%
Temp Cel
800.0
700.0
600.0
500.0
400.0
300.0
200.0
100.0
TG %
0.0
-10.0
-20.0
-30.0
-40.0
-50.0
-60.0
-70.0
-80.0
-90.0
-100.0
5.00
10.00
15.00
20.00
25.00
30.00
35.00
40.00
Time min

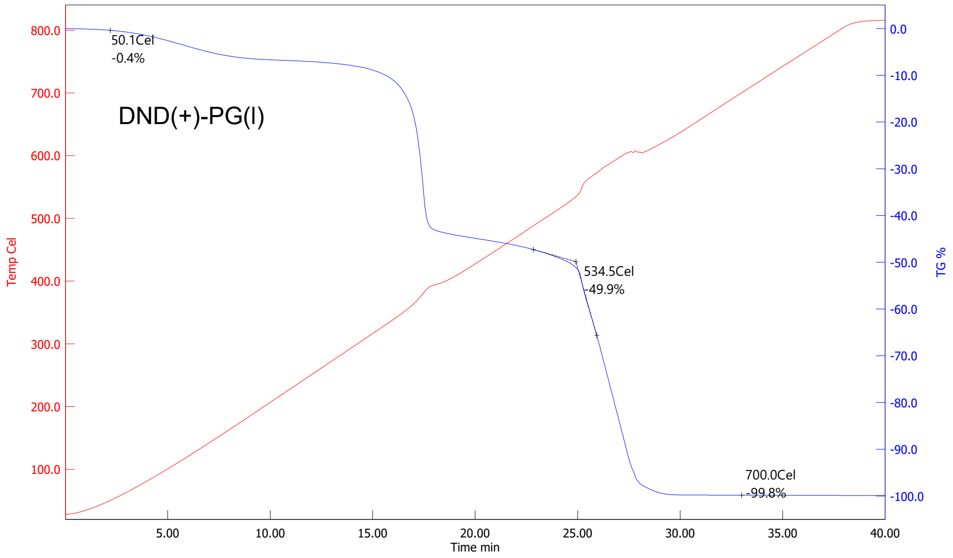
DND(+)-PG(l)
50.1Cel
-0.4%
534.5Cel
-49.9%
700.0Cel
-99.8%
Temp Cel
800.0
700.0
600.0
500.0
400.0
300.0
200.0
100.0
TG %
0.0
-10.0
-20.0
-30.0
-40.0
-50.0
-60.0
-70.0
-80.0
-90.0
-100.0
5.00
10.00
15.00
20.00
25.00
30.00
35.00
40.00
Time min

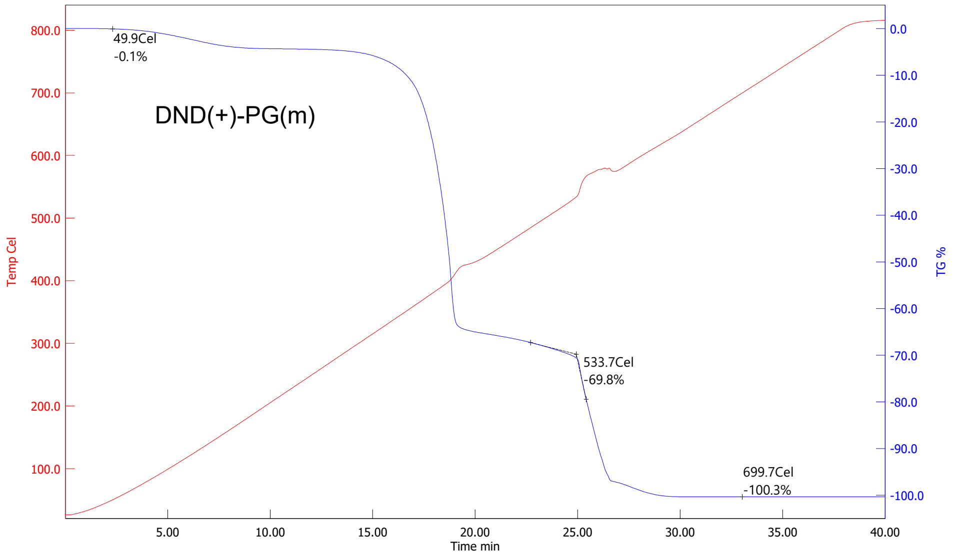
DND(+)-PG(m)
49.9Cel
-0.1%
533.7Cel
-69.8%
699.7Cel
-100.3%
Temp Cel
800.0
700.0
600.0
500.0
400.0
300.0
200.0
100.0
TG %
0.0
-10.0
-20.0
-30.0
-40.0
-50.0
-60.0
-70.0
-80.0
-90.0
-100.0
5.00
10.00
15.00
20.00
25.00
30.00
35.00
40.00
Time min

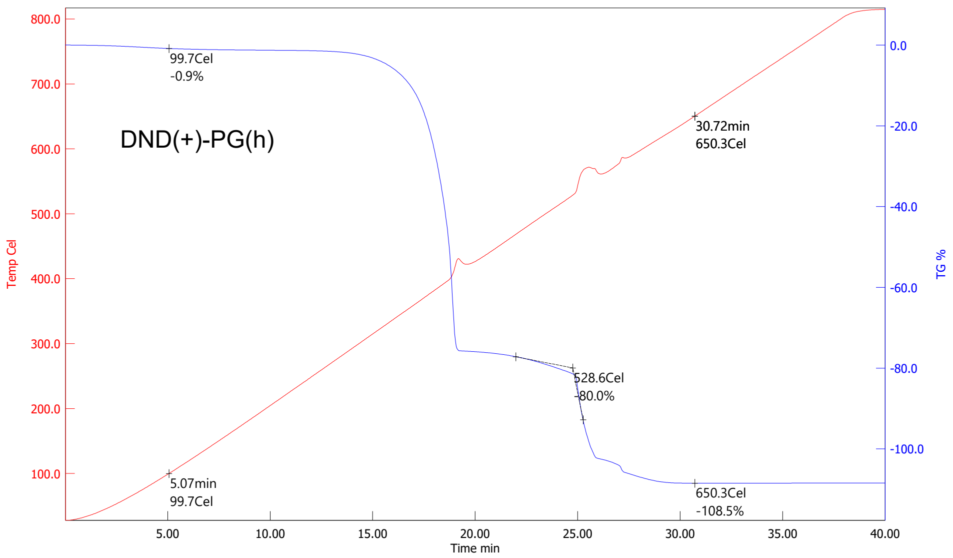
DND(+)-PG(h)
Temp Cel
800.0
700.0
600.0
500.0
400.0
300.0
200.0
100.0
TG %
0.0
-20.0
-40.0
-60.0
-80.0
-100.0
5.00
10.00
15.00
20.00
25.00
30.00
35.00
40.00
Time min
99.7Cel
-0.9%
30.72min
650.3Cel
528.6Cel
-80.0%
5.07min
99.7Cel
650.3Cel
-108.5%

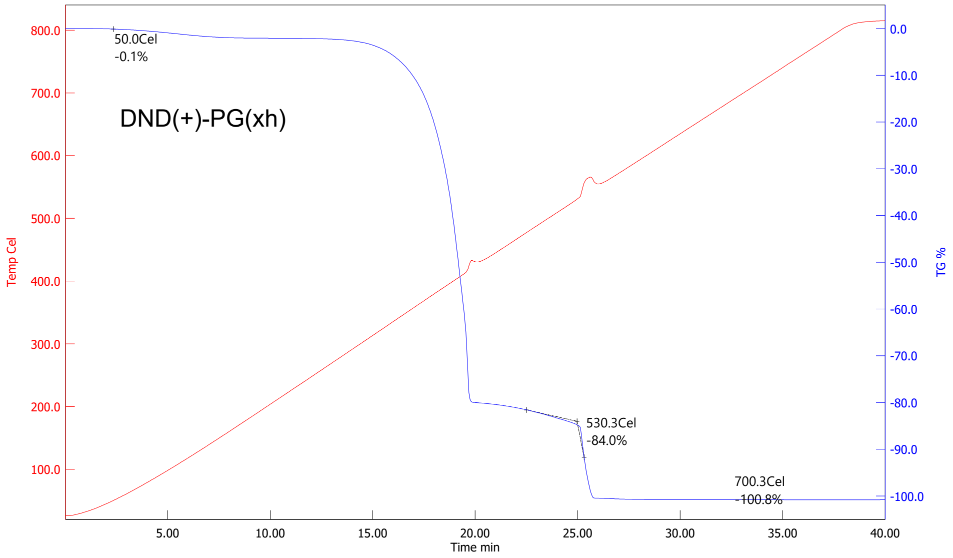
DND(+)-PG(xh)
Temp Cel
800.0
700.0
600.0
500.0
400.0
300.0
200.0
100.0
TG %
0.0
-10.0
-20.0
-30.0
-40.0
-50.0
-60.0
-70.0
-80.0
-90.0
-100.0
5.00
10.00
15.00
20.00
25.00
30.00
35.00
40.00
Time min
50.0Cel
-0.1%
530.3Cel
-84.0%
700.3Cel
-100.8%

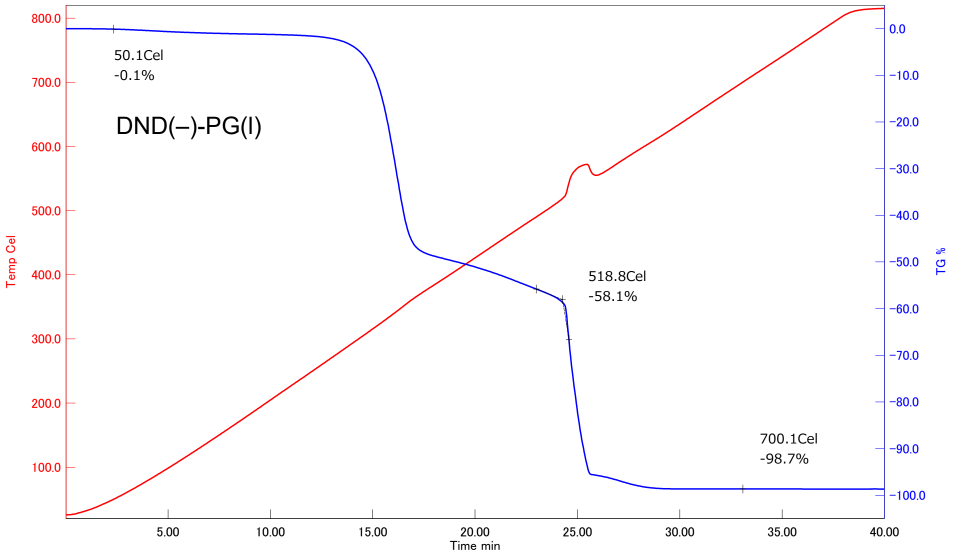
DND(–)-PG(l)
Temp Cel
800.0
700.0
600.0
500.0
400.0
300.0
200.0
100.0
TG %
0.0
-10.0
-20.0
-30.0
-40.0
-50.0
-60.0
-70.0
-80.0
-90.0
-100.0
5.00
10.00
15.00
20.00
25.00
30.00
35.00
40.00
Time min
50.1Cel
-0.1%
518.8Cel
-58.1%
700.1Cel
-98.7%

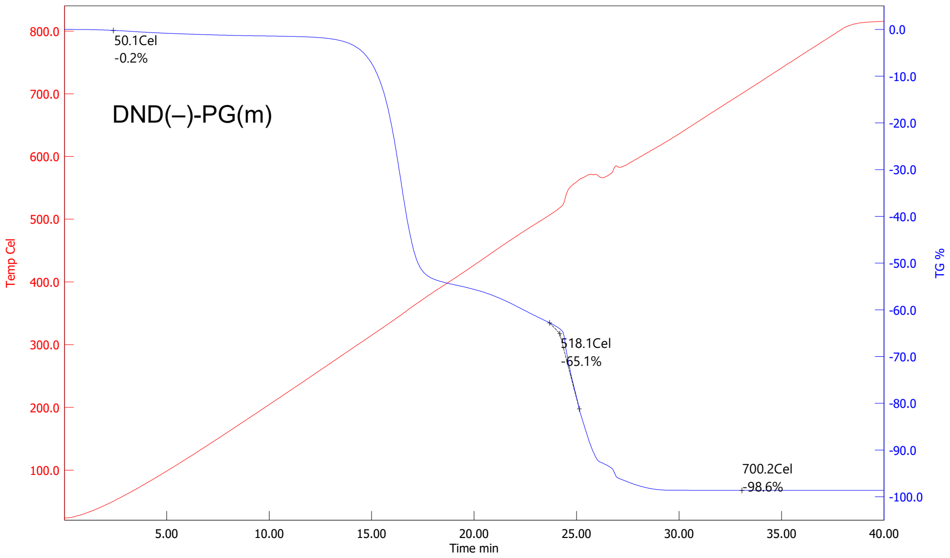
DND(–)-PG(m)
Temp Cel
800.0
700.0
600.0
500.0
400.0
300.0
200.0
100.0
TG %
0.0
-10.0
-20.0
-30.0
-40.0
-50.0
-60.0
-70.0
-80.0
-90.0
-100.0
5.00
10.00
15.00
20.00
25.00
30.00
35.00
40.00
Time min
50.1Cel
-0.2%
518.1Cel
-65.1%
700.2Cel
-98.6%

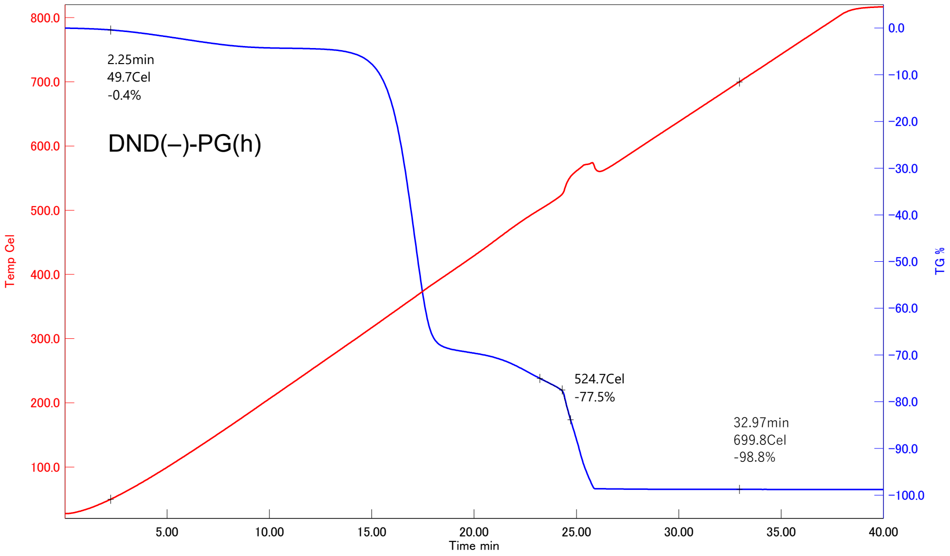
DND(–)-PG(h)
Temp Cel
800.0
700.0
600.0
500.0
400.0
300.0
200.0
100.0
TG %
0.0
-10.0
-20.0
-30.0
-40.0
-50.0
-60.0
-70.0
-80.0
-90.0
-100.0
5.00
10.00
15.00
20.00
25.00
30.00
35.00
40.00
Time min
2.25min
49.7Cel
-0.4%
524.7Cel
-77.5%
32.97min
699.8Cel
-98.8%

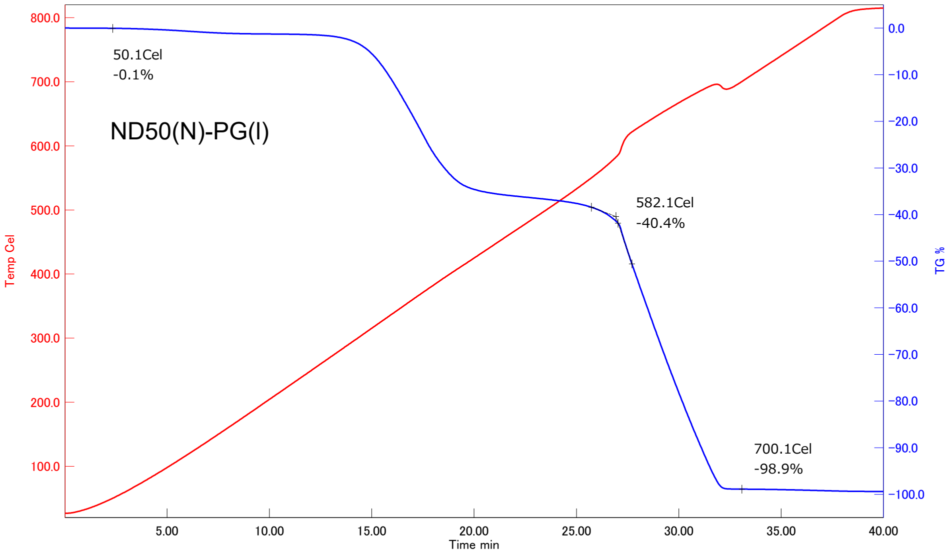
ND50(N)-PG(l)
Temp Cel
800.0
700.0
600.0
500.0
400.0
300.0
200.0
100.0
TG %
0.0
-10.0
-20.0
-30.0
-40.0
-50.0
-60.0
-70.0
-80.0
-90.0
-100.0
5.00
10.00
15.00
20.00
25.00
30.00
35.00
40.00
Time min
50.1Cel
-0.1%
582.1Cel
-40.4%
700.1Cel
-98.9%

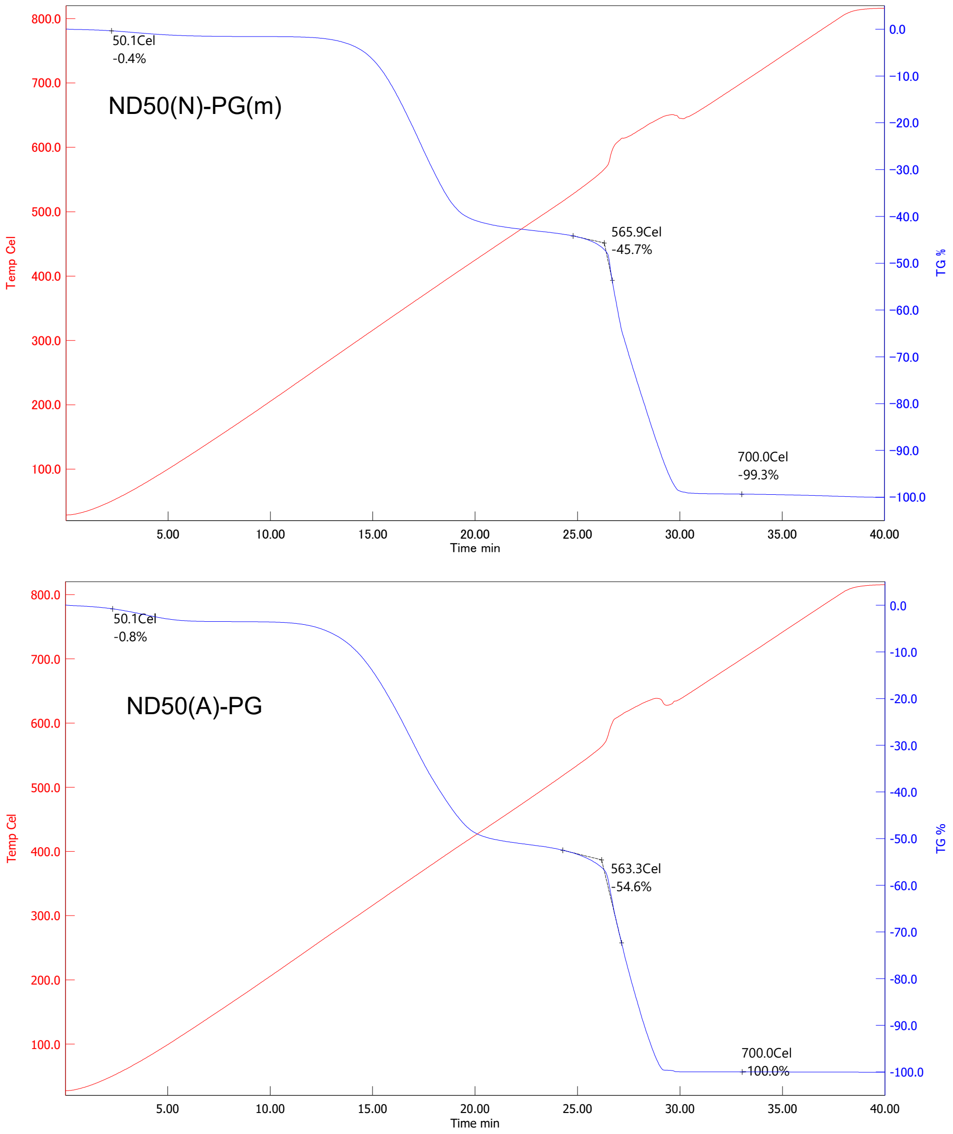

Figure 2-2. TGA results of DND-PGs and ND50-PGs. All measurements were done in air at 20 °C/min of temperature increasing rate. In each profile, the weight loss at the lower and higher temperatures is assigned to the modified PG layer and the ND core. The values of TG% indicated in the charts are subsequently normalized so that the difference between 50 °C and 700 °C is 100.0% to determine PG/ND (Table 2-2).

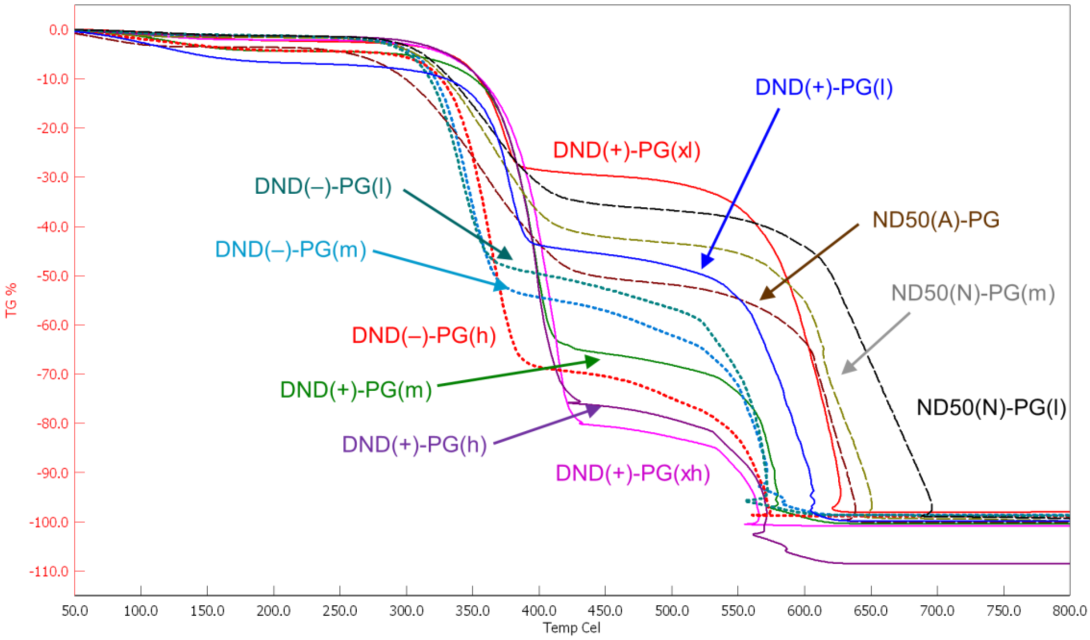

Figure 2-3. Overwriting of all data of TGA results.

Table 2-2. Summary of TGA results.

	DND(+)-PG(xl)	DND(+)-PG(l)	DND(+)-PG(m)	DND(+)-PG(h)	DND(+)-PG(xh)	ND(–)-PG(l)	ND(–)-PG(m)	ND(–)-PG(h)
PG (%)	32.4	49.8	69.6	73.7	83.3	58.8	64.8	78.4
ND (%)	67.6	50.2	30.4	26.3	16.7	41.2	35.2	21.6
PG/ND ($W_{\mathrm{PG}}/W_{\mathrm{ND}}$)	0.48	0.99	2.29	2.80	4.99	1.43	1.84	3.62

	ND50(N)-PG(l)	ND50(N)-PG(m)	ND50(A)-PG
PG (%)	40.8	45.8	54.2
ND (%)	59.2	54.2	45.8
PG/ND ($W_{\mathrm{PG}}/W_{\mathrm{ND}}$)	0.69	0.85	1.19

Table 2-3. Results of elemental analysis.

	Elemental analysis results (%)			
	H	C	N	O
DND(+)-1 *	1.37	89.67	2.26	5.14
DND(+)-2 **	1.29	87.61	2.20	4.84
DND(–)	1.00	81.70	2.14	9.51
ND50(A)	0.20	95.97	0.00	2.92
ND50(N)	0.15	95.61	0.07	2.69
DND(+)-PG(xl) *	3.32	76.87	1.51	16.59
DND(+)-PG(l) *	4.19	71.40	1.21	21.78
DND(+)-PG(m) **	5.93	60.53	0.70	31.84
DND(+)-PG(h) **	6.52	57.39	0.61	35.24
DND(+)-PG(xh) **	7.05	54.81	0.48	37.60
DND(–)-PG(l)	4.82	64.55	1.11	29.23
DND(–)-PG(m)	5.42	60.46	0.81	28.55
DND(–)-PG(h)	6.53	55.65	0.51	36.48
ND50(N)-PG(l)	3.65	75.73	0.09	25.01
ND50(N)-PG(m)	4.05	71.60	0.00	24.42
ND50(A)-PG	4.69	67.05	0.00	24.76

* DND(+)-1 was used for DND(+)-PG(xl) and DND(+)-PG(l).

** DND(+)-2 was used for DND(+)-PG(m), DND(+)-PG(h) and DND(+)-PG(xh).

Table 2-4. PG content calculated by the results of elemental analysis.

	DND(+)-PG(xl)	DND(+)-PG(l)	DND(+)-PG(m)	ND(+)-PG(h)	DND(+)-PG(xh)	DND(–)-PG(l)	DND(–)-PG(m)	DND(–)-PG(h)
C_{ND} (%)	89.67	89.67	87.61	87.61	87.61	81.70	81.70	81.70
$C_{\mathrm{ND\text{-}PG}}$ (%)	76.87	71.40	60.53	57.39	54.81	64.55	60.46	55.65
C_{GD} (%)	48.64	48.64	48.64	48.64	48.64	48.64	48.64	48.64
PG content by C (%)	31.20	44.54	69.49	77.55	84.18	51.88	64.25	78.81
N_{ND} (%)	2.26	2.26	2.20	2.20	2.20	2.14	2.14	2.14
$N_{\mathrm{ND\text{-}PG}}$ (%)	1.51	1.21	0.70	0.61	0.48	1.11	0.81	0.51
N_{GD} (%)	0	0	0	0	0	0	0	0
PG content by N (%)	33.19	46.68	68.11	72.21	78.36	48.01	62.30	76.35
O_{ND} (%)	5.14	5.14	4.84	4.84	4.84	9.51	9.51	9.51
$O_{\mathrm{ND\text{-}PG}}$ (%)	16.59	21.78	31.84	35.24	37.60	29.23	28.55	36.48
O_{GD} (%)	43.19	43.19	43.19	43.19	43.19	43.19	43.19	43.19
PG content by O (%)	30.10	43.73	70.39	79.27	85.41	58.55	56.52	80.08

Table 2-4 (continued).

	ND50(N)-PG(l)	ND50(N)-PG(m)	ND50(A)-PG
C_{ND} (%)	95.61	95.61	95.97
$C_{\text{ND-PG}}$ (%)	75.73	71.60	67.06
C_{GD} (%)	48.64	48.64	48.64
PG content by C (%)	42.80	51.11	61.09
N_{ND} (%)	---	---	---
$N_{\text{ND-PG}}$ (%)	---	---	---
N_{GD} (%)	---	---	---
PG content by N (%)	---	---	---
O_{ND} (%)	2.69	2.69	2.92
$O_{\text{ND-PG}}$ (%)	25.01	24.42	24.76
O_{GD} (%)	43.19	43.19	43.19
PG content by O (%)	55.11	53.65	54.24

PG content in ND-PG can be calculated by the following equations:

$$PG\ content\ by\ C(\%) = \frac{C_{\text{ND-PG}} - C_{\text{ND}}}{C_{\text{GD}} - C_{\text{ND}}} \times 100$$

$$PG\ content\ by\ N(\%) = \frac{N_{\text{ND-PG}} - N_{\text{ND}}}{N_{\text{GD}} - N_{\text{ND}}} \times 100$$

$$PG\ content\ by\ O(\%) = \frac{O_{\text{ND-PG}} - O_{\text{ND}}}{O_{\text{GD}} - O_{\text{ND}}} \times 100$$

Where:

$C, N, O_{\text{ND-PG}}$: C, N or O content in ND-PG by elemental analysis.

C, N, O_{ND}: C, N or O content on ND core (raw material) by elemental analysis.

C, N, O_{GD}: C, N or O content in glycidol (calculated value).

As shown in Figure 2-4, W_{PG}/W_{GD} corresponding to the weight of GD immobilized on the ND surface (W_{PG}) against total amount of GD (W_{GD}) is found to be proportional to W_{GD} against the weight of DND(+) ($W_{DND(+)}$), namely $W_{GD}/W_{DND(+)}$. The larger PG content is obtained in DND(+)-PG(xh) under the previously reported conditions, which are different from those in the reactions for the other DND(+)-PGs. That is, a suspension of DND(+) in GD without EG was reacted at higher temperature, instead of dropwise addition of GD to DND(+) suspension in EG (see the details in 2-4 Experimental). Surprisingly, the result of DND(+)-PG(xh) is placed on the linear plots drawn by those of the other DND(+)-PGs (blue squares with blue dotted line in Figure 2-4). The following eq. (1) is derived from Figure 2-4 and Table 2-1.

$$W_{\mathrm{PG}}/W_{\mathrm{GD}} = 0.00110 \times W_{\mathrm{GD}}/W_{\mathrm{DND(+)}} \qquad \text{eq. (1)}$$

$$W_{\mathrm{PG}} = 0.00110 \times {W_{\mathrm{GD}}}^2/W_{\mathrm{DND(+)}} \qquad \text{eq. (2)}$$

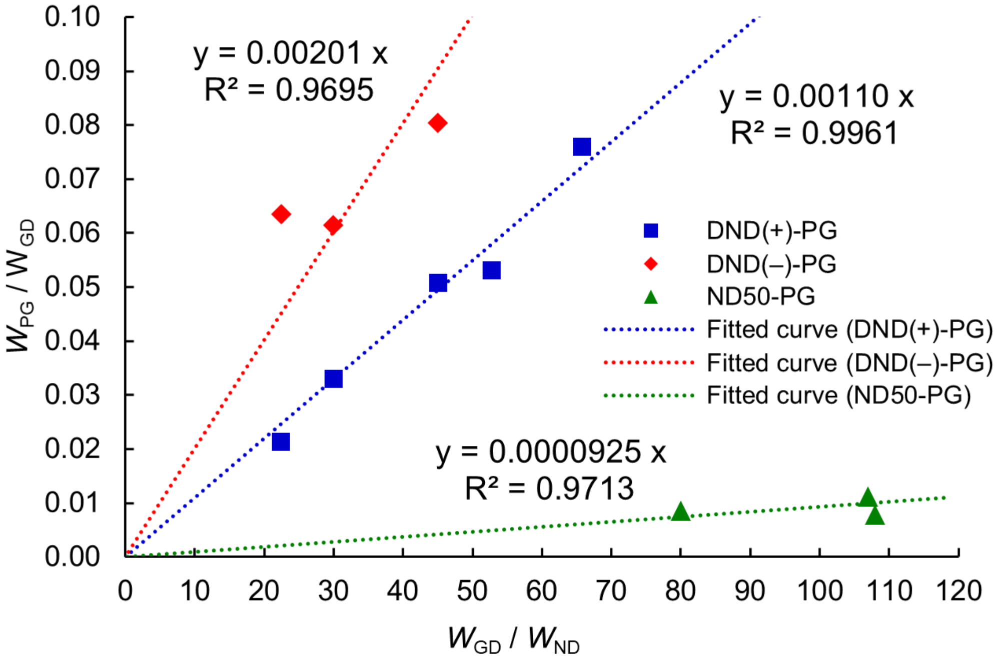

Figure 2-4. Relationships of the experimental results (W_{PG}/W_{GD}) with the calculated values from the eq. (1) based on the reaction conditions (W_{GD} and W_{ND}).

The eq. (2) derived from eq. (1) indicates that W_{PG} is proportionate to the square of W_{GD}. This can be interpreted by the reaction mechanism; one GD molecule reacted with PG chain generates two hydroxy groups in either cationic or anionic mechanism (Figure 2-5), which can react with two GD molecules to increase W_{PG} quadratically. The eq. (2) also shows that W_{PG} can be determined solely by W_{GD} and $W_{\mathrm{DND(+)}}$, not by the concentrations of DND(+) and GD ($W_{\mathrm{DND(+)}}/W_{\mathrm{EG}}$ and $W_{\mathrm{GD}}/W_{\mathrm{EG}}$, respectively) nor by the reaction temperature. These phenomena indicate that the reactions of GD with EG and GD are much slower than those of GD with PG in ND-PG and/or free PG in the reaction mixture. In other words, the hydroxy groups in EG and GD are much less reactive than those in PG. It may be connected to the differences in p*K*a of EG (15.1) and GD (14.6) to PG (or glycerol, 13.5~14.4). To confirm this experimentally, the reactions under more diluted conditions were conducted in 3, 5 and 6 times larger $W_{\mathrm{EG}}/W_{\mathrm{DND(+)}}$, corresponding to DND(+)-PG(m)-d1, -d2 and -d3 in Table 2-5 respectively, than that in DND(+)-PG(m) in Table 2-1.

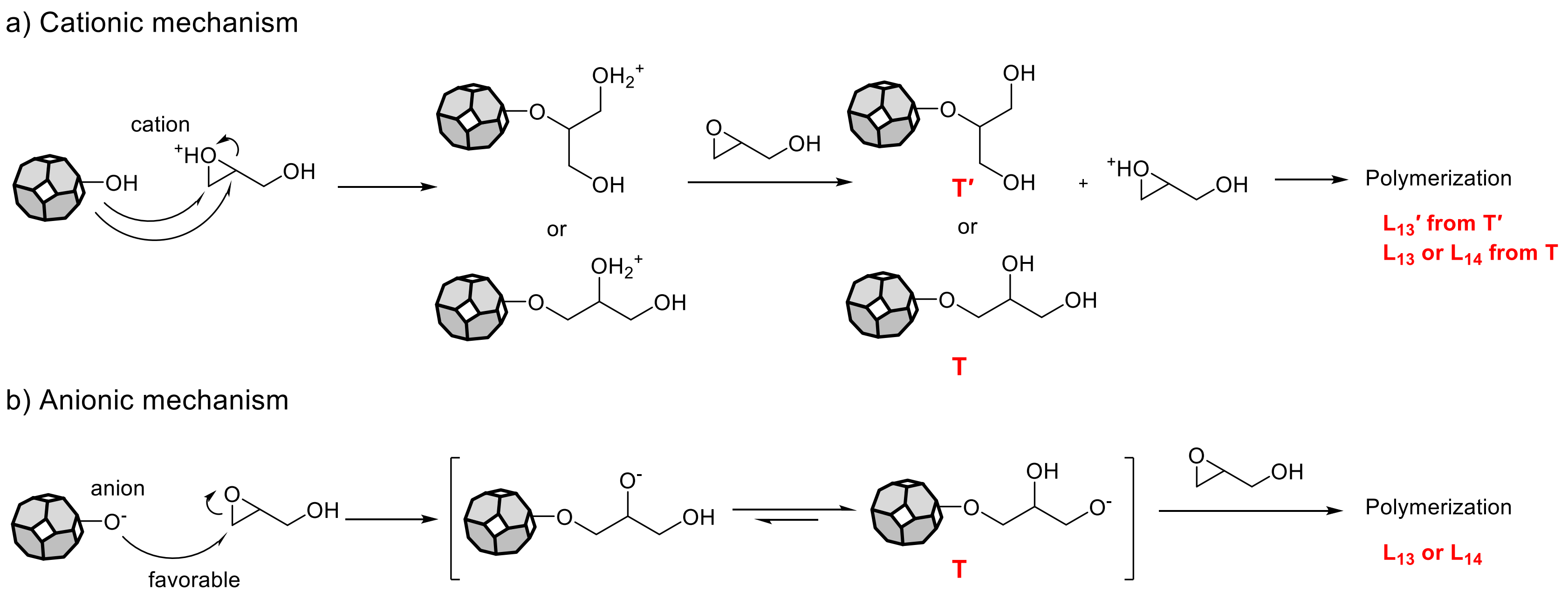

Figure 2-5. a) Cationic and b) anionic mechanisms in ring-opening polymerization of GD on ND surface. The red letters stand for the substructures shown in Figure 2-12.

Table 2-5. Summary of ND property, reaction conditions and results in PG functionalization of NDs under diluted conditions.

	DND(+)-PG(m)-d1	DND(+)-PG(m)-d2	DND(+)-PG(m)-d3
ND (raw material)			
Oxygen content (O_{ND}, × 10^{-2}) *	5.14	4.84	4.84
Reaction condition			
Ethylene glycol (EG) ($W_{\mathrm{EG}}/W_{\mathrm{ND}}$)	90.0	75.0	45.0
Glycidol (GD) ($W_{\mathrm{GD}}/W_{\mathrm{ND}}$)	45.0	45.0	45.0
Temperature (°C)	100	100	100
Results			
PG/ND ratio by TGA ($W_{\mathrm{PG}}/W_{\mathrm{ND}}$)	0.66	0.99	1.52
PG content ($W_{\mathrm{PG}}/(W_{\mathrm{PG}}+W_{\mathrm{ND}})$)	0.396	0.497	0.603

* Determined by elemental analysis.

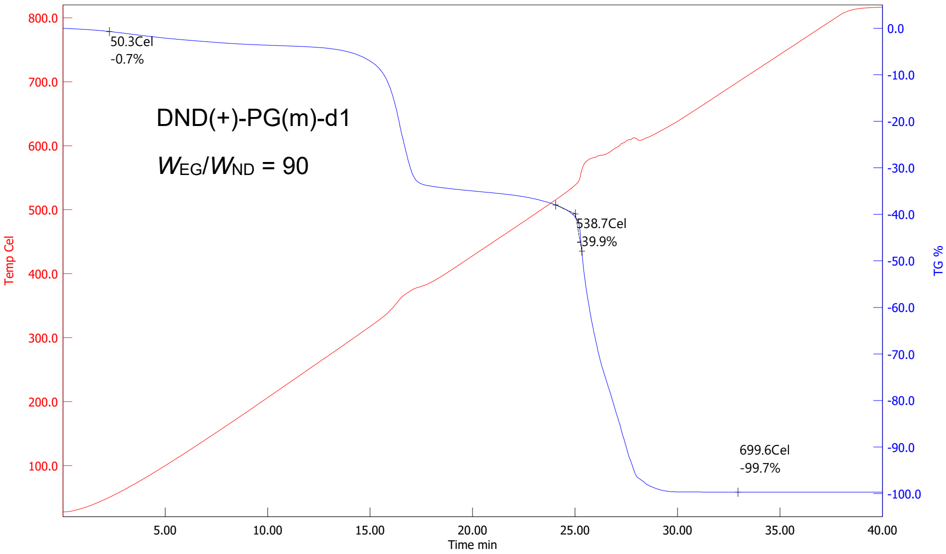
800.0
700.0
600.0
500.0
400.0
300.0
200.0
100.0
Temp Cel
50.3Cel
-0.7%
DND(+)-PG(m)-d1
W_{EG}/W_{ND} = 90
538.7Cel
-39.9%
699.6Cel
-99.7%
0.0
-10.0
-20.0
-30.0
-40.0
-50.0
-60.0
-70.0
-80.0
-90.0
-100.0
TG %
5.00
10.00
15.00
20.00
25.00
30.00
35.00
40.00
Time min

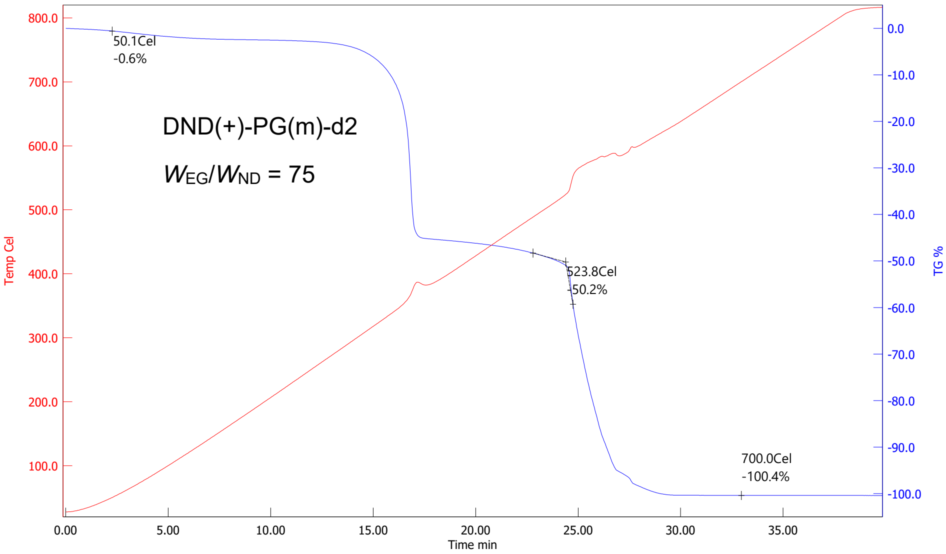
800.0
700.0
600.0
500.0
400.0
300.0
200.0
100.0
Temp Cel
50.1Cel
-0.6%
DND(+)-PG(m)-d2
W_{EG}/W_{ND} = 75
523.8Cel
-50.2%
700.0Cel
-100.4%
0.0
-10.0
-20.0
-30.0
-40.0
-50.0
-60.0
-70.0
-80.0
-90.0
-100.0
TG %
0.00
5.00
10.00
15.00
20.00
25.00
30.00
35.00
Time min

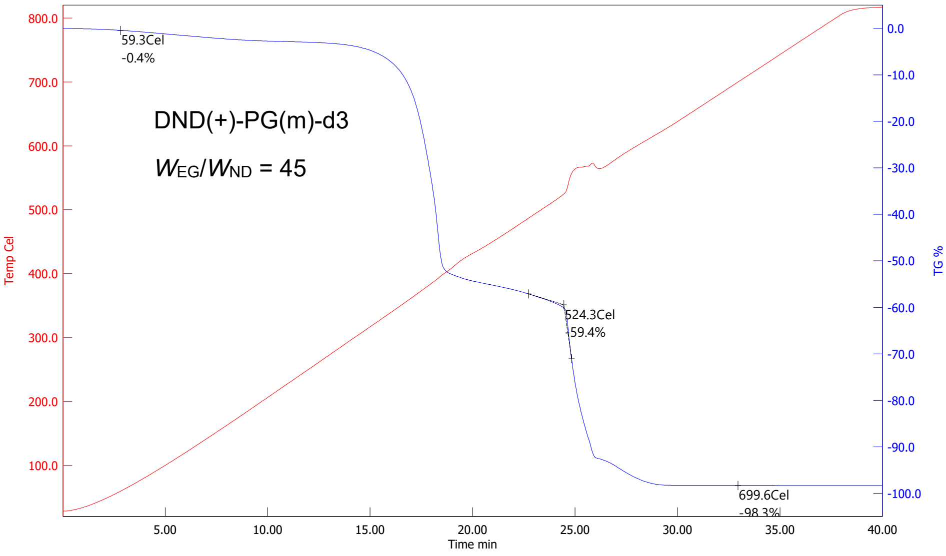
800.0
700.0
600.0
500.0
400.0
300.0
200.0
100.0
Temp Cel
59.3Cel
-0.4%
DND(+)-PG(m)-d3
W_{EG}/W_{ND} = 45
524.3Cel
-59.4%
699.6Cel
-98.3%
0.0
-10.0
-20.0
-30.0
-40.0
-50.0
-60.0
-70.0
-80.0
-90.0
-100.0
TG %
5.00
10.00
15.00
20.00
25.00
30.00
35.00
40.00
Time min

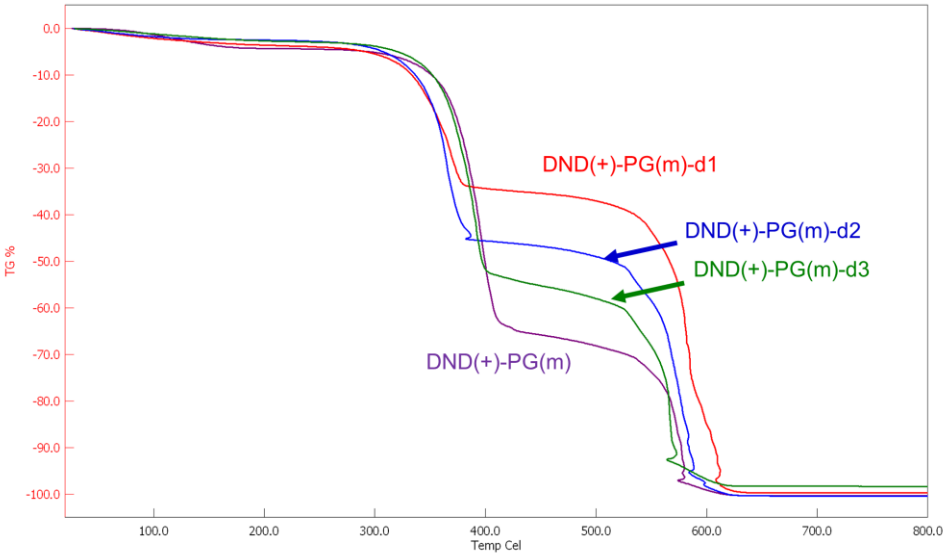

Figure 2-6. TGA results of DND(+)-PG(m) (W_{GD}/W_{ND} = 45) with different W_{EG}/W_{ND} in the reaction (DND(+)-PG(m)-d1 – d3).

Table 2-6. Summary of TGA results.

	DND(+)-PG(m)-d1	DND(+)-PG(m)-d2	DND(+)-PG(m)-d3
PG (%)	39.6	49.7	60.3
ND (%)	60.4	50.3	39.7
PG/ND (W_{PG}/W_{ND})	0.66	0.99	1.52

Table 2-7. Results of elemental analysis.

	Elemental analysis results (%)			
	H	C	N	O
DND(+)-PG(m)-d1	3.81	73.56	1.45	19.28
DND(+)-PG(m)-d2	4.68	68.62	1.18	23.73
DND(+)-PG(m)-d3	5.41	64.22	0.94	32.76

* DND(+)-1 was used for DND(+)-PG(m)-d1.

** DND(+)-2 was used for DND(+)-PG(m)-d2 and -d3.

Table 2-8. PG content calculated by the results of elemental analysis.

	DND(+)-PG(m)-d1	DND(+)-PG(m)-d2	DND(+)-PG(m)-d3
C_{ND} (%)	89.67	87.61	87.61
$C_{ND\text{-}PG}$ (%)	73.56	68.62	64.22
C_{GD} (%)	48.64	48.64	48.64
PG content by C (%)	39.26	48.74	60.02
N_{ND} (%)	2.26	2.20	2.20
$N_{ND\text{-}PG}$ (%)	1.45	1.18	0.94
N_{GD} (%)	0	0	0
PG content by N (%)	35.84	46.47	57.18
O_{ND} (%)	5.14	4.84	4.84
$O_{ND\text{-}PG}$ (%)	19.28	23.73	32.76
O_{GD} (%)	43.19	43.19	43.19
PG content by O (%)	37.16	49.26	72.81

PG content in ND-PG can be calculated by the equations in Table 2-4.

Based on the PG contents determined by TGA (Tables 2-5 and 2-6, and Figure 2-6 (Results from elemental analysis are shown in Tables 2-7 and 2-8), $W_{\mathrm{PG}}/W_{\mathrm{GD}}$ is found to have a negative exponential relationship with $W_{\mathrm{EG}}/W_{\mathrm{DND(+)}}$ as shown in Figure 2-7 and eq. (3). The coefficient (y-intercept) corresponds to an extrapolated $W_{\mathrm{PG}}/W_{\mathrm{GD}}$, when $W_{\mathrm{EG}}/W_{\mathrm{DND(+)}}$ is zero (0).

$$W_{\mathrm{PG}}/W_{\mathrm{GD}} = 0.0671/e^{0.0160 \times W_{\mathrm{EG}}/W_{\mathrm{DND(+)}}} \qquad \text{eq. (3)}$$

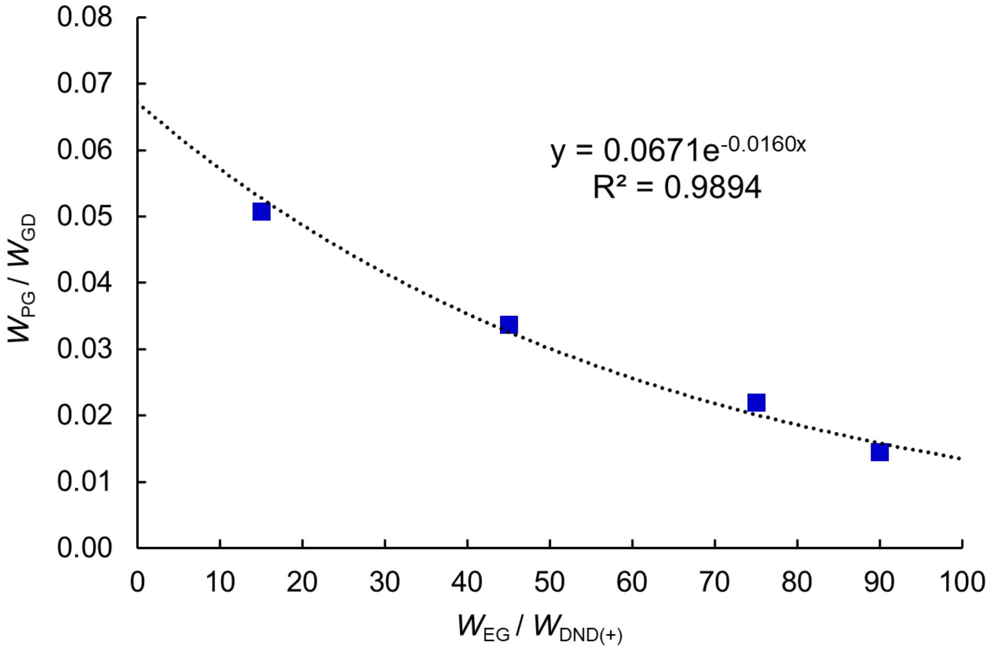

Figure 2-7. Relationships of the experimental results ($W_{\mathrm{PG}}/W_{\mathrm{GD}}$) based on the reaction conditions (W_{EG} and $W_{\mathrm{DND(+)}}$).

In eq. (3), the more diluted conditions with increase of $W_{\mathrm{EG}}/W_{\mathrm{DND(+)}}$ reduces $W_{\mathrm{PG}}/W_{\mathrm{GD}}$, meaning that more GD reacts with EG rather than DND(+) under the conditions with the same $W_{\mathrm{GD}}/W_{\mathrm{DND(+)}}$ (45.0 in Table 2-5). When $W_{\mathrm{PG}}/W_{\mathrm{GD}}$ becomes half of the y-intercept ($W_{\mathrm{EG}}/W_{\mathrm{DND(+)}} = 0$), $W_{\mathrm{EG}}/W_{\mathrm{DND(+)}}$ is 43.3 ($\ln 2/0.0160$), which corresponds to > 430 in the ratio of the oxygen contents between EG ($O_{\mathrm{EG}} = 52$ wt%) and DND(+) ($O_{\mathrm{DND(+)}} = {\sim}5$ wt% in Table 2-1) in the reaction mixture. This indicates that the reactivity of EG towards GD is much lower than that of DND(+), because ratio of the oxygen contents is assumed as that of the number of oxygen containing functional groups which are the potential reaction sites for GD. Although DND(+) was prepared by heating as-synthesized DND under hydrogen atmosphere followed by bead milling (see 2-4 Experimental), it still shows the IR absorptions at 1717 and 3109 cm^{-1} corresponding to carbonyl and hydroxy groups, respectively (Figure 2-8b) as well as ~5 wt% $O_{\mathrm{DND(+)}}$ (Tables 2-1 and 2-4).

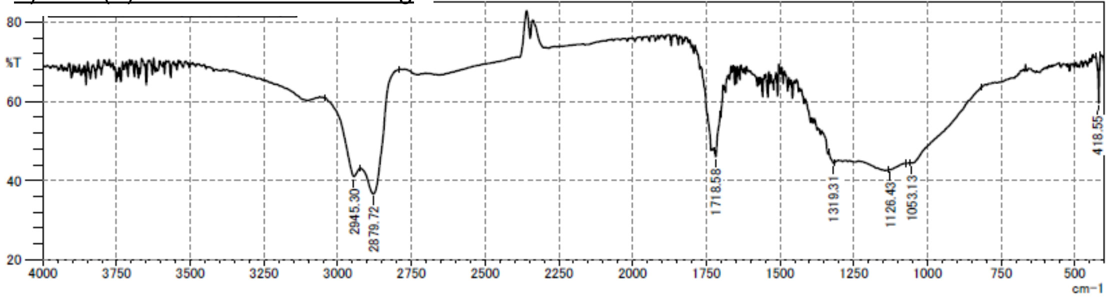
a) DND(+) Before the bead-milling

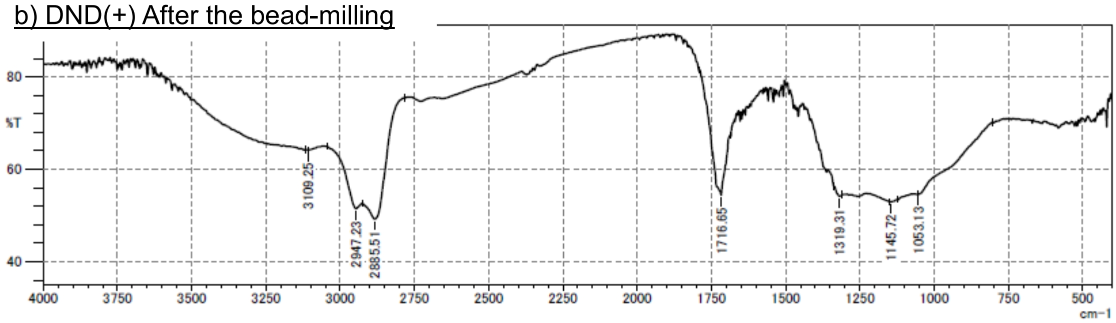
b) DND(+) After the bead-milling

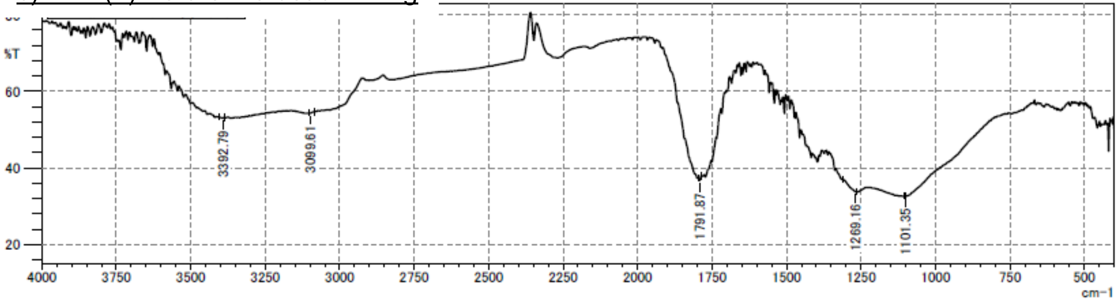
c) DND(–) Before the bead-milling

d) DND(–) After the bead-milling

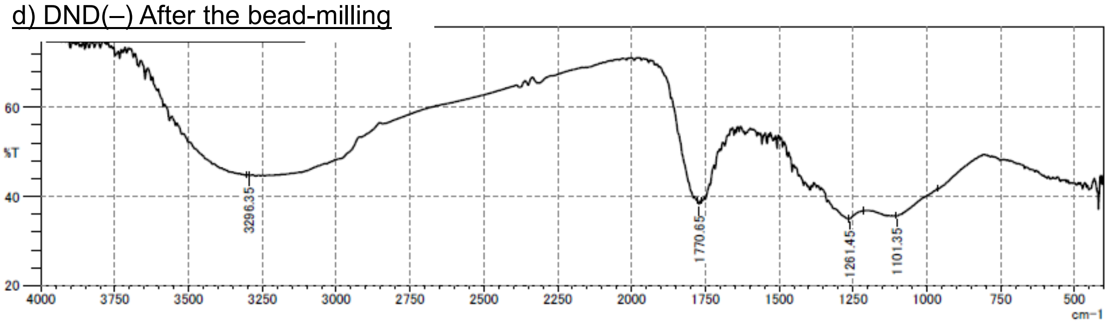

e) ND50(N) As-received

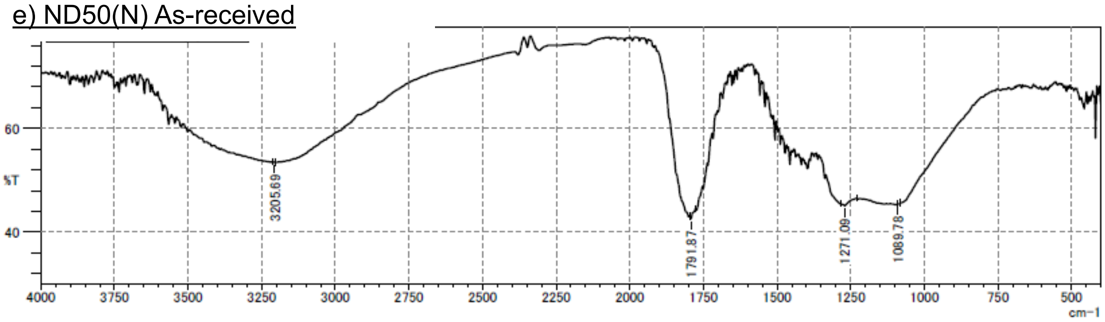

f) ND50(N) Acid treatment

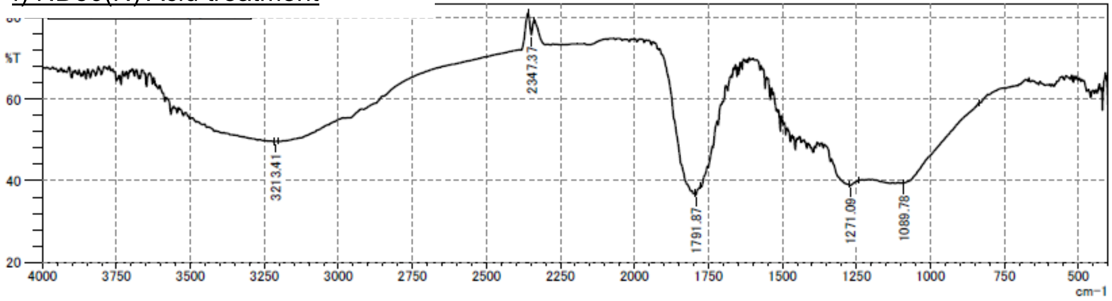

Figure 2-8. FT-IR spectra of nanodiamond raw materials for PG functionalization. The samples were dried at 150 °C under vacuum in the DRIFT chamber to remove adsorbed water. All spectra were measured under this condition (150 °C under vacuum).

Therefore, a number of oxygen-containing functional groups including hydroxy and carboxy groups may exist and the ring-opening polymerization of GD may be facilitated by the protons at carboxy groups on DND(+) surface through cationic mechanism (Figure 2-5a). The influence of EG, or concentration of DND(+) in EG ($W_{\mathrm{EG}}/W_{\mathrm{DND(+)}}$), to $W_{\mathrm{PG}}/W_{\mathrm{GD}}$ shown in Figure 2-7 and eq. (3) is incorporated into the linear relationship between $W_{\mathrm{PG}}/W_{\mathrm{GD}}$ and $W_{\mathrm{GD}}/W_{\mathrm{DND(+)}}$ as shown in

Figure 2-4 (blue dotted line) and eq. (1) to give Figure 2-9 (blue squares and dotted line) and eq. (4). The eq. (4) consists of the relationship between $W_{\mathrm{GD}}/W_{\mathrm{DND(+)}}$ and $W_{\mathrm{PG}}/W_{\mathrm{GD}}$ in the former part, and the influence by EG in the latter part. Two coefficients, 0.00119 and 0.0111, in eq. (4) are determined by a least-square method to give good correlations with the experimental results (the blue squares and the dotted line in Figure 2-9).

$$W_{\mathrm{PG}}/W_{\mathrm{GD}} = 0.00119 \times (W_{\mathrm{GD}}/W_{\mathrm{DND(+)}})/e^{0.0111\times(W_{\mathrm{EG}}/W_{\mathrm{DND(+)}})} \qquad \text{eq. (4)}$$

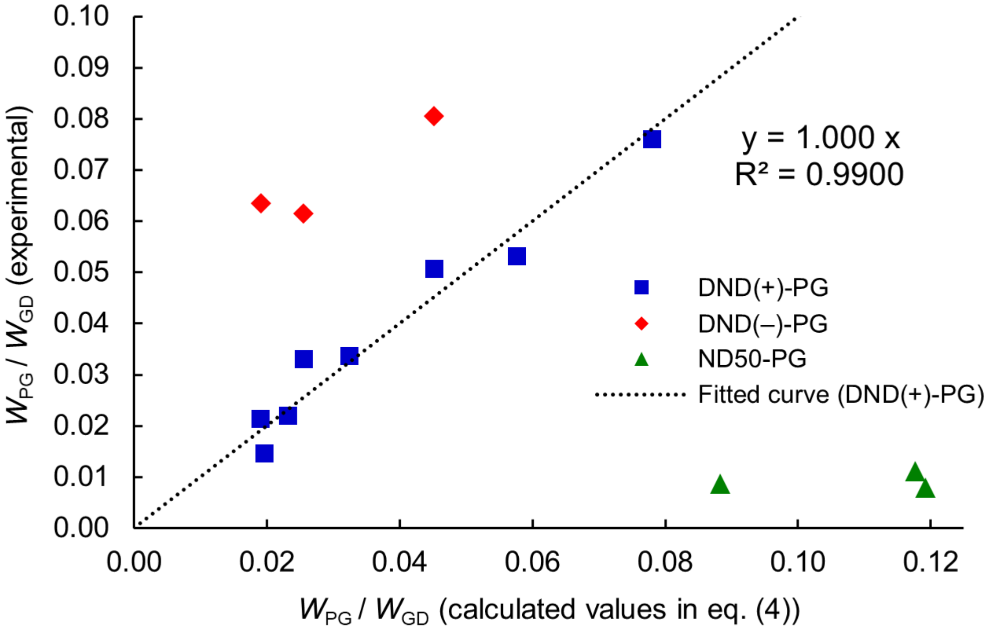

Figure 2-9. Relationships of the experimental results ($W_{\mathrm{PG}}/W_{\mathrm{GD}}$) with the calculated values from the eq. (4) based on the reaction conditions (W_{GD}, W_{EG} and W_{ND}).

When the ζ-potential of DND turned into negative, $W_{\mathrm{PG}}/W_{\mathrm{GD}}$ in DND(–)-PG(l), -PG(m) and -PG(h) are 3.0, 1.9 and 1.6 times as large as $W_{\mathrm{PG}}/W_{\mathrm{GD}}$ in DND(+)-PG(xl), -PG(l) and -PG(m) prepared under the same conditions, respectively (Table 2-1). This can be attributed to the difference in the oxygen contents (O_{DND}) of DND(+) and DND(–); 5.14 × 10^{-2} and 4.84 × 10^{-2} in $O_{\mathrm{DND(+)}}$, and 9.51 × 10^{-2} in $O_{\mathrm{DND(-)}}$ (Table 2-1), because the ring-opening polymerization of GD on the surface of DND is initiated and/or facilitated by the oxygen containing functional groups corresponding to O_{DND}. Although not all the oxygen atoms in DND are involved in the reaction, O_{DND} is incorporated into the former part of eq. (4) as a multiplier. Meanwhile, it is added as a divisor in the exponential part, because the influence of EG relatively decreases as O_{DND} increases. The coefficients 0.0238 and 0.000512 in eq. (5) are determined by a least-square method to give Figure 2-10 (blue squares and red rhombi with dotted line), indicating that W_{PG} in DND-PGs can be controlled by O_{DND}, W_{GD}, W_{EG} and W_{DND} irrespective of the ζ-potential of DNDs.

$$W_{\mathrm{PG}}/W_{\mathrm{GD}} = 0.0238 \times (W_{\mathrm{GD}}/W_{\mathrm{DND}}) \times O_{\mathrm{DND}}/e^{0.000512\times(W_{\mathrm{EG}}/W_{\mathrm{DND}})/O_{\mathrm{DND}}} \quad \text{eq. (5)}$$

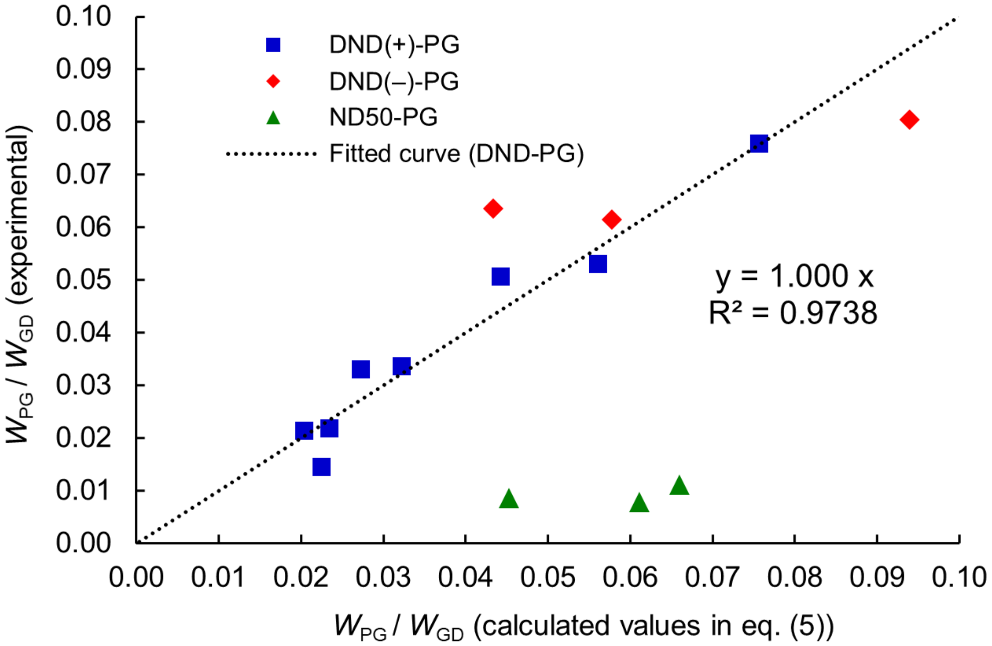

Figure 2-10. Relationships of the experimental results ($W_{\mathrm{PG}}/W_{\mathrm{GD}}$) with the calculated values from the eq. (5) based on the reaction conditions (W_{GD}, W_{EG} and W_{ND}) and the ND properties (O_{ND}).

Since the diameters of ND50 and DND are determined to be 43.35 and 4.96 – 5.15 nm which will be mentioned below, specific surface area of DNDs is calculated to be 8.4 – 8.7 times larger than that of ND50. Since the specific surface area should influence the W_{PG}/W_{GD} in the same direction as the oxygen content, the diameters (D_{ND}), which is inversely proportional to the specific surface area, are incorporated into eq. (5) as a divisor of O_{ND} for both former and exponential parts as shown in eq. (6). The coefficients 0.122 and 0.0000990 are determined in similar manners to those of eq. (4) and eq. (5). Since all the results of DND(+)-PG (blue squares), DND(–)-PG (red rhombi) and ND50-PG (green triangles) are almost on the dotted line as shown in Figure 2-11, it is concluded that W_{PG} in the PG functionalization for any NDs is determined by the properties of ND (diameter and oxygen content) and reaction conditions (weights of GD, ND and EG).

$$W_{\mathrm{PG}}/W_{\mathrm{GD}} = 0.122 \times (W_{\mathrm{GD}}/W_{\mathrm{ND}}) \times (O_{\mathrm{ND}}/D_{\mathrm{ND}})/e^{0.0000990 \times (W_{\mathrm{EG}}/W_{\mathrm{ND}})/(O_{\mathrm{ND}}/D_{\mathrm{ND}})}$$

eq. (6)

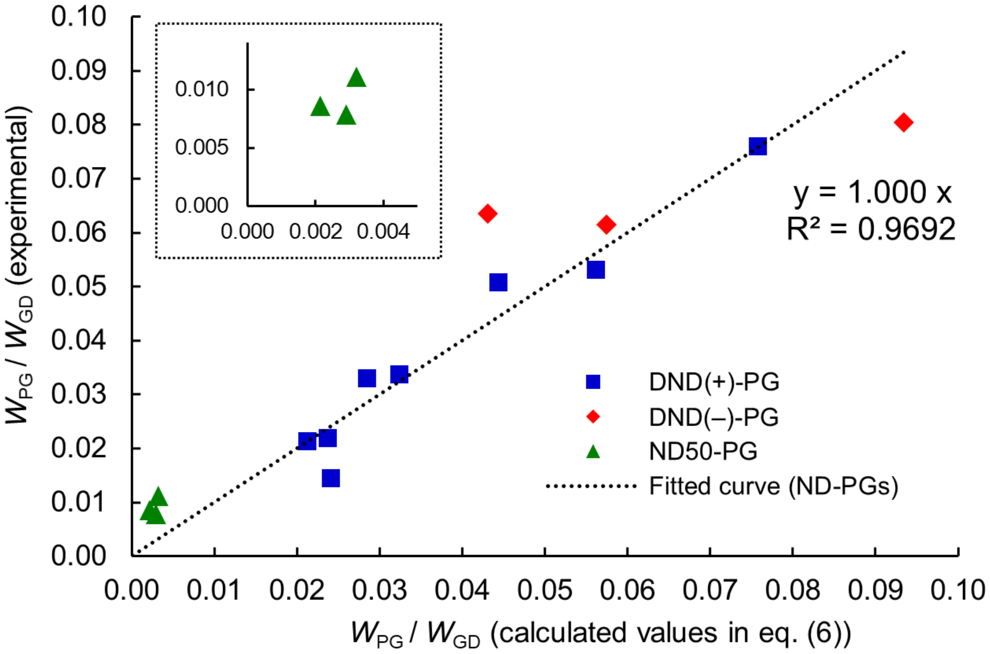

Figure 2-11. Relationships of the experimental results (W_{PG}/W_{GD}) with the calculated values from the eq. (6) based on the reaction conditions (W_{GD}, W_{EG} and W_{ND}) and the ND properties (O_{ND} and D_{ND}). The inset shows the magnification of the area of ND50-PGs.

2-2-2. Structural elucidation of ND-PG by ^{13}C NMR analyses

The PG chain consists of several substructures of glycerol as shown in Figure 2-12. On the ring-opening polymerization, 2- and 3-positions of GD (CH and CH_2 in oxirane ring of 2,3-epoxy-1-propanol, respectively) are subject to nucleophilic attack, giving various structural isomers via two possible reaction mechanisms, cationic and anionic ones shown in Figure 2-5a and 2-5b, respectively. There are dendritic (D and D′), linear (L_{13}, L_{13}' and L_{14}) and terminal (T and T′) glycerol units having three, two and one ether linkage(s), respectively (Figure 2-12). They are also divided into two patterns having ether linkage with the preceding unit at the primary carbon (D, L_{13}, L_{14} and T) and secondary one (D′, L_{13}' and T′). The linear structures including three and two carbons between the ether linkages are L_{14} unit, and L_{13} and L_{13}' units, respectively. Hereafter, L_{13} includes L_{13}' unless otherwise specified, since these two substructures are indistinguishable each other in ^{13}C NMR.

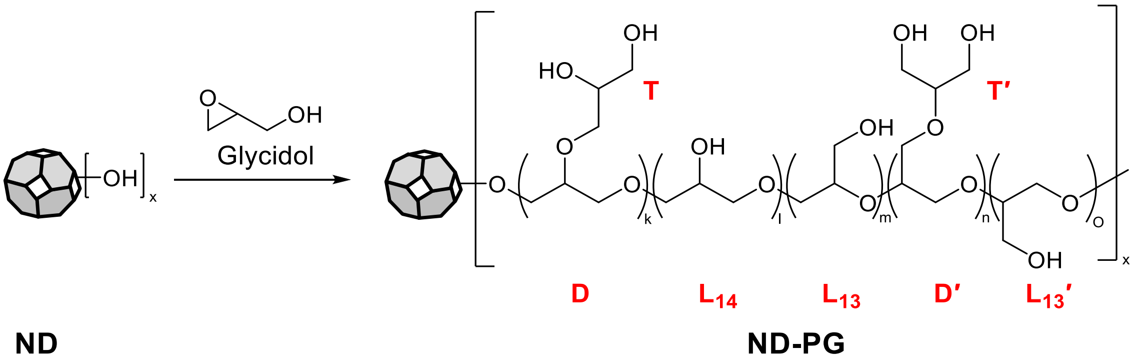

Figure 2-12. Substructures in PG chain on ND surface.

To elucidate the structures in PG on ND quantitatively, solution phase ^{13}C NMR (Figure 2-13) was measured by inverse gated decoupling experiment with repetition time of 8 s which is more than 10 times as long as the T_1 relaxation time shown in S2-1 in Appendix I. As shown in our previous papers, a broad signal from diamond core is detected and set at 36.3 ppm as a reference [42, 114]. The signals of PG chain were assigned by DEPT, HMQC and HMBC spectra described in detail in S2-2 in Appendix I and by previously reported ^{13}C NMR spectra of free PG [107–110]. The signal assignments and relative integration values are shown in Table 2-9 and Figure 2-14. Since the separation of two signals at 73.0 and 72.7 ppm, and 71.4 and 71.1 ppm are not enough, they are treated as one peak.

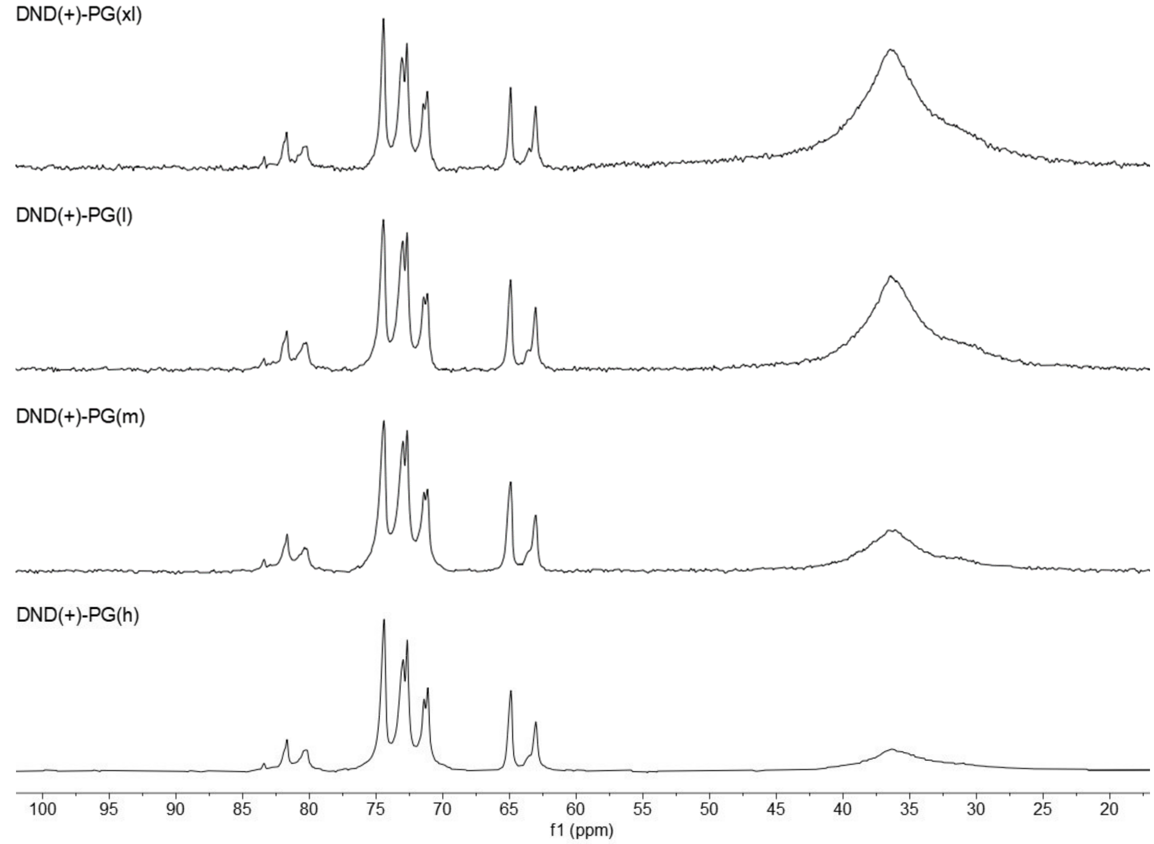

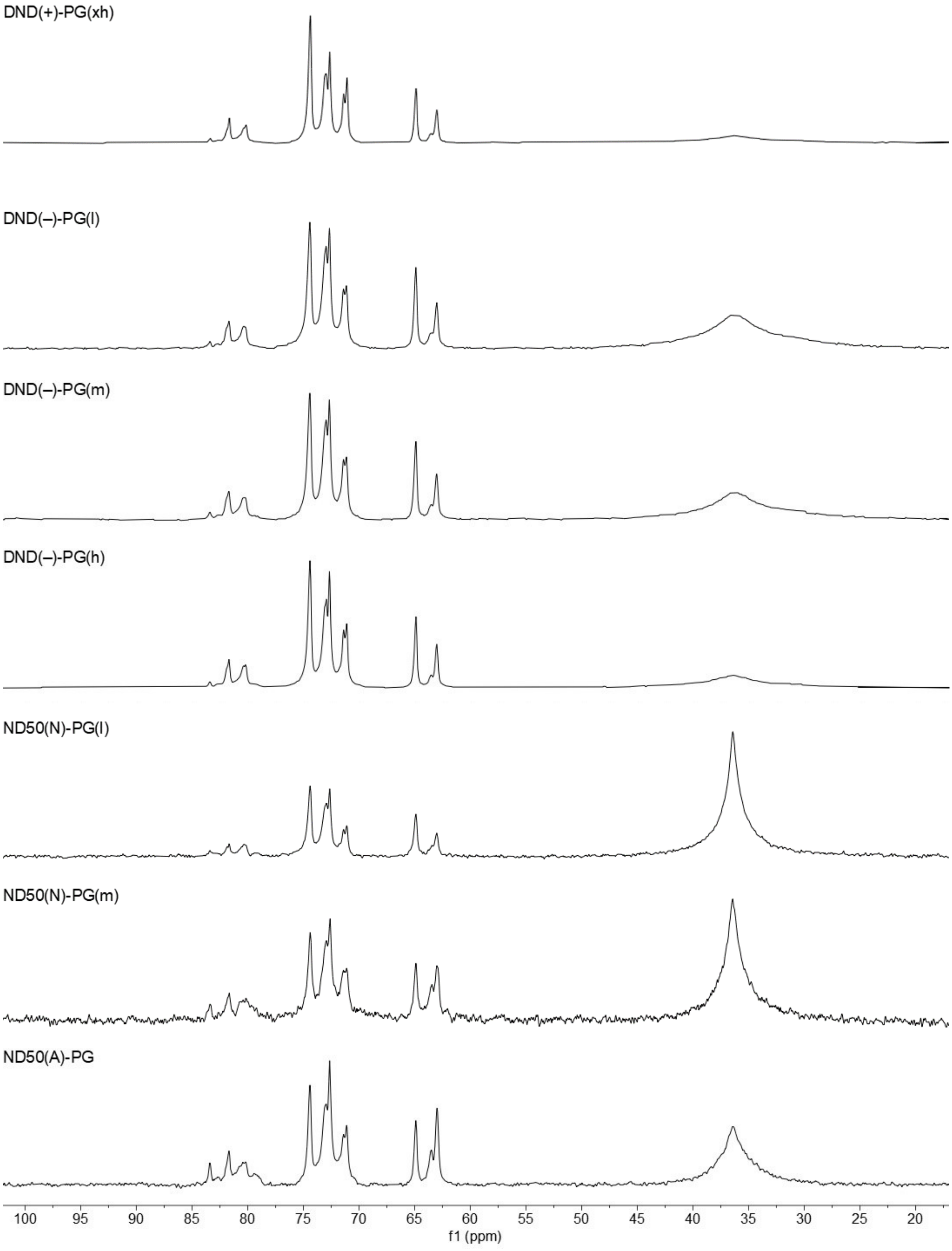

Figure 2-13. ^{13}C NMR spectra of ND-PGs in D_2O. Chemical shift of the peak top of diamond core is adjusted to 36.3 ppm as a reference.

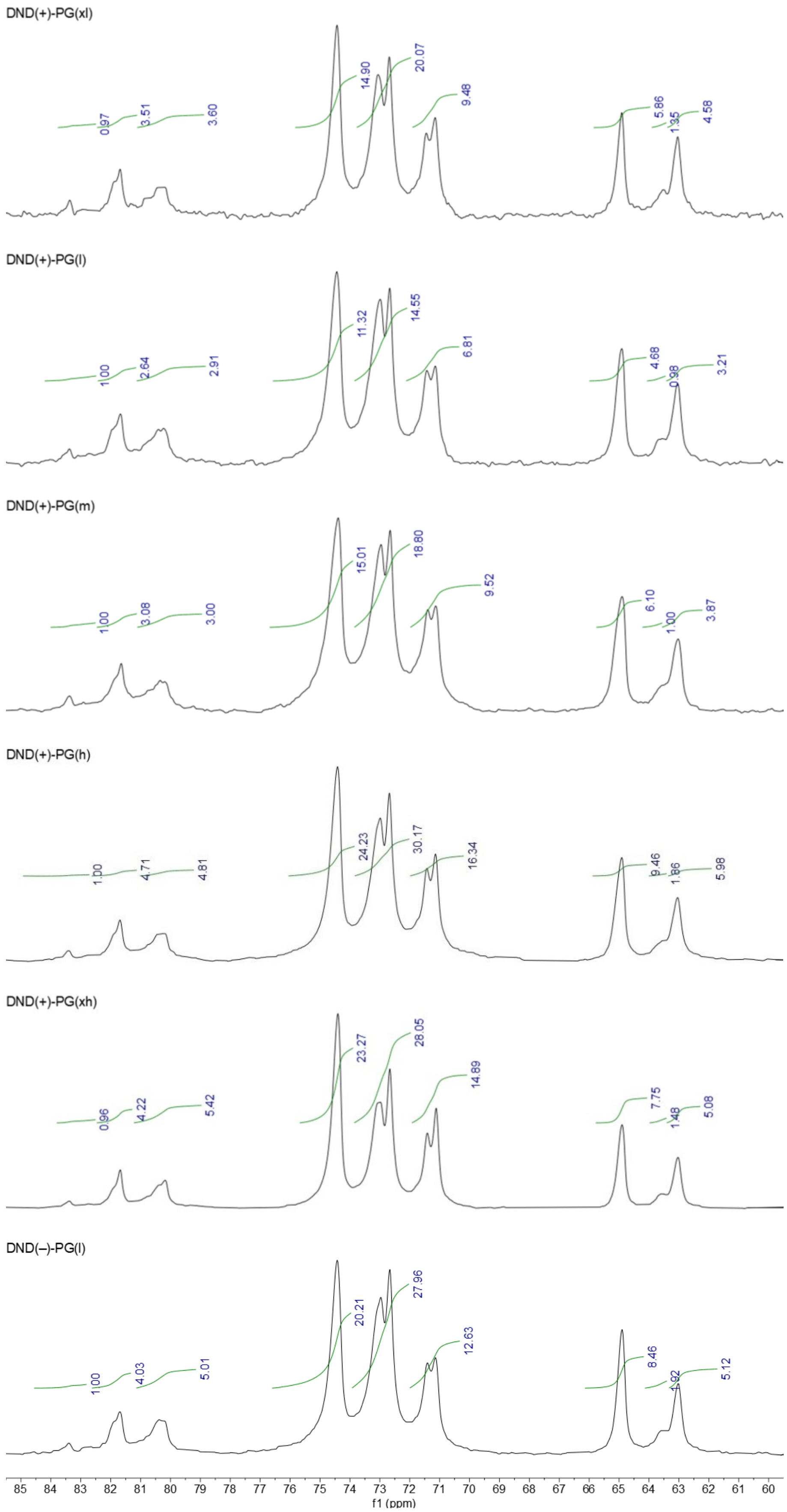
DND(+)-PG(xl)
0.97
3.51
3.60
14.90
20.07
9.48
5.86
1.35
4.58
DND(+)-PG(l)
1.00
2.64
2.91
11.32
14.55
6.81
4.68
0.98
3.21
DND(+)-PG(m)
1.00
3.08
3.00
15.01
18.80
9.52
6.10
1.00
3.87
DND(+)-PG(h)
1.00
4.71
4.81
24.23
30.17
16.34
9.46
1.86
5.98
DND(+)-PG(xh)
0.96
4.22
5.42
23.27
28.05
14.89
7.75
1.48
5.08
DND(–)-PG(l)
1.00
4.03
5.01
20.21
27.96
12.63
8.46
1.92
5.12
85 84 83 82 81 80 79 78 77 76 75 74 73 72 71 70 69 68 67 66 65 64 63 62 61 60
f1 (ppm)

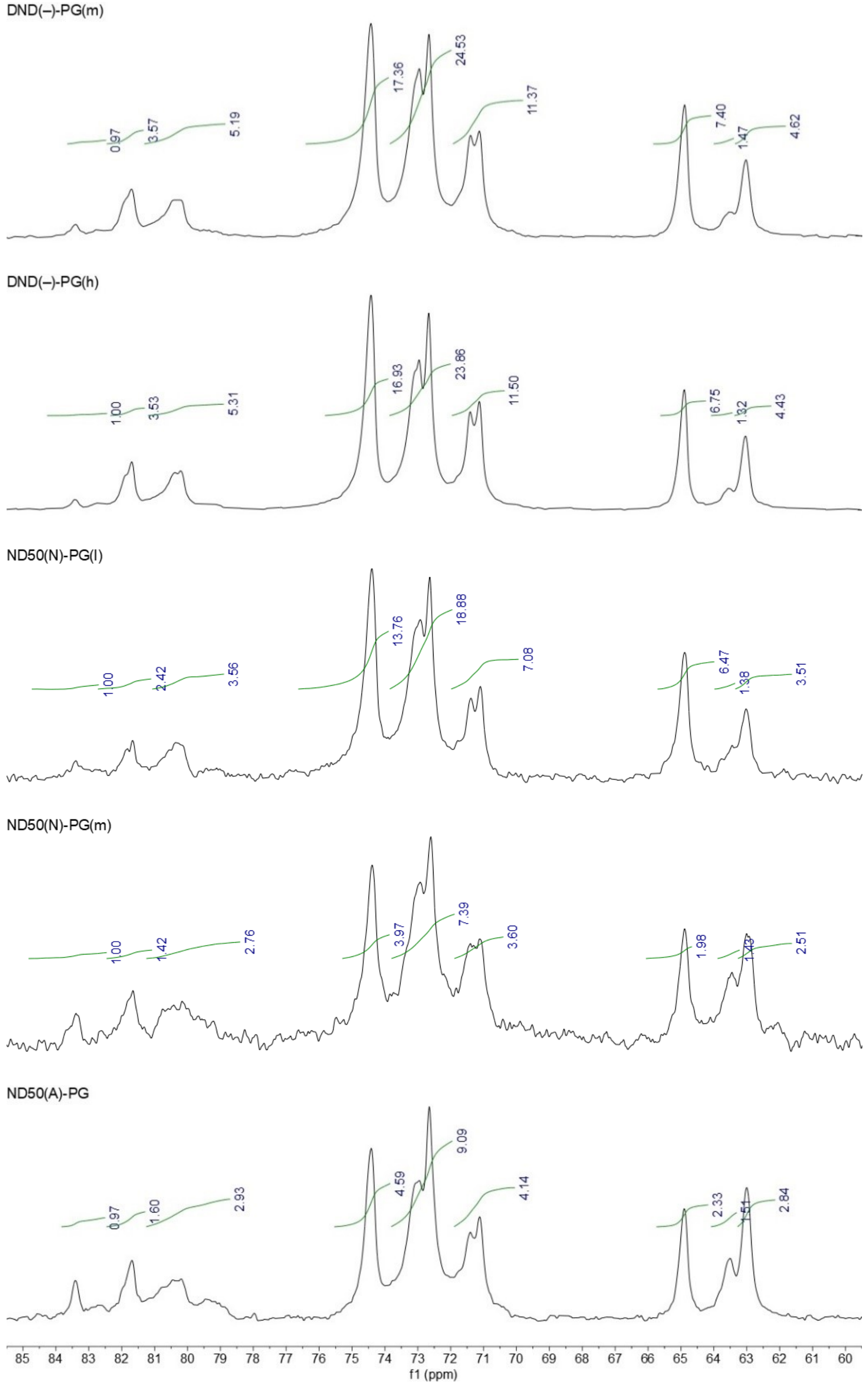

Figure 2-14. Expanding spectra of the region of carbon from PG chain.

Table 2-9. Signal assignments of ^{13}C NMR of ND-PG and relative integration values of each peak by inverse gated decoupling experiments.

Chemical shifts (ppm) *	Assignments	Relative integration values of PG chain signals							
		DND(+)-PG(xl)	DND(+)-PG(l)	DND(+)-PG(m)	DND(+)-PG(h)	DND(+)-PG(xh)	DND(–)-PG(l)	DND(–)-PG(m)	DND(–)-PG(h)
83.4	T′	1.47	2.05	1.61	1.03	1.05	1.17	1.26	1.35
81.7	L_{13} **	5.46	5.52	5.01	4.77	4.64	4.67	4.68	4.73
80.2	D (D′)	5.62	6.05	4.89	4.87	5.94	5.79	6.79	7.15
74.4	L_{14}, T	23.15	23.53	24.47	24.58	25.52	23.43	22.71	22.68
73.0, 72.7	T, D, L_{14}	31.21	30.22	30.63	30.61	30.79	32.39	32.06	31.96
71.4, 71.1	L_{13} **, L_{14}	14.75	14.14	15.51	16.59	16.34	14.63	14.88	15.39
64.9	T	9.13	9.74	9.94	9.60	8.51	9.80	9.67	9.02
63.6	T′	2.12	2.05	1.61	1.89	1.62	2.21	1.93	1.77
63.1	L_{13} **	7.09	6.69	6.33	6.07	5.59	5.92	6.03	5.93
36.3	DND core ***	278.0	148.7	58.16	38.91	21.16	80.74	62.23	28.76
$(W_{PG}/W_{DND})_{NMR}$		0.65	1.21	3.17	4.74	8.71	2.08	2.70	5.84

Table 2-9 (continued).

Chemical shifts (ppm) *	Assignments	Relative integration values of PG chain signals		
		ND50(N)-PG(l)	ND50(N)-PG(m)	ND50(A)-PG
83.4	T′	1.66	3.79	3.25
81.7	L$_{13}$ **	4.14	5.56	5.33
80.2	D (D′)	6.08	10.61	9.86
74.4	L$_{14}$, T	23.76	15.15	15.27
73.0, 72.7	T, D, L$_{14}$	32.60	28.28	30.26
71.4, 71.1	L$_{13}$ **, L$_{14}$	12.16	13.89	13.82
64.9	T	11.19	7.58	7.77
63.6	T′	2.35	5.56	5.06
63.1	L$_{13}$ **	6.08	9.60	9.49
36.3	ND50 core ***	186.74	112.88	61.97
$(W_{\mathrm{PG}}/W_{\mathrm{ND50}})_{\mathrm{NMR}}$		1.05	1.73	3.15

* Chemical shift at peak-top of each signal.

** L$_{13}$ includes L$_{13}$′.

*** The value when the sum of the values of PG carbon is 100.

First, the integral ratio between PG and ND (I_{PG}/I_{ND}) leads to their weight ratio (W_{PG}/W_{ND}) by dividing them with their carbon contents, C_{PG} and C_{ND}, according to the eq. (7).

$$W_{\mathrm{PG}}/W_{\mathrm{ND}} = (I_{\mathrm{PG}}/C_{\mathrm{PG}})/(I_{\mathrm{ND}}/C_{\mathrm{ND}}) \qquad \text{eq. (7)}$$

The W_{PG}/W_{DND} determined by ^{13}C NMR (Table 2-9), namely $(W_{PG}/W_{DND})_{NMR}$, exhibits a linear relationship with that determined by TGA (Table 2-1), namely $(W_{PG}/W_{ND})_{TGA}$, as shown in Figure 2-15a and eq. (8).

$$(W_{\mathrm{PG}}/W_{\mathrm{DND}})_{\mathrm{NMR}} = 1.808 \times (W_{\mathrm{PG}}/W_{\mathrm{DND}})_{\mathrm{TGA}} - 0.529 \qquad \text{eq. (8)}$$

The slope of 1.808 implies that approximately 55% of the carbon atoms in the DND core (DND carbons) in DND-PGs are detected by ^{13}C NMR, because it should be 1.0 when all the DND carbons are detected. The undetected DND carbons (approximately 45%) may be included in disordered carbon layer near the surface and/or deep inside the core [115, 116]. The negative *y*-intercept shown in Figure 2-15a indicates that some of the carbon atoms in PG layer (PG carbons) are not detected by ^{13}C NMR probably due to the motility inhibition of these PG carbons near the DND surface. The undetected PG carbons are calculated to be 29 wt% at $(W_{PG}/W_{DND})_{TGA}$ from the *x*-intercept at $(W_{PG}/W_{DND})_{NMR} = 0.0$ in Figure 2-15a and eq. (8). The excellent linearity ($R^2 > 0.99$) means that the PG carbons detected by ^{13}C NMR in weight or number are strictly proportional to the PG content determined by TGA regardless of the electrical potential of DND. Hereafter, the detailed structures of DND-PGs will be discussed quantitatively based on the integration values of the carbon atoms detected by inverse gated decoupling measurement.

A similar relationship is observed in ND50-PGs as shown in Figure 2-15b and eq. (9), where ND50-PG shows the larger slope and larger negative *y*-intercept than DND-PG. They indicate that only about 24 wt% of the ND50 carbons are detected by ^{13}C NMR due to much larger diameter than DND, and that 44 wt% of the PG carbons are undetected probably due to larger PG carbon content near the ND50 surface.

$$(W_{\mathrm{PG}}/W_{\mathrm{ND50}})_{\mathrm{NMR}} = 4.210 \times (W_{\mathrm{PG}}/W_{\mathrm{ND50}})_{\mathrm{TGA}} - 1.854 \qquad \text{eq. (9)}$$

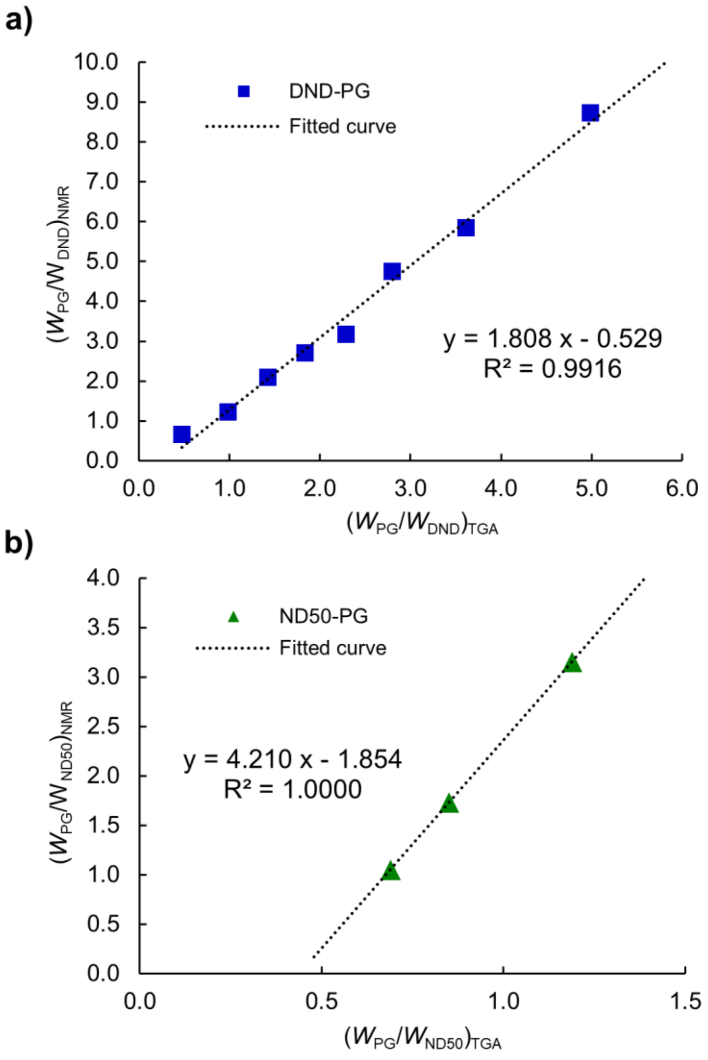

Figure 2-15. Relationship in a) PG/DND and b) PG/ND50 weight ratios between TGA ($(W_{\mathrm{PG}}/W_{\mathrm{ND}})_{\mathrm{TGA}}$) and ^{13}C NMR integration values ($(W_{\mathrm{PG}}/W_{\mathrm{ND}})_{\mathrm{NMR}}$). DND and ND50 include a) DND(+) and DND(–), and b) ND50(N) and ND50 (A), respectively.

Next, the contents of the substructures in PG chain are discussed based on their relative abundance determined by the formulas shown in Table 2-10. As the signals in lower magnetic field (85–80 ppm) are split with low signal/noise (S/N) ratio, the integration values in this region are not used. The results are shown in Table 2-11. The degree of branching (DB) is determined by eq. (10), representing the reactivity of hydroxy groups in the ring-opening polymerization.

$$DB = 2D/(2D + L_{13} + L_{14}) \qquad \text{eq. (10)}$$

Table 2-10. Formulas to obtain the amount of substructures.

Substructure	Calculation formula for each substructure *
T	$I_{64.9} \times 3$
T′	$I_{63.6} \times 3/2$
L_{13}	$I_{63.1} \times 3$
L_{14}	$(I_{71.4\ and\ 71.1} - I_{63.1}) \times 3$
D	$\{I_{73.0\ and\ 72.7} + I_{74.4} - 2 \times (I_{71.4\ and\ 71.1} - I_{63.1}) - 2 \times I_{64.9}\} \times 3/2$

* I_x: Integration value of peak at *x* ppm.

Table 2-11. Relative abundance of substructures in PG chain* and degree of branching (DB)**.

Substructure	Relative abundances (%) and DB							
	DND(+)-PG(xl)	DND(+)-PG(l)	DND(+)-PG(m)	DND(+)-PG(h)	DND(+)-PG(xh)	DND(–)-PG(l)	DND(–)-PG(m)	DND(–)-PG(h)
T	25.8	28.2	28.7	27.7	24.6	28.0	28.1	26.5
T′	3.0	3.0	2.3	2.7	2.3	3.2	2.8	2.6
L_{13}	20.1	19.3	18.2	17.5	16.2	16.9	17.5	17.4
L_{14}	21.7	21.5	26.5	30.4	31.1	24.9	25.8	27.7
D	29.4	28.0	24.3	21.6	25.7	26.9	25.8	25.9
DB	0.58	0.58	0.52	0.47	0.52	0.56	0.54	0.53

Substructure	Relative abundances (%) and DB		
	ND50(N)-PG(l)	ND50(N)-PG(m)	ND50(A)-PG
T	31.6	22.2	22.3
T′	3.3	8.1	7.3
L_{13}	17.2	28.1	27.3
L_{14}	17.2	12.6	12.5
D	30.8	28.9	30.6
DB	0.64	0.59	0.61

* Total amount of all the substructures in each ND-PG is 100.

** DB is calculated by eq. (10)

DB should be between 0.0 for linear structure and 1.0 for complete dendritic structure. It would be around 0.5, if the ring-opening reaction of GD, or the chain extension of PG, happens at the all the hydroxy groups at equal possibility [107, 117]. As shown in Table 2-11, DB values of DND-PGs range from 0.47 to 0.58 which are in the same range as that of free PG, indicating that steric and electrostatic effects of DND is negligible in the ring-opening polymerization on DND surface. This supports the above assumption of almost the same reactivity of the PG layer with or without ND core.

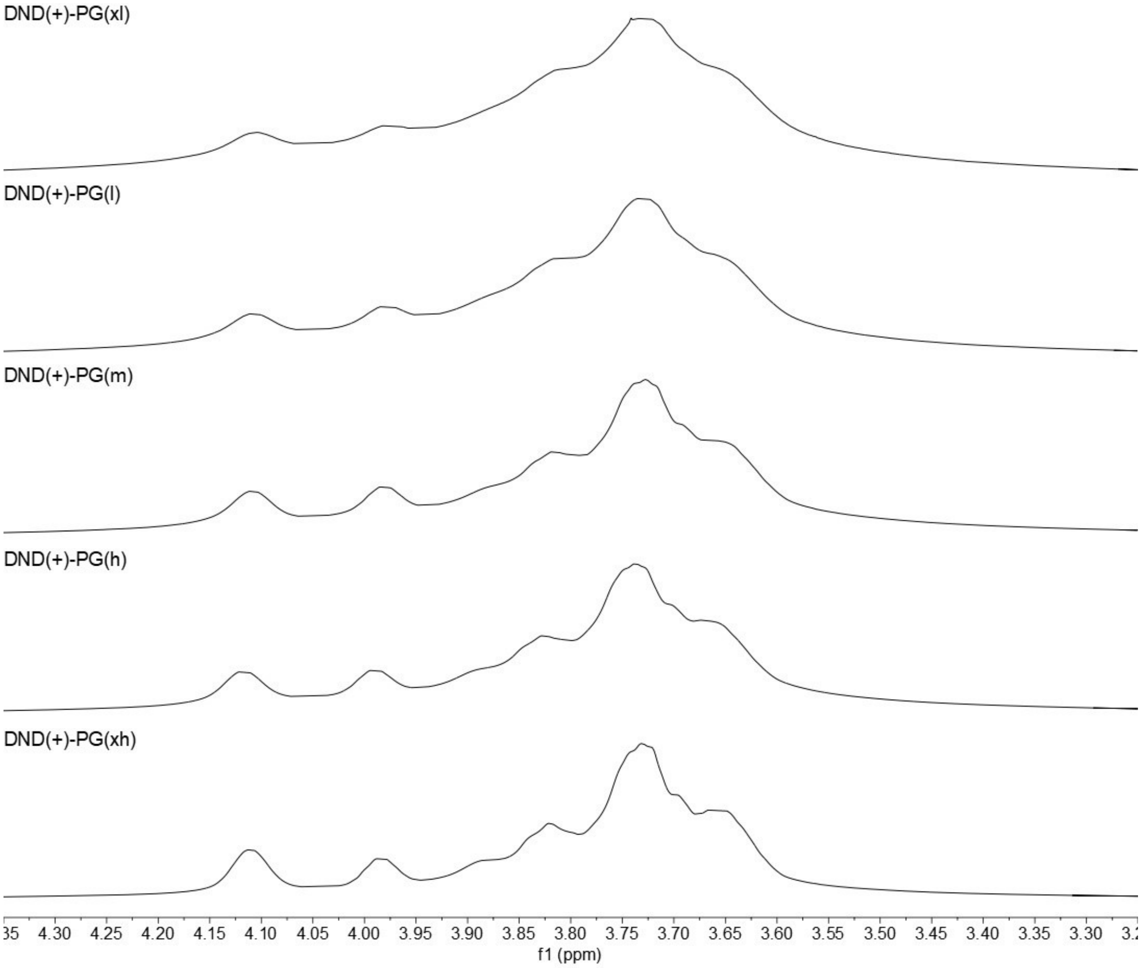

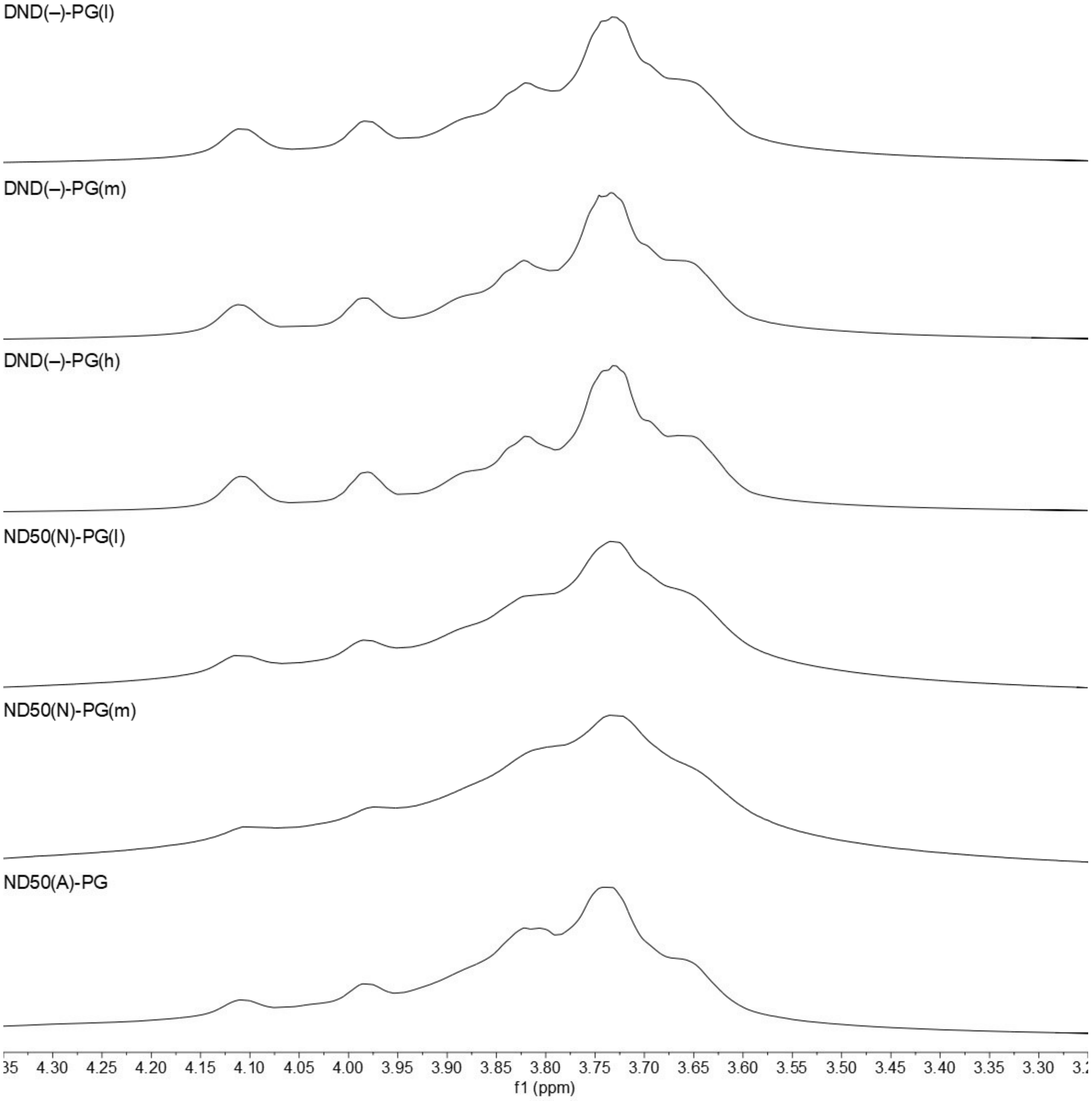

Figure 2-16. ^{1}H NMR spectra of ND-PGs.

As for the contents of the substructures, L_{13} and L_{14} in the DND-PG are found to linearly correlate with the W_{PG}/W_{DND} as shown in Figure 2-17. ^1H NMR spectra also support the relationship qualitatively (Figure 2-16); the signal height at 4.11 ppm corresponding to 2-position of L_{14} substructure (–C$\underline{H}$(OH)–) increases according to the increase of W_{PG}/W_{DND}. This phenomenon can be interpreted by the reaction mechanism of the oxirane ring opening in GD (Figure 2-5a and 2-5b). In cationic mechanism, the nucleophilic attack at 2-position leading to L_{13}' and T′ is considered to happen more frequently than that to 3-position, because the carbon at 2-position is more electrophilic than that at 3-position (Figure 2-5a). In contrast, the nucleophilic attack at the 3-position of GD leading to L_{14} is favored more than that at the 2-position leading to L_{13}' in anionic mechanism, because the steric hindrance become larger at the higher W_{PG}/W_{DND} (Figure 2-5b). There may be a contribution of cationic mechanism in DND-PGs judging from the fact of the existence of T′ substructure, which is characteristic of the cationic mechanism [109, 110]. The higher L_{13} abundance must be due to the contribution of L_{13}' derived from T′ structure. The observation in Figure 2-17 under the circumstances can be interpreted that the nucleophilic attack at 3-position is facilitated by the steric hindrance increasing along with the extension of PG chain, making the L_{14} abundance larger.

The contents of the substructures (Table 2-11) are also correlated with those of primary and secondary hydroxy groups. Since the primary hydroxy groups are in T, T′ and L_{13} substructures, their contents are calculated to be 46 – 53 % for DND-PGs and 55 – 67 % for ND50-PGs out of the total hydroxy groups, and 21 – 46 % and 20 – 40 %, respectively, for hydroxy group in ^{13}C NMR detectable PG layer (Table 2-12). In terms of the further chemical modification, the higher abundance of primary hydroxy group especially in ^{13}C NMR detectable PG layer would be preferable.

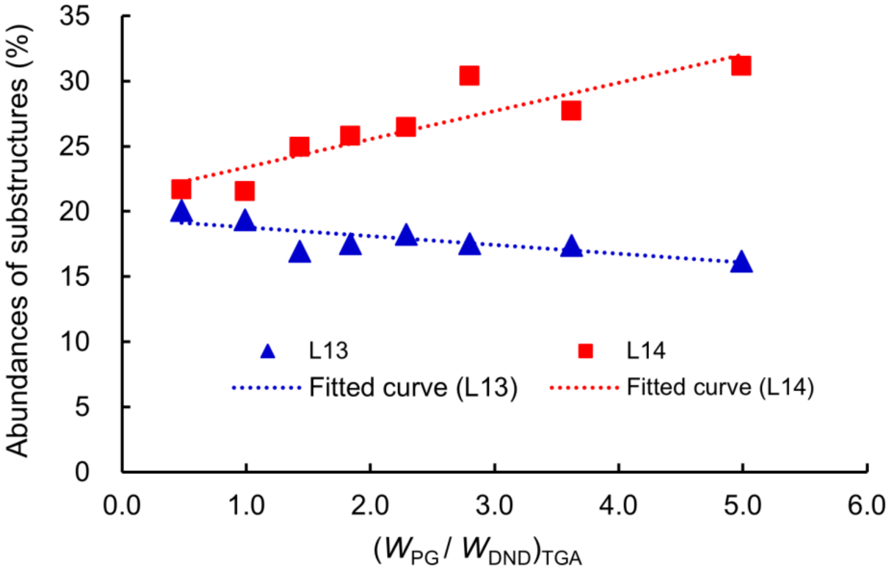

Figure 2-17. Abundance in L_{13} and L_{14} substructures in DND-PGs (DND(+) and DND(–)) at various $(W_{PG}/W_{ND})_{TGA}$.

Table 2-12. Amounts of hydroxy groups in PG layer in various ND-PGs.

	Amount of GD unit and hydroxy group in 1 g of DND-PG							
	DND(+)-PG(xl)	DND(+)-PG(l)	DND(+)-PG(m)	DND(+)-PG(h)	DND(+)-PG(xh)	DND(–)-PG(l)	DND(–)-PG(m)	DND(–)-PG(h)
Hydroxy group in whole PG layer (mmol/g) *	4.37	6.72	9.40	9.95	11.24	7.94	8.75	10.58
Hydroxy group in ^{13}C NMR detectable PG layer (mmol/g) *	1.73	4.76	8.21	8.92	10.59	6.32	7.37	9.74
Primary hydroxy group in whole PG layer (mmol/g) **	2.27	3.59	4.84	5.05	5.11	4.07	4.49	5.19
Primary hydroxy group in ^{13}C NMR detectable PG layer (mmol/g)	0.90	2.54	4.23	4.52	4.82	3.25	3.78	4.77
Content of primary hydroxy group (%)	51.9	53.4	51.6	50.7	45.5	51.3	51.3	49.0
Content of ^{13}C NMR detectable primary hydroxy group in whole PG layer (%)	20.5	37.8	45.0	45.5	42.8	40.9	43.2	45.1

Table 2-12 (continued).

	Amount of GD unit and hydroxy group in 1 g of ND50-PG		
	ND50(N)-PG(l)	ND50(N)-PG(m)	ND50(A)-PG
Hydroxy group in whole PG layer (mmol/g) *	5.51	6.18	7.32
Hydroxy group in ^{13}C NMR detectable PG layer (mmol/g) *	1.99	2.96	4.60
Primary hydroxy group in whole PG layer (mmol/g) **	3.05	4.12	4.69
Primary hydroxy group in ^{13}C NMR detectable PG layer (mmol/g)	1.10	1.98	2.95
Content of primary hydroxy group (%)	55.4	66.7	64.2
Content of ^{13}C NMR detectable primary hydroxy group in whole PG layer (%)	20.0	32.0	40.3

* Equivalent of the amount of glycerol unit (Hydroxy groups on ND surface are not accounted).

** Assuming that the ^{13}C NMR undetectable part has the same substructure abundances as the ^{13}C NMR detectable part.

2-2-3. Structural elucidation of ND-PG by DLS measurements

The thickness of PG layer is calculated from the difference between the hydrodynamic diameter of ND-PG determined by DLS and the ND core size. The DLS of ND-PG was measured in water and 10 mM NaCl, since it has been reported that ionic strength of the medium affects the behavior of ND-PG in dispersion [39]. Among the data processing on number, volume and intensity (scattered light intensity) bases, the number basis is adopted for discussion.

To determine the sizes of ND-PGs, we first investigated their concentration dependence on the DLS size as shown in Figure 2-18. DLS results were not corrected by the viscosity of dispersion, since no significant change in viscosity was observed in the concentration range of 0.1 – 1.0% (Table 2-13). A significant concentration dependence is observed in both DND(+)-PG(m) and ND50(A)-PG in water. ND-PGs with higher concentration exhibits smaller size as shown in Figure 2-18a and 2-18c, while ND-PGs in 10 mM NaCl show almost no concentration dependence (Figure 2-18b and 2-18d). This discrepancy can be interpreted by the difference in dispersion state with different ionic strengths. In the literature [39], the cryogenic transmission electron microscopy (Cryo-TEM) analysis reveals that DND-PG tends to form aggregates at lower ionic strength (10^{-7} M), rather than higher one (10^{-2} M), in water likely due to the electrostatic interaction between the surfaces of ND cores. As the particle concentration increases, the diffusion coefficient increases with the increase of volume fraction, resulting in the decrease of hydrodynamic diameter according to the Stokes-Einstein equation [118]. At higher concentration especially in water, the cooperative diffusion due to diffusion inhibition and the rotational diffusion of non-spherical aggregates may be observed as well as the translation diffusion of single spherical particles that leads the larger diffusion coefficient [119]. The values are approaching to those in 10 mM NaCl (about 72 nm in Figure 2-18d) according to the decrease of concentration in ND50(A)-PG due to decrease in the diffusion coefficients (Figure 2-18c). Similar phenomena were observed in DND(+)-PG(m) shown in Figure 2-18a and 2-18b, though the value becomes unstable at the concentration too low (< 0.016 % in water) to obtain sufficient scattered light intensity. From these observations, the DLS sizes in 10 mM NaCl at 0.10% concentration of ND core were adopted for the actual sizes of ND-PGs as shown in Figure 2-19. DLS results of DND- and ND50-PGs in water, 10 mM NaCl and PBS (phosphate buffered saline, pH 7.4 including 137 mM NaCl) are summarized in Figure 2-20 and Table 2-14, where the dispersions are confirmed to be stable.

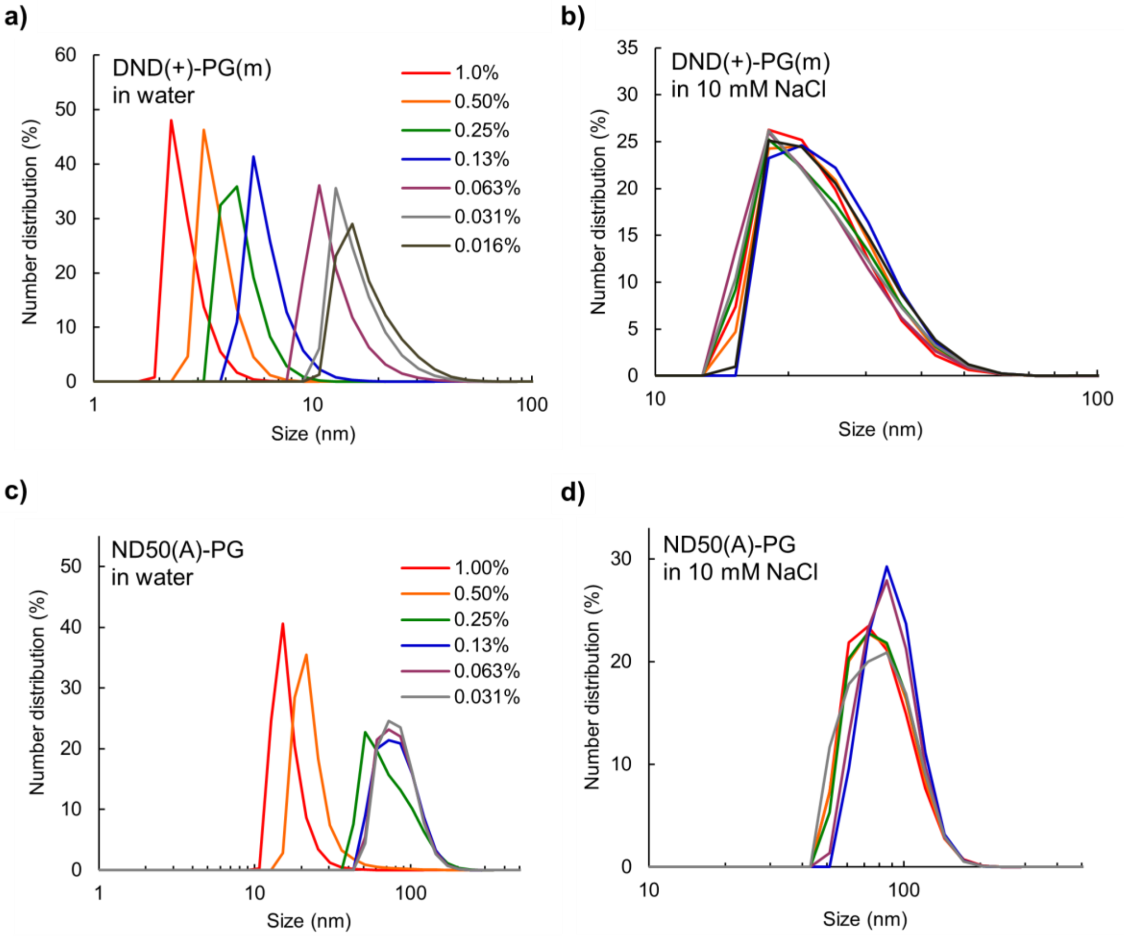

Figure 2-18. Concentration dependence of DLS results of a, b) DND(+)-PG(m) and c, d) ND50(A)-PG in a, c) water and b, d) 10 mM NaCl on number basis. The concentrations are based on the ND core.

Table 2-13. Viscosity of ND-PG dispersions by electro-magnetically spinning sphere (EMS) viscometer.

Sample	Dispersion medium	Concentration	Viscosity (mPa·s)		
			25 °C	30 °C	35 °C
Blank	Water		1.03	0.92	0.82
	0.1 mM NaCl		1.07	1.01	0.87
DND(+)-PG(m)	Water	0.10 %	1.05	0.94	0.87
		0.50 %	1.16	1.04	0.94
		1.0 %	1.12	1.01	0.93
	0.1 mM NaCl	0.10 %	1.07	0.97	0.91
		0.50 %	1.13	1.04	0.95
		1.0 %	1.08	0.99	0.89
ND50(A)-PG	Water	0.10 %	1.03	0.93	0.81
		0.50 %	1.08	1.02	0.96
		1.0 %	1.14	1.00	0.90
	0.1 mM NaCl	0.10 %	1.11	0.97	0.93
		0.50 %	1.15	1.04	0.94
		1.0 %	1.08	0.98	0.87

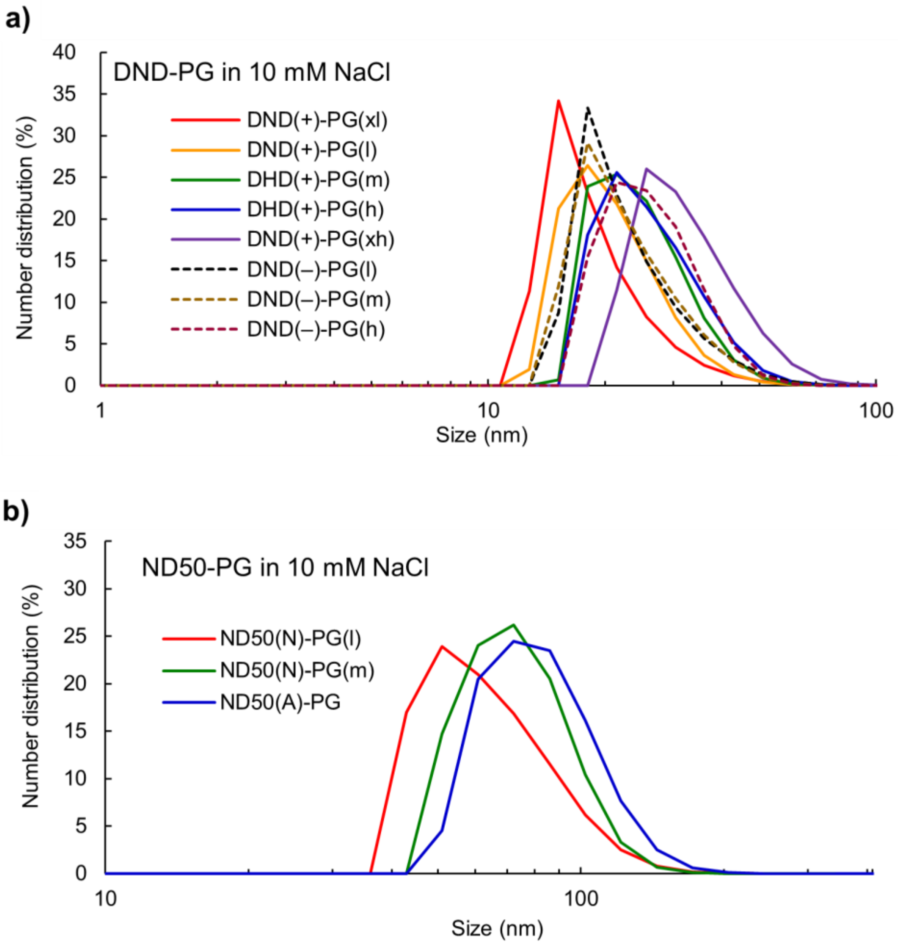

Figure 2-19. DLS results of a) DND-PG and b) ND50-PG at ND concentrations of 0.10% in 10 mM NaCl on number basis.

a) DND(+)-PGs

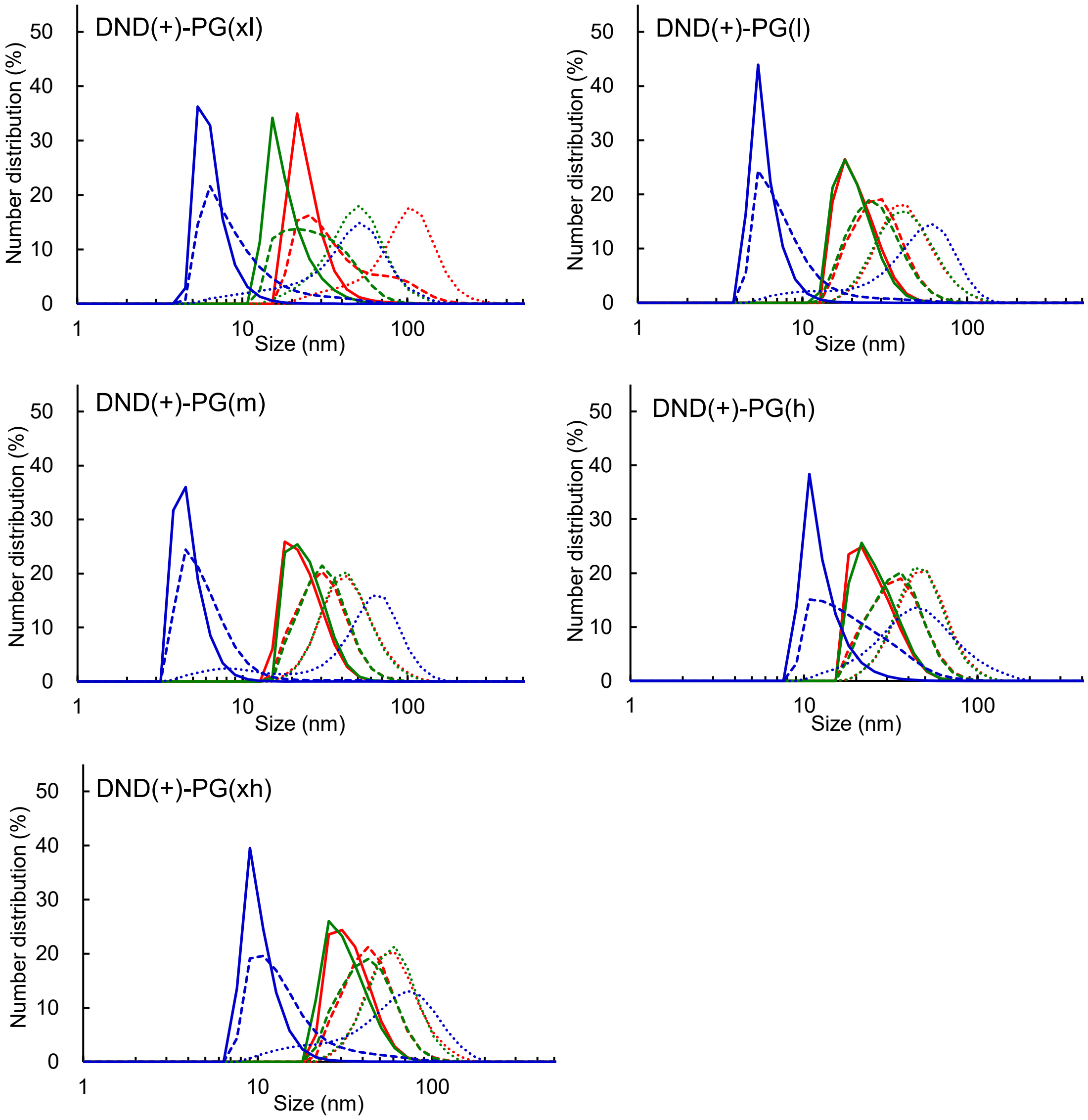

b) DND(–)-PGs

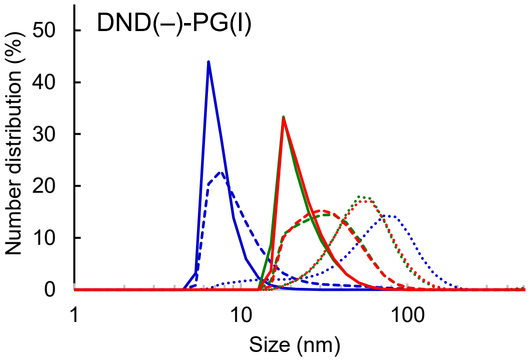

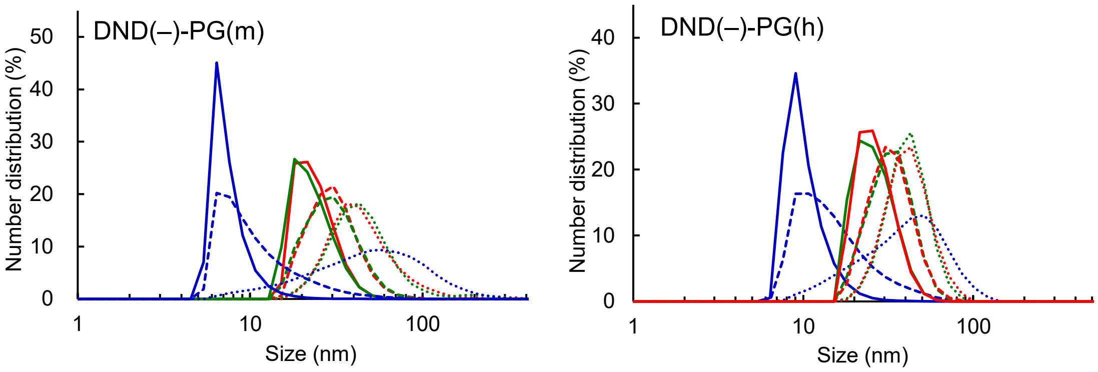

c) ND50-PG

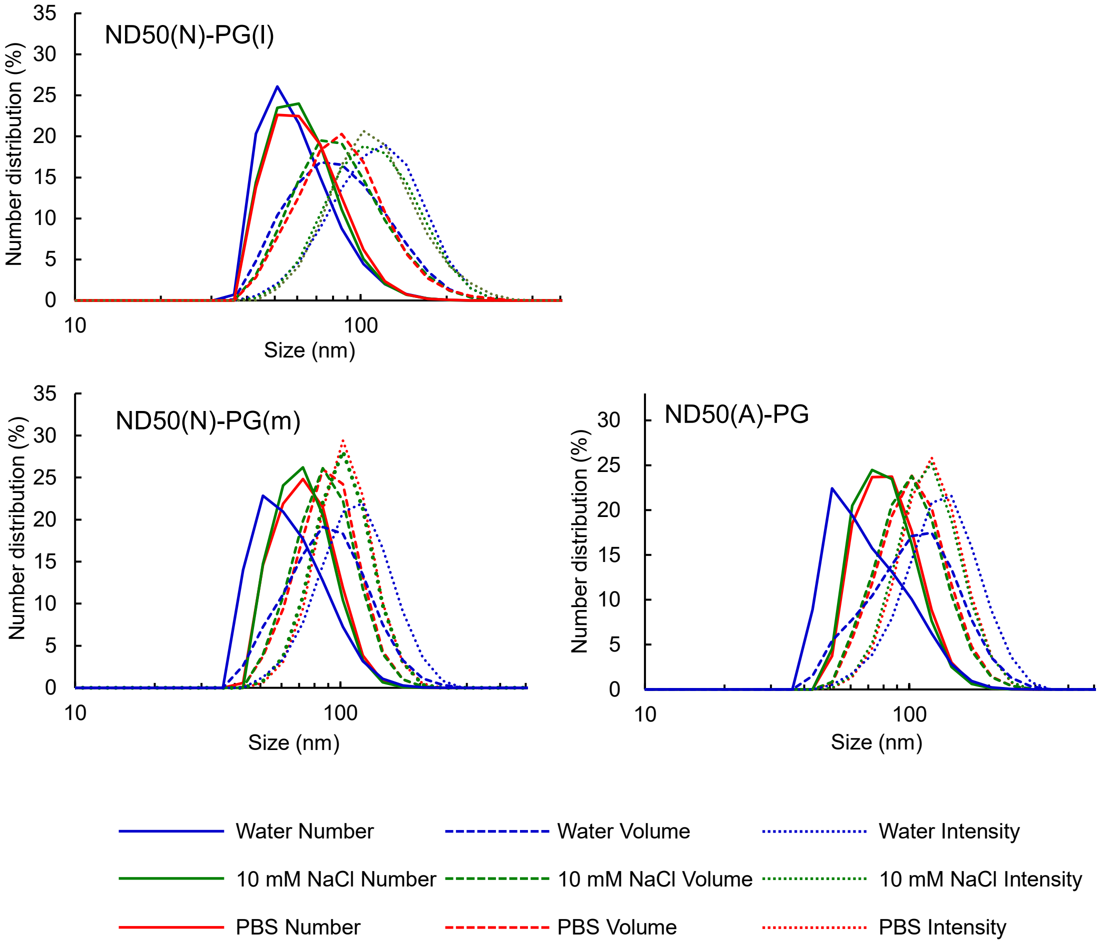

Figure 2-20. Hydrodynamic diameter (particle size) distributions of DND-PG of different PG/DND ratio in three ionic strengths plotted on number, volume and scattered light intensity basis.

Table 2-14. Median hydrodynamic diameter (D_{50}) by DLS measurements on number basis, volume basis and intensity basis.

Number basis

	PBS (nm)	10 mM NaCl (nm)	Water (nm)
DND(+)-PG(xl)	21.31	15.64	4.12
DND(+)-PG(l)	18.70	18.09	5.64
DND(+)-PG(m)	20.59	21.52	5.14
DND(+)-PG(h)	21.77	22.50	10.64
DND(+)-PG(xh)	29.69	28.00	8.93
DND(–)-PG(l)	19.64	18.99	6.47
DND(–)-PG(m)	21.14	19.21	6.90
DND(–)-PG(h)	23.40	23.11	8.67
ND50(N)-PG(l)	56.64	55.62	52.20
ND50(N)-PG(m)	66.53	65.40	56.82
ND50(A)-PG	74.07	72.54	60.92

Volume basis

	PBS (nm)	10 mM NaCl (nm)	Water (nm)
DND(+)-PG(xl)	29.98	23.92	4.98
DND(+)-PG(l)	25.78	24.61	7.25
DND(+)-PG(m)	27.47	28.08	6.35
DND(+)-PG(h)	30.74	31.02	15.84
DND(+)-PG(xh)	39.27	38.37	11.49
DND(–)-PG(l)	29.18	29.46	7.99
DND(–)-PG(m)	28.17	28.03	8.74
DND(–)-PG(h)	29.43	29.82	12.15
ND50(N)-PG(l)	74.61	74.96	74.94
ND50(N)-PG(m)	82.14	80.13	81.51
ND50(A)-PG	94.10	91.94	96.26

Intensity basis

	PBS (nm)	10 mM NaCl (nm)	Water (nm)
DND(+)-PG(xl)	90.14	44.26	52.13
DND(+)-PG(l)	37.68	37.84	41.95
DND(+)-PG(m)	38.71	38.37	46.46
DND(+)-PG(h)	43.35	42.48	40.48
DND(+)-PG(xh)	53.15	53.45	56.27
DND(–)-PG(l)	49.31	48.97	60.63
DND(–)-PG(m)	43.15	42.61	54.85
DND(–)-PG(h)	37.38	37.32	36.79
ND50(N)-PG(l)	100.22	99.99	104.70
ND50(N)-PG	94.42	92.88	103.90
ND50(A)-PG	110.07	108.00	122.50

To determine the ND size, NDs before PG functionalization were analyzed by DLS in water as shown in Figure 2-21. DND(+) and DND(–) exhibit the concentration dependence even at the low concentrations such as 0.016 and 0.031%, respectively. The DLS sizes at these low concentrations, 32.16 and 25.11 nm, are much larger than the sizes evaluated by transmission electron microscopy (TEM) probably due to the strong electrostatic interaction [39]. The sizes of DNDs were therefore determined by BET specific surface area (BET-SSA) to be 5.12 and 4.96 nm for DND(+) (2 different lots) and 5.15 nm for DND(–) (Tables 2-15 and 2-16). On the other hand, the size of ND50 was determined to be 43.35 nm by DLS at the low concentrations of 0.063 – 0.008% (Figure 2-21 and Table 2-16), although the concentration dependence was observed at higher concentrations. Contrary to the case of DNDs, the calculated diameter of ND50 from BET-SSA is 21.1 – 20.4 nm (2 samples, Table 2-15), which seems to be much smaller than the diameters of commercial ND50 in microscopic images shown in previous reports [46, 120–122]. It would be due to the non-spherical shape of crashed HPHT diamond, or existence of cracks and defects, whereas DNDs are almost spherical shape.

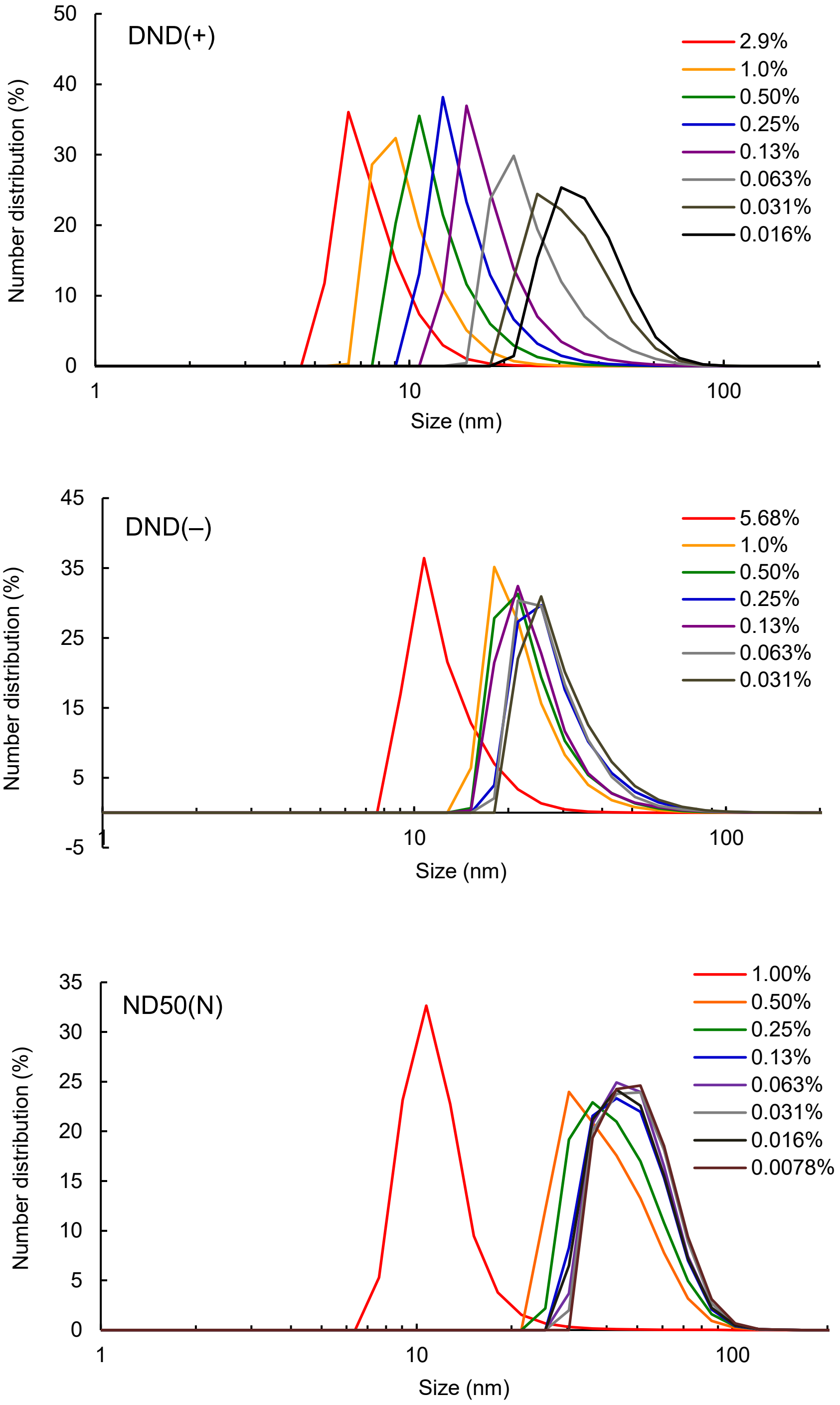

Figure 2-21. Concentration dependence of DLS results of DND(+), DND(–) and ND50(N) in water on number basis. The core size of ND50(N) is determined to be 43.35 nm from the average of the results from 0.063 % to 0.008 % which reach to constant values in high-diluted condition.

Table 2-15. BET specific surface area (BET-SSA) and the density of oxygen on the surface.

	DND(+)-1*	DND(+)-2**	DND(–)	ND50(A)	ND50(N)
Results of the measurement					
BET-SSA (m^2/g)	345.90	334.55	333.10	81.17	83.88
Pore volume (cm^3/g)	0.2264	0.2208	0.21980	0.052934	0.054301
Average pore size (nm)	2.6408	2.6400	2.6389	2.6085	2.5896
Density of oxygen (O) on the surface					
O content by elemental analysis (mmol/g)	3.21	3.03	5.94	1.83	1.68
Density of O on the surface ($\mu mol/m^2$)	9.29	9.04	17.84	22.48	20.05

* Raw material for DND(+)-PG(xl) and DND(+)-PG(l).

** Raw material for DND(+)-PG(h) and DND(+)-PG(xh).

Based on the above results in the sizes of ND-PGs and NDs (Table 2-16), the lengths of PG chain on NDs are estimated; 5.34 – 11.44 nm for DND(+)-PG(xl) to DND(+)-PG(xh) corresponding to 11 – 24 generations, and 6.13 – 14.60 nm for ND50-PGs corresponding to 13 – 31 generations, if the length of the one glycerol unit is assumed to be 0.47 nm (Table 2-16). On the other hand, the calculated numbers of glycerol unit based on the DB of 0.47 – 0.64 (Table 2-11) exceed those determined experimentally if all PG chains on the surface have the full generations; 11 – 24 for DND(+)-PGs and 13 – 31 for ND50-PGs (Table 2-16). This indicates that the PG chains shorter than these generations should exist on the surface, probably because the chain growth may be restricted by the adjacent longer chains. Meanwhile, theoretical thickness of PG layer in each ND-PG is calculated from the TGA results on the premise that the PG layer densely covers the ND surface without void space. Assuming the density of PG layer to be 1.261 g/cm^3 (the density of glycerol), the thicknesses of PG layer and the diameter of ND-PGs are calculated to be 0.81 – 3.74 nm and 6.57 – 12.60 nm for DND-PGs, and 9.29 – 13.58 nm and 61.93 – 70.51 nm for ND50-PGs as shown in Table 2-17.

Table 2-16. PG chain length calculated from the DLS results in 10 mM NaCl.

	DND(+)-PG(xl)	DND(+)-PG(l)	DND(+)-PG(m)	DND(+)-PG(h)	DND(+)-PG(xh)	DND(–)-PG(l)	DND(–)-PG(m)	DND(–)-PG(h)
DLS size in 10 mM NaCl (nm)	15.64	18.09	21.52	22.50	28.00	18.99	19.21	23.11
Diameter of ND core (nm)	4.96 *	4.96 *	5.12 *	5.12 *	5.12 *	5.15 *	5.15 *	5.15 *
Thickness of PG layer (nm) ***	5.34	6.57	8.20	8.69	11.44	6.92	7.03	8.98
Numbers of generation of PG ****	11.4	14.0	17.4	18.5	24.3	14.7	15.0	19.1

	ND50(N)-PG(l)	ND50(N)-PG(m)	ND50(A)-PG
DLS size in 10 mM NaCl (nm)	55.61	65.40	72.54
Diameter of ND core (nm)	43.35 **	43.35 **	43.35 **
Thickness of PG layer (nm) ***	6.13	11.03	14.60
Numbers of generation of PG ****	13.0	23.5	31.1

* Calculated from BET-SSA.

** DLS result in water at high-diluted condition.

*** (DLS size in 10 mM NaCl – Diameter of DND core)/2.

****Assuming that the length of GD unit is 0.47 nm.

Table 2-17. Calculated thickness of PG layer in compact structure from the TGA results

	DND(+)-PG(xl)	DND(+)-PG(l)	DND(+)-PG(m)	DND(+)-PG(h)	DND(+)-PG(xh)	DND(–)-PG(l)	DND(–)-PG(m)	DND(–)-PG(h)
PG/ND ratio by TGA	0.48	0.99	2.29	2.80	4.99	1.43	1.84	3.62
Weight of PG layer (10^{-18} g/particle)	0.107	0.221	0.565	0.690	1.230	0.357	0.460	0.904
Volume of PG (nm^3) *	84.9	175.1	447.8	547.5	975.7	283.3	364.5	717.1
Volume of ND core (nm^3)	63.7	63.7	70.4	70.4	70.4	71.4	71.4	71.4
Calculated diameter of ND-PG (nm)	6.57	7.70	9.97	10.57	12.60	8.78	9.41	11.46
Calculated thickness of PG (nm)	0.81	1.37	2.42	2.72	3.74	1.82	2.13	3.16
Numbers of glycerol unit ($\times 10^3$) **	0.87	1.80	4.59	5.61	10.0	2.90	3.74	7.35
Thickness ratio (DLS/calculated) ***	6.61	4.79	3.39	3.19	3.06	3.81	3.30	2.84
Volume ratio (DLS/calculated) ***	22.84	17.53	11.50	10.76	11.71	12.41	9.99	8.91

Table 2-17 (continued).

	ND50(N)-PG(l)	ND50(N)-PG(m)	ND50(A)-PG
PG/ND ratio by TGA	0.69	0.85	1.19
Weight of PG layer (10^{-18} g/particle)	103.0	126.9	177.7
Volume of PG (nm^3) *	8,169	100,632	140,884
Volume of ND core (nm^3)	42,665	42,665	42,665
Calculated diameter of ND-PG (nm)	61.93	64.92	70.51
Calculated thickness of PG (nm)	9.29	10.79	13.58
Numbers of glycerol unit ($\times 10^6$) **	0.837	1.03	1.44
Thickness ratio (DLS/calculated) ***	0.66	1.02	1.07
Volume ratio (DLS/calculated) ***	0.58	1.03	1.12

* Density of PG layer is assumed to be 1.261 g/cm^3.

** Molecular weight of GD is 74.08 (g/mol).

*** Ratio of the size from DLS in 10 mM NaCl to calculated value.

The PG layer determined above by DLS (Table 2-16) are 3 – 7 times as thick as that calculated from the TGA results in DND-PG, but they are matched in ND50(N)-PG(m) and ND50(A)-PG. In ND50(N)-PG(l), the theoretical thickness of PG layer was larger than the DLS result, but it can be said that the trend is the same as former two results. The difference indicates that the PG layer on the DND is flexible and swells with water to expand their DLS sizes in the aqueous dispersion, while the PG on ND50 did not change their shapes in aqueous solutions due to their strong intra- and/or inter-polymer chain interactions in a dense and rigid structure. Due to the radial spatial extension on DND particle with higher curvature, a void space between the individual PG chains may be larger than ND50, which can make PG chains more flexible and accommodate more ionic species to dissociate the strong interaction between the chains. In ND50s, the PG chain packs more with less void space due to the smaller curvature.

The above discussion is supported by the relationship of $W_{\mathrm{PG}}/W_{\mathrm{ND}}$ by TGA with the volume ratio of the expanded structure in 10 mM NaCl to the calculated compact structure (Figure 2-22). DND-PGs of higher $W_{\mathrm{PG}}/W_{\mathrm{ND}}$ have the lower volume ratio, indicating that the density of PG chain becomes higher in DND-PG as $W_{\mathrm{PG}}/W_{\mathrm{ND}}$ becomes higher. When the ring-opening polymerization proceeds to increase the diameter, the curvature of the particle decreases the resulting less spatial extension and higher density of PG layer in the expanded structure. The increase of density may relate to the increase of abundance of sterically favored L_{14} substructure suggested by ^{13}C NMR described above. In addition, DND-PGs from bare DND with higher oxygen content give higher density of PG chain.

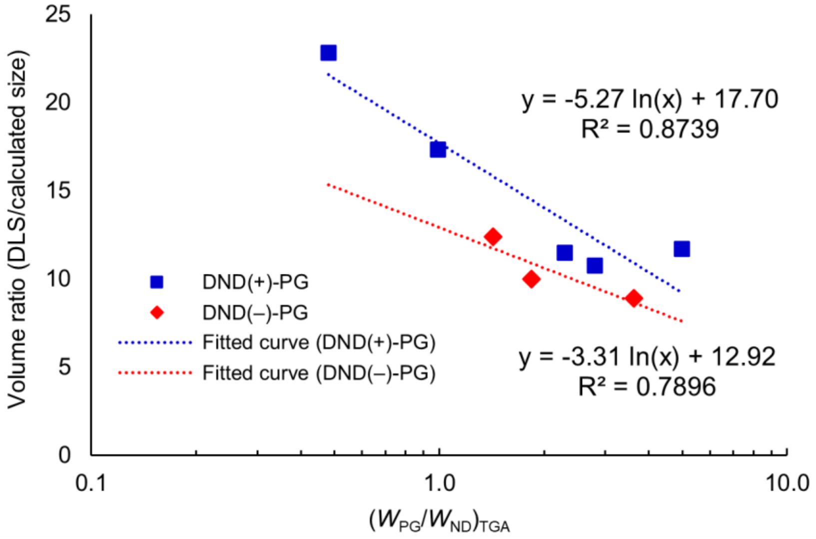

Figure 2-22. Relationship between the PG/ND weight ratio and the volume increase ratio of PG layer of compact structure (calculated) to the expanded structure (in 10 mM NaCl) of DND-PGs.

2-3. Conclusion

We develop a scalable process for PG functionalization of ND using EG as a solvent along with dropwise-addition of GD, making the ring-opening polymerization of GD safely. DND-PGs and ND50-PGs with various PG/ND ratios (W_{PG}/W_{ND}) are prepared under various conditions. After thorough elucidation of the reaction, it is found that the PG amount on ND surface (W_{PG}) can be theoretically controlled by the properties of ND, the diameter and the oxygen content of ND core (D_{ND} and O_{ND}, respectively), and the reaction conditions, the weights of GD, ND and EG (W_{GD}, W_{ND} and W_{EG}, respectively). In ^{13}C NMR analysis of the resulting ND-PGs, we estimate the substructure abundances of the monomer (glycerol) units, implying that cationic mechanism is preferable in the ring-opening reaction of GD. DLS measurement is also performed to determine the thickness of PG layer and the length of PG chain in 10 mM NaCl, where the more reliable data are obtained than those in the other solvents. In addition, the differences in the sizes determined by DLS and calculated by TGA indicate that the PG chain in DND-PG might be flexible to swell with water in aqueous dispersion probably due to the higher curvature of DND.

The results presented here should provide useful information for the quantitative design of further chemical functionalization of ND-PGs especially for biomedical application. For example, the substructure abundance would be important for a regioselective and stoichiometric control of the reaction. In addition, the size information may provide new insights for *in vivo* behavior of the ND-PGs.

2-4. Experimental

Materials

DNDs were manufactured by Daicel Corporation (DINNOVARE™). ND50 was purchased from Tomei Diamond Corporation. Hydrochloric acid, 2,3-epoxy-1-propanol (GD) and ethylene glycol for PG functionalization of DNDs, and sodium chloride and 10× phosphate-buffered saline (10× D-PBS(–)) for DLS measurement were purchased from FUJIFILM Wako Pure Chemical Corporation (Osaka Japan). D_2O for ^{13}C and ^{1}H NMR measurement was purchased from Tokyo Chemical Industry Co., Ltd. (Tokyo Japan).

Equipment

^{13}C and ^{1}H NMR spectra were measured by ECX500 NMR spectrometer (JEOL). FT-IR spectra were recorded on IR Tracer-100 FT-IR spectrometer (Shimadzu) equipped with DiffusIR DRIFT chamber (PIKE Technologies). Elemental analyses were conducted at Organic Elemental Microanalysis Center of Kyoto University. Thermogravimetric analysis (TGA) was performed with TG/DTA 6200 (SII). DLS measurement was done by Nanotrac Wave II particle size analyzer (MicrotracMRB). Specific surface area was measured by Belsorp mini-II (Microtrac BEL Corporation). Viscosity was measured by EMS-1000 electro magnetically spinning viscometer (Kyoto Electronics).

Water dispersion of ζ-positive DND (DND(+))

DND powder was annealed in H_2/N_2 (2/98 (v/v)) at 550 °C for 2 h. Resulting powder was suspended in water (3.0 %) and pH was adjusted to 3.5, and then agitated vigorously with ZrO_2 beads (30 μmφ) at the tip speed of 8 m/s for 2 h. ZrO_2 beads were removed by decantation and then, centrifuged at 20000*g* for 10 min to give black dispersion. The median hydrodynamic diameter measured by DLS (D_{50}, number basis) was 3.89 nm.

Water dispersion of ζ-negative DND (DND(–))

DND powder was annealed in O_2/N_2 (4/96 (v/v)) at 420 °C for 2 h. Resulting powder was suspended in water (3.0 %) and pH was adjusted to 10.5, and then agitated vigorously with ZrO_2 beads (30 μmφ) at the tip speed of 8 m/s for 2 h. ZrO_2 beads were removed by decantation and then, centrifuged at 20000*g* for 10 min to give black dispersion. The median hydrodynamic diameter measured by DLS (D_{50}, number basis) was 4.44 nm.

DND(+)-PG(xl)

An aqueous dispersion of ζ-positive DND was evaporated to dryness. The solid residue was dried at 105 °C for 2 h. To a suspension of resulting DND powder (0.50 g) in ethylene glycol (15.0 g), GD (11.3 g, 0.152 mol) was added dropwise over 1.5 h to keep the temperature in the range of 93–109 °C. The resulting black dispersion was stirred at the same temperature overnight. After the reaction was cooled below 40 °C, water (40 mL) was added slowly to degrade the unreacted GD. The dispersion was diluted with water to ca. 400 mL and concentrated with ultrafiltration membrane (Ultracel® membrane, 100 kDa) to < 40 mL. The concentrate was diluted and concentrated again, which was repeated five times, and the weight of resulting black water dispersion was adjusted to 50.0 g with water. To remove free PG, 40.0 g of water dispersion was ultracentrifuged at 183400*g* (50000 rpm) for 2 h. Supernatant (80–90 % of total amount) was removed carefully and remained lower layer was diluted with water, and ultracentrifuged again, which was repeated four times (The centrifugation time ranged 1.5–2.5 h). The resulting lower layer was adjusted to 40.0 g with water. An aliquot of the dispersion was accurately weighed (3.0153 g) and dried on heated PTFE sheet. From the weight of the residue (0.0417 g), the sample concentration was determined to be 1.38 % (w/w). The net yield of DND(+)-PG(xl) was 0.55 g from 0.40 g of DND.

FT-IR (DRIFT with KBr, cm^{-1}): 3332, 2918, 2875, 1458, 1118, 1078 (C–O). ^{1}H NMR (500 MHz, D_2O): δ ppm 3.42, 3.50, 3.58, 3.75, 3.88. The results of TGA (Air atmosphere, 20 °C/min) and elemental analysis are in Tables 2-2 and 2-3, respectively.

DND(+)-PG(l) and DND(+)-PG(h) were prepared as the same manner except for the quantity of reagents was changed according to the values in Table 2-1 as the quantitative ratio. Yield of DND(+)-PG(h) was 0.17 g from 0.10 g of DND (corresponds to the size of ultracentrifugation). Yield of DND(+)-PG(h) was 3.06 g from 1.01 g of DND.

DND(+)-PG(xh)

DND powder prepared by above procedure (0.25 g) was suspended in GD (5.0 mL = 5.57 g, 0.075 mol). After DND was dispersed to result a black dispersion, GD (10.0 mL, 0.15 mol) was additionally added. The reaction was stirred at 140 °C for 6.5 h. Purification was done in the same manner as DND(+)-PG(xl). Yield (net) 1.58 g.

DND(–)-PG(m)

To an aqueous dispersion of ζ-negative DND, 1 M HCl was added to adjust pH to about 3.5. The resulting precipitate was collected by centrifugation at 30000*g* for 30 min. The precipitate was washed with water once and dried at 70 °C *in vacuo* overnight, then at 120 °C for 4 h. Using the resulting DND powder, sample was prepared in the same manner as DND(+)-PG samples.

The net yield of DND(–)-PG was 1.18 g from 0.50 g of DND.

DND(–)-PG(h) and DND(–)-PG(l) were prepared as the same manner except for the quantity of reagents was changed according to the values in Table 2-1 as the quantitative ratio. Yield of DND(–)-PG(h) was 0.91 g from 0.25 g of DND, and DND(–)-PG(l) was 0.52 g from 0.25 g of DND

ND50(A)-PG

ND50 (0.20 g, MD50 from Tomei Diamond) was treated with a mixture of conc-H_2SO_4 (15.0 mL) and HNO_3 (70 %, 5.0 mL) at 150 °C for 5 h. The treatment mixture was poured into 200 mL of water, and centrifuged (20000*g*, 10 min). Precipitate was washed with water twice (40 mL and 25 mL) and dried at 105 °C *in vacuo* to give black powder (0.18 g).

The acid treated ND50 (ND50(A), 0.15 g) was dispersed in ethylene glycol (1.03 mL) and heated at 140 °C. GD (16.12 g, 0.218 mol) was added to the dispersion slowly for 1 h, and the reaction was stirred at the same temperature overnight. Work-up and purification was done in the same manner as DND(+)-PG(xl) except for the concentration with ultrafiltration membrane was done only once before the ultracentrifugation. Yield (net) 0.34 g.

DND(N)-PG(m) and DND(N)-PG(l) were prepared by the same procedure but ND50 was just dried at 105 °C *in vacuo* without acid treatment before the reaction (ND50(N)). The net yield of ND50(N)-PG(m) was 0.36 g from 0.20 g of ND50(N), and ND50(N)-PG(l) was 0.41 g from 0.25 g of ND50(N).

^{13}C NMR measurement

^{13}C NMR measurements were done in 5 mmϕ tube at the ND-PG concentration of approx. 20 % in D_2O except for ND50(N)-PG(m) and ND50(N)-PG(l) that were measured at 10 % and 15%, respectively. All measurements were done at 30 °C. Chemical shift of diamond core was adjusted to 36.3 ppm at the peak top as a reference.

Appendix I to Chapter 2

S2-1. ^{13}C T_1 relaxation time measurement of DND(+)-PG(m)

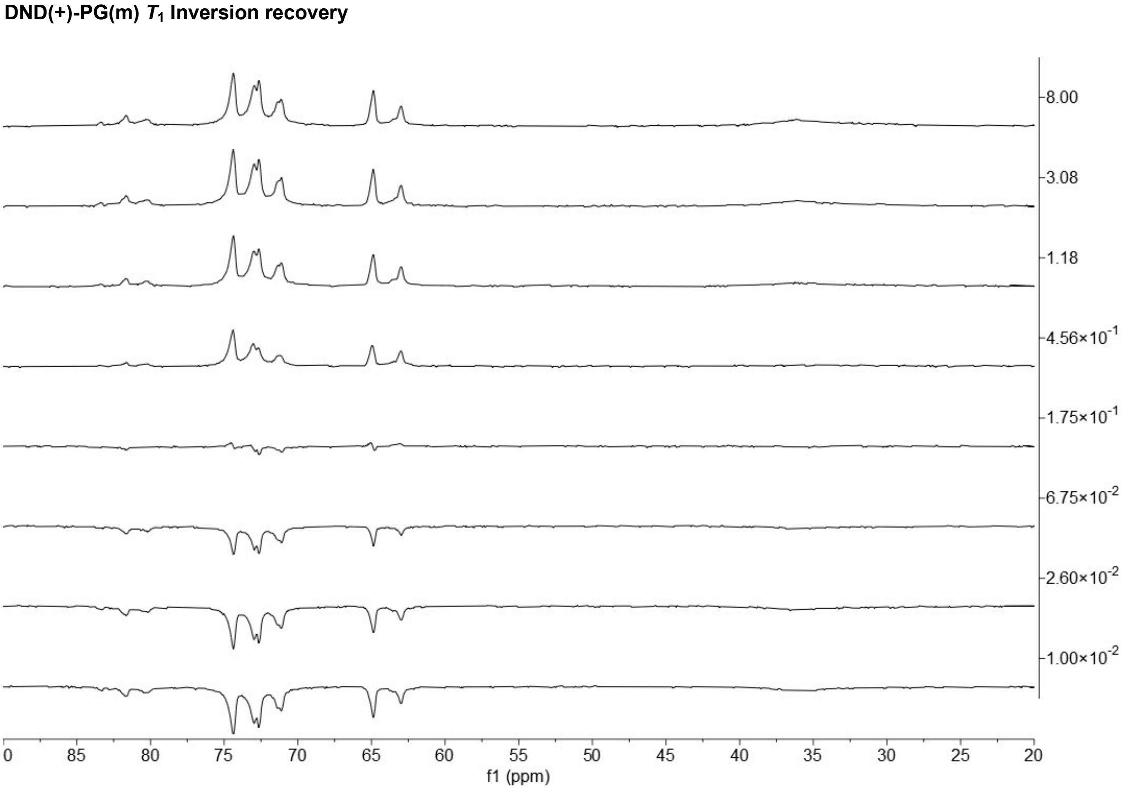

DND(+)-PG(m) T_1 Inversion recovery

Figure S2-1. Stacked spectra of T_1 measurement by inversion recovery method. The numbers on the right are the inversion time (sec).

Table S2-1. T_1 value of each signal calculated by the peak intensity.

Chemical shift (ppm)	83.4	81.7	80.2	74.4	73.0, 72.7	71.4, 71.1	64.9	63.1	36.6
T_1 (sec)	0.44	0.43	0.48	0.25	0.31	0.39	0.31	0.22	0.64

S2-2. Assignment of ^{13}C NMR by DEPT and 2D NMR spectra

The ^{13}C NMR spectrum of PG chain of DND-PG is almost the same as that of free PG with three peak regions, the ranges between 85 and 80 ppm, 76 and 70 ppm, and 66 and 62 ppm. In the range of 85 to 80 ppm, three groups of signals, with unseparated shoulder peaks, are detected, all of which are from CH carbons according to DEPT spectra (Figure S2-2). Peaks at around 83.4, 81.7 and 80.2 ppm are assigned as secondary carbons at the middle of glycidol unit with ether linkage ($–\underline{C}H(OR)–$) of T′, L_{13} and D or D′, respectively, in accordance with the assignment for free PG. Three signals of CH_2 in the region of high magnetic field (66 to 62 ppm) represent carbons of primary hydroxy group ($–\underline{C}H_2OH$). Signals at 64.9, 63.6 and 63.1 ppm are assigned as T, T′ and L_{13}, respectively. The assignments are confirmed by HMQC and HMBC spectra (Figure S2-3). Existence of cross-peaks at 3.66 to 83.4 ppm, and 3.83 to 63.6 ppm in HMQC (C–H connection), and 3.83 to 83.4 ppm in HMBC (C–C–H connection) indicates that two small signals at around 83.4 and 63.6 ppm are in the identical spin system of T′ substructure. On the other hand, signals at around 81.7 and 63.1 ppm are from the same substructure of L_{13}. There are cross-peaks at 3.75 to 81.7, 3.79 to 81.7 ppm and 3.84 to 63.1 ppm in HMQC, and 3.75 to 63.1, 3.80 to 63.1 ppm and 3.84 to 81.7 ppm in HMBC, which is consistent with the assignment for L_{13}. In addition, the carbon at 81.7 ppm connects to the carbon at 71.4 ppm according to the cross-peak at 3.75 to 71.4 ppm in HMBC. The region of 76 to 70 ppm must include the signals of primary carbon with ether linkage ($–\underline{C}H_2OR$) and secondary carbon with hydroxy group ($–\underline{C}H(OH)–$), three carbons of L_{14} (CH_2 and CH), two CH_2 carbons of D (D′) and T and one CH of L_{13}. Chemical shifts of L_{14} are determined to be 71.1 ppm for CH carbon, and 74.4 and 73.0 ppm for CH_2 carbons since cross-peaks at 4.11 to 71.1 ppm in HMQC, and 4.11 to 74.4 and 4.11 to 73.0 ppm in HMBC are detected. The signal at 4.11 ppm in ^{1}H NMR can be assigned as the proton of secondary carbon with free hydroxy group. The proportion between signals of two chemical shifts is uncertain.

Likewise, the signal of CH_2 carbons of T are assigned at 74.4 and 72.7 ppm, the same and similar chemical shifts as L_{14}. Cross-peaks at 3.99 to 74.4 ppm and 3.99 to 72.7 ppm are detected where the cross-peak at 3.99 to 64.9 ppm is observed in HMBC. Two CH_2 carbons of D (D′) are assigned to be at 73.0 ppm based on the cross-peak at 3.89 to 72.7 ppm in HMBC. The CH carbon of L_{13} substructure is located at 63.1 ppm as mentioned above.

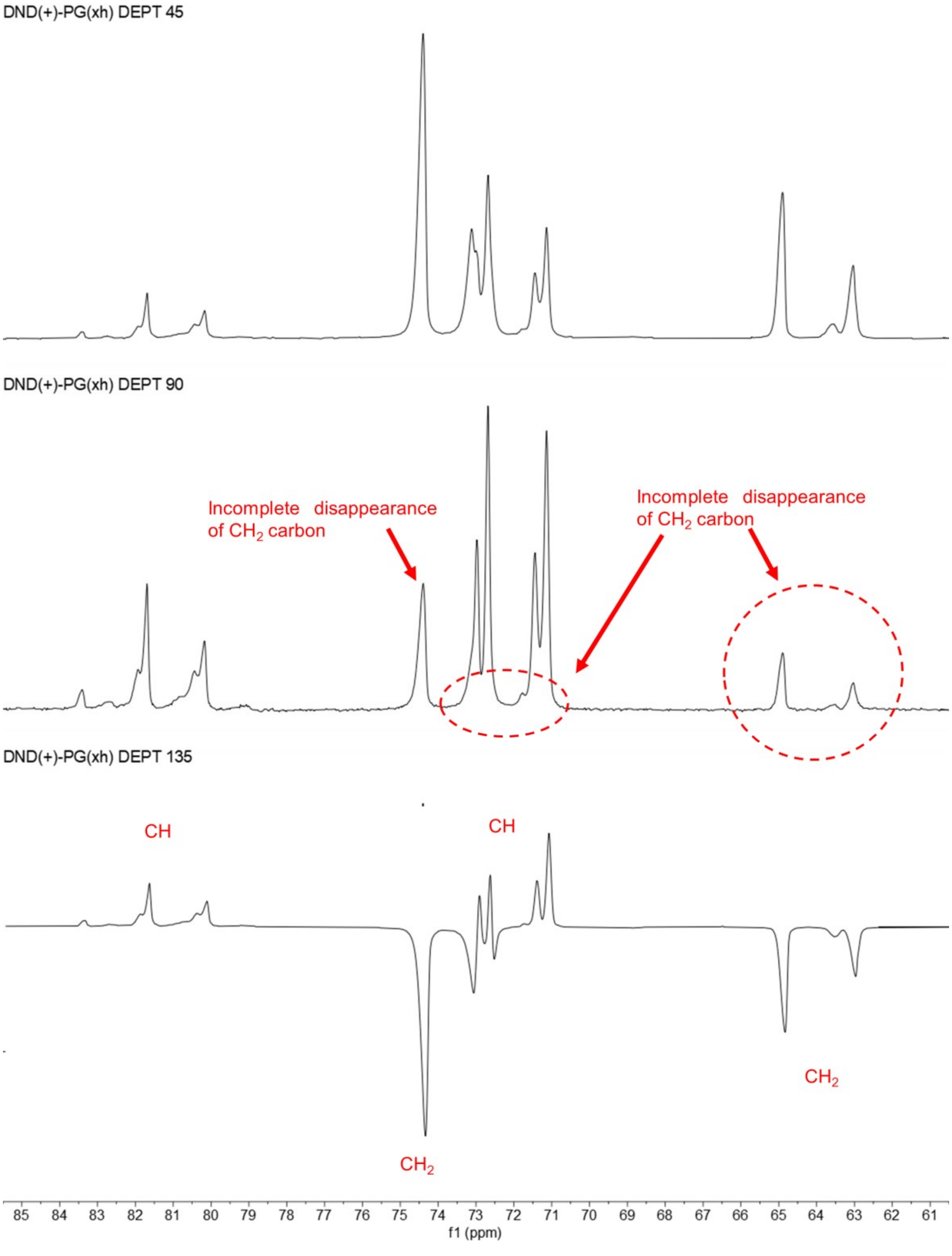

Figure S2-2. DEPT spectra.

DND(+)-PG(xh) HMQC

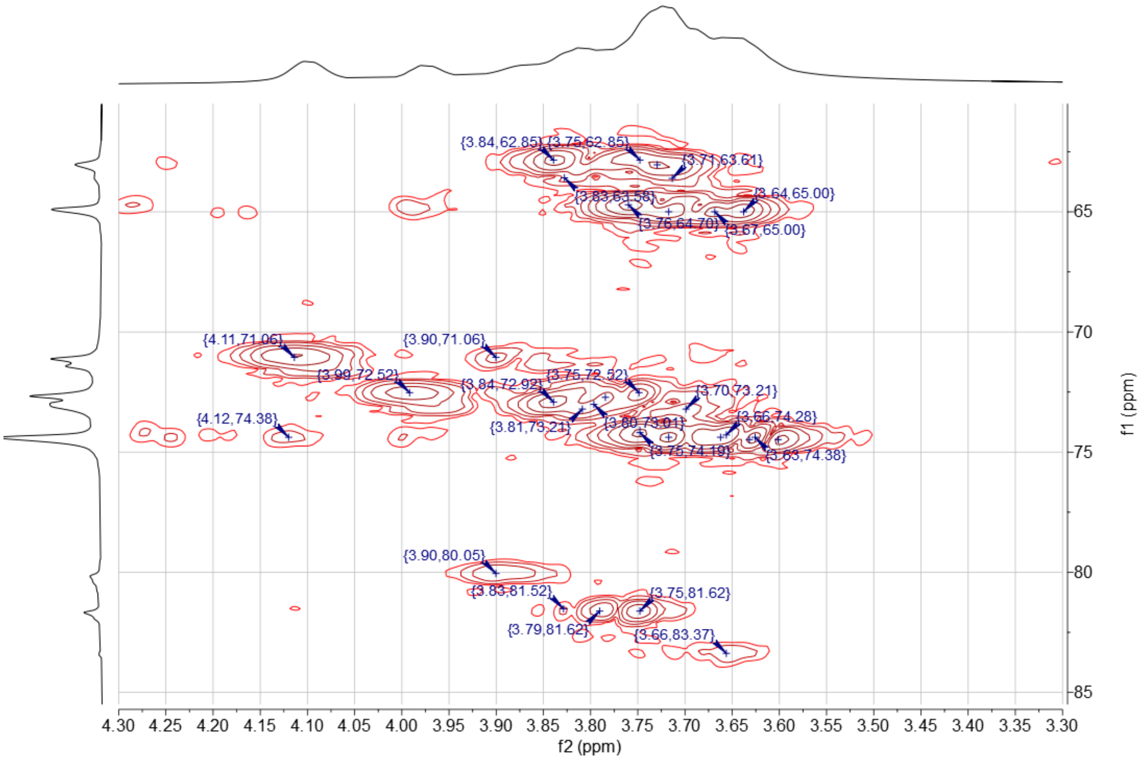

DND(+)-PG(xh) HMBC

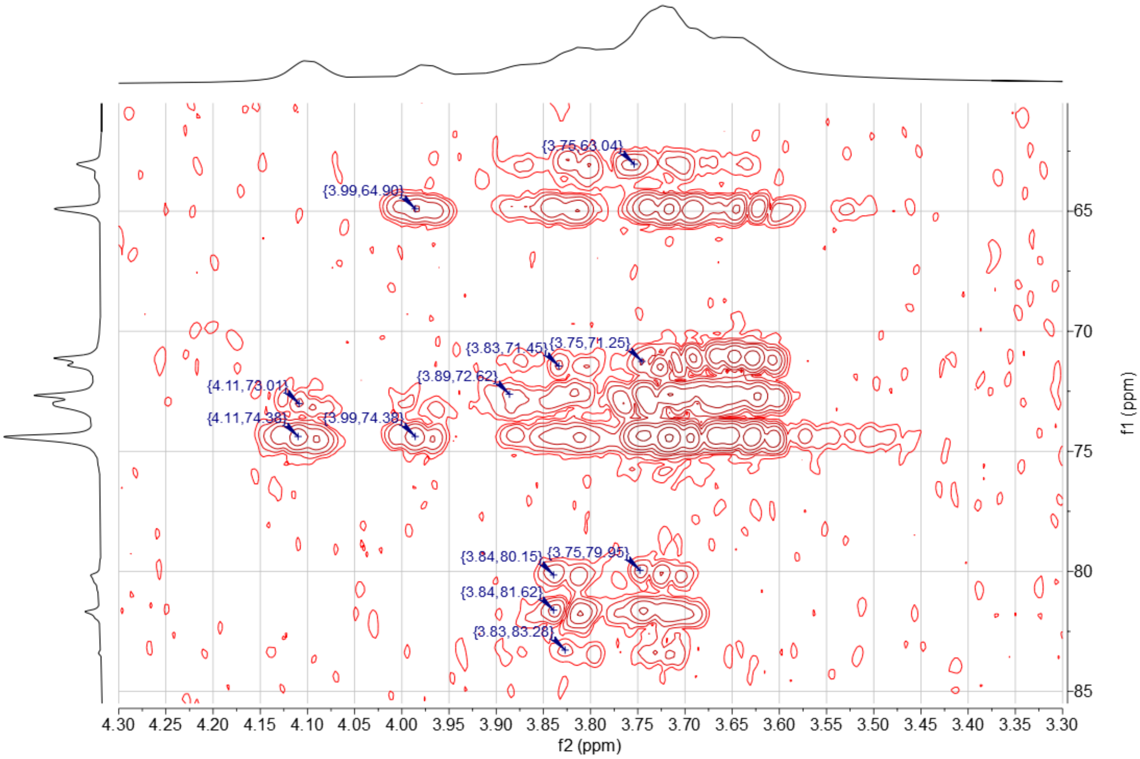

Figure S2-3. HMQC and HMBC spectra of DND(+)-PG(xh).

Chapter 3: Poly(glycerol-*co*-glyceric acid) functionalized nanodiamonds by nitroxyl radical-catalyzed oxidation of primary alcohols in poly(glycerol) as scaffolds for further conjugation

3-1. Introduction

Introduction of another functional group in the PG layer in ND-PG is meaningful as a scaffold to conjugate another functionality. Among the functional groups, carboxy group (–COOH) is one of the most useful ones to covalently bind various functional moieties such as peptides, proteins including antibodies and small molecules like anticancer drugs [53, 60, 63, 73]. Although carboxy groups were introduced by the reaction of –OH with succinic anhydride in pyridine [53, 60, 63, 71, 73, 123], the resulting ester linkage is susceptible to hydrolysis in aqueous, or physiological, environments. In this work, we developed the other means to introduce carboxy groups in the PG layer through direct oxidation of the primary alcohols (–CH_2OH) in glycerol units by nitroxyl radical catalyst (Scheme 3-1) [124–128]. The resulting PG-functionalized detonation ND (DND) with carboxy groups (DND-PG-COOH) should be more chemically robust and less hydrophobic than that prepared from succinic anhydride mentioned above. After the oxidation, the content of carboxy groups is determined by acid-base titration and is found to be controlled by the amount of the oxidants, sodium hypochlorite (NaClO) and sodium chlorite ($NaClO_2$), in the presence of nitroxyl radical catalyst such as 2,2,6,6-tetramethylpiperidine-1-oxyl (TEMPO) or its analogues.

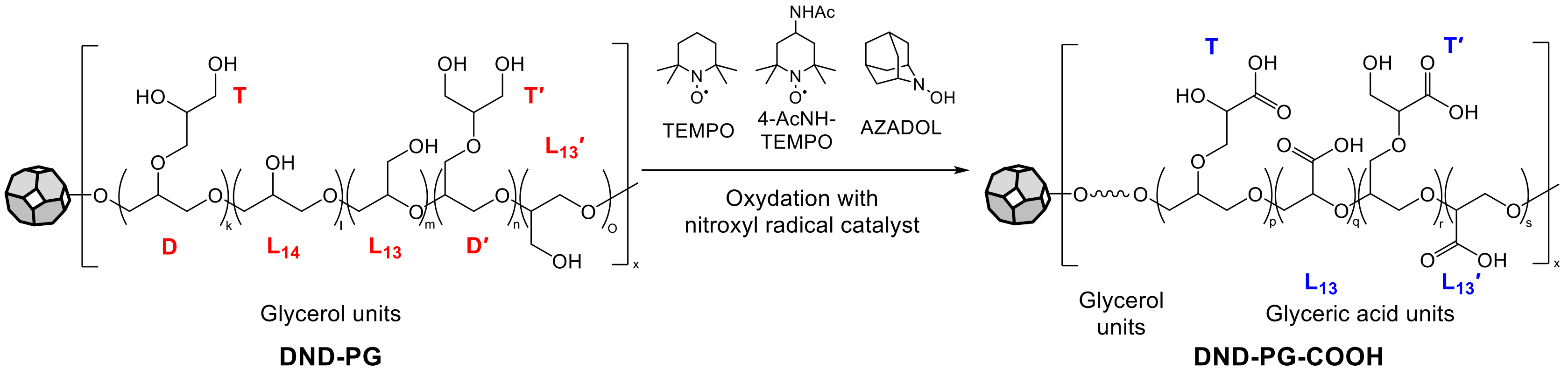

Scheme 3-1. Synthesis of DND-PG-COOH by the oxidation of DND-PG with nitroxyl radical catalyst. Red letters on DND-PG indicate substructure of glycerol units (**D**: dendritic, **L**: linear and **T**: terminal in ref. [129]). Blue letters on DND-PG-COOH indicate substructures with carboxy groups after CH$_2$OH in DND-PG is oxidized.

3-2. Results and discussion

The following two reaction systems were applied to the TEMPO-catalyzed oxidation of DND-PG; NaClO supplemented by sodium bromide (NaBr) under basic conditions (pH ~10) [130] and $NaClO_2$ with small amount of NaClO under neutral to slightly acidic conditions [131, 132]. Among the various substructures of glycerol unit in DND-PG as indicated in the red letters in Scheme 3-1 [129], the primary alcohols are subjected to be oxidized to carboxy groups in DND-PG-COOH as indicated in the blue letters. In the former reaction system, DND-PG was oxidized in the presence of TEMPO, NaClO and NaBr at pH around 10 and temperature below 5 °C (entry 1 in Table 3-1 and the details in 3-4 Experimental). At the beginning, the reaction was so fast that the pH value decreased immediately upon the addition of NaClO solution. Then, the decrease of pH, or consumption of NaClO, slowed down and stopped, when 9.2 mmol of NaClO to 1 g of DND-PG (entry 1 in Table 3-1) was added. After purification by ultrafiltration, the resulting carboxy group was confirmed qualitatively by FT-IR at 1734 cm^{-1} due to the stretching vibration of carbonyl group (Figure 3-1) and quantitatively by acid-base titration to be 1.34 mmol of COOH in 1 g of the material.

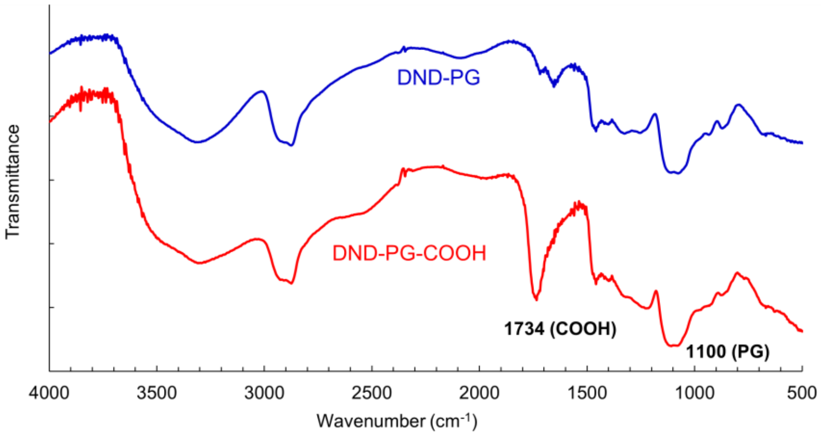

Figure 3-1. FT-IR spectra of DND-PG and DND-PG-COOH of entry 1 in Table 3-1 (DRIFT with KBr).

Table 3-1. Summary of oxidation reactions of DND-PG to DND-PG-COOH with nitroxyl radical catalyst.

Entry	Reagents (mmol) to 1 g of DND-PG (mmol/g)				Solvent (pH) [a]	Reaction time (h)	COOH content in 1 g of DND-PG-COOH (mmol/g)
	Catalyst		NaClO	NaClO$_2$			***A*** [b]
1	TEMPO	0.36	9.18	---	Water (10–12)	0.6	1.34
2	TEMPO	0.31	2.91	---	Water (10–12)	0.7	0.06
3	4-AcNH-TEMPO	0.20	0.55	10.14	Acetate (4.7)	48	2.31
4	4-AcNH-TEMPO	0.19	0.22	9.99	Acetate (4.7)	48	2.04
5	4-AcNH-TEMPO	0.15	0.17	7.43	Acetate (4.7)	24	2.60
6	4-AcNH-TEMPO	0.21	0.23	5.18	Acetate (4.7)	48	1.84
7	4-AcNH-TEMPO	0.24	0.27	3.97	Acetate (4.7)	24	1.51
8	4-AcNH-TEMPO	0.25	0.27	1.83	Acetate (4.7)	24	1.17
9	4-AcNH-TEMPO	0.15	0.17	1.26	Acetate (4.7)	23	1.01
10	4-AcNH-TEMPO	0.14	0.17	1.02	Acetate (4.7)	24	0.81
11	4-AcNH-TEMPO	0.11	0.11	0.63	Acetate (4.7)	25	0.47
12	TEMPO	0.16	0.17	5.00	Phosphate (6.8)	21	0.69
13	TEMPO	0.22	0.28	2.95	Phosphate (6.8)	18.5	1.04
14	4-AcNH-TEMPO	0.20	0.22	10.05	Phosphate (6.8)	48	1.36
15	4-AcNH-TEMPO	0.16	0.17	5.01	Phosphate (6.8)	22	0.65
16	4-AcNH-TEMPO	0.15	0.17	1.48	Phosphate (6.8)	22	0.30
17	AZADOL	0.20	0.34	10.07	Acetate (4.7)	45	1.47
18	AZADOL	0.15	0.17	3.00	Acetate (4.7)	23	1.27
19	AZADOL	0.16	0.17	1.03	Acetate (4.7)	21	0.69
20 [c]	4-AcNH-TEMPO	0.16	0.17	0.99	Acetate (4.7)	22	0.78

[a] Acetate: 0.4 M acetate buffer, Phosphate: 0.4 M phosphate buffer.

[b] ***A*** will be used in Table 3-3.

[c] ND50-PG was used instead of DND-PG.

a) entry 2 (0.06 mmol/g)

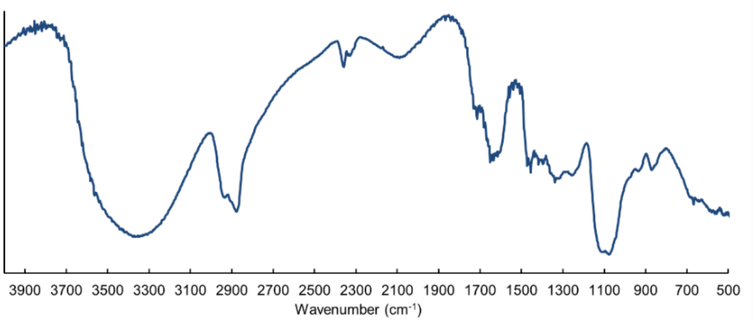

b) entry 3 (2.31 mmol/g)

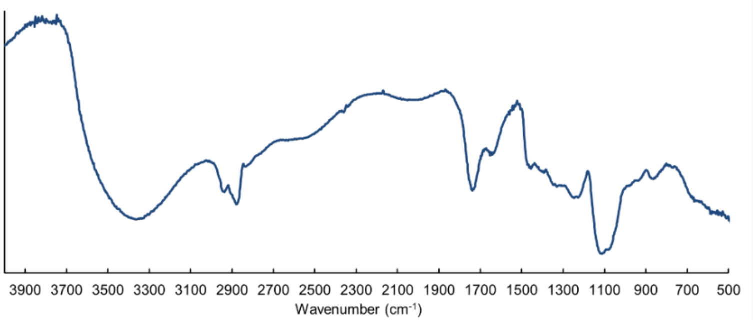

c) entry 4 (2.04 mmol/g)

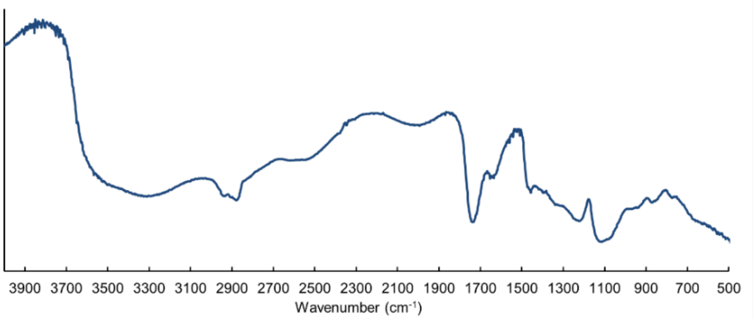

d) entry 5 (2.60 mmol/g)

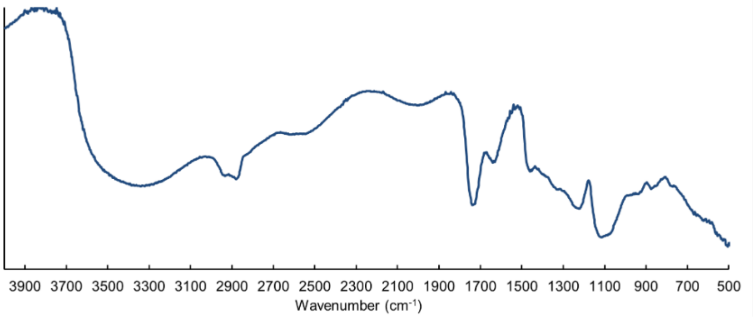

e) entry 6 (1.84 mmol/g)

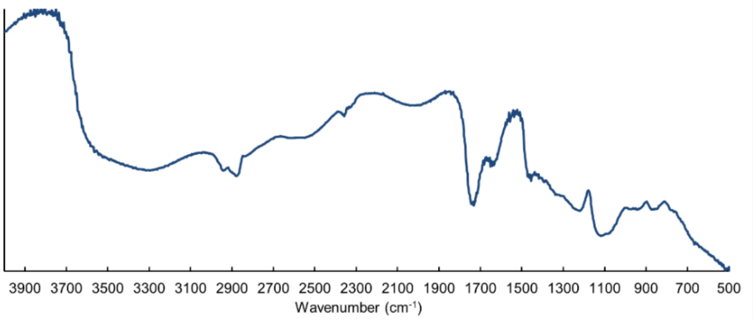

f) entry 7 (1.51 mmol/g)

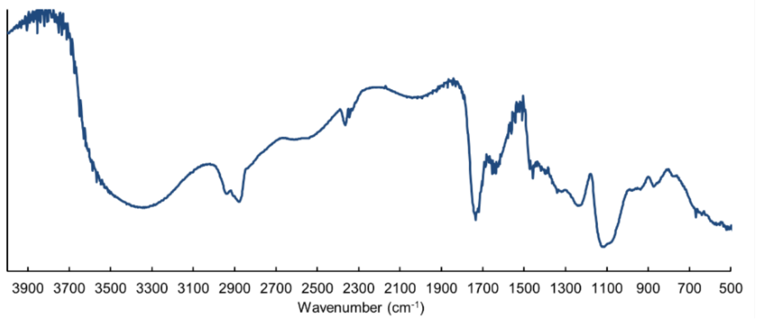

g) entry 8 (1.17 mmol/g)

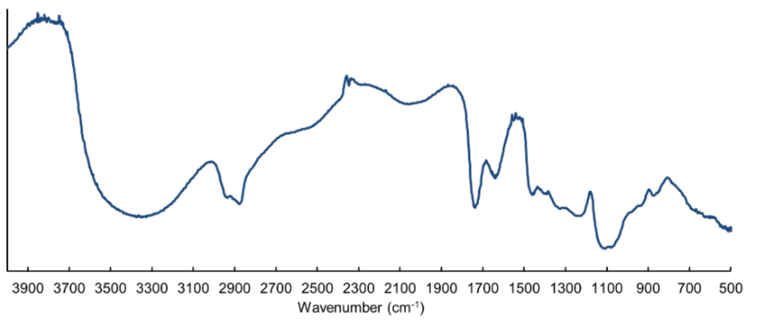

h) entry 9 (1.01 mmol/g)

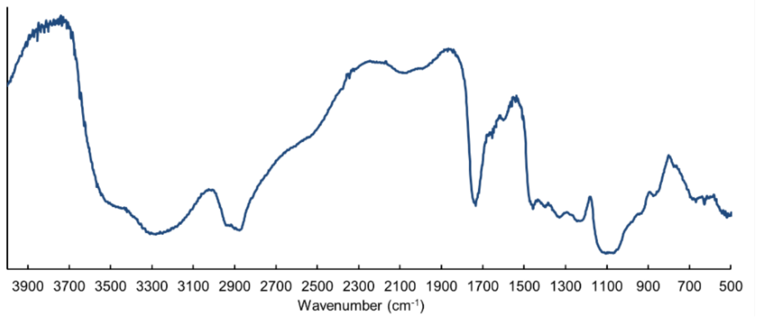

i) entry 10 (0.81 mmol/g)

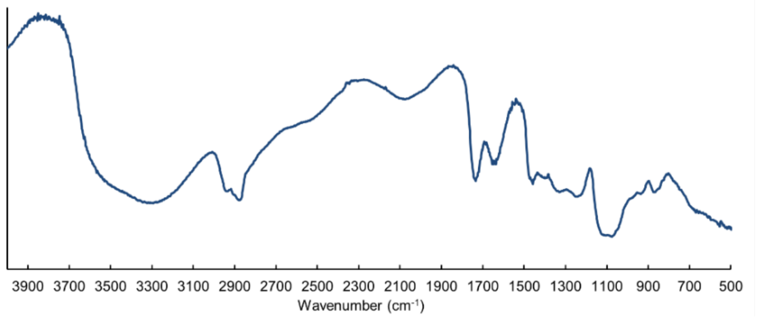

j) entry 11 (0.47 mmol/g)

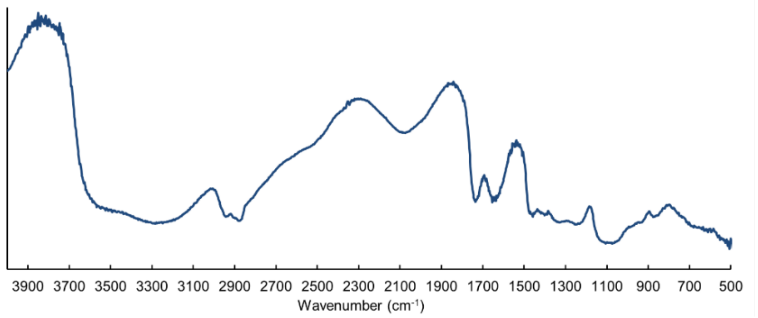

k) entry 12 (0.69 mmol/g)

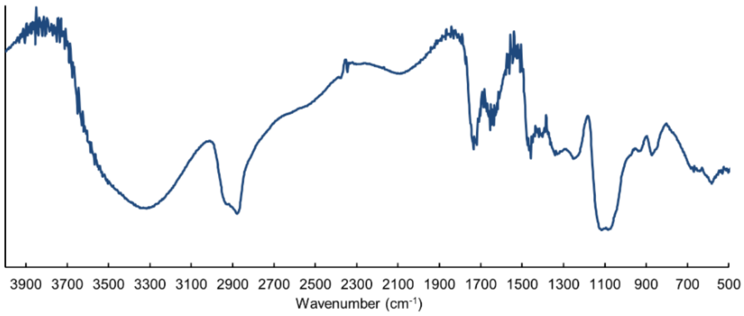

l) entry 13 (1.04 mmol/g)

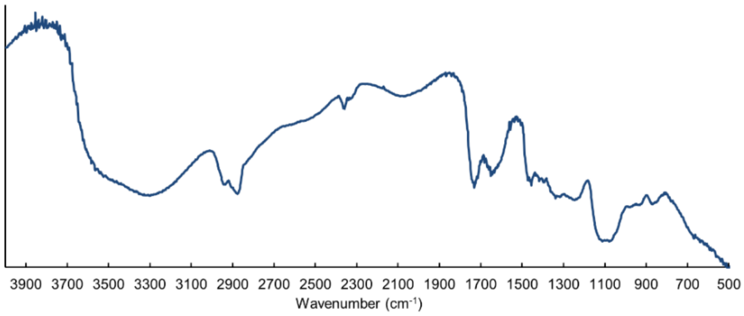

m) entry 14 (1.36 mmol/g)

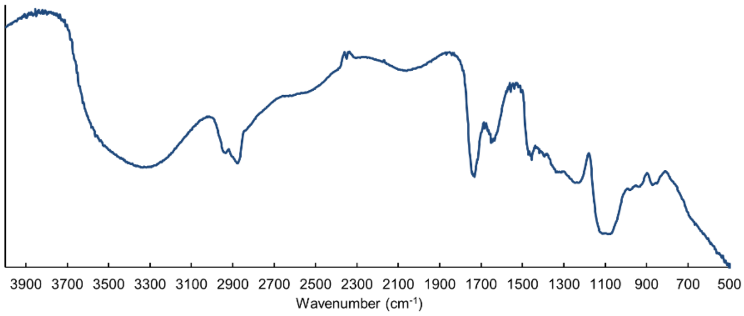

n) entry 15 (0.65 mmol/g)

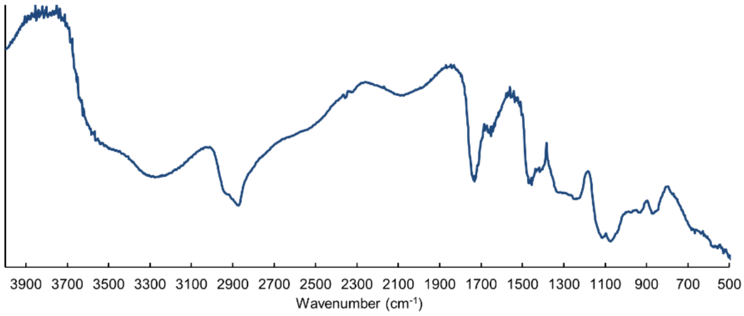

o) entry 16 (0.30 mmol/g)

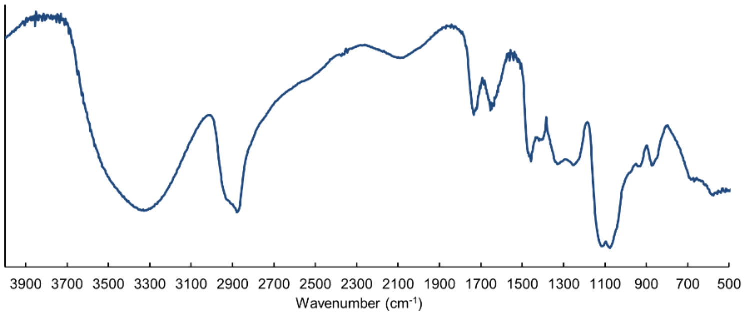

p) entry 17 (1.47 mmol/g)

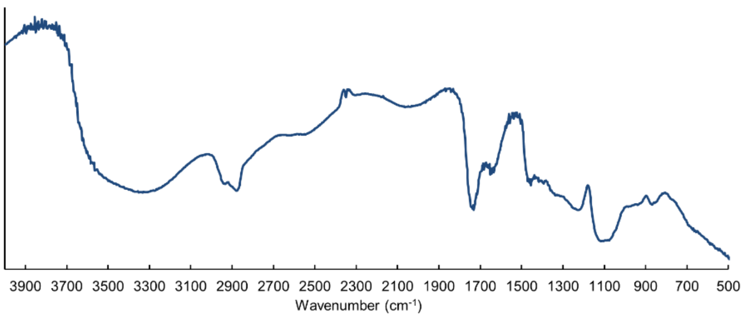

q) entry 18 (1.27 mmol/g)

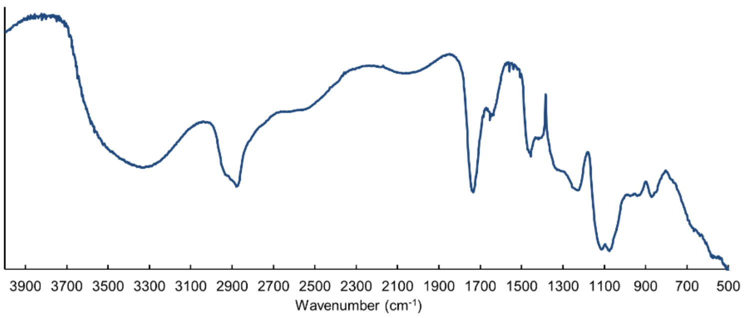

r) entry 19 (0.69 mmol/g)

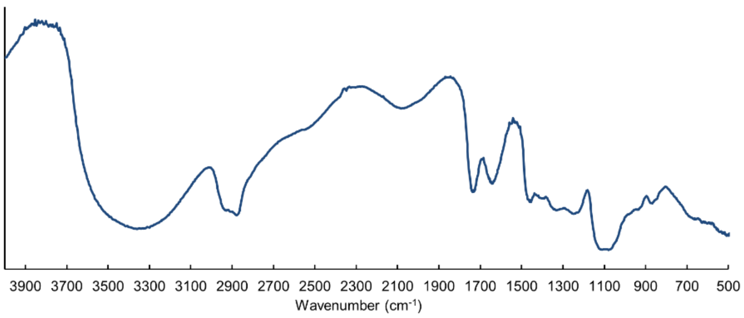

s) entry 20 (ND50-PG-COOH, 0.78 mmol/g)

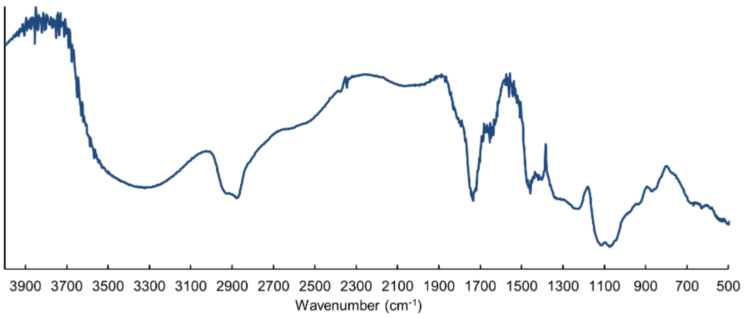

t) Raw material for entry 20 (ND50-PG from HPHT ND)

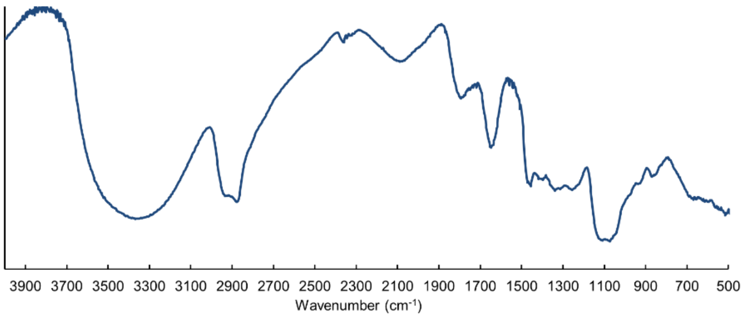

Figure 3-2. FT-IR spectra of DND-PG-COOH (entries 2–20 in Table 1). The COOH contents (mmol/g, ***A*** in Table 3-1) are indicated in parentheses. For FT-IR spectrum of entry 1, see Figure 3-1.

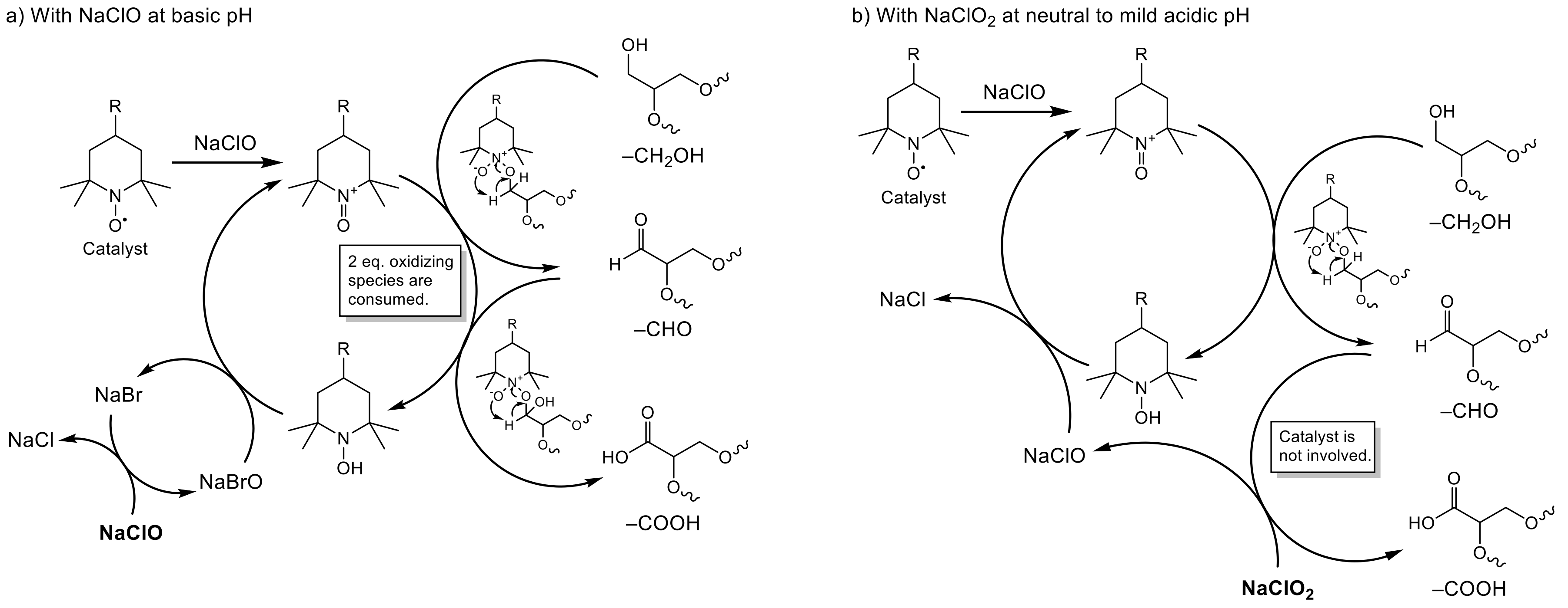

Figure 3-3. Reaction mechanism of nitroxyl-radical oxidation (a) with NaClO under basic conditions and (b) with NaClO$_2$ under neutral to acidic conditions.

When the amount of NaClO was reduced to 2.9 mmol/g (entry 2 in Table 3-1), almost no COOH was produced (Figure 3-2a), resulting in poor aqueous dispersibility. The possible reaction mechanism is illustrated in Figure 3-3a. The oxidation of –CH_2OH to –COOH consists of the following two steps, –CH_2OH → –CHO (aldehyde) → –COOH. Since *N*-oxoammonium ion is involved in both steps, the reaction of this oxidizing species with –CH_2OH should be much faster than –CHO. Hence, –CHO or its hydrate form remains in the reaction mixture, if a sufficient amount of the oxidizing species is not provided. This limitation in the former reaction system motivated us to apply the latter one using $NaClO_2$ with TEMPO and small amount of NaClO, realizing the precise control of COOH content. In the reaction, 4-AcNH-TEMPO was applied under acidic conditions (pH 4.7) [131]. The results are summarized in Table 3-1 (entries 3–11), and FT-IR spectra of the products are shown in Figure 3-2b – j to find that the products by two reaction systems are the same. Table 3-1 and Figure 3-2 indicate that the COOH content increases as the amount of $NaClO_2$ increases. In particular, the conversion is nearly stoichiometric, when the amount of $NaClO_2$ is small (≤ 1 mmol/g); 1.01, 0.81 and 0.47 mmol/g of –COOH is produced by the addition of 1.26, 1.02 and 0.63 mmol/g of $NaClO_2$, respectively (entries 9–11 in Table 3-1). However, the oxidation efficiency decreased gradually, as the amount of $NaClO_2$ increased. The relationship can be fitted with a natural log approximation (dotted line and equation in Figure 3-4) in the reactions with 4-AcNH-TEMPO catalyst at pH 4.7 (blue squares). In this system, $NaClO_2$ oxidizes *in situ* –CHO intermediate to –COOH as shown in Figure 3-3b. The resulting NaClO (HClO as the reactive species) oxidizes the catalyst to generate *N*-oxoammonium ion and convert –CH_2OH to –CHO. NaClO added at the beginning serves as an initiator to oxidize the TEMPO catalyst. The reactions with TEMPO or 4-AcNH-TEMPO at neutral pH (entries 12 and 13, and 14–16, Table 3-1, respectively) and with 2-hydroxy-2-azaadamantane (AZADOL) at pH 4.7 (entries 17–19, Table 3-1) exhibited lower reaction efficiency (yellow solid circle, red rhombi and green triangles in Figure 3-4 and FT-IR spectra in Figure 3-2k – r, respectively). It may be caused by the differences in the activity of oxidant, or oxidizing species, and the selectivity of catalyst, which will be discussed later.

Colloidal stability of the oxidized products with negative ζ-potential (Table 3-2) is confirmed by dynamic light scattering (DLS) measurements on number, volume and scattering light intensity bases (Figure 3-5 for entries 4 and 10, Table 3-1), indicating that no coarse particles by aggregation have appeared by the reaction. The product contains a trace amount of –CHO (≤ 1/1000 to the amount of glycerol unit) which is detected by ^{1}H NMR (Figure 3-6), and no free radical derived from nitroxyl radical catalyst is observed by EPR (Figure 3-7) while radical species from carbon dangling bonds and nitrogen defects in DND core are detected. In addition, the reaction with 4-AcNH-TEMPO at pH 4.7 was applied to ND50-PG (high pressure high temperature (HPHT) ND of 50 nm-size) to give similar result (0.78 mmol/g of COOH content with 0.99 mmol/g of $NaClO_2$) to DND-PG (entry 20 in Table 3-1 and FT-IR spectrum in Figure 3-2s).

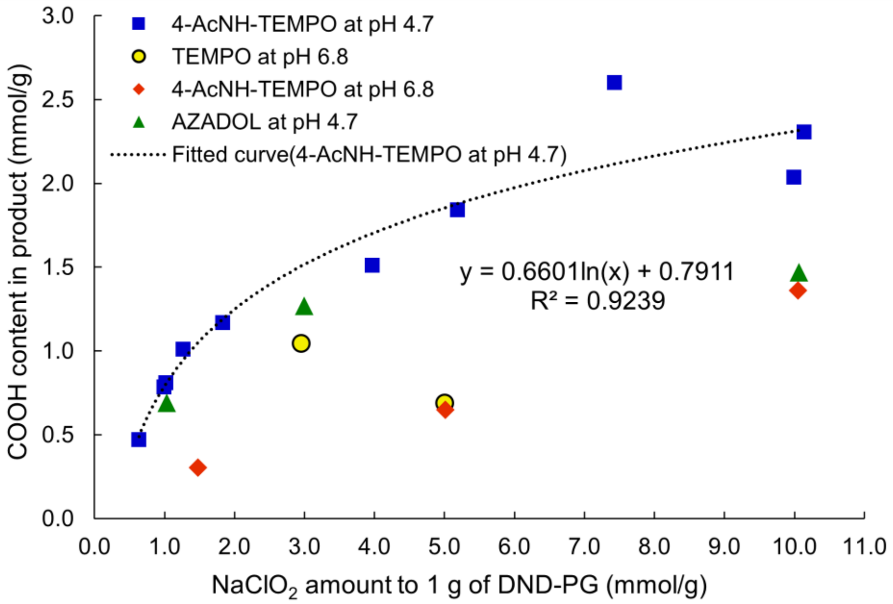

Figure 3-4. Relationship between the amount of $NaClO_2$ and COOH content of DND-PG-COOH through the oxidation of DND-PG except for one result (entry 20 in Table 3-1) from ND50-PG to ND50-PG-COOH by 4-AcNH-TEMPO at pH 4.7 (blue square).

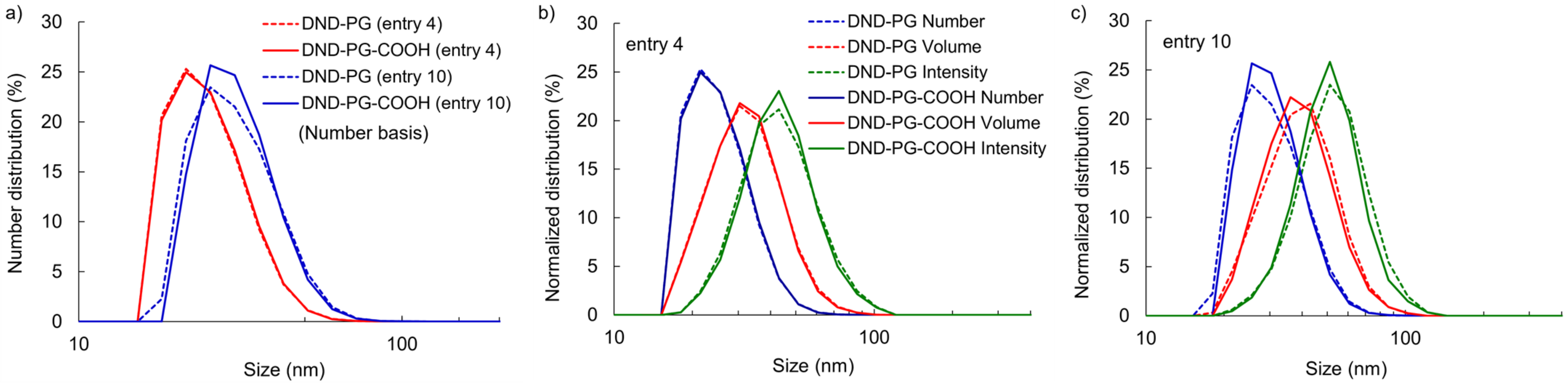

Figure 3-5. Hydrodynamic diameter of (a) DND-PG (dashed lines) and DND-PG-COOH (solid lines) with red and blue lines corresponding to entries 4 and 10 in Table 3-1 on number basis, (b, c) DLS of DND-PG (dashed lines) and DND-PG-COOH (solid lines) in entries 4 (b) and 10 (c) in Table 3-1 on number (blue), volume (red) and scattering light intensity (green).

Table 3-2. ζ-potential and DLS size of DND-PG-COOH.

	Entry 4, Table 3-1		Entry 10, Table 3-1	
	DND-PG	DND-PG-COOH	DND-PG	DND-PG-COOH
COOH content (mmol/g)	---	2.04	---	0.81
ζ-potential in PBS (mV)	–2.83	–27.83	–2.75	–19.30
D_{50} on number basis (nm)	22.11	22.23	26.78	27.24
Thickness of PG layer from the DLS result (nm) [a]	8.49	8.55	10.83	11.06
PG/DND ratio by TGA	2.43	1.55	3.58	3.46
Relative volume of PG layer compared with DND-PG (%)	---	63.8	---	96.6
Theoretical relative thickness of PG layer (%) [b]	---	76.0	---	98.1

[a] Assuming that the diameter of DND core is 5.12 nm determined by BET specific surface area measurement.

[b] Calculated value assuming the density of PG layer does not change after the oxidation.

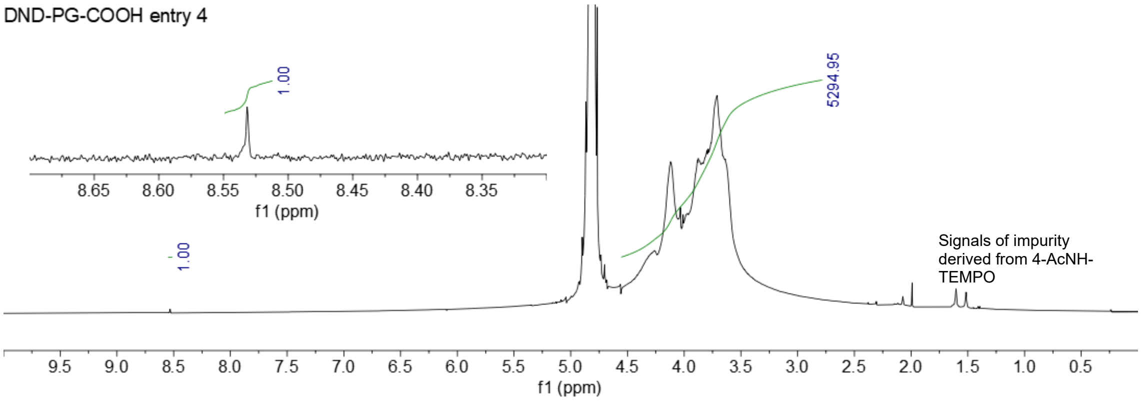

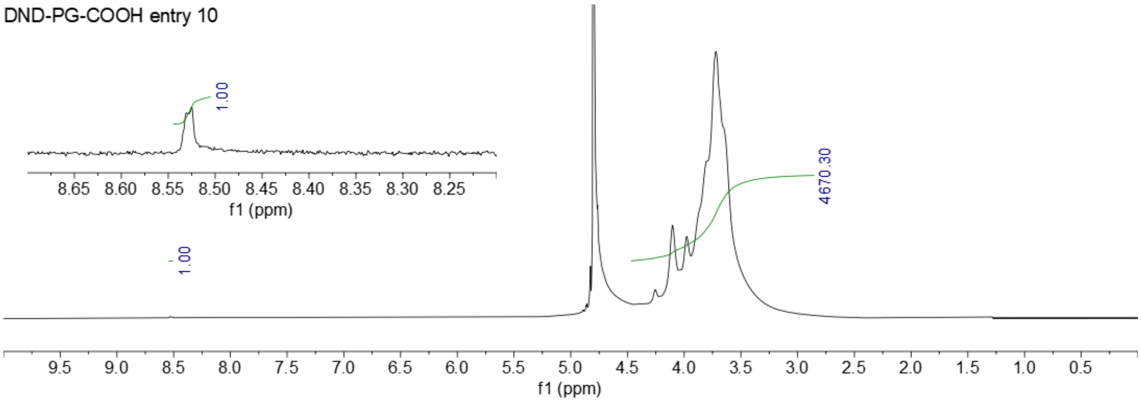

Figure 3-6. ^{1}H NMR of DND-PG-COOH of entries 4 and 10 in Table 3-1 (in 0.1% NaOD). Peak at 8.53 ppm is deemed to be the signal of –CHO. From the integration value of 1/5000 compared to that of PG chain (5H in glycerol unit and 3H in glyceric acid unit), content of –CHO is estimated to be about ≤ 1/1000 of the amount of glycerol and glyceric acid units.

a) 4-AcNH-TEMPO in water (100 µg/mL)

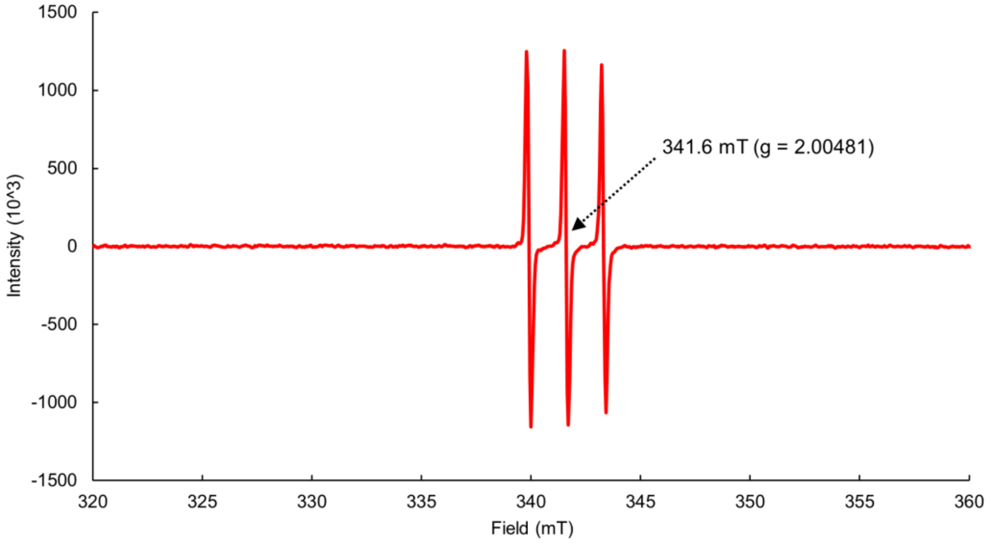

b) DND-PG (raw material of DND-PG-COOH entry 10, Table 3-1, 3.95 wt%)

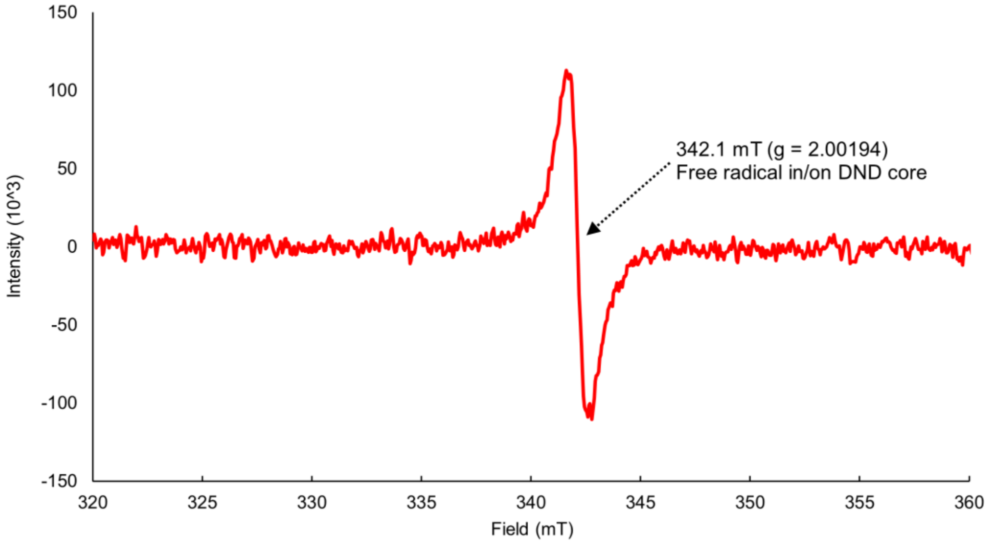

c) DND-PG-COOH (entry 10, Table 3-1, 3.81 wt%)

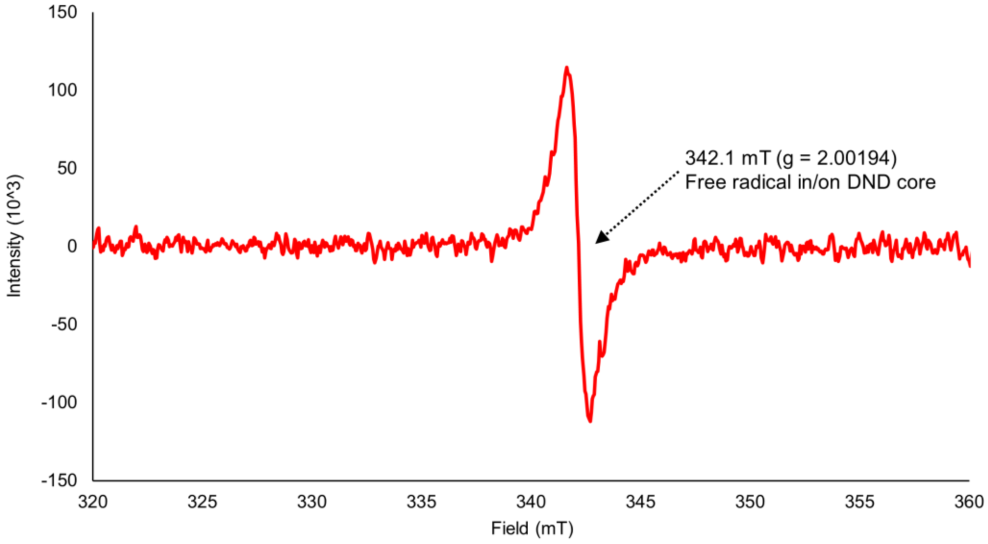

Figure 3-7. EPR spectra of 4-AcNH-TEMPO (in water 100 μg/mL), DND-PG (raw material of entry 10, Table 3-1, 3.95 wt%) and DND-PG-COOH (entry 10, Table 3-1, 3.81 wt%). In DND-PG and DND-PG-COOH, only signal of free radical from DND core is detected in the same intensity level and peak shape (width).

In ^{13}C NMR spectra by inverse gated decoupling measurement, the –COOH and –CH_2OH signals in DND-PG and DND-PG-COOH are found around 176 ppm (Figure 3-8b and d) and around 65 ppm (Figure 3-8a – d), respectively. Based on the integral of the secondary carbons with ether linkage (–CH(OR)–) around 80 ppm, those of –COOH are appeared to be 1.05 and 0.25 in Figure 3-8b and d, respectively, after the oxidation of DND-PG (entries 4 and 10 in Table 3-1, respectively). Simultaneously, the integrals of –CH_2OH decreases from 1.50 and 1.44 (Figure 3-8a and c, respectively) to 0.43 and 0.97 (Figure 3-8b and d, respectively) after the oxidation (entries 4 and 10 in Table 3-1, respectively), indicating that the primary alcohols are oxidized to carboxylic acids.

According to our previous report regarding structural analysis of ND-PGs [129], –CH_2OH contents in DND-PG (DND(+)-PG(m) and -PG(h) with PG/DND weight ratios of 2.43 and 3.58) in entries 4 and 10 (Table 3-1) are determined to be around 5.0 mmol/g. On the other hand, the COOH contents in the corresponding DND-PG-COOH in entries 4 and 10 (Table 3-1) are 2.04 and 0.81 mmol/g, respectively. Particularly in entry 4, after most of the –CH_2OH in the DND-PG (DND(+)-PG(m)) is oxidized as shown in Figure 3-8b, only 2.04 mmol/g of –COOH was produced. This discrepancy implies that some of the PG chains may be lost during the oxidation. Therefore, DND-PG-COOH shown in Figure 3-8b and 3-8d (entries 4 and 10 in Table 3-1, respectively) were compared with the corresponding DND-PG in thermogravimetric analysis (TGA, in air).

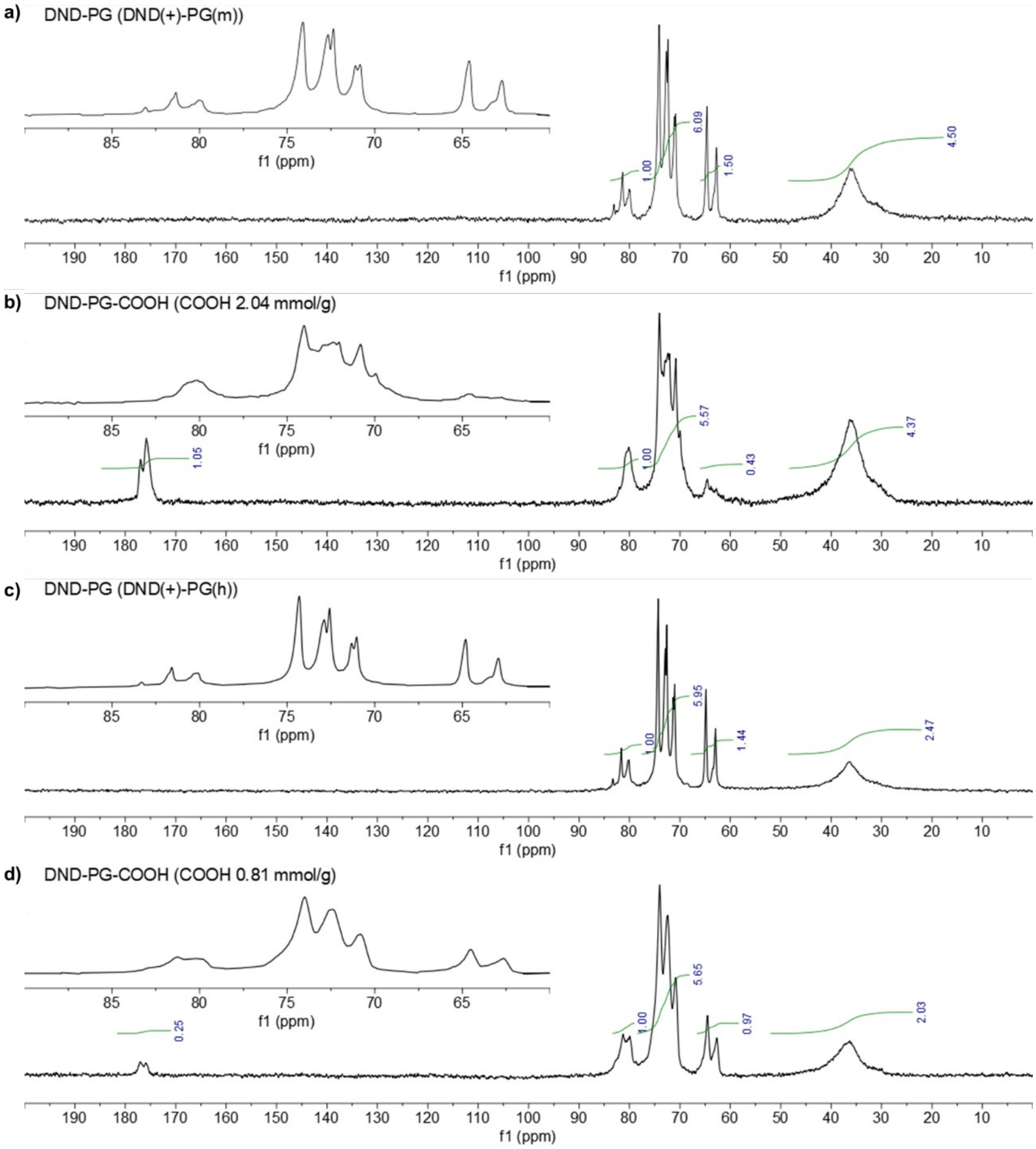

Figure 3-8. ^{13}C NMR spectra by inverse gated decoupling measurement of (a) DND-PG (raw material in entry 4, Table 3-1), (b) DND-PG-COOH (COOH content 2.04 mmol/g, entry 4, Table 3-1), and (c) DND-PG (raw material in entry 10, Table 3-1) and (d) DND-PG-COOH (COOH content 0.81 mmol/g, entry 10, Table 3-1). The signal of diamond core at 36.3 ppm is set as a reference.

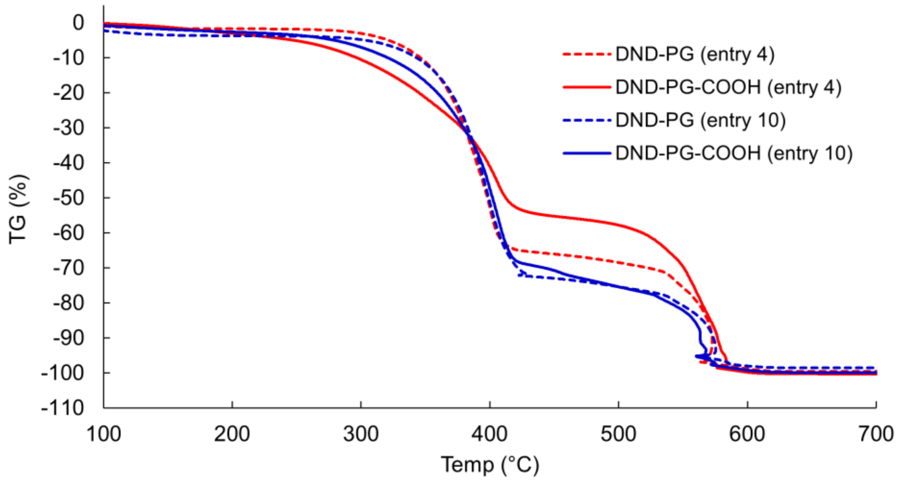

Figure 3-9. TGA profiles of DND-PG (dashed lines) and DND-PG-COOH (solid lines) with red and blue lines corresponding to entries 4 and 10 in Table 3-1.

As shown in Figure 3-9, the two-step weight decrease below and above 450 °C may result from the degradation of PG chain followed by the combustion of DND core. While oxidation of the DND-PG in entry 10 does not change the TGA profile (blue lines in Figure 3-9), the PG content significantly decreases through the oxidation of DND-PG in entry 4 (red lines). This indicates that PG chains should have detached from the PG layer on DND surface at larger degree as the oxidation proceeds from 0.81 mmol/g (entry 10) to 2.04 mmol/g (entry 4). On the other hand, almost no change in hydrodynamic diameters is observed by DLS (Figure 3-5) before and after oxidation, despite the significant weight loss in entry 4 (Figure 3-9 and Table 3-2). This indicates that the PG layer decreases in its density, but the thickness does not change by the oxidation of DND-PG especially in entry 4.

To quantify the PG chains cleaved by the oxidation, molar amounts of glycerol and glyceric acid units on 1 g of DND core in DND-PG and DND-PG-COOH were calculated from the

PG/DND weight ratio by TGA and the COOH content by acid-base titration. These results and calculation details are shown in Table 3-3. In Figure 3-10, the loss of PG chains in Table 3-3 correlates quadratically with the COOH content in DND-PG-COOH (*A* in Table 3-1). Therefore, little or no PG loss is observed at the COOH content smaller than 1.2 mmol/g. However, more than 20% of PG chain is lost in the DND-PG-COOH with the COOH content at 1.5 mmol/g and more. The loss of PG chain may be attributed to the oxidation of the secondary –OH in PG chain as shown in Figure 3-11. When the secondary –OH is oxidized into ketone, ether linkage to the carbon atoms next to the carbonyl group is subjected to C–O bond cleavage via tautomerization to the enol form. Although TEMPO is known to catalyze the oxidation of primary alcohol due to the steric hindrance in the surrounding of the nitroxyl radical (Figure 3-3), oxidation at secondary alcohol in the PG layer occurs in some extent. The quadratic relationship shown in Figure 3-10 may be due to the increase of the proportion of secondary –OH against primary –OH, which is preferentially oxidized to –COOH, to increase the relative oxidation rate of the secondary –OH. This results in more cleavage of the PG chains. In addition, AZADOL (entries 17–19 in Table 3-1) with higher catalytic activity and less selectivity to primary alcohol caused larger loss of PG chain than 4-AcNH-TEMPO at pH 4.7 (green triangles in Figure 3-10) [128], supporting the above interpretation that the cleavage of PG chain occurs by the oxidation of secondary alcohols shown in Figure 3-11. The reactions using TEMPO or 4-AcNH-TEMPO under neutral conditions gave a different trend; the loss of PG chain is comparable with the reaction of 4-AcNH-TEMPO at pH 4.7 (yellow solid circles and red rhombi in Figure 3-10), while the COOH contents to the $NaClO_2$ amounts are lower and much less relationship (yellow solid circles and red rhombi in Figure 3-4). This may be because the reactivity of NaClO (HClO) or *N*-oxoammonium ion that react with the primary or secondary –OH may be lower at the neutral pH, while the selectivity is almost the same. Since the performance of the reaction is affected by pH and the amount of $NaClO_2$, the reaction at stable pH is critical especially for the precise control of COOH content.

Table 3-3. Compositions of glycerol and glyceric acid units in DND-PG-COOH in Table 3-1, and the losses of PG chain during oxidation reaction.

Entry [a]	Amount on 1 g of DND core in DND-PG		Amount on 1 g of DND core in DND-PG-COOH						Loss of PG chain
	PG chain determined by TGA	Mole amount of glycerol unit	PG chain determined by TGA	Glyceric acid unit		Glycerol unit		Total mole amount	
	(g)	(mmol)	(g)	(mmol)	(g)	(g)	(mmol)	(mmol)	(%)
	B	***C*** = ***B*** / 74.08 × 1000 [b]	***D***	***E*** = ***A***[c] × (1 + ***D***)	***F*** = ***E*** × 88.06 / 1000 [d]	***G*** = ***D*** – ***F***	***H*** = ***G*** / 74.08 × 1000 [b]	***I*** = ***E*** + ***H***	(1 – ***I*** / ***C***) × 100
1	2.16	29.1	1.40	3.22	0.28	1.12	15.11	18.33	37.1
2	0.99	13.4	--- [e]						
3	2.67	36.0	1.74	6.32	0.56	1.18	15.98	22.30	38.0
4	2.43	32.8	1.55	5.18	0.46	1.09	14.71	19.89	39.4
5	3.85	52.0	2.02	7.85	0.69	1.33	17.94	25.80	50.4
6	2.67	36.0	1.90	5.35	0.47	1.43	19.33	24.69	31.4
7	0.99	13.4	0.82	2.75	0.24	0.58	7.80	10.55	21.2
8	2.43	32.8	2.38	3.95	0.35	2.03	27.45	31.40	4.3
9	3.83	51.7	3.85	4.90	0.43	3.42	46.15	51.05	1.2
10	3.58	48.4	3.46	3.61	0.32	3.14	42.35	45.96	5.0
11	3.83	51.7	3.94	2.32	0.20	3.73	50.37	52.69	–2.0
12	3.85	52.0	3.69	3.23	0.28	3.40	45.91	49.14	5.4
13	0.99	13.4	1.02	2.11	0.19	0.83	11.27	13.38	0.1
14	2.43	32.8	2.19	4.34	0.38	1.81	24.37	28.71	12.5
15	3.85	52.0	3.74	3.08	0.27	3.47	46.83	49.91	4.0
16	3.85	52.0	3.76	1.45	0.13	3.63	49.05	50.49	2.8
17	2.43	32.8	1.70	3.97	0.35	1.35	18.27	22.25	32.2
18	3.85	52.0	3.08	5.18	0.46	2.63	35.45	40.63	21.8
19	3.85	52.0	3.46	3.08	0.27	3.19	43.10	46.18	11.2
20	0.85	11.5	0.87	1.47	0.13	0.74	10.05	11.52	–0.4

[a] Experimental conditions are described in the same entry in Table 3-1.

[b] 74.08: molecular weight of GD.

[c] ***A*** : COOH content in 1 g of DND-PG-COOH (mmol/g). See the same entry in Table 3-1.

[d] 88.06: molecular weight of 2,3-epoxypropionic acid.

[e] TGA was not measured. Accordingly, the following calculations were not done.

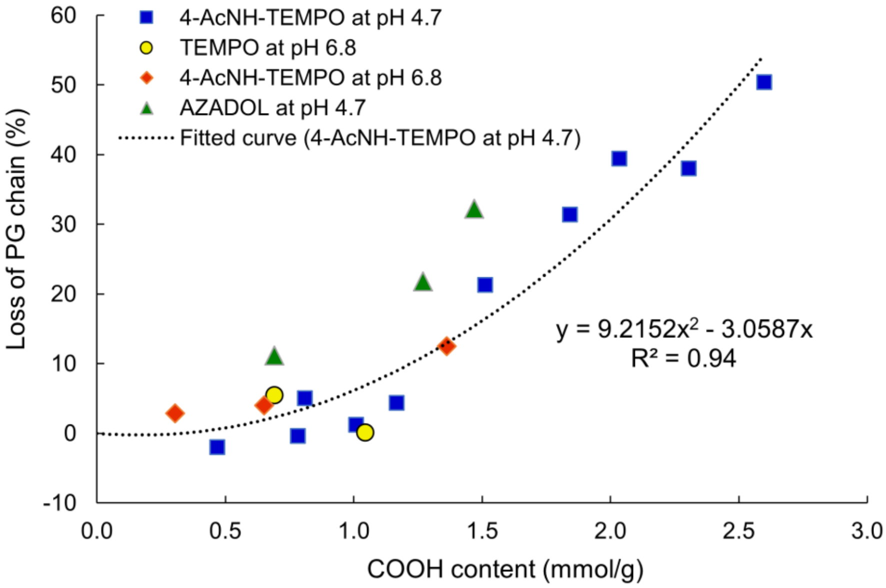

Figure 3-10. Relationship between the PG chains lost by the oxidation and the COOH content in the resulting DND-PG-COOH except for one result (entry 20 in Table 3-1) from ND50-PG to ND50-PG-COOH by 4-AcNH-TEMPO at pH 4.7 (blue square).

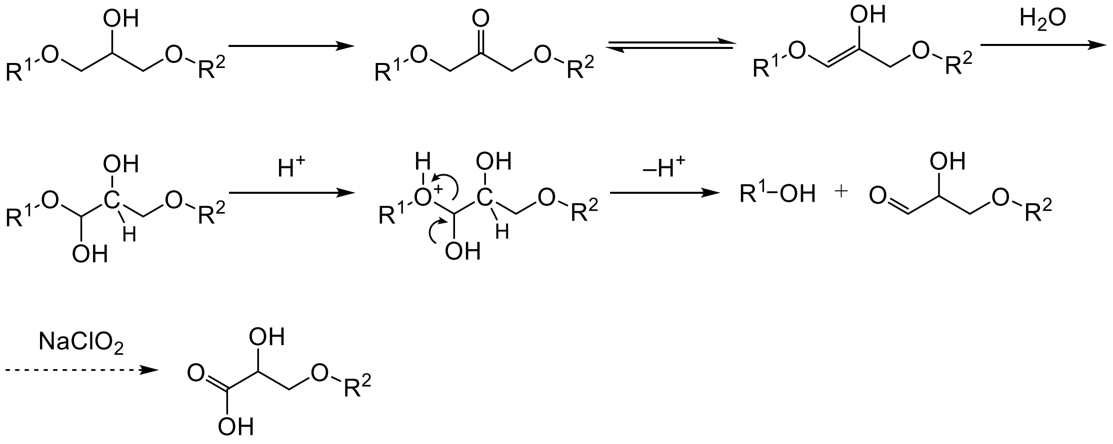

Figure 3-11. Plausible mechanism for cleavage of ether linkage caused by the oxidation at secondary hydroxy group.

3-3. Conclusion

We developed the process for poly(glycerol-*co*-glyceric acid) functionalized DND (DND-PG-COOH), a novel –COOH containing PG functionalized DNDs, via oxidation of primary –OH in PG chain by nitroxyl radical catalysts known as TEMPO. The product should be chemically robust, since the –COOH functionality is incorporated in PG chain. The reaction is so simple that it can be performed under aqueous conditions with inexpensive fundamental inorganic oxidant like $NaClO_2$ and NaClO. The amount of –COOH can be precisely controlled by the amount of $NaClO_2$ in an almost stoichiometric manner for a range of COOH content ≤ 1 mmol/g. On the other hand, the reaction for higher COOH content with large amount of oxidant has a limitation to cleave the PG chains probably due to the oxidation of secondary –OH. Despite the limitation, the product with controlled COOH content can be applied to further functionalization for various applications especially in biomedical field.

3-4. Experimental

Materials

Single-digit nanometer-sized water dispersion of DNDs was manufactured by Daicel Corporation (DINNOVARE^{TM}). For the modification of DNDs, the following reagents and solvents were purchased from FUJIFILM Wako Pure Chemical Corporation (Osaka Japan); 2,3-epoxypropan-1-ol (glycidol or GD), sodium hypochlorite (NaClO) solution, hydrochloric acid (HCl), sodium hydroxide (NaOH), ethanolic solution of potassium hydroxide (KOH), acetic acid, sodium acetate, potassium dihydrogen phosphate, ethylene glycol, methanol and ethanol. 2,2,6,6-Tetramethylpiperidine-1-oxyl free radical (TEMPO), 4-acetamido-2,2,6,6-tetramethylpiperidine-1-oxyl free radical (4-AcNH-TEMPO), AZADOL and sodium bromide (NaBr) were purchased from Tokyo Chemical Industry Co., Ltd. (Tokyo Japan). Sodium chlorite ($NaClO_2$) was purchased from Sigma-Aldrich Japan G. K. (Tokyo, Japan).

Equipment

NMR spectra were measured with an ECX500 NMR spectrometer (JEOL). FT-IR spectra were recorded on an IR Tracer-100 FT-IR spectrometer (Shimadzu) equipped with DiffusIR DRIFT chamber (PIKE Technologies). Elemental analyses were conducted at Organic Elemental Microanalysis Center of Kyoto University. Thermogravimetric analysis (TGA) was performed with TG/DTA 6200 (SII). DLS measurement was done with a Nanotrac Wave II particle size analyzer (MicrotracMRB). Zeta-potential was measured by ZetaSizer Nano (Malvern, UK). EPR spectra were measured with EMX spectrometer (Bruker).

DND-PG (raw material, entry 1 in Table 3-1)

An aqueous dispersion of DND with positive ζ-potential, DND(+), was evaporated to dryness. The solid residue was dried at 105 °C for 2 h. To a suspension of resulting DND powder (1.0 g) in ethylene glycol (15.0 g), GD (45.1 g, 0.61 mol) was added dropwise over 160 min to keep the temperature in the range of 95–100 °C. The resulting black dispersion was stirred at the same temperature for 4 h. After the reaction was cooled below 40 °C, water (40 mL) was added slowly to degrade the unreacted GD. The dispersion was diluted with water to ca. 400 mL and concentrated with ultrafiltration membrane (Ultracel® membrane, 30 kDa) to < 20 mL. The concentrate was diluted and concentrated again, which was repeated five times, and the weight of resulting black water dispersion was adjusted to 100.0 g with water. An aliquot of the dispersion was accurately weighed and dried on heated PTFE sheet. From the weight of the residue, the concentration was determined to be 4.10 % (w/w).

To remove free PG, 30.0 g of above water dispersion (net 1.23 g) was ultracentrifuged at 183400*g* (50000 rpm) for 2 h. Supernatant (ca. 20 mL) was removed carefully and remained lower layer was diluted and re-dispersed with water (20 mL), and ultracentrifuged again, which was repeated two times. The resulting lower layer was adjusted to 30.8 g with water, which was used in the following oxidation step. To obtain a sample for analysis (titration), 15.8 g of this aqueous dispersion was once adjusted to pH 1.93 with HCl, then washed with water with the ultrafiltration membrane five times in the same manner as described above to recover 15.8 g of dispersion. An aliquot of the dispersion was accurately weighed (1.5391 g) and dried on heated PTFE sheet. From the weight of the residue (0.0441 g), the sample concentration was determined to be 2.87 % (w/w). The net yield of DND-PG was 0.88 g from 1.23 g (net) of crude product.

FT-IR (DRIFT with KBr, cm^{-1}): 3332, 2918, 2875, 1456, 1118, 1075 (C–O). ^{1}H NMR (500 MHz, D_2O): δ ppm 3.42, 3.50, 3.58, 3.75, 3.88. Elemental analysis: C; 60.75%, H: 5.87%, N; 0.81%, O; 31.79%. TGA (Air atmosphere, 20 °C/min, % weight loss): 50–530 °C; 68.2%, 530–650 °C; 31.6% (PG/DND ratio was estimated to be 2.16).

DND-PG-COOH (oxy-radical oxidation with NaClO under basic condition, entry 1 in Table 3-1)

Water dispersion of purified DND-PG as described above (15.0 g, 2.87 % (w/w), net 0.43 g, PG/DND 2.16) was diluted with water (10.0 mL) and added with NaBr (0.61 g, 5.9 mmol). The mixture was cooled in ice-bath and added with TEMPO (24.5 mg, 0.16 mmol). NaClO solution (effective chlorine concentration: 12.9 wt%) was added slowly with keeping the temperature at around 2 °C (below 5 °C). As pH decreased with the reaction progress, NaClO solution and/or 1 M NaOH was added to keep pH around 10 (10–12). The reaction was stopped when 2.5 g of NaClO solution (net 0.294 g, 4.0 mmol) was added in total for 35 min. After the addition of small amount of methanol to degrade unreacted NaClO, pH was adjusted to 1.97 with 6 M HCl. The dispersion was diluted with water to ca. 400 mL and concentrated with ultrafiltration membrane (Ultracel® membrane, 30 kDa) to < 10 mL. The concentrate was diluted and concentrated again, which was repeated four times, and the weight of resulting black water dispersion was adjusted to 15.0 g with water. An aliquot of the dispersion was accurately weighed and dried on heated

PTFE sheet. From the weight of the residue, the concentration was determined to be 2.81 % (w/w). The net yield of DND-PG-COOH was 0.42 g. FT-IR (DRIFT with KBr, cm^{-1}): 3273, 2906, 2878, 1734, 1456, 1122, 1080. ^1H NMR (500 MHz, 0.5% NaOD): δ ppm 4.13, 3.97, 3.90, 3.53. Elemental analysis: C; 59.12%, H: 5.29%, N; 0.78%, O; 34.36%. TGA (Air atmosphere, 20 °C/min, % weight loss): 50–487 °C; 57.8%, 487–650 °C; 41.2% (PG/DND ratio was estimated to be 1.40).

The carboxylic acid (COOH) content was determined to be 1.34 mmol by acid-base titration. Aqueous dispersion of DND-PG-COOH (1.6989 and 1.5458 g for two-time operation, net weight 47.7 and 43.4 mg, respectively) was accurately weighed and diluted with 30 mL of ultrapure water. After a few drops of phenolphthalein solution was added as the indicator, titration was done with 0.05 mol/L KOH ethanolic solution ($f = 1.0$). The endpoint was determined when the pink color of indicator was kept up for 30 sec (1.30 and 1.21 mL, respectively). Blank test without sample was also done by the same procedure (0.03 mL). The COOH content was calculated as the following equation.

$$C_{\mathrm{COOH}} = \left((T^1 - T^2) \times 0.05 \times f\right)/(W \times S)$$

where C_{COOH}: COOH content (mmol/g), T^1: titer of 0.05 mol/L KOH to the sample (mL), T^2: titer of blank test (mL), f: factor value of KOH solution, W: weight of sample dispersion (g), and S: sample concentration (wt/wt). By the same procedure, COOH content of raw material (DND-PG) was determined to be 0.04 mmol/g.

DND-PG-COOH (oxy-radical oxidation with 4-AcNH-TEMPO and $NaClO_2$ under acidic condition, entry 4 in Table 3-1)

Aqueous dispersion of purified DND-PG (DND(+)-PG(m), 3.23 % (w/w), 18.6 g, net 0.60 g, PG/DND 2.43) were added with 0.4 M acetate buffer (pH 4.7, 30 mL), water (10.0 mL),

$NaClO_2$ (content 81%, 671 mg, 6.0 mmol) and 4-AcNH-TEMPO (24.9 mg, 0.12 mmol). NaClO solution (74 μL, 0.14 mmol) was added into the mixture and the flask was equipped with an air-cooled condenser capped with a universal glass plug, then the reaction was heated at 50 °C for 24 h. After ethanol (1.0 mL) was added to decompose unreacted oxidant, the dispersion was diluted with water to ca. 400 mL and concentrated with ultrafiltration membrane (Ultracel® membrane, 30 kDa) to < 10 mL. The concentrate was washed with water once by dilution and concentration with ultrafiltration membrane, and pH was adjusted to ca. 2.0 with 6 M HCl. The mixture was concentrated and then washed with water three times, and the weight of resulting black water dispersion was adjusted to 20.0 g with water. An aliquot of the dispersion was accurately weighed and dried on heated PTFE sheet. From the weight of the residue, the concentration was determined to be 2.49 % (w/w). The net yield of DND-PG-COOH was 0.50 g. COOH concentration was determined by acid-base titration to be 2.04 mmol/g. Elemental analysis: C; 60.69%, H: 5.45%, N; 0.79%, O; 32.91%. TGA (Air atmosphere, 20 °C/min, % weight loss): 50–533 °C; 68.7%, 533–650 °C; 31.4% (PG/DND ratio was estimated to be 2.19).

DND-PG-COOH (entry 10 in Table 3-1)

The oxy-radical oxidation with $NaClO_2$ was done on DND-PG (DND(+)-PG(h), 3.95 % (w/w), 44.3 g, net 1.75 g, PG/DND 3.58) were conducted with 0.4 M acetate buffer (pH 4.7, 35 mL), $NaClO_2$ (199 mg, 1.7 mmol), 4-AcNH-TEMPO (54.0 mg, 0.25 mmol) and NaClO solution (161 μL, 0.26 mmol) as described above. The weight of resulting black water dispersion was adjusted to 45.3 g with water. The concentration was determined to be 3.81 % (w/w) and net yield was 1.72 g. COOH concentration was determined by acid-base titration to be 0.81 mmol/g. Elemental analysis: C; 57.72%, H: 6.24%, N; 0.63%, O; 35.44%. TGA (Air atmosphere, 20 °C/min, % weight loss): 50–527 °C; 77.4%, 527–650 °C; 22.4% (PG/DND ratio was estimated to be 3.46).

Chapter 4: Conjugation of phenylboronic acid moiety through multistep organic transformations on nanodiamond surface for an anticancer nanodrug of boron neutron capture therapy

4-1. Introduction

A novel BNCT nanodrug consisting of the following three components were designed and explored (Figure 4-1); nanoparticle core (DND), hydrophilic polymer (poly(glycerol), PG) [42], and boron moiety (phenyl-^{10}B-boronic acid), expecting scalability and reproducibility in the synthesis, and the stability of the nanodrug under physiological conditions. The multilayered construction was fabricated by covalent bonding through multistep chemical transformations [133]. The whole process is highly reliable and scalable because fundamental reactions are piled up and the product in each step is fully characterized qualitatively and even quantitatively. In addition, further derivatization is accomplished for fine tuning of the physical properties and the biocompatibility. Pharmacokinetic studies using mice showed long-term retention of the nanodrug in the tumor at least for 48 h with rapid clearance from blood in 14 h. BNCT efficacy was eventually observed *in vivo* in which the tumor growth of drug-injected mice was suppressed by neutron irradiation.

4-2. Results and discussion

4-2-1. Material design

We designed the nanodrug to expect the following functions in each component as shown in Figure 4-1. The core DND makes the nanodrug robust to fix the outer two layers firmly, avoiding structural and topological deterioration. DND is one of the most reliable nanoparticles to be grafted densely with PG due to appropriate density of oxygen-containing functional groups, typically hydroxy (–OH) group, initiating ring-opening polymerization of glycidol on the DND surface [42]. In addition, more functions can be expected for DND as radio- and photo-sensitizers for therapy and as a fluorescence probe for diagnosis, as mentioned above [15, 26–31, 35, 36].

PG in the medium layer is a highly branched polymer with many hydroxy groups, which serve as scaffolds for further functionalization. PG also provides enough hydrophilicity for the nanodrug to be dispersed well under physiological conditions. In addition, PG is also expected to retain the nanodrug in the blood stream for longer time, because PG is reported to circumvent the immune system by preventing the protein corona formation and the subsequent macrophage uptake [71, 72]. It has been clearly demonstrated that the "stealth" efficiency of PG is better than that of poly(ethylene glycol) (PEG) [72].

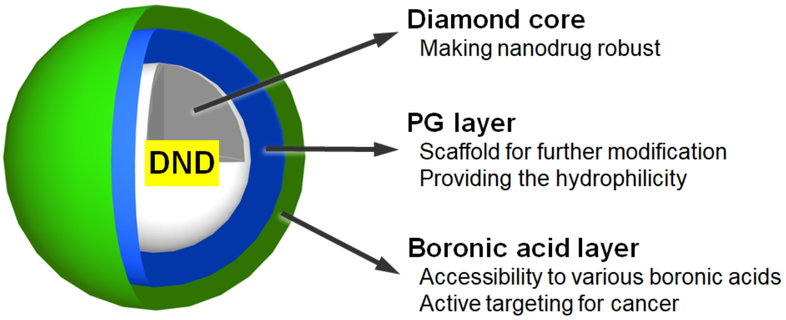

Figure 4-1. Schematic illustration for design of the three-layered structure of DND-based nanodrug.

As for the boron functionality in the outermost layer, we chose phenylboronic acid (PBA) moiety, whereas icosahedral boron clusters or carboranes were applied in many studies [134]. The PBA moiety was immobilized on the surface of amine-functionalized PG on DND (DND-PG-

NH_2) by C–N bond to leave the boronic acid moiety intact. This is not a typical approach to immobilize boronic acid by boronate. Our method includes the following advantages over the conventional ones; 1) various PBA moieties can be introduced onto the DND-PG because a variety of the precursors, PBA derivatives, can be synthesized through a simple and scalable process, and 2) the boronic acid moiety can work as an active targeting to the sialic acid overexpressed on cancer cell [90, 135].

4-2-2. Preparation of amino functionalized DND-PG

In order to add the boronic acid layer as shown in Figure 4-1, the DND-PG was first converted to amino functionalized DND-PG (DND-PG-NH_2·HCl as HCl salt of the amine) as shown in Scheme 4-1.

At the beginning, the DND core was functionalized with PG through ring opening polymerization of glycidol to give DND-PG. Although PG functionalization of nanoparticles has been performed in glycidol at 140 °C in our previous papers [42, 47, 48, 136, 137], we employed milder conditions in this thesis in view of larger scale synthesis; glycidol was added dropwise to a DND suspension in ethylene glycol around 100 °C (see details in Chapter 2 and 4-4 Experimental section).

The resulting DND-PG was characterized by FT-IR and solution phase ^{1}H NMR as shown in Figures 4-2b and 4-3a, respectively. In FT-IR spectrum, the absorptions corresponding to stretching vibrations of O–H at 3333 cm^{-1}, asymmetrical and symmetrical C–H at 2918 and 2876 cm^{-1}, and asymmetric C–O–C and C–O of PG at 1118 and 1078 cm^{-1} are observed. In ^{1}H NMR, signals at 3 – 4 ppm indicate that all the hydrogens are on the carbons next to the oxygens at hydroxy groups or ether linkages. In the size exclusion chromatography (SEC) as shown in Figure 4-4 , PG without DND core (free PG) was found to contaminate in the DND-PG at ca. 30% estimated from the RI peak area ratio (Figure 4-4b), though it was purified with ultrafiltration after PG functionalization. This sample was used in the next step without further purification because the free PG is expected to be removed in the subsequent steps. The PG content including free PG is 80.2 wt% on thermogravimetric analysis (TGA, in Figure 4-5b). The resulting material was dispersed well in various aqueous solutions. Although the free PG remained due to the difference in the purification procedure, we confirmed that the DND-PG is almost identical to that prepared in our previous works in FT-IR, ^{1}H NMR and TGA [42, 137], and is different from DND in FT-IR (Figure 4-2a and 4-2b).

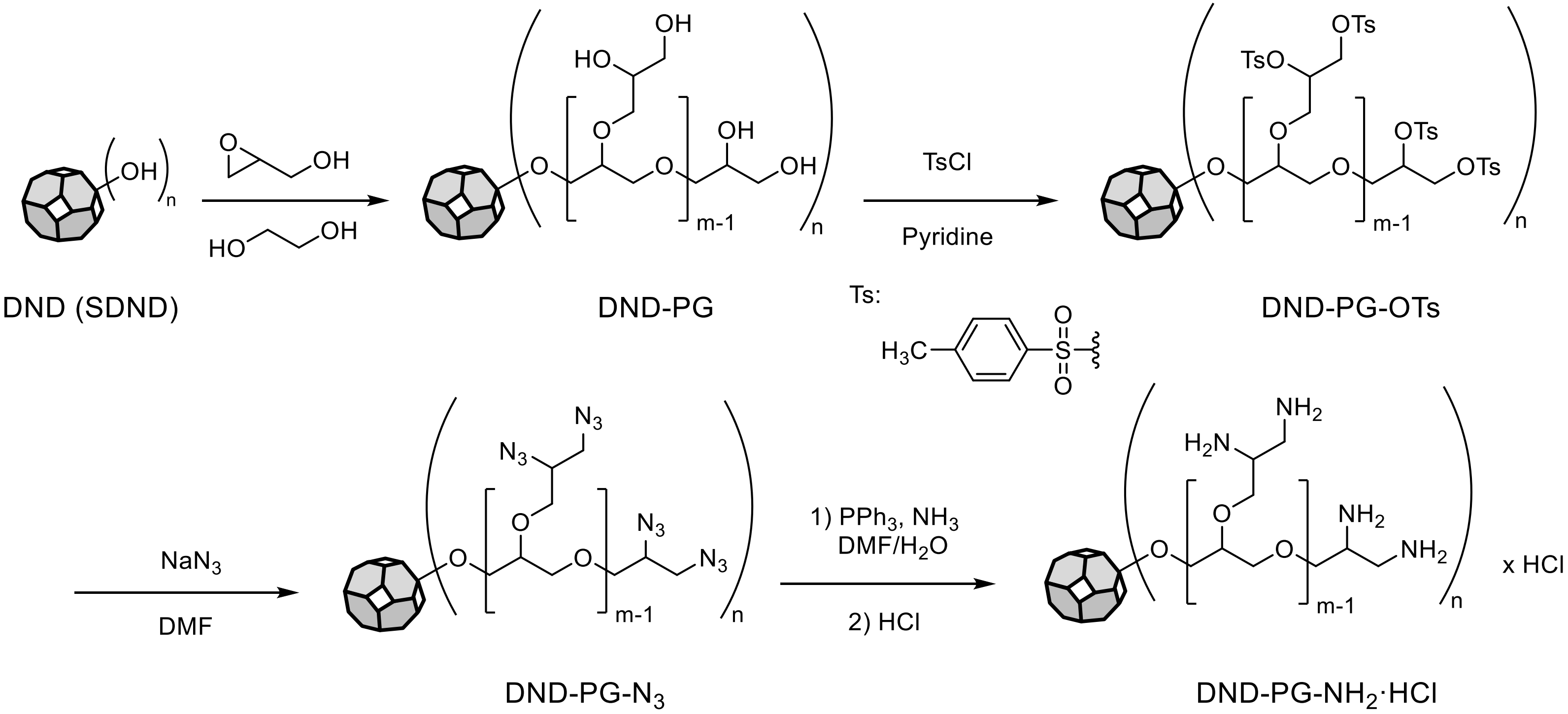

Scheme 4-1. PG functionalization of DND core and further modification of hydroxy groups in the PG layer to amino groups. For the sake of expediency, PG chain is tentatively represented as the dendritic structure where *m* is the number of generations and *n* is the number of dendrons. Also note that not all OH groups in DND-PG, especially the secondary hydroxy groups, are necessarily tosylated and consequently converted to amino groups.

a) DND

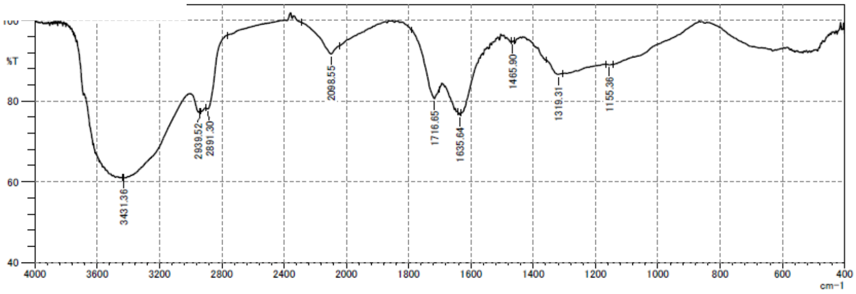

b) DND-PG

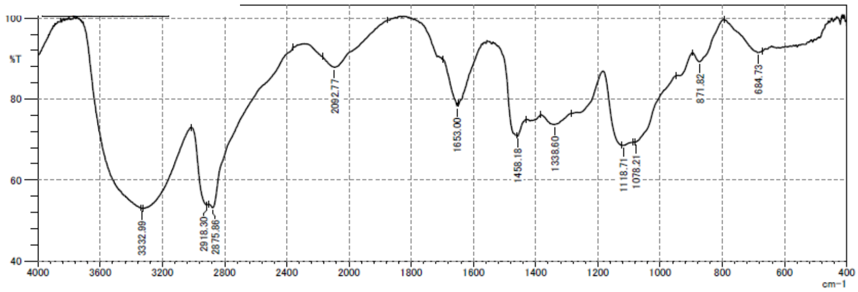

c) DND-PG-OTs

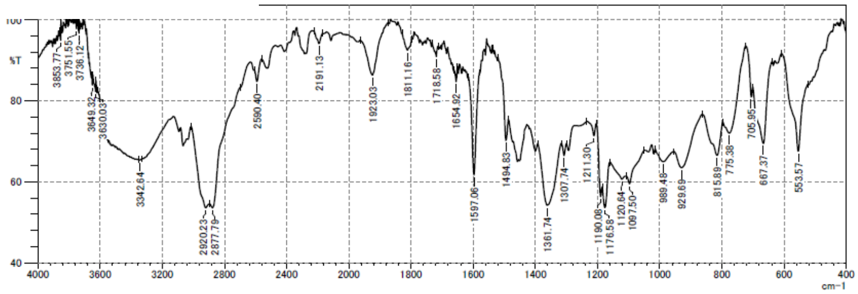

d) DND-PG-N$_3$

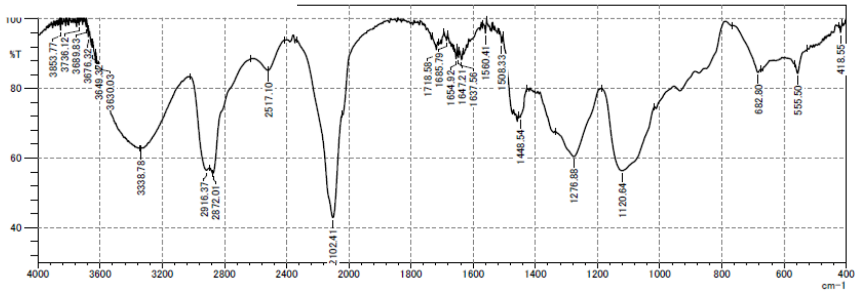

e) DND-PG-NH$_2$·HCl

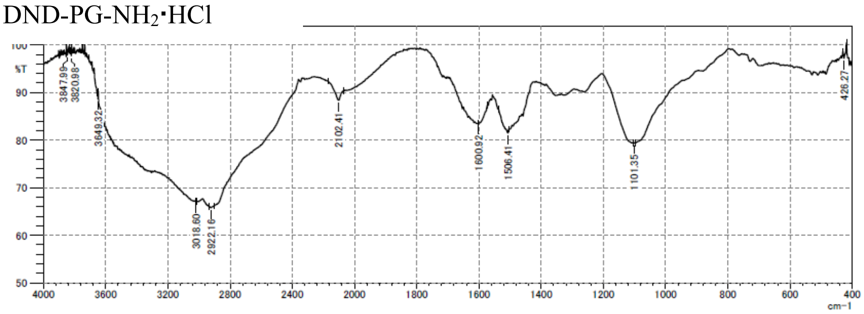

Figure 4-2. FT-IR spectra of series of materials to DND-PG-NH^{2}·HCl (DRIFT with KBr).

a) DND-PG (D_2O)

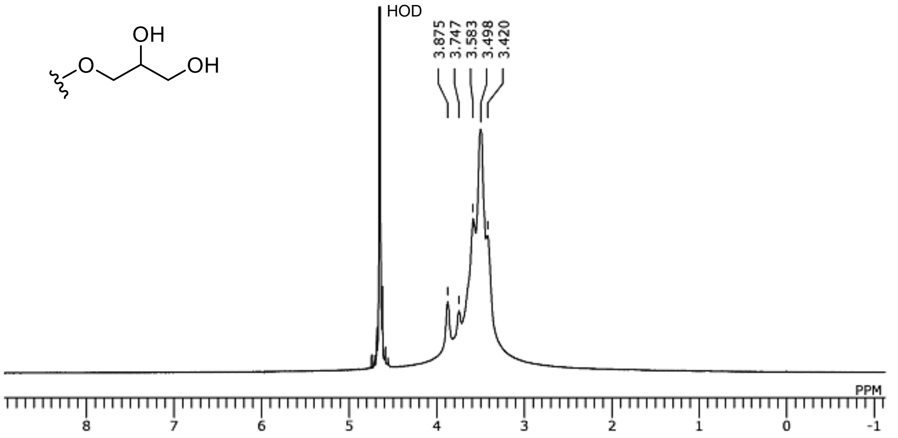

b) DND-PG-OTs ($CDCl_3$)

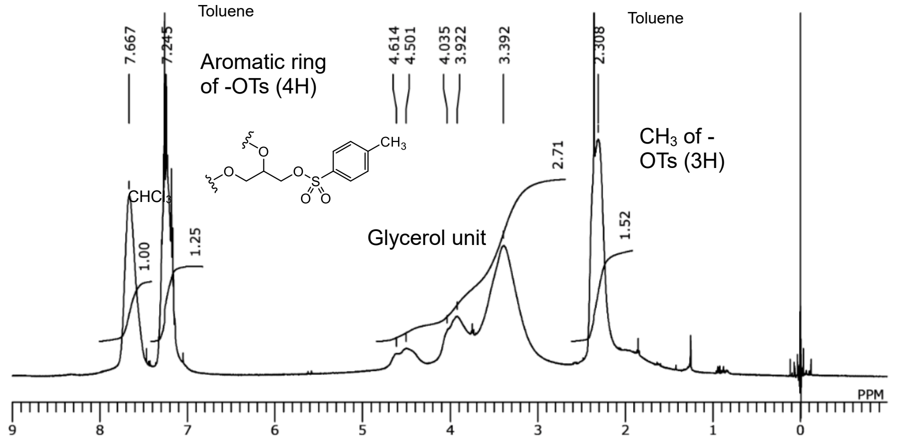

c) DND-PG-N_3 (DMSO-d_6)

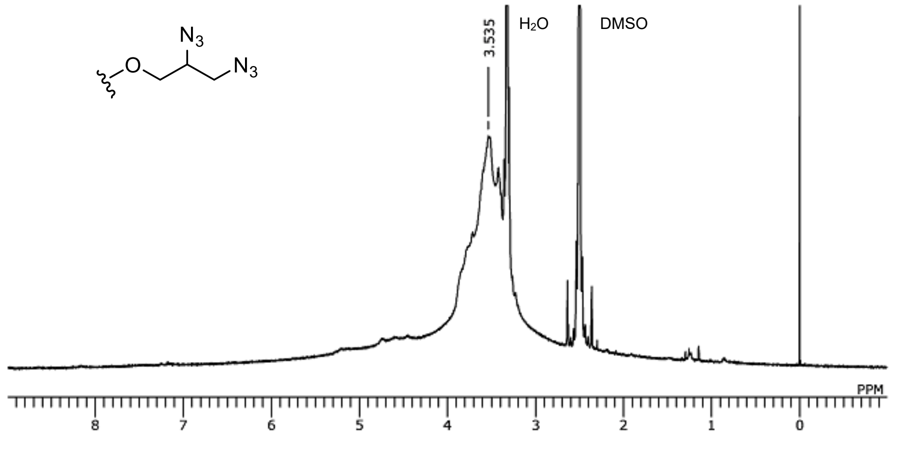

d) DND-PG-NH_2·HCl (0.1 M DCl)

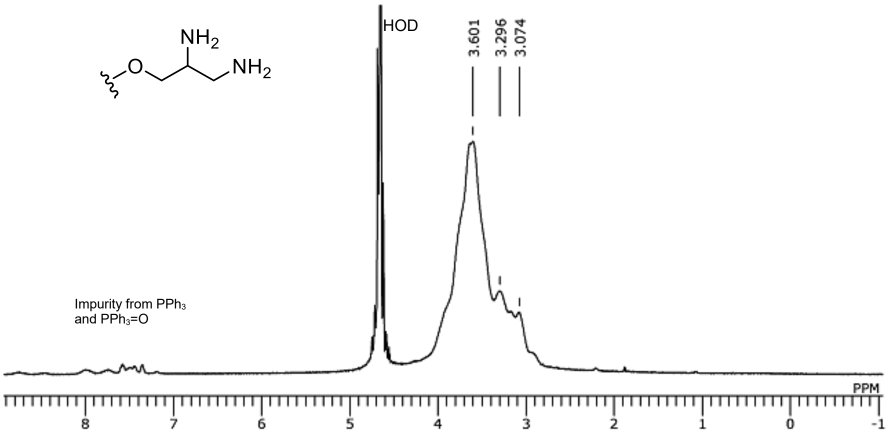

Figure 4-3. ^{1}H NMR spectra of DND-PG (a), DND-PG-OTs (b), DND-PG-N_3 (c) and DND-PG-NH_2·HCl (d).

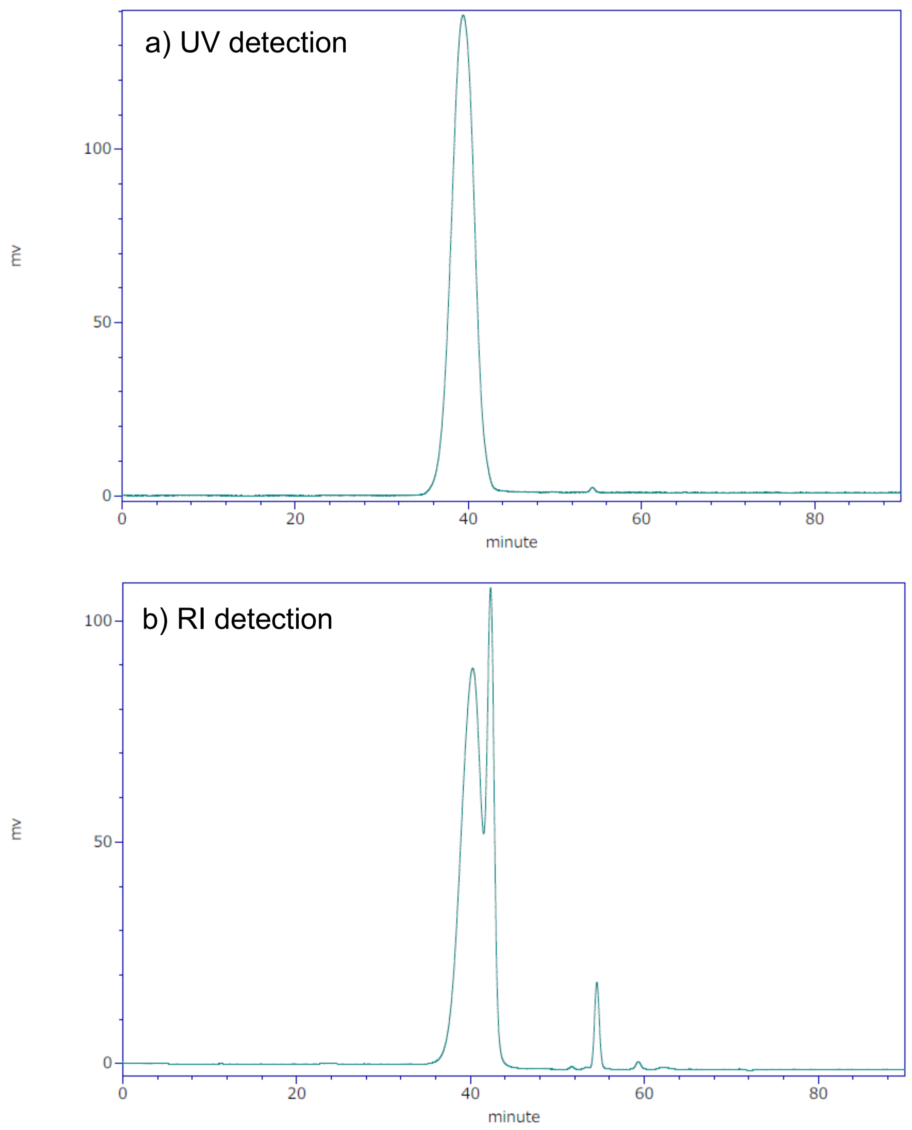

Figure 4-4. Size exclusion chromatogram (SEC) of DND-PG (Column: Shodex OHpak SB-806 HQ × 3 (in series), eluent: 0.5 M $NaNO_3$, 0.6 mL/min, column temp. 40 °C): UV detection (a) and RI detection (b).

a)

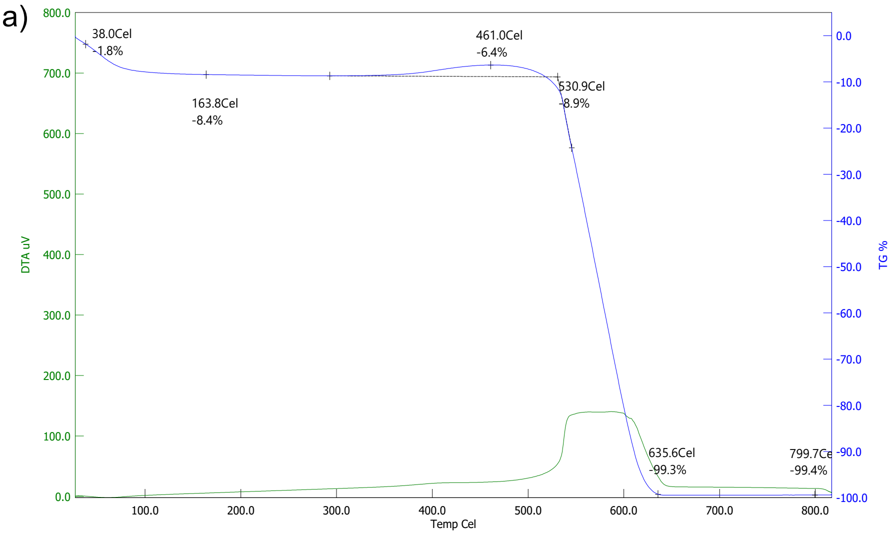
38.0Cel
-1.8%
461.0Cel
-6.4%
163.8Cel
-8.4%
530.9Cel
-8.9%
635.6Cel
-99.3%
799.7Cel
-99.4%
DTA uV
TG %
Temp Cel
800.0
700.0
600.0
500.0
400.0
300.0
200.0
100.0
0.0
-10.0
-20.0
-30.0
-40.0
-50.0
-60.0
-70.0
-80.0
-90.0
-100.0
100.0
200.0
300.0
400.0
500.0
600.0
700.0
800.0

b)

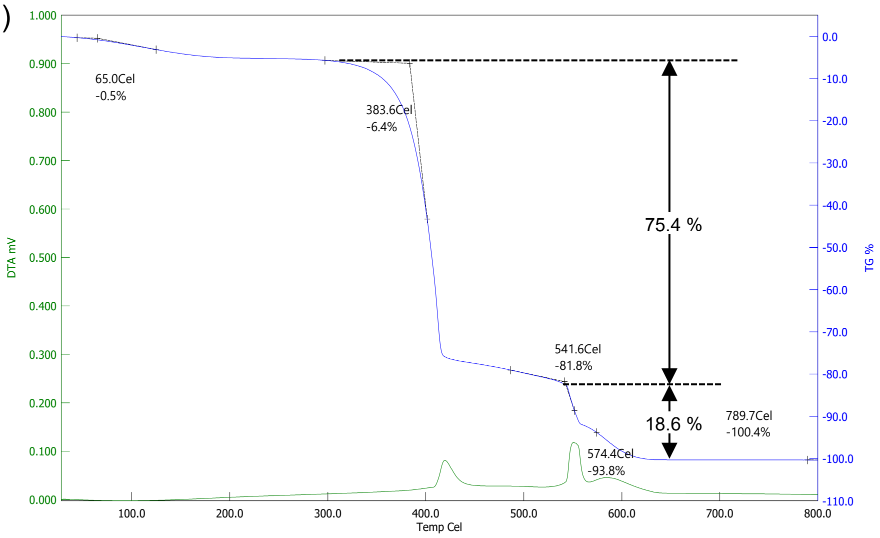
65.0Cel
-0.5%
383.6Cel
-6.4%
75.4 %
541.6Cel
-81.8%
18.6 %
789.7Cel
-100.4%
574.4Cel
-93.8%
DTA mV
TG %
Temp Cel
1.000
0.900
0.800
0.700
0.600
0.500
0.400
0.300
0.200
0.100
0.000
0.0
-10.0
-20.0
-30.0
-40.0
-50.0
-60.0
-70.0
-80.0
-90.0
-100.0
-110.0
100.0
200.0
300.0
400.0
500.0
600.0
700.0
800.0

c)

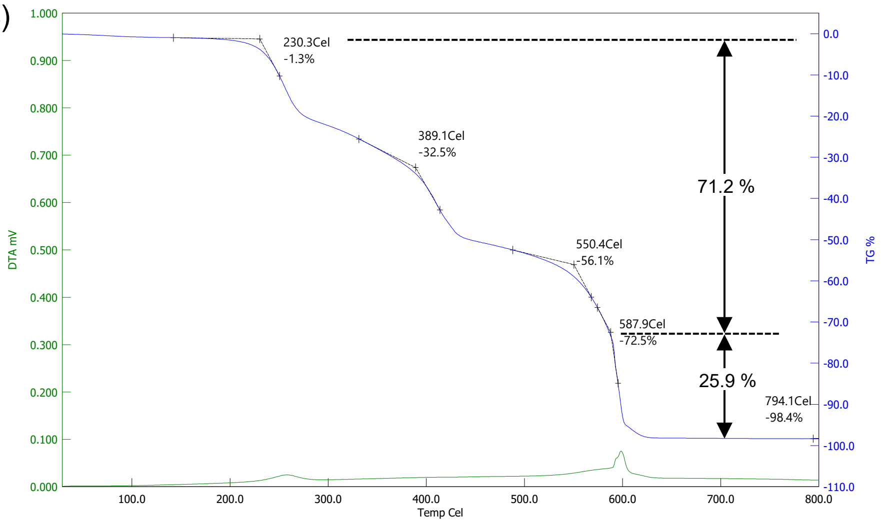
230.3Cel
-1.3%
389.1Cel
-32.5%
71.2 %
550.4Cel
-56.1%
587.9Cel
-72.5%
25.9 %
794.1Cel
-98.4%
DTA mV
TG %
Temp Cel
1.000
0.900
0.800
0.700
0.600
0.500
0.400
0.300
0.200
0.100
0.000
0.0
-10.0
-20.0
-30.0
-40.0
-50.0
-60.0
-70.0
-80.0
-90.0
-100.0
-110.0
100.0
200.0
300.0
400.0
500.0
600.0
700.0
800.0

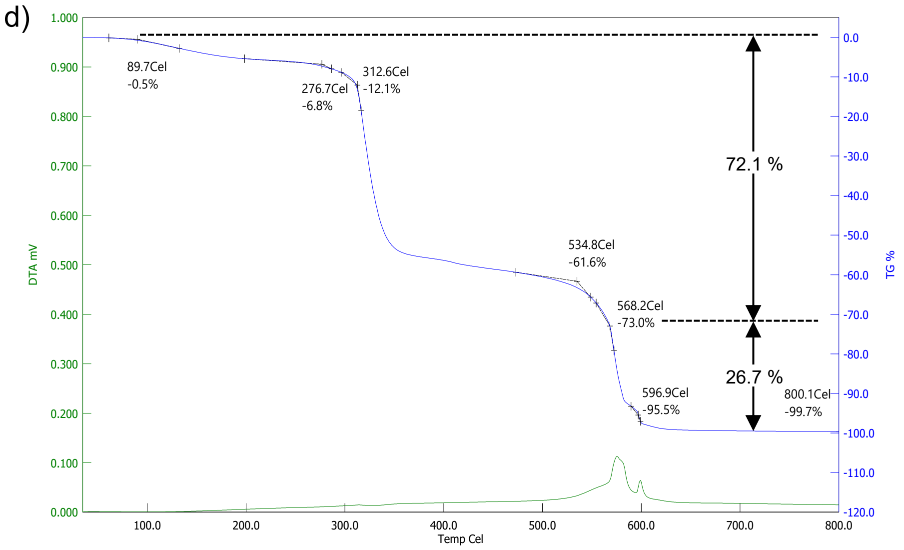

Figure 4-5. TGA results of series of materials (Air atmosphere, 20 °C/min):DND (a), DND-PG (b), DND-PG-N_3 (c) and DND-PG-NH_2•HCl (d). All measurements were done in air at 20 °C/min of temperature increasing rate. In each profile, the weight loss at the lower and higher temperatures is assigned to the modified PG layer and the DND core.

Although we employed the process for DND-PG-NH_2 reported previously [71, 138], more precise characterizations were carried out qualitatively and quantitatively in each step. For the DND-PG, some of the hydroxy groups in the PG layer was tosylated to give DND-PG-OTs. The content of tosylate was determined to be 3.28 mmol/g by the sulfur content of the elemental analysis (Table S4-2 in Appendix II). In FT-IR, SO_2 of the tosylate is characterized by the peaks at 1362 and 1177 cm^{-1} for the asymmetric and symmetric stretching vibrations, respectively (Figure 4-2c). In ^{1}H NMR, signals of the benzene ring and methyl group are observed at 7.67 and 7.24 ppm, and 2.31 ppm, respectively (Figure 4-3b). In the next steps, the tosyl group was substituted with azide and the resulting DND-PG-N_3 was reduced to the amino group by the Staudinger reaction with triphenylphosphine (PPh_3) to give DND-PG-NH_2•HCl. Both DND-PG-

N_3 and DND-PG-NH_2•HCl were qualified and quantified by FT-IR, solution phase ^{1}H NMR and elemental analysis. FT-IR spectra (Figures 4-2d and 4-2e) support the substitution with azide by the absorption at 2102 cm^{-1} for asymmetric stretching vibration and the subsequent reduction to amine by disappearance of the azide peak. Instead, the new peaks appear at 1601 and 1506 cm^{-1} corresponding to asymmetrical and symmetrical bending vibrations of $-NH_3^+$, respectively. In the ^{1}H NMR (Figures 4-3c and 4-3d), the transformations of OTs → N_3 → NH_2 are traced by disappearance of signals of tosylate in the spectrum of DND-PG-N_3 and appearance of signals at 3.0 – 3.3 ppm in the spectrum of DND-PG-NH_2•HCl. The amounts of azide in DND-PG-N_3 and amino group in DND-PG-NH_2•HCl are calculated to be 4.45 and 4.22 mmol/g, respectively, from the TGA (Figures 4-5c and 4-5d) and the nitrogen content in the elemental analysis (Table S4-2 in Appendix II). As we expected, the free PG contaminating DND-PG is considered to be fully removed at the syntheses of DND-PG-N_3 and DND-PG-NH_2•HCl due to the consistent results of the PG contents at TGA (Figures 4-5c and 4-5d) and the functional group density (Table S4-3 in Appendix II). While the "as-prepared" DND-PG contains 80.2 wt% including free PG as mentioned above (Figure 4-5b), PG content in the "fully purified" DND-PG without free PG is calculated to be 69 – 70 wt% based on TGA of DND-PG-N_3 and DND-PG-NH_2•HCl and the functional group content of each material. The content of free PG in the "as-prepared" DND-PG is estimated to be 37 wt% which is roughly comparable to ca. 30% in the SEC (Figure 4-4b).

4-2-3. Introduction of PBA moiety and further modification

As shown in Scheme 4-2, PBA moiety was introduced by reductive amination of 2-formylphenylboronic acid (*o*-boronobenzaldehyde) with DND-PG-NH_2. The one-pot reaction was carried out in methanol to form the corresponding imine followed by reduction with $NaBH_4$ to give DND-PG-PBA. ^{10}B enriched 2-formylphenylboronic acid was readily synthesized from commercially available ^{10}B boric acid via its triisopropyl ester (experimental detail is shown in

S4-2 in Appendix II) and was employed for the synthesis of ^{10}B enriched DND-PG-PBA [139]. The DND-PG-PBA-^{10}B was used in *in vivo* experiments, which will be described below. The regioisomers of DND-PG-PBA were also prepared from 3- and 4-formylphenylboronic acid (*m*- and *p*-boronobenzaldehyde) to discuss the structure – property relationship, which also will be described below.

The introduction of PBA moiety to DND-PG-NH_2 was confirmed by FT-IR spectrum at 1352 and 754 cm^{-1} corresponding to B–O stretching and out-of-plane bending for 1,2-disubstituted benzene ring, respectively (Figure 4-6a). In ^{1}H NMR, the hydrogens at benzene ring and benzylic position of the PBA moiety are observed at 7.50 and 7.20 ppm, and at 4.05 ppm, respectively (Figure 4-7a). According to the elemental analysis by combustion method (Table S4-4 in Appendix II), The amount of PBA moiety (2.24 mmol in 1.0 g of DND-PG-PBA) is calculated to be introduced onto DND-PG through the reaction between *o*-boronobenzaldehyde and the NH_2 group (3.15 mmol and 4.22 mmol to 1.0 g of DND-PG-NH_2·HCl, respectively).

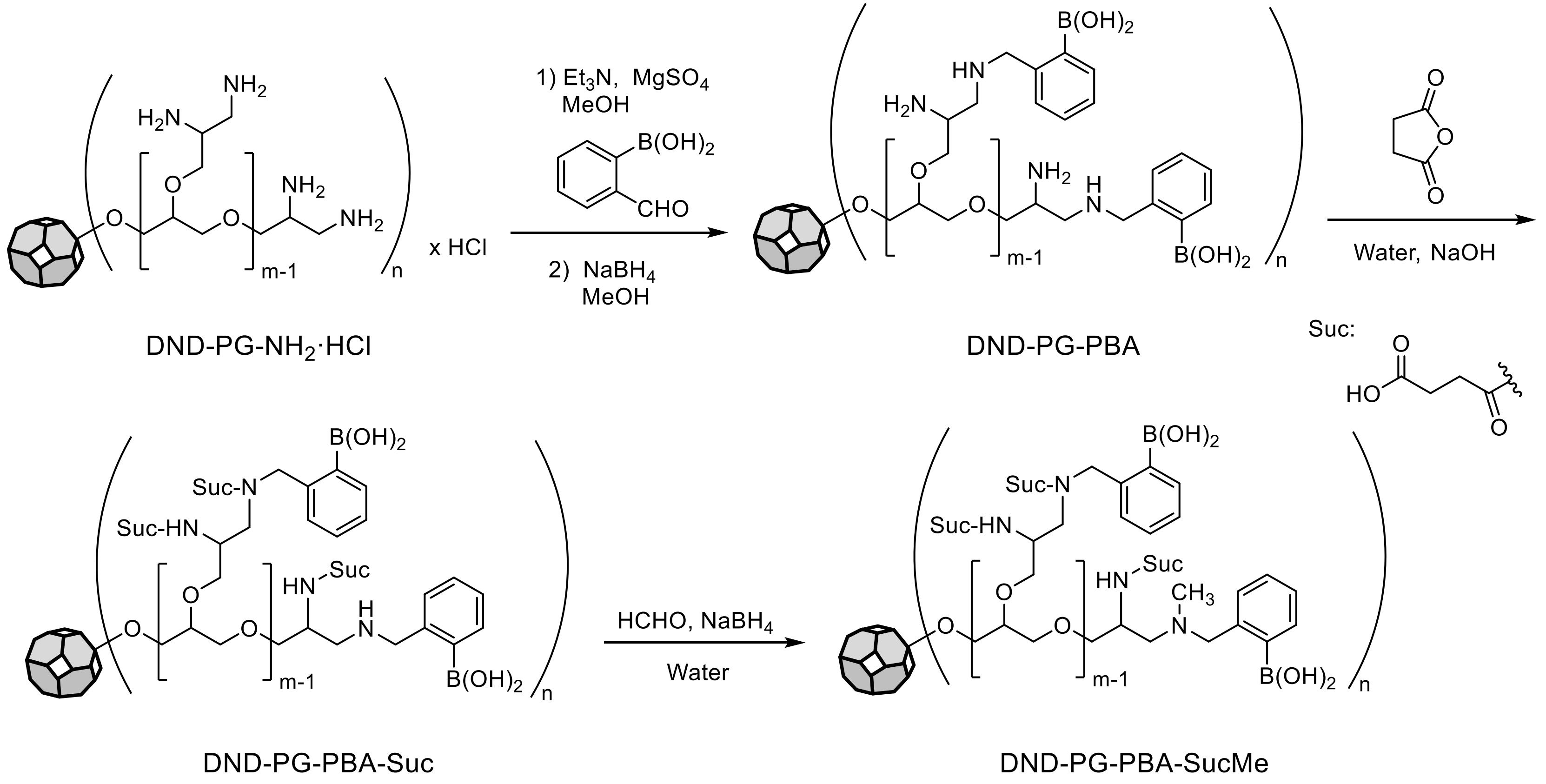

Scheme 4-2. Addition of boronic acid layer on DND-PG though the reaction of 2-formylphenylboronic acid with DND-PG-NH$_2$ and further modification by succinylation and methylation. Note that the regioselectivity between 1- and 2-positions of glycerol unit is uncertain in the reductive amination of DND-PG-NH$_2$ by 2-formylphenylboronic acid.

a) DND-PG-PBA

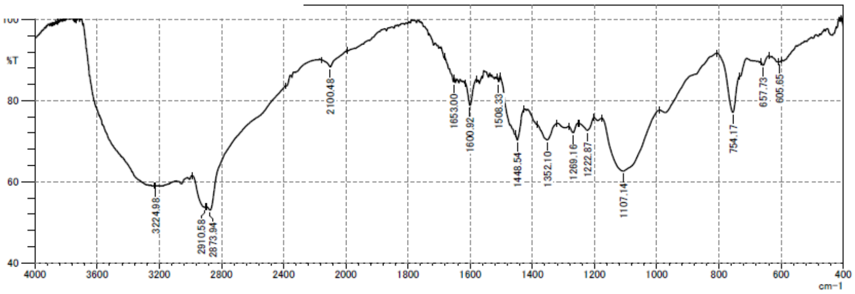

b) DND-PG-PBA-Suc

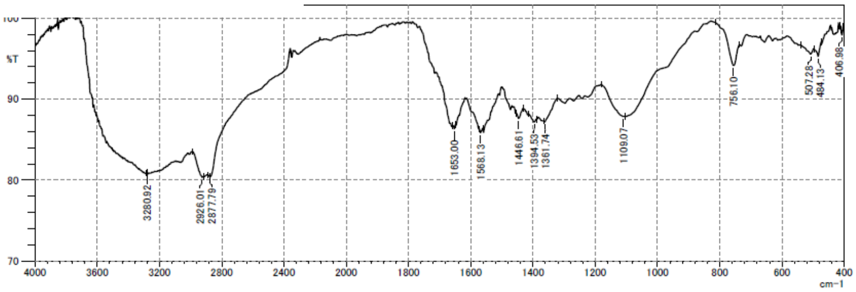

c) ND-PG-PBA-SucMe

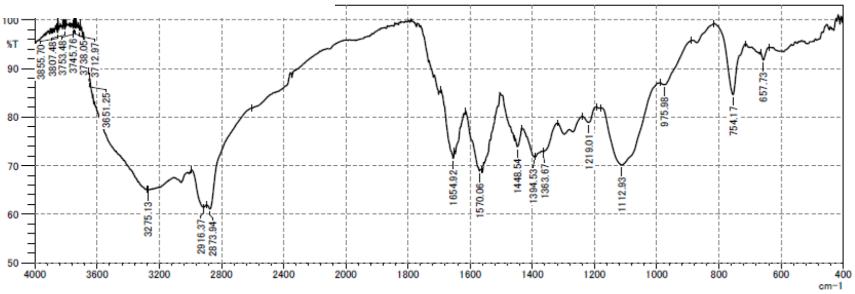

Figure 4-6. FT-IR spectra of series of PBA introduced materials (DRIFT with KBr).

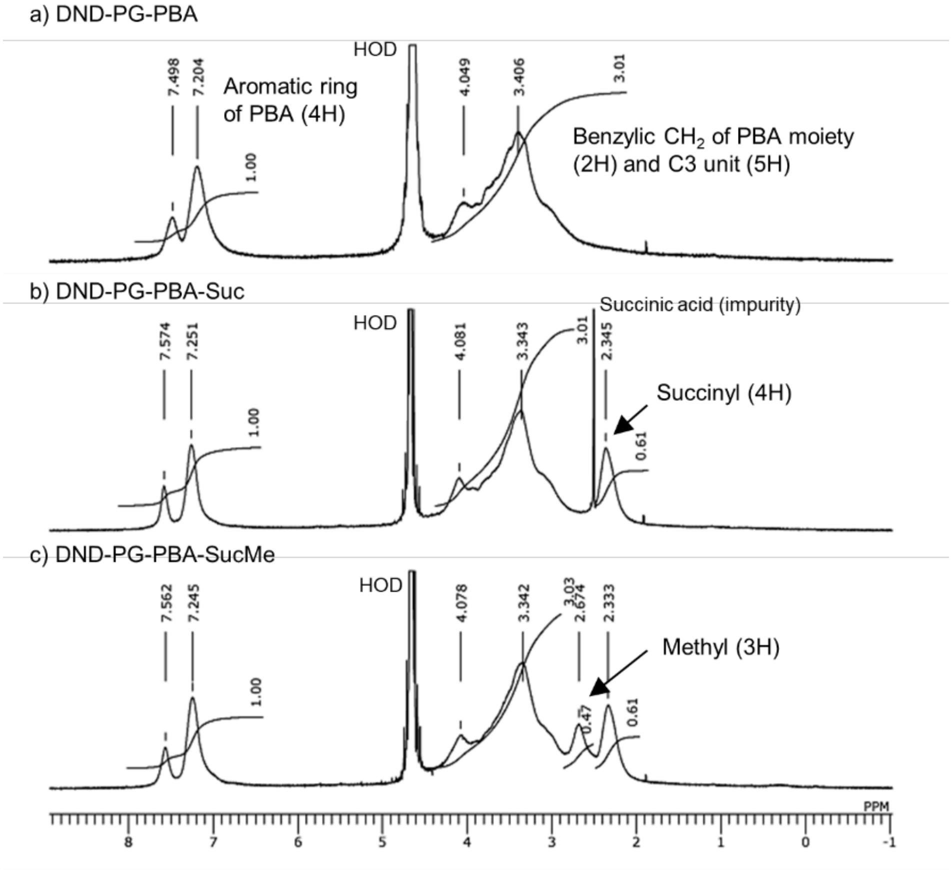

Figure 4-7. ^{1}H NMR spectra of (a) DND-PG-PBA, (b) DND-PG-PBA-Suc and (c) DND-PG-PBA-SucMe (500 MHz, 0.1 M DCl).

The DND-PG-PBA exhibited the dispersibility at 50 mg/mL in phosphate buffered saline (PBS), which is enough for the subsequent *in vitro* and *in vivo* experiments. Such a high dispersibility can be attributed to the “Wulff-type” PBA [140–144], in which the nitrogen atom of the aminomethyl group at *o*-position (**1** in Figure 4-8) coordinates with the boron atom of the boronic acid moiety to give five-membered ring (**2** in Figure 4-8). The Wulff-type coordination is reported to make the boron atom to be tetrahedral (sp^3) to lower the p*K*a of PBA from 8 – 10 to 5.7, which should enhance the dispersibility of DND-PG-PBA at the neutral pH [142, 143]. In contrast, almost no dispersibility in PBS was observed for the regioisomers of DND-PG-PBA prepared by *m*- and *p*-boronobenzaldehyde (**3** and **4** in Figure 4-8, respectively). This phenomenon can be interpreted by high p*K*a of PBA of these regioisomers due to the lack of Wulff-type coordination.

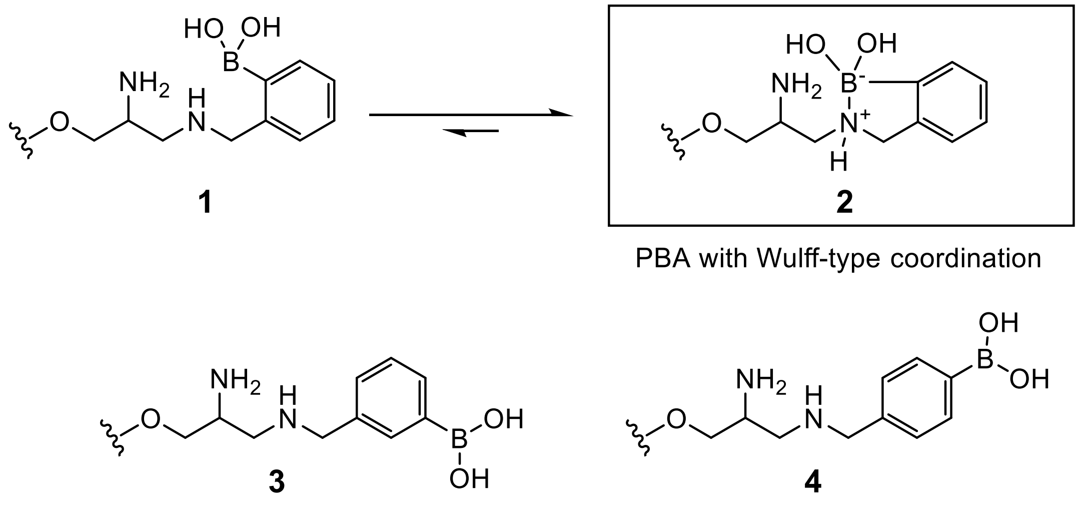

PBA with Wulff-type coordination

PBAs without Wulff-type coordination

Figure 4-8. Structures of PBA with and without Wulff-type coordination under neutral conditions.

Since we obtained the nanodrug candidate which fulfils the materials design described above, DND-PG-PBA was injected into tumor mice. However, the mice died immediately after the injection probably due to embolism. In fact, we observed the heavy aggregation of DND-PG-PBA in a PBS mixture of FBS (fetal bovine serum) in the *in vitro* experiment (**B** in Figure 4-9). Since we recently reported that amino groups on the PG layer attract proteins to form corona layer [71], amino groups were tried to convert to amide and methylamine through the succinylation and methylation, respectively (Scheme 4-2). Some of the secondary amino groups were not intentionally succinylated and were subsequently methylated to enable Wulff-type coordination as described above (Figure 4-8). Actually, about 0.6 eq. of succinic anhydride to the total numbers of the amino groups including primary and secondary amines was used for succinylation of DND-

PG-PBA to give DND-PG-PBA-Suc. The intact secondary amines were methylated by the reductive amination with formaldehyde (Scheme 4-2). As we expected, the resulting DND-PG-PBA-SucMe showed no aggregation in a PBS mixture of FBS (**F** in Figure 4-9).

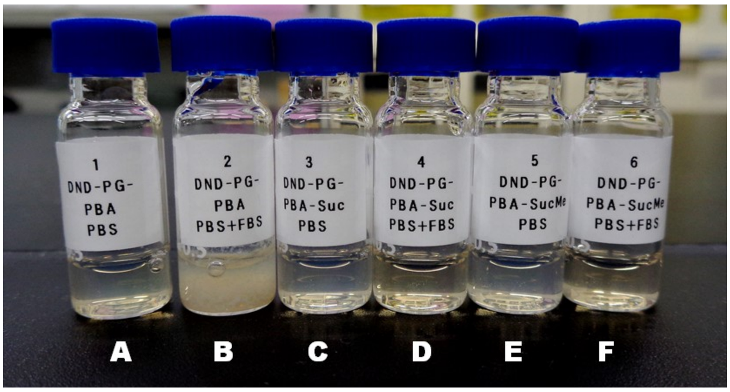

Figure 4-9. Dispersions (**A**, **C**–**F**) and suspension (**B**) of modified DNDs in the physiological media; DND-PG-PBA in PBS (ca. 0.5 wt%, **A**) and in the mixture of PBS with FBS (45/55 (v/v), **B**), DND-PG-PBA-Suc in PBS (**C**) and in the mixture of PBS with FBS (**D**), and DND-PG-PBA-SucMe in PBS (**E**) and in the mixture of PBS with FBS (**F**).

Since all the primary amines in DND-PG-PBA are supposed to be converted to amide (Table 4-1) by succinylation (Scheme 4-2), no precipitation in DND-PG-PBA-Suc in the presence of FBS (**D** in Figure 4-9) implies that primary amines in DND-PG-BPA attract proteins to form aggregates which may cause embolism *in vivo* [71]. Actually, the primary amines at the surface of DND-PG-PBA can interact with proteins through hydrogen bonding and/or electrostatic interaction with less steric hindrance, while amide and secondary amines inside the polymer layer are difficult to attract proteins. Although primary amines significantly affect the precipitation and toxicity of the nanodrugs in the presence of proteins, secondary and tertiary amines can coordinate with boron to form the Wulff-type coordination (**2** in Figure 4-8), improving the dispersibility of DND-PG-PBA, DND-PG-PBA-Suc and DND-PG-PBA-SucMe in PBS significantly.

These derivatives of DND-PG-PBA are characterized by FT-IR, ^{1}H NMR, ICP-AES and DLS, qualitatively and quantitatively. In FT-IR of DND-PG-PBA-Suc (Figure 4-6b), peaks of the C=O stretching vibrations of amide and carboxylate ($–COO^–$) are observed at 1653 and 1568 $cm^{–1}$, respectively. In ^{1}H NMR spectrum (Figure 4-7b), the signal at 2.34 ppm is assigned to the hydrogens at the succinyl moiety ($–CH_2CH_2–$). After the methylation, a new signal appears at 2.67 ppm corresponding to the methyl group in ^{1}H NMR (Figure 4-7c), though no significant change is observed in FT-IR (Figure 4-6c). The loading amounts of succinyl and methyl groups are estimated by the integral values of ^{1}H NMR as indicated in Table S4-5 in Appendix II. Succinyl moiety in DND-PG-PBA-Suc is 1.20 mmol, and succinyl and methyl moieties in DND-PG-PBA-SucMe are 1.17 and 1.20 mmol, respectively, in 1.0 g of each material.

Boron content in DND-PG-PBA-SucMe is 1.85 wt% by ICP-AES, which is comparable to 2.06 wt% determined by the content of PBA moiety. The loading amount of the functional groups in each material is summarized in Table 4-1.

Table 4-1. Content of functional groups in DND-PG derivatives.

	Functional group content (mmol/g)						Boron content[a]
	OTs	N_3	NH_2	PBA	Succinyl	Methyl	(%)
DND-PG-OTs	3.28						
DND-PG-N_3		4.45					
DND-PG-NH_2·HCl			4.22				
DND-PG-PBA			1.31	2.24			2.42
DND-PG-PBA-Suc				1.97	1.20		2.13
DND-PG-PBA-SucMe				1.91	1.17	1.20	2.06 (1.85[b])

[a] Calculated value from the molar ratio of PBA moiety.

[b] Result from ICP-AES.

As for the hydrodynamic diameters measured by DLS, no significant difference is observed in their median sizes and the size distributions of DND-PG-NH_2, -PBA, -PBA-Suc and -PBA-SucMe in water as shown in Figure 4-10, indicating no aggregation and no cross-linking in the transformations shown in Scheme 4-2. Since the chemically modified DND-PG is reported to have 51 nm median diameter with 18 nm core [137], the DND-PG shown in Scheme 4-1 may have small aggregates of the primary DND particles with 5 nm-size.

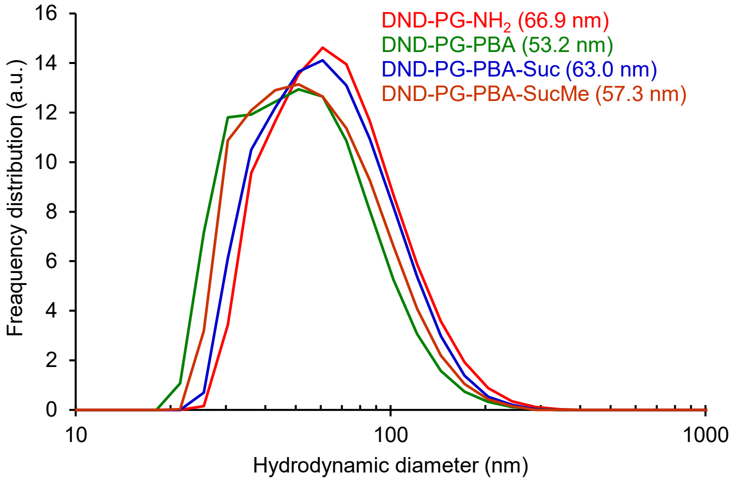

Figure 4-10. DLS results of PBA functionalized DNDs in water. The volume mean diameters are indicated in the brackets.

4-2-4. *In vitro* cytotoxicity of the nanodrug

Before *in vivo* BNCT, cytotoxicity of DND-PG-PBA-Suc and -SucMe was evaluated as shown in Figure 4-11. CT26 murine colon tumor cells were used as is the case with the *in vivo* tumor model. Both of these materials stably dispersed in cell culture medium including FBS for 24 h and exhibited no toxicity without neutron irradiation even at relatively high concentration (500 µg/mL).

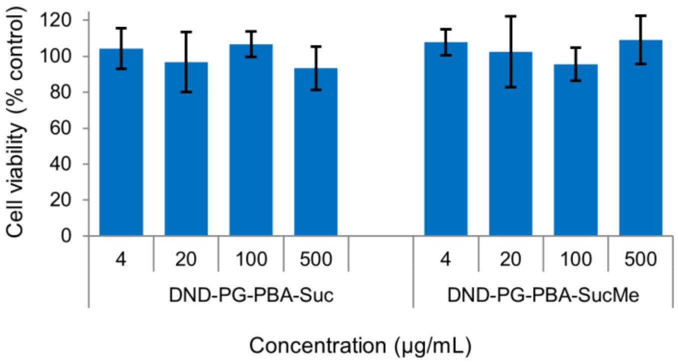

Figure 4-11. Cell viability of DND-PG-PBA-Suc and DND-PG-PBA-SucMe against CT26 cells (*n* = 5).

4-2-5. Pharmacokinetic study

In order to determine the timing of drug injection before neutron irradiation, pharmacokinetic studies were conducted by use of ^{10}B enriched DND-PG-PBA-SucMe (DND-PG-PBA-SucMe-^{10}B) through conjugation of ^{10}B enriched 2-formylphenylboronic acid with DND-PG-NH_2 (Scheme 4-2) to increase the sensitivity of ^{10}B in its quantification. In the experiments, after PBS dispersion of DND-PG-PBA-SucMe-^{10}B (4.0 wt%, 200 μL) was injected intravenously to a tumor mouse, the ^{10}B concentration in tumor, blood and major organs were measured by the neutron-induced prompt γ-ray analysis (PGA) [145]. No acute symptoms on mice were observed upon the sample injection. The result of the pharmacokinetics is summarized in Figure 4-12.

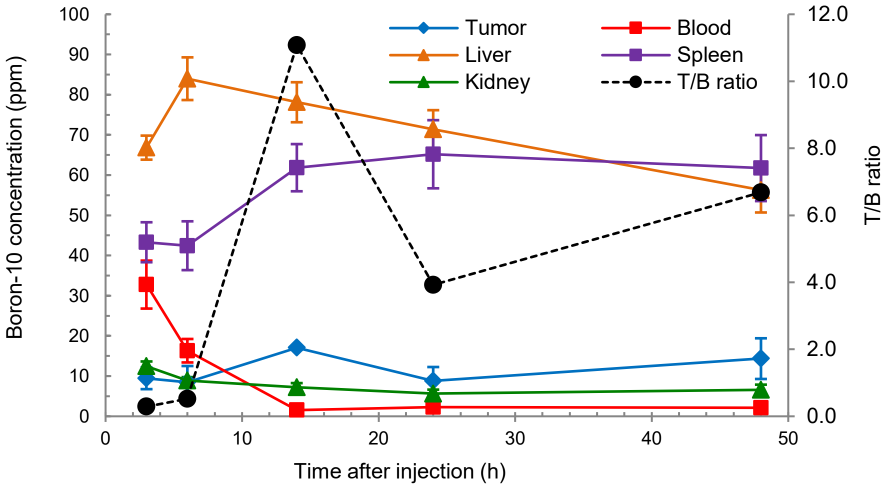

Figure 4-12. Pharmacokinetic study of DND-PG-PBA-SucMe-^{10}B; ^{10}B concentrations in tumor, blood and major organs (solid lines) and the concentration ratio of tumor (T) to blood (B) (T/B ratio, dotted line). The number of mice at each time point is 3.

The ^{10}B concentrations of liver and spleen (orange and purple solid lines, respectively) are higher than those of blood, tumor and kidney (red, blue and green solid lines, respectively) from 3 h to 48 h after injection, indicating that DND-PG-PBA-SucMe-^{10}B tends to accumulate in these organs. Assuming the average weights of liver and spleen to be 0.96 and 0.08 g, respectively, more than half amount of the injected nanodrug is calculated to be accumulated in these organs. Since PG was reported to show high stealth efficiency to avoid the accumulation in liver and spleen [56], the PBA and/or SucMe moieties may reduce the efficiency. On the other hand, the ^{10}B concentration of kidney is low, implying that DND-PG-PBA-SucMe-^{10}B was not excreted through kidney due to the hydrodynamic diameters larger than 20 nm determined by DLS (Figure 4-10).

To elucidate the BNCT conditions, the ratio of ^{10}B concentrations of tumor and blood (T/B ratio) is added in Figure 4-12 (black dashed line). In addition to the high tumor accumulation of the drug aiming at the high BNCT efficacy, we should also consider the safety to avoid the side effect. The T/B ratio is the important index other than the toxicity of the material itself. The ^{10}B concentrations of tumor were 17.1 and 14.3 ppm at 14 and 48 h, respectively, which are higher than those at other time points. The T/B ratio was 11.1 and 6.7 at 14 and 48 h, respectively, which are also higher than those at other time points, while the ^{10}B concentration in blood decreased from 32.8 ppm at 3 h at half-valued period of ca. 3 h. Since the requirement of the T/B ratio is > 3 for the safety of BNCT, we decided to irradiate the neutron around 14 and 48 h after the injection of DND-PG-PBA-SucMe-^{10}B.

4-2-6. BNCT study

Neutron was irradiated to the tumor implanted BALB/c mice at 16 and 48 h after the nanodrug was injected in the same way as that of the pharmacokinetic experiments. Although the highest T/B ratio was observed at 14 h in Figure 4-12, we irradiated neutron at 16 h after the injection because of experimental arrangement. The tumor size and body weight were monitored for 29 days after the neutron irradiation and the results are summarized in Figure 4-13. While the nanodrug itself exhibited no effect on the tumor growth (injection control in Figure 4-14), neutron irradiation suppressed it to some extent without the injection of the nanodrug (hot control in Figure 4-14). As compared with the hot control, DND-PG-PBA-SucMe-^{10}B showed statistically significant BNCT efficacy on days 17, 21 and 26 after the neutron irradiation (BNCT 48 h in Figure 4-13). Although the faster growth of one mouse increased the average tumor size (Figure S4-4 in Appendix II), the result of BNCT 16 h supports that of BNCT 48 h to some extent. As for the body weight, no significant difference between the hot control and BNCT groups was observed, indicating no acute or subacute toxicity of the nanodrug (Figure S4-5 in Appendix II). Since the reproducibility is confirmed by the experiments using smaller number of mice ($n = 3$ except injection control ($n = 2$)) as shown in Figure S4-6 (Appendix II), we conclude that DND-

PG-PBA-SucMe-^{10}B is a promising nanodrug for BNCT.

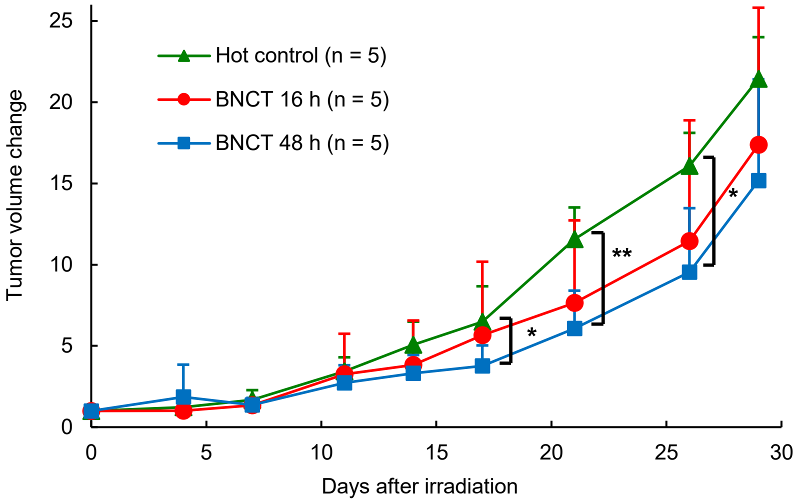

Figure 4-13. BNCT results of DND-PG-PBA-SucMe-^{10}B. Relative tumor volume was monitored in BNCT and control groups for 29 days after neutron irradiation. (*n* = 5, the Student's t-test, $*p < 0.05$, $**p < 0.01$).

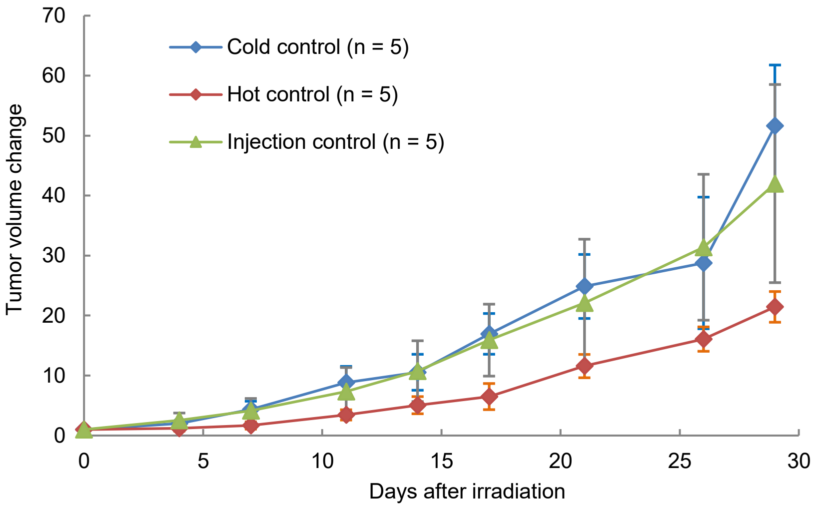

Figure S4-14. Tumor growth of control groups (without drug injection).

4-3. Conclusion and outlook

We synthesized PBA functionalized DNDs for BNCT agent via the PG modified DNDs (DND-PG). PBA moiety was introduced to contain the percent order of boron atoms. The Wulff-type coordination of the resulting DND-PG-PBA may help disperse it well under physiological conditions. To address the aggregation problem in the presence of protein, the amino groups of DND-PG-PBA were succinylated and methylated to give individually dispersed solution without precipitation. The resulting nanodrug was confirmed to be accumulated in the tumor tissue and exert BNCT efficacy upon the neutron irradiation. The result demonstrates that, as the first step for proof of concept, the boronic acid functionalized DNDs can be a promising candidate of BNCT agent.

To enhance the BNCT efficacy, we would like to elucidate relationship of the structures of PBA, succinyl and methyl moieties with cellular uptake. To improve anticancer efficiency, multimodal system can be conceivable; BNCT combined with chemotherapy by an anticancer drug such as cisplatin incorporated at the succinyl moiety [146], and radiotherapy sensitized by the DND core [27]. In the course of above investigations, the nanodrug can be imaged by fluorescent color center in DND. We are sure that the present work can create novel DND-based BNCT agents with multimodality.

4-4. Experimental

Materials

Single-digit nanometer-sized water dispersion of DNDs was manufactured by Daicel Corporation (DINNOVARE™). For the modification of DNDs, the following reagents and solvents were purchased from FUJIFILM Wako Pure Chemical Corporation (Osaka Japan); 2,3-epoxy-1-propanol (glycidol), *N,N*-dimethylaminopyridine (DMAP), sodium azide, triphenylphosphine, magnesium sulfate (anhydrous), formaldehyde solution (36%), ammonia water, hydrochloric acid, sodium hydroxide, ethylene glycol, pyridine, tetrahydrofuran (THF), toluene, *N,N*-dimethylformamide (DMF), ethyl acetate, methanol, ethanol, 2-propanol, cyclohexane, diethyl ether, *t*-butyl methyl ether *n*-hexane, Roswell Park Memorial Institute (RPMI) 1640, 0.25% trypsin-EDTA·4Na solution, Dulbecco's phosphate-buffered saline (PBS(−)), 10× PBS(−) and Cell counting kit-8 (CCK-8, a formulation of 2-(2-methoxy-4-nitrophenyl)-3-(4-nitrophenyl)-5-(2,4-disulfophenyl)-2*H*-tetrazolium, monosodium salt (WST-8) and 1-Methoxy-5-methylphenazinium methylsulfate (1-methoxy PMS), produced by Dojindo Laboratories, Japan). *p*-Toluenesulfonyl chloride (TsCl), 2-formylphenylboronic acid (natural abundance boron), 2-(2-bromophenyl)-1,3-dioxolane, butyllithium hexane solution and succinic anhydride were purchased from Tokyo Chemical Industry Co., Ltd. (Tokyo Japan). Sodium borohydride was purchased from Kanto Chemical Co., Inc. (Tokyo Japan). Boron-10 boric acid (^{10}B 99%) is a product of Cambridge Isotope Laboratories, Inc. (MA USA). Antibiotics solution (penicillin-streptomycin-amphotericin B, 100×) is produced by Thermo Fisher Scientific (MA USA). Fetal bovine serum (FBS) was supplied by Biosera Inc. (France). RPMI 1640 from Nacalai Tesque, Inc. (Kyoto Japan) was also used.

Equipment

^{1}H NMR spectra were measured by ECX500 NMR spectrometer (JEOL). FT-IR spectra were recorded on IR Tracer-100 FT-IR spectrometer (Shimadzu) equipped with DiffusIR DRIFT chamber (PIKE Technologies). Elemental analyses were conducted at Organic Elemental Microanalysis Center of Kyoto University. ICP-AES analysis for boron content was done with SPS3100 (SII Nanotechnology) at Nippon Steel Technology Co., Ltd. Thermogravimetric analysis (TGA) was performed with TG/DTA 6200 (SII). The absorbance of CCK-8 was measured with Multiskan FC plate reader (Thermo Scientific). ESI-MS was measured with micrOTOF mass spectrometer (Bruker). DLS measurement was done by Nanotrac Wave II particle size analyzer (MicrotracMRB). Size exclusion chromatography (SEC) was carried out by LC-20AD HPLC system (Shimadzu) with Shodex RI-501 RI detector.

DND-PG

An aqueous dispersion of DND was concentrated into solid residue which was dried at 105 °C for 2 h. To a suspension of the DND powder (1.0 g) in ethylene glycol (15.0 g), glycidol (45.1 g, 0.61 mol) was added dropwise over 105 min to keep the temperature in the range of 95 – 102 °C. The resulting black dispersion was stirred at the same temperature for 4 h, and then at room temperature overnight. Water (40 mL) was added slowly to degrade the unreacted glycidol. The dispersion was diluted with water to ca. 400 mL and concentrated with ultrafiltration membrane (Ultracel® membrane, 30 kDa) to 20 mL. The concentrate was diluted and concentrated again, which was repeated five times to obtain the purified DND-PG as black water dispersion. Yield: 100.1 g (5.07 wt%, net 5.08 g). An aliquot of the dispersion was dried on heated PTFE sheet to obtain a sample for analyses. FT-IR (DRIFT with KBr, cm^{-1}): 3332, 2918, 2875, 1458, 1118, 1078 (C–O). ^1H NMR (500 MHz, D_2O): δ ppm 3.42, 3.50, 3.58, 3.75, 3.88 (C3 unit). Elemental analysis: C; 55.72%, H: 7.06%, N; 0.57%, O; 36.86%. Elemental analysis for DND (before PG modification): C; 86.90%, H: 1.81%, N; 2.29%, O; 4.13%. TGA (Air atmosphere, 20 °C/min, % weight loss): 383 – 541 °C; 75.4%, 541 – 790 °C; 18.6% (the ratio (PG/DND) is estimated as 4.1).

DND-PG-OTs

Water dispersion of DND-PG (39.4 g, 5.07 wt%, net 2.0 g) was evaporated to dryness. The residue was dissolved in pyridine (20 mL) and evaporated to dryness to remove remained water by azeotropic distillation. After repeated once, the residue was dissolved in pyridine (30 mL) and cooled in ice-bath. To the solution, *p*-toluenesulfonyl chloride (TsCl, 3.9 g, 202 mmol) and *N,N*-dimethylaminopyridine (DMAP, 0.10 g, 0.84 mmol) was added. The reaction mixture was allowed to stir at room temperature for 24 h. Water (30 mL) was added and the precipitate was separated by centrifugation at 30000*g* for 10 min. The precipitate was washed with water twice with small amount of tetrahydrofuran (THF), precipitated again with water, centrifuged, and washed with THF-toluene twice in the same manner. The precipitate was dried *in vacuo* at 40 °C to give black solid. Yield: 3.91 g. FT-IR (DRIFT with KBr, cm^{-1}): 3342, 2920, 2878, 1597, 1362, 1177 (SO_2), 929, 815, 667, 553. ^1H NMR (500 MHz, $CDCl_3$): δ ppm 3.39 – 4.61 (C3 unit), 2.31 (CH_3 of –OTs), 7.24, 7.67 (aromatic ring of –OTs). Elemental analysis: C; 55.88%, H: 5.30%, N; 0.32%, O; 27.20%, S; 10.50%.

DND-PG-N_3

Sodium azide (0.66 g, 10.2 mmol) was added to the solution of DND-PG-OTs (2.0 g) in DMF (20 mL). The reaction was stirred at 60 °C for 3 h and then 90 °C for 19 h. Water (20 mL) was added and the precipitate was separated by centrifugation at 30000*g* for 10 min. The precipitate was washed with water twice by small amount of THF, precipitated again with water, centrifuged, and washed with THF-toluene twice in the same manner. The precipitate was dried *in vacuo* at 40 °C to give black solid. Yield: 0.67 g. FT-IR (DRIFT with KBr, cm^{-1}): 3338, 2916, 2872, 2102 (azide), 1276, 1120. ^1H NMR (DMSO-d_6): δ ppm 3.54 (C3 unit). Elemental analysis: C; 53.59%, H: 5.04%, N; 19.40%, O; 21.68%. TGA (Air atmosphere, 20 °C/min, % weight loss): 230 – 587 °C; 71.2%, 587 – 794 °C; 25.9%.

DND-PG-NH_2·HCl

DND-PG-N_3 (257 mg) in DMF (12 mL) was sonicated for 15 min. To the dispersion, water (1.0 mL), triphenylphosphine (PPh_3, 798 mg, 3.00 mmol) and conc. NH_3 (0.50 mL) were added, and stirred at 60 °C for 24 h. The reaction mixture was concentrated to half volume. After water (10 mL) and 6 M HCl (1.0 mL) were added, triphenylphosphine oxide was extracted with ethyl acetate (AcOEt, 20 mL). The aqueous phase was washed with AcOEt twice, diluted to 400 mL with water and concentrated to less than 10 mL with ultrafiltration membrane (Ultracel® membrane, 30 kDa). The concentrate was again diluted and concentrated, which was repeated twice to obtain the purified DND-PG-NH_2•HCl as black to dark-brown water dispersion. An aliquot of the dispersion was dried on heated PTFE sheet for analyses. Yield (net): 265 mg. FT-IR (DRIFT with KBr, cm^{-1}): 3018, 2922, 1601, 1506 (–NH_2), 1101. ^{1}H NMR (0.1 M DCl): δ ppm 3.07, 3.30, 3.60 (C3 unit). Elemental analysis: C; 49.16%, H: 6.69%, N; 6.55%, Cl; 13.49%. TGA (Air atmosphere, 20 °C/min, % weight loss): 90 – 568 °C; 72.1%, 568 – 800 °C; 26.7%.

DND-PG-PBA

Water dispersion of DND-PG-NH_2•HCl (net 108 mg) was evaporated to dryness. After the residue was dispersed in methanol, ethanol was added and then evaporated to dryness. Methanol (10 mL) was added to the residue and sonicated for 30 min. 2-Formylphenylboronic acid (50.4 mg, 0.34 mmol), triethylamine (145 mg, 1.43 mmol) and anhydrous magnesium sulfate ($MgSO_4$, 254 mg) were added and stirred at 60 °C for 19 h. The reaction mixture was cooled to 0 °C in ice-bath and sodium borohydride ($NaBH_4$, 119 mg, 3.20 mmol) was added in two parts in 2 h, and then stirred at 60 °C for 6 h. The reaction mixture was evaporated to remove methanol, and water (10 mL) and 6 M HCl (5.0 mL) were added. The precipitate was separated by centrifugation at 30000 g for 20 min and dissolved again in water (8 mL). After 6 M HCl (2.0 mL) was added, the mixture was stirred at 100 °C for 2.5 h. The reaction mixture was concentrated by ultrafiltration (Amicon Ultra®, 10 kDa, 3300 rpm, 30 min), and the material on the membrane was washed with water by dilution followed by ultrafiltration four times. After the material was diluted with water (6.0 g after the dilution), pH was adjusted to 7.4. The solution was washed by the dilution followed by ultrafiltration four times. To prepare the analytical sample, the resulted dispersion was lyophilized to give DND-PG-PBA as off-white powder. Yield: 104 mg (net). FT-IR (DRIFT with

KBr, cm^{-1}): 3224, 2910, 2873, 1448 (B–N), 1352 (B–O), 1107, 754 (1,2-disubstituted benzene). ^{1}H NMR (0.1 M DCl): δ ppm 7.50, 7.20 (aromatic ring of PBA), 4.05, 3.41 (benzylic position of PBA and C3 unit). Elemental analysis: C; 60.11%, H: 6.14%, N; 5.51%.

DND-PG-PBA-Suc

To a water dispersion of DND-PG-PBA (ca. 21 g, net 180 mg, pH 3.59) was added succinic anhydride (39.1 mg, 0.390 mmol) in several parts in 2 h by adjusting the pH range at 8.0 – 9.5 with 1 M NaOH. The reaction was allowed overnight at room temperature at pH 8.4. A part of the reaction mixture (6.0 g out of 24.0 g) was washed with water by the dilution followed by the ultrafiltration five times to obtain the partially succinylated material. Yield (net): 45.1 mg, which corresponded to 180 mg for the whole reaction. FT-IR (DRIFT with KBr, cm^{-1}): 3275, 2916, 2874, 1654 (amide C=O), 1570, 1448, 1394, 1363, 1112, 754. ^{1}H NMR (0.1 M DCl): δ ppm 7.57, 7.25 (aromatic ring of PBA), 4.08, 3.34 (benzylic position of PBA and C3 unit), 2.35 (succinyl). Elemental analysis: C; 57.62%, H: 6.27%, N; 5.77%.

DND-PG-PBA-SucMe

A part of the aforementioned reaction mixture of DND-PG-PBA-Suc (18.0 g out of 24.0 g), which contained 135 mg of material, was cooled in ice-bath. After formaldehyde solution (HCHO, 36%, 0.80 mL) and $NaBH_4$ (136.3 mg, 3.67 mmol) were added, the reaction mixture was stirred at room temperature overnight. 6 M HCl (3.0 mL) was added carefully and the mixture was stirred at 80 °C for 2 h. After the washing with water by the dilution followed by the ultrafiltration, pH was adjusted to about 7.0 with 1 M NaOH. Small amount of succinic anhydride (7.6 mg in total) was added in several parts to keep the pH at ≥ 6.9 to make the material dispersible. pH was adjusted to 7.4 and the resulting solution was washed by the ultrafiltration (Ultracel® membrane, 30 kDa and Amicon Ultra®, 10 kDa) several times. Yield (net): 135 mg. FT-IR (DRIFT with KBr, cm^{-1}): 3280, 2926, 2878, 1653, 1568, 1446, 1394, 1362, 1109, 756. ^{1}H NMR (0.1 M DCl): δ ppm 7.56, 7.25 (aromatic ring of PBA), 4.08, 3.34 (benzylic position of PBA and C3 unit), 2.67 (N–CH$_3$), 2.33 (succinyl). Elemental analysis: C; 56.60%, H: 6.36%, N; 5.83%. Boron content (ICP-AES): 1.85%.

Preparation of ^{10}B enriched PBA modified materials

^{10}B enriched materials (DND-PG-PBA-^{10}B, DND-PG-PBA-Suc-^{10}B and DND-PG-PBA-SucMe-^{10}B) were prepared in the same manner using 2-formylphenylboronic acid-^{10}B instead of the compound containing natural abundance boron. Procedure for the ^{10}B sample is described in S4-2 in Appendix II. For the samples for *in vivo* experiments, the solution was concentrated by the ultrafiltration, diluted with water if necessary and filtered through a 0.45 μm membrane. Then 10× PBS(−) or PBS(−) were added to make intended concentration and isotonicity.

In vitro cytotoxicity

CT26 murine colonic tumor cells were seeded on 96-well microplates by 4×10^3 cells/well suspended in 160 μL of RPMI 1640 culture medium (containing 10% FBS and 1% of 100× penicillin-streptomycin-amphotericin B solution) for each well. After incubation in CO$_2$ incubator at 37 °C for 24 h, culture medium was replaced once, PBS (control) or PBS solution of nanoparticles (4, 20, 100 and 500 μg/mL, 40 μL for each) were added, and the cells were further incubated for 24 h. After that, culture medium was replaced and incubated for 48 h. Once cells were washed with PBS, CCK-8 in culture medium (10 μL of CCK-8 and 100 μL medium for each well) was added. After 1.5 h, the absorbance at 450 nm was measured for each well using the microplate reader.

Pharmacokinetic study

BALB/c mice (female, 6 weeks old) were kept in the designated animal room in the Radioisotope Research Center of Kyoto University. All animal experiments were conducted in accordance with standards approved by the Kyoto University Ethics Committee. CT26 tumor cells were transplanted (1×10^6 cells for each mouse) under the skin of right thigh of BALB/c mice (female, 6 weeks old) one week before the sample injection. To the mice, DND-PG-PBA-SucMe-^{10}B solution in PBS (4.0%, 200 µL for each mouse) was intravenously injected. After 0.5, 3, 6, 14, 24 and 48 h, the mice were sacrificed and the tumor, blood, liver, spleen and kidneys were extracted and put into individual PTFE tubes. ^{10}B concentration in each specimen was measured by neutron-induced prompt gamma-ray analysis (PGA) with the apparatus equipped at Kyoto University Research Reactor (KUR).

In vivo BNCT study

BALB/c mice (female, 6 weeks old) were kept in the KUR animal facility (Kumatori campus, Kyoto University). CT26 tumor cells were transplanted (1×10^6 cells for each mouse) under the skin of right thigh of BALB/c mice one week before the neutron irradiation. To the mice, DND-PG-PBA-SucMe-^{10}B sample solution in PBS (4.0%, 200 µL for each mouse) was intravenously injected at 16 and 48 h before neutron irradiation (five mice in each group). Groups of injection control (with the sample injection and without the irradiation), hot control (with the irradiation and without the sample injection) and cold control (no treatment) were also prepared. At the neutron irradiation, the mice were anesthetized and individually held in custom-made acrylic tube holders with fixing the tumor-baring thigh and leg extended so that only tumor-baring part could be exposed in the neuron flux. The tube holders were fixed on acrylic plate radially (12 mice on one plate) to place the tumor-baring part in the center. Other parts of mice were covered with the shielding plate to prevent from the neutron exposure. The tumors were irradiated with neutrons for 10 min. The fluence of neutron was either 3.99×10^{12} or 3.55×10^{12} neutrons/cm^2 (The mice were divided into two irradiation batches). The irradiated mice were kept in the radiation controlled area for the designated period. The changes in the tumor size and body weight were monitored periodically. For the tumor size, dimensions of two axes of the oval-shaped tumor were measured with a caliper. The tumor volume was calculated as "volume = (major axis × minor axis^2)/2" where major axis was the longer axis and minor was the shorter one.

Appendix II to Chapter 4

S4-1. Loading amount of functional groups

The loading amounts of functional groups in each material was estimated from the results of TGA (Figure 4-5), elemental analysis (CHN(O) and S in Table S4-1) or ^{1}H NMR (Figure 4-7 in the body document) of materials of consecutive batches.

Table S4-1. Results of elemental analysis from DND to DND-PG-NH-PBA of consecutive batches.

(%)	H	C	N	Cl	O	S
DND	1.81	86.90	2.29		4.13	
DND-PG	7.06	55.72	0.57		36.86	
DND-PG-OTs	5.30	55.88	0.32		27.20	10.50
DND-PG-N_3	5.04	53.59	19.40		21.68	
DND-PG-NH_2·HCl	6.69	49.16	6.55	13.49		
DND-PG-PBA	6.14	60.11	5.51			

Elemental analysis for oxygen was not carried out for DND-PG-NH_2·HCl and DND-PG-PBA because small amount of impurity of phosphorus in DND-PG-NH_2·HCl and boron in DND-PG-PBA would disturb the accuracy for oxygen content.

i) Content of functional group from DND-PG to DND-PG-NH_2·HCl

As shown in Table S4-2, content of functional groups are calculated using the results of TGA and elemental analysis. The ratio of PG chain to DND is 4.05, by which PG content in DND-PG is estimated to be 80.2 wt%; 10.83 mmol of glycidol (74.08) was reacted to make 1 g of DND-PG. Although the weight loss of PG by TGA includes hydroxy group from the DND surface (Figure S4-1), we presume that the contribution of such hydroxy group is less than 1 wt% and it can be negligible. As shown in Figure 4-4, as-prepared DND-PG contains free PG which does not connect to DND, and above values includes this impurity. The real PG loading in DND-PG is discussed in the next section.

For the amount of tosyl group in DND-PG-OTs, sulfur content by elemental analysis is 10.50 wt%, all of which are attributed to the tosylate. The content of tosylate is estimated to be 3.28 mmol/g. As for DND-PG-N_3 and DND-PG-NH_2•HCl, the amount of azide or amino groups is estimated by the nitrogen content by elemental analysis after the nitrogen content in DND core is excluded by TGA. The ratio between of azidated PG chain to DND core in DND-PG-N_3 is 2.74, which represents that 1 g of material contains 0.267 g of DND and 0.61 wt% of nitrogen is from DND. The nitrogen content from azide is 18.8 wt% corresponding to 4.45 mmol of azide. By the same manner, the amount of amino group in DND-PG-NH_2•HCl is estimated to be 4.22 mmol/g.

Table S4-2. Content of functional groups based on TGA and elemental analysis.

	DND	DND-PG[b]	DND-PG-OTs	DND-PG-N_3	DND-PG-NH_2•HCl
Content of each component by TGA					
PG[a]/DND ratio		4.05		2.74	2.70
DND content (wt%)	100.0	19.80		26.74	27.03
PG[a] content (wt%)		80.20		73.26	72.97
Elemental analysis (EA) results					
Total nitrogen (wt%)	2.29	0.57	0.32	19.40	6.55
Nitrogen in DND (wt%)	2.29	0.57	0.32	0.61	0.62
Nitrogen in PG[a] (wt%)				18.79	5.93
Sulfur content (wt%)			10.50		
Chloride content (wt%)					13.49
Functional group content					
Functional group		PG	OTs	N_3	NH_2
Amount in mole (mmol/g)		10.83	3.28	4.45	4.22

[a] PG or modified PG chain with –N_3 or –NH_2 moiety.

[b] Including free PG impurity.

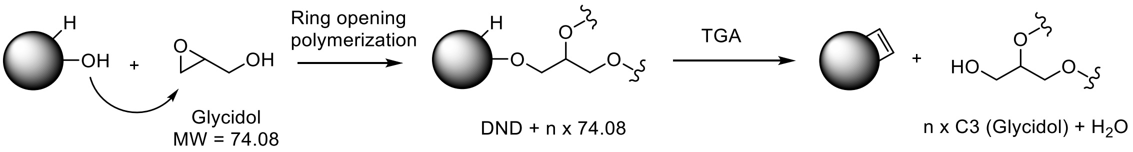

Figure S4-1. Weight loss on TGA.

ii) Estimation of glycerol (C3) unit content and behavior of the free PG in DND-PG

The amount of glycerol (C3) unit is calculated from the amount of modified PG layer of DND-PG-N_3 and DND-PG-NH_2•HCl as shown in Table S4-3. DND-PG-N_3 contains 0.733 g of azidated PG chain in 1 g of material. This PG chain has 4.47 mmol of azide group which corresponds to 0.188 g of –N_3 moiety. The weight of unmodified PG chain of equivalent is calculated by the replacement of azide to hydroxy group to be 0.621 g and PG content in it to be 69.9 wt%. As-prepared DND-PG contains 80.2 wt% of PG and the difference from above estimation attributes to the amount of free PG in DND-PG (0.369 g in 1 g of material) which was removed up to the azidation. PG content in DND-PG-NH_2•HCl is consistent with this estimation.

Table S4-3. Glycerol (C3) unit content estimation.

	DND-PG	DND-PG-N_3	DND-PG-NH_2•HCl
PG (glycerol unit) content in each material			
DND content (g/g)	0.198	0.267	0.270
PG content in each material (g/g)	0.802	0.733	0.730
Functional group content (mmol/g)	10.83 (PG)	4.45 (N_3)	4.22 (NH_2)
Formula weight (g/mol)	74.1	42.0	16.0
Amount of functional group (g/g)	0.802	0.187	0.068
Equivalent OH group[a] (g/g)		0.076	0.072
HCl content from EA (g/g)			0.135
PG of equivalent (g/g)[b]		0.621	0.591

	DND-PG	DND-PG-N$_3$	DND-PG-NH$_2$·HCl
Content of “PG of equivalent” in 1 g of purified DND-PG			
DND + PG of equivalent (mg)		0.889	0.861
PG of equivalent content (wt%)		69.91	68.61
Content in mole (mmol/g)		9.44	9.26
Impurity in as-prepared DND-PG			
Content of purified DND-PG (mg/g)	0.631[c]		
Free PG as impurity (mg)	0.369		

[a] The amount of OH group of equivalent moles of functional group.

[b] PG of equivalent = (PG content) – (Amount of functional group) – (HCl content) + (Equivalent OH group).

[c] Contains 0.433 mg of PG (68.61%) + 0.198 mg of DND.

iii) DND-PG-PBA

The loading amount of PBA moiety is calculated by the nitrogen content change from DND-PG-NH$_2$ as no nitrogen is added or removed upon the PBA introduction. The content of carbon from PBA moiety is estimated to be 18.81% where the carbon from DND-PG is 41.30% (Table S4-4). The PBA (consists of 7 carbons) content is 2.24 mmol/g corresponding to 0.300 g of PBA moiety ($–CH_2–C_6H_4–B(OH)_2$ = 133.94) in 1 g of material.

Table S4-4. Amount of PBA based on the change of nitrogen content.

	DND-PG-NH$_2$·HCl	DND-PG-PBA
Carbon content by EA (wt%)	49.10	60.11
Nitrogen content by EA (wt%)	6.55	5.51
Carbon from DND-PG-NH$_2$·HCl (wt%)	49.10	41.30[a]
Carbon from PBA moiety (wt%)		18.81
Amount of PBA (mmol/g)		2.24
Amount of PBA (g/g)		0.300
Amino group content (mmol/g)	4.22	3.55
Unreacted amino group (mmol/g)		1.31

[a] Calculated by (C in DND-PG-NH$_2$·HCl)/(N in DND-PG-NH$_2$·HCl) × (N in DND-PG-PBA).

iv) DND-PG-PBA-Suc and DND-PG-PBA-SucMe

The loading amount of succinyl and methyl groups are estimated by the integral values in ^{1}H NMR spectra on a premise that all of PBA, succinyl and methyl moieties attached on DND-PBA can be observed in ^{1}H NMR (Table S4-5). On 1 g of DND-PG-PBA which has 2.24 mmol of PBA moiety, 1.36 mmol of succinic anhydride ($C_4H_4O_3$ = 100.07) was reacted, which corresponds 1.20 mmol/g in the succinylated material. By the same manner, in DND-PG-PBA-SucMe, the loading amounts of methyl and succinyl groups are 1.20 mmol and 1.17 mmol in 1 g of material, respectively.

Table S4-5. Amount of succinyl and methyl groups by ^{1}H NMR.

	DND-PG-PBA	DND-PG-PBA-Suc	DND-PG-PBA-SucMe
Integral values			
PBA (Aromatic, 4H)	1.00	1.00	1.00
Succinyl (4H)		0.61	0.61
Methyl (3H)			0.47
Amount based on 1 g of DND-PG-PBA			
Amount of PBA (mmol/g)	2.24	2.24	2.24
Succinyl (mmol/g)		1.36	1.36
Methyl (mmol/g)			1.40
Amount of functional groups in each material[a]			
PBA moiety (g/g)	0.300	0.300	0.300
Succinyl (g/g)		0.137	0.137
Methyl (g/g)			0.034
DND-PG-NH_2 (g/g)	0.700	0.700	0.700
Total weight (g)	1.000	1.137	1.171
Amount of functional groups in mole			
PBA (mmol/g)	2.24	1.97	1.91
Succinyl (mmol/g)		1.20	1.17
Methyl (mmol/g)			1.20

[a] Difference in weight between the functionalized amino group and free amino group (PBA: 133.94 g/mol, Succinyl: 100.07 g/mol, Methyl: 24.21 g/mol).

S4-2. Preparation of 2-formylphenylboronic acid-^{10}B

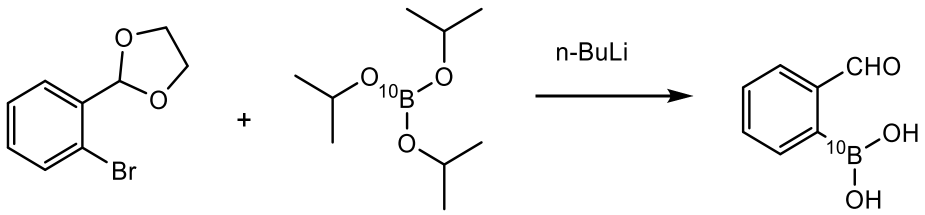

Scheme S4-1. Synthetic scheme of ^{10}B enriched PBA.

Triisopropyl borate-^{10}B

Boric acid-^{10}B (1.0 g, 16.4 mmol) was added in the mixture of 2-propanol (10 mL) and cyclohexane (30 mL), stirred for 30 min and refluxed in 10 min. Dean-Stark apparatus (cyclohexane was in advance filled in the receiver) was attached and refluxed for 6 h until the vapor temperature reached 80 °C with removing water and 2-propanol by azeotropic distillation. Residual solvent was removed and the residue (3.46 g) was used without further purification for the following borylation reaction.

2-Formylphenylboronic acid-^{10}B

2-(2-Bromophenyl)-1,3-dioxolane (1.30 g, 5.7 mmol) was dissolved in anhydrous diethyl ether (10 mL) under the nitrogen atmosphere and cooled to −78 °C in dry-ice acetone bath. *n*-Hexane solution of *n*-butyllithium (1.6 M, 3.9 mL, 6.24 mmol) was added slowly and stirred at −78 °C for 1 h. To the slurry of lithium salt at −78 °C, aforementioned crude triisopropyl borate-^{10}B (1.69 g, from 8.2 mmol of boric acid-^{10}B) was added and stirred for 3 h at < -60 °C, then allowed to stir at room temperature overnight. Water (20 mL), methyl t-butyl ether (MTBE, 20 mL) and 2.5 M (10%) NaOH (5.0 mL) were added and phases were separated. The aqueous phase was washed with MTBE twice, and then acidified with 6 M HCl (5.0 mL). Precipitated material was extracted with MTBE three times and the combined organic phase was dried over anhydrous MgSO$_4$. After MgSO$_4$ was filtered off, the filtrate was evaporated. The crude product was recrystallized from MTBE and *n*-Hexane to obtain off-white crystalline powder. Yield: 0.50 g (59%). FT-IR (DRIFT with KBr, cm^{-1}): 3346, 3072, 1670, 1490, 1463, 1427, 1384 (^{10}B–O), 1195, 858, 765, 748, 648. ^{1}H NMR (methanol-d$_4$): 6.00, 7.42, 7.47, 7.59, 7.67, 7.92, 9.96 (mixture of 2 tautomers). ESI-MS (negative, m/z): Anal. 148.08818 (M−H^{-}); Calc. for $C_7H_6{}^{10}BO_3$ 148.0441.

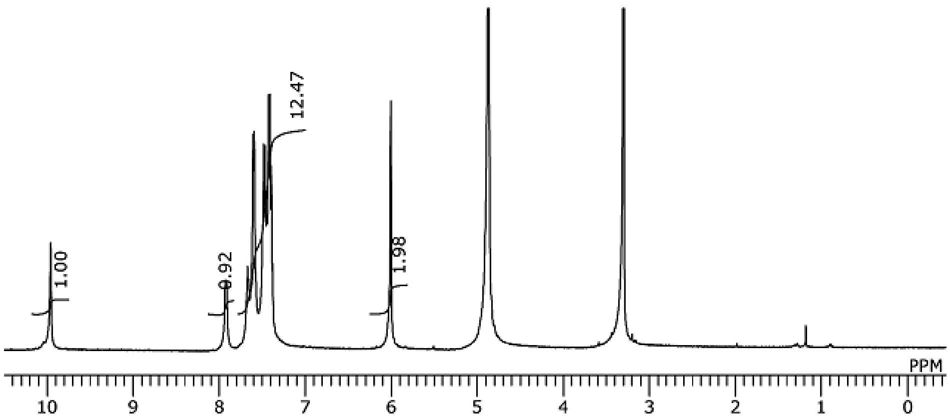

Figure S4-2. ^{1}H NMR spectrum of 2-formylphenylboronic acid-^{10}B.

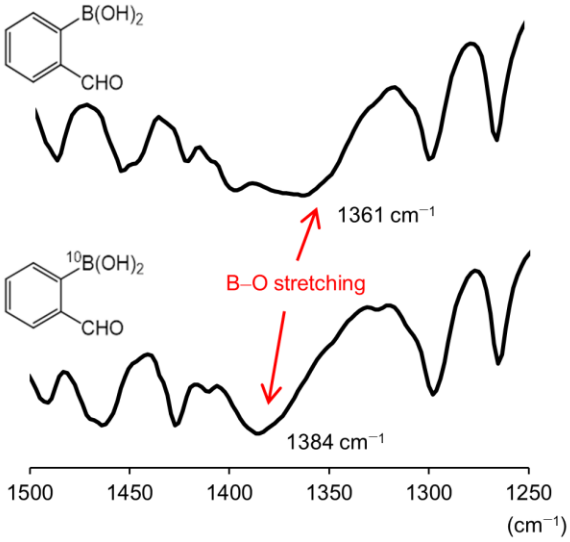

Figure S4-3. FT-IR spectra (the region of B–O stretching) of 2-formyl-PBA.

S4-3. Supporting data in BNCT experiments

(a) Hot control

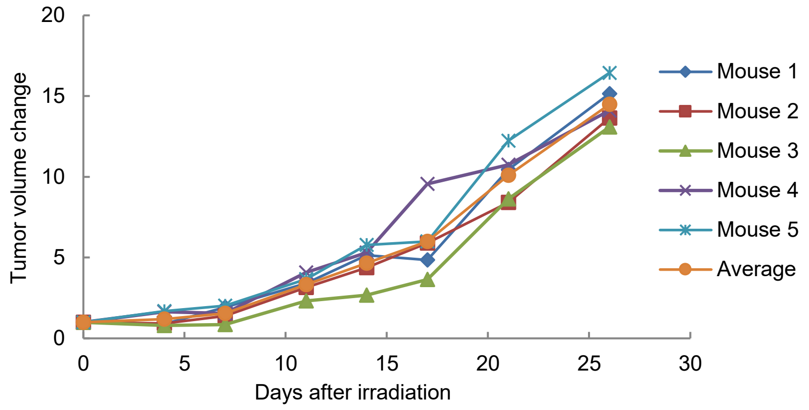

(b) BNCT 16 h

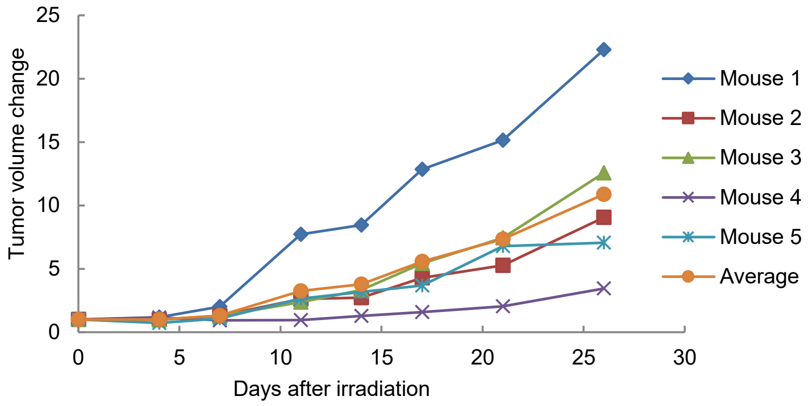

(c) BNCT 48 h

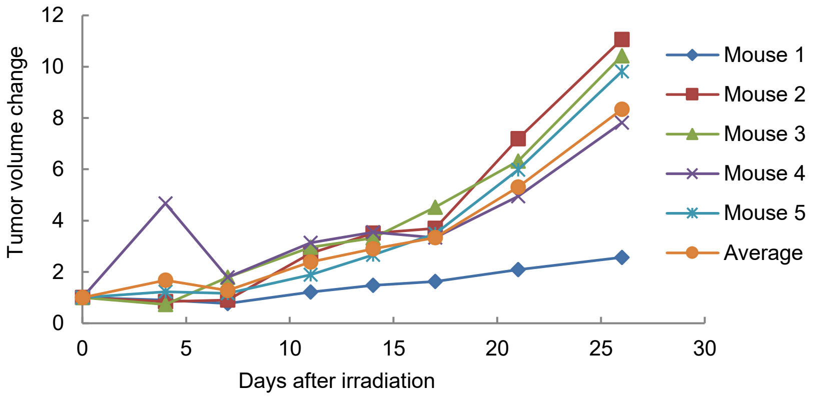

Figure S4-4. Tumor growth of individual mouse of Hot control, BNCT 16 h and BNCT 48 h after neutron irradiation.

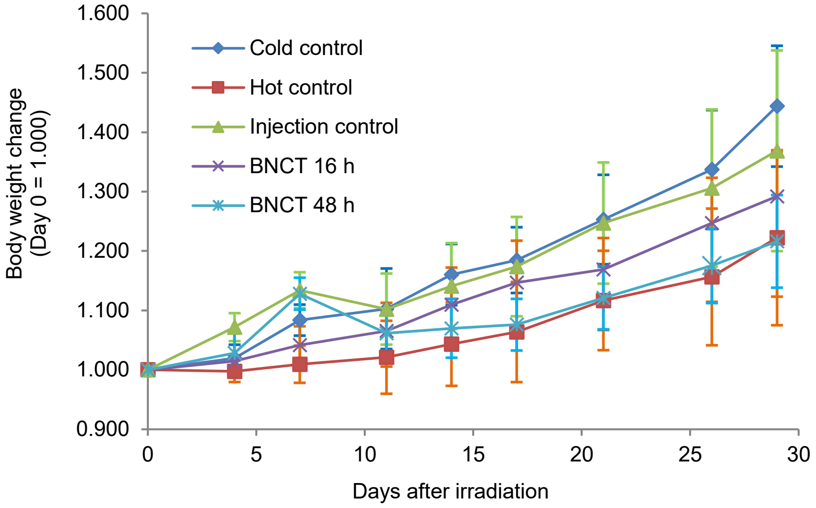

Figure S4-5. Average body weight change of each group.

S4-4. The BNCT study with smaller number of mice

CT26 tumor cells were transplanted (1 × 10^6 cells for each mouse) under the skin of right thigh of BALB/c mice (female, 6 weeks old) one week before the neutron irradiation. To the mice, DND-PG-PBA-SucMe-^{10}B sample solution in PBS (3.5%, 200 μL for each mouse) was intravenously injected at the predetermined time points (3 mice for one group, 24 and 44 h before the irradiation). Groups of injection control (with the sample injection and without the irradiation), hot control (with the irradiation and without the sample injection) and cold control (no treatment) were also prepared. At the irradiation, the mice were anesthetized and individually held in custom-made acrylic tube holders with fixing the tumor-baring thigh and leg extended so that only tumor-baring part could be exposed in the neuron flux. The tube holders were fixed on acrylic plate radially (12 mice on one plate) to place the tumor-baring part in the center. Other parts of mice were covered with the shielding plate to prevent from the neutron exposure. The fluence of thermal neutron was either 3.82 × 10^{12} or 3.78 × 10^{12} neutrons/cm^2 (The mice were divided into two irradiation batches) The irradiated mice were kept in the radiation controlled area for the designated period. The changes in the tumor size and body weight were monitored periodically.

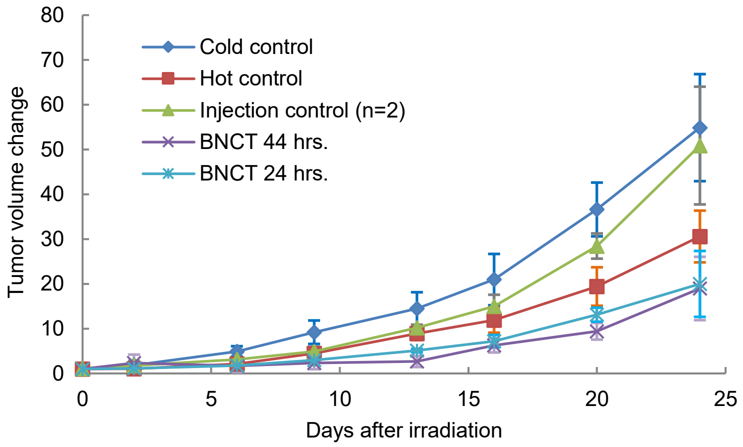

Figure S4-6. Result of the preliminary BNCT evaluation. All groups consisted of 3 mice except for injection control, for which outlying tumor growth value of one mouse was rejected.

Chapter 5: Rational design, multistep synthesis and *in vitro* evaluation of poly(glycerol) functionalized nanodiamond conjugated with boron-10 cluster and active targeting moiety for boron neutron capture therapy

5-1. Introduction

A lot of works for BNCT drugs with small compounds, macromolecules or nanomaterials have been reported [49, 88–106, 113], including poly(glycerol) (PG) functionalized detonation nanodiamonds (DNDs), namely DND-PG, conjugated with ^{10}B-containing moiety as described in Chapter 4 [113]. In that work, although the resulting DND-PG-PBA suppressed tumor growth *in vivo* upon neutron irradiation, the efficacy was not enough to treat cancer probably due to insufficient ^{10}B content in tumor.

To improve the BNCT efficacy, we designed new DND-PG based nanodrugs conjugated with ^{10}B-enriched sodium borocaptate, or mercaptoundecahydro-*closo*-dodecaborate (^{10}BSH, $^{10}B_{12}H_{11}SH{\cdot}2Na$) as a boron-10 source and PBA or RGD peptide as a cancer targeting moiety. ^{10}BSH, which has been used in BNCT clinical studies [147, 148], should increase the boron-10 density due to its icosahedral boron cluster ($^{10}B_{12}H_{11}{}^{2-}$) containing 12 boron-10 atoms. Whereas the DND-PG moiety is expected to exhibit passive targeting known as EPR effect, we try to increase the targeting efficiency to connect an active targeting moiety; PBA and RGD peptide are known to recognize sialic acid containing sugar chains and $\alpha_v\beta_3$ integrin, respectively, in the tumor cell membrane to facilitate cellular uptake. To introduce these functionalities, some of the primary alcohols in DND-PG were oxidized to carboxy groups to give DND-PG-COOH as described in Chapter 3 [149], where $^{10}B_{12}H_{11}{}^{2-}$ and PBA or RGD moieties were incorporated at the hydroxy and carboxy groups, respectively. The *in vitro* thermal neutron irradiation resulted in high BNCT efficacies with small differences with and without active targeting moiety. These results will be discussed based on the TEM observation.

5-2. Results and discussion

5-2-1. Synthesis and characterization of BNCT nanodrugs from DND-PG

DND-PG was prepared from aqueous dispersion of single-digit nanometer sized DND with positive ζ-potential (DND(+)) in glycidol as previously reported [129], and was fully characterized by FT-IR, ^{1}H NMR, elemental analysis and thermogravimetric analysis (TGA) (S5-1 in Appendix III). As shown in Scheme 5-1a, DND-PG (PG/DND weight ratio: 3.83) was oxidized with 4-AcNH-TEMPO according to our recent paper to give DND-PG-COOH having 1.01 mmol/g of –COOH (see S5-1 in Appendix III for the experimental detail and Table S5-1 in Appendix III for characterization data). Some of the OH groups were tosylated under Schotten-Baumann conditions; aqueous dispersion of DND-PG-COOH with NaOH was added to tetrahydrofuran (THF) solution of *p*-toluenesulfonyl chloride (TsCl) with vigorous stirring. Typical reaction conditions, TsCl in pyridine, were not applied, because the raw material was hardly dispersed in pyridine. The loading amount of –OTs was controlled by tuning the amount of TsCl; 1.22 and 0.96 mmol/g of –OTs were obtained by using 7.5 and 5.0 mmol/g of TsCl to the raw material, respectively, which were calculated based on the elemental analysis results (Table S5-2, and calculation details in S5-2-1(ii) in Appendix III). On the other hand, 35.4% of PG chain was found to be lost. Although the tosylation was conducted in ice bath, Schotten-Baumann conditions may cleave the ether linkage via E2-elimination of –OTs as illustrated in Figure 5-1 [150]. The PG loss of 25% was also observed in the tosylation for DND-PG without carboxy groups (Table S5-3 in Appendix III), supporting the reaction mechanism through E2-elimination under highly basic conditions (Figure 5-1). The COOH content was accordingly decreased from 1.01 mmol/g to 0.907 mmol/g on DND-PG-COOH, assuming that the proportion of glyceric acid unit was not changed.

The tosyl groups (–OTs) in DND-PG(OTs)-COOH were substituted with azide groups (–N_3) by sodium azide (NaN_3) in *N,N*-dimethylformamide (DMF) with small amount of water to obtain DND-PG(N_3)-COOH. Completion of the substitution reaction was confirmed by appearance of the peak for –N_3 at 2102 cm^{-1} and disappearance of –OTs at 1176 and 1359 cm^{-1} in FT-IR (Figure 5-2a and b). The –N_3 content in the product, DND-PG(N_3)-COOH, is calculated to be 1.12 mmol/g, indicating that 72.5% of –OTs in DND-PG(OTs)-COOH was converted into –N_3 (Table S5-4 and S5-2-2 in Appendix III).

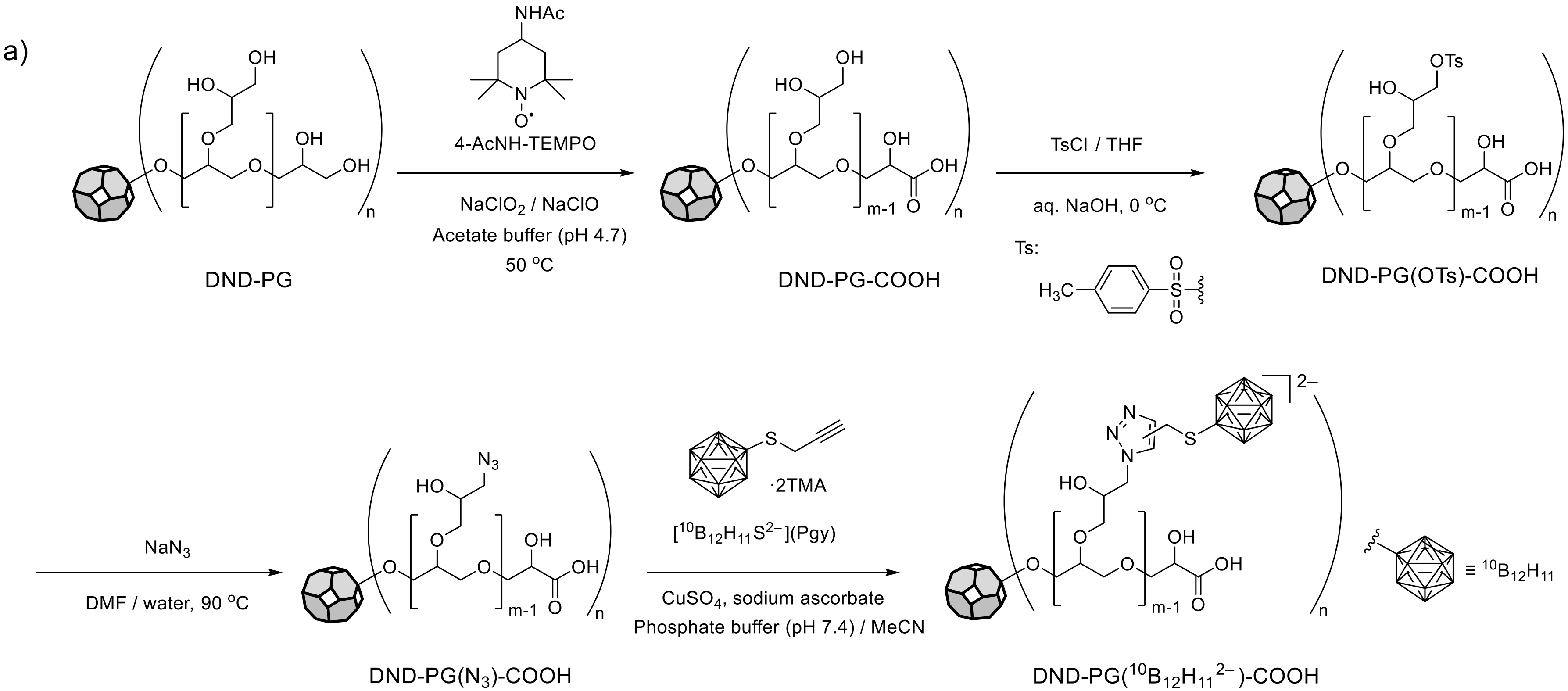
a)
DND-PG
4-AcNH-TEMPO
NaClO2 / NaClO
Acetate buffer (pH 4.7)
50 °C
DND-PG-COOH
TsCl / THF
aq. NaOH, 0 °C
Ts:
DND-PG(OTs)-COOH
NaN3
DMF / water, 90 °C
DND-PG(N3)-COOH
·2TMA
[10B12H11S2−](Pgy)
CuSO4, sodium ascorbate
Phosphate buffer (pH 7.4) / MeCN
DND-PG(10B12H11 2−)-COOH
≡ 10B12H11

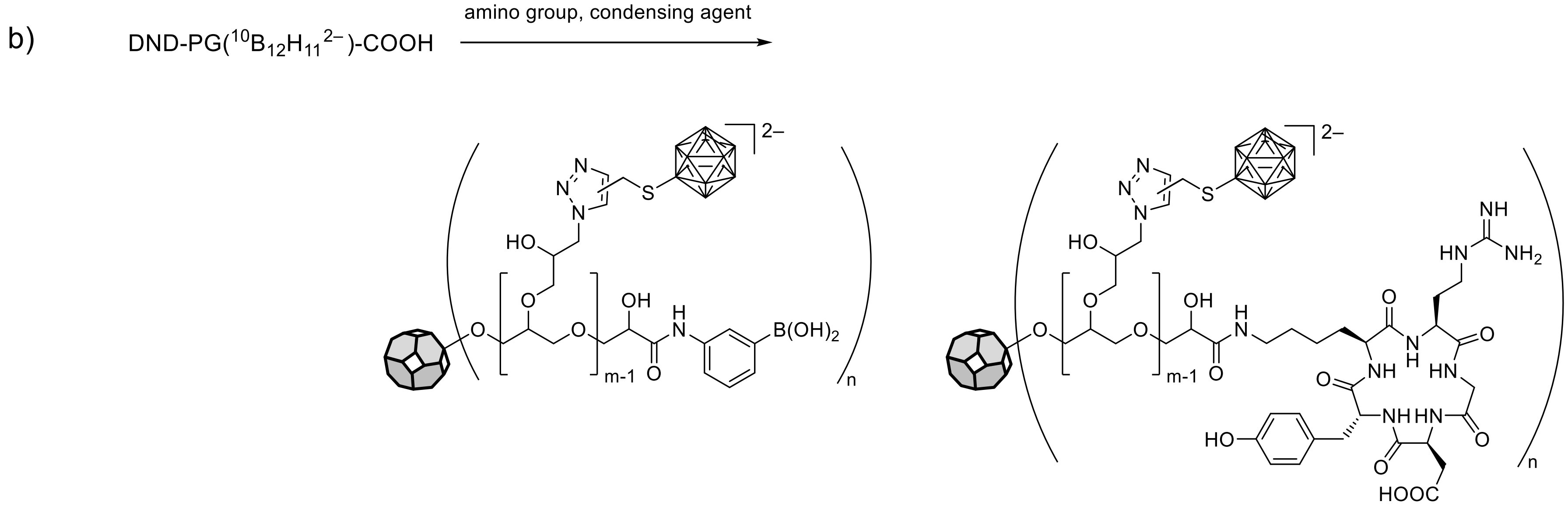

DND-PG($^{10}B_{12}H_{11}^{2-}$)-PBA

DND-PG($^{10}B_{12}H_{11}^{2-}$)-c(RGDyK)

Scheme 5-1. Synthetic routes of BNCT nanodrugs starting from DND-PG. Introduction of a) $^{10}B_{12}H_{11}^{2-}$ moiety via Hüisgen alkyne-azide cycloaddition (click reaction) at OH group and b) active targeting moieties through amide linkage at COOH group.

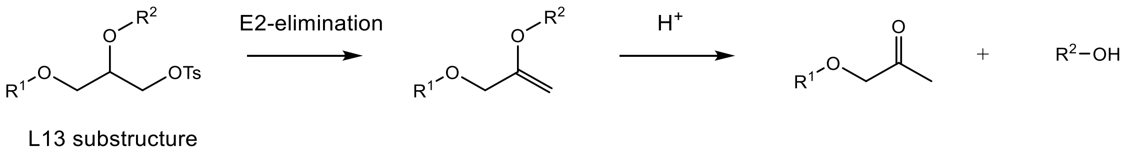

Figure 5-1. Loss of PG chain via E2-elimination of –OTs in the Schotten-Baumann reaction.

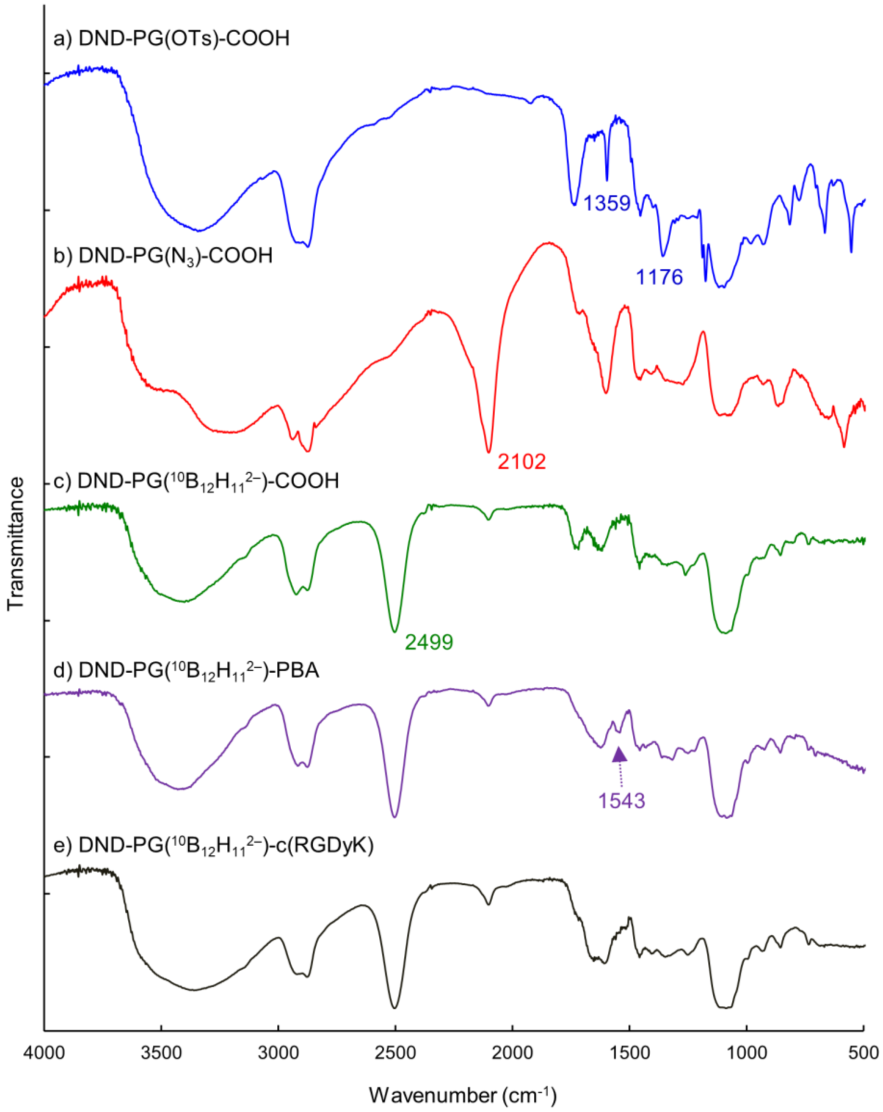

Figure 5-2. FT-IR spectra of BNCT nanodrugs and intermediates. a) DND-PG(OTs)-COOH, b) DND-PG(N_3)-COOH, c) DND-PG($^{10}B_{12}H_{11}^{2-}$)-COOH, d) DND-PG($^{10}B_{12}H_{11}^{2-}$)-PBA, and e) DND-PG($^{10}B_{12}H_{11}^{2-}$)-c(RGDyK).

The $^{10}B_{12}H_{11}^{2-}$ moiety was introduced via Hüisgen alkyne-azide cycloaddition (click reaction) [95–98, 62, 151, 152]. *S*-Propargylated boron cluster, $[(^{10}B_{12}H_{11}^{2-})S](Pgy)$ was prepared from commercially available ^{10}BSH·2Na via *S*-(2-cyanoethyl) and *S,S*-(2-cyanoethyl)-(2-propynyl)sulfonio derivatives as previously reported (Scheme S5-1 and experimental details in S5-3 in Appendix III) [96–98]. Click reaction between DND-PG(N_3)-COOH and $[(^{10}B_{12}H_{11}^{2-})S](Pgy)$ was conducted in the presence of $CuSO_4$ and sodium ascorbate in the mixture of phosphate buffer and acetonitrile (MeCN) in an inert atmosphere. The reaction was monitored by the characteristic peak at 2499 cm^{-1} for B–H stretching vibration of boron cluster in FT-IR as shown in Figure 5-2c. Small amount of $-N_3$ remained, even though the reaction time was prolonged, probably due to the steric hindrance of icosahedral boron cluster. The resulting DND-PG($^{10}B_{12}H_{11}^{2-}$)-COOH was characterized by ^{1}H, ^{13}C and ^{10}B NMR. In ^{1}H NMR (Figure 5-3a), a broad signal around 1.5 ppm and small signals at 8.04 and 8.16 ppm are assigned to hydrogens in boron cluster and 4- or 5-position of 1,2,3-triazole ring, respectively. 1,2,3-Triazole ring is confirmed also by ^{13}C NMR (Figure 5-3b); the four signals at 125, 137, 143 and 150 ppm are attributable to the carbons in the two isomers of 1,4- and 1,5-disubstituted triazole rings [153]. ^{10}B NMR gives the signal around –16 ppm corresponding to the boron cluster in DND-PG($^{10}B_{12}H_{11}^{2-}$)-COOH (Figure 5-3c) as well as $[(^{10}B_{12}H_{11}^{2-})S](Pgy)$ (Figure S5-1b in Appendix III) [154]. The ^{10}B content in DND-PG($^{10}B_{12}H_{11}^{2-}$)-COOH was determined to be 7.97% by ICP-AES corresponding to 0.664 mmol/g as $^{10}B_{12}H_{11}^{2-}$ moiety (Table 5-1) which is consistent with the estimation from elemental analysis as shown in Table S5-5 and S5-2-3 in Appendix III. This indicates that 70.8% of $-N_3$ in DND-PG(N_3)-COOH underwent the cycloaddition reaction to bind $^{10}B_{12}H_{11}^{2-}$ moiety covalently.

As active targeting moieties, we chose two kinds of molecules, PBA and RGD peptide (Scheme 5-1b). PBA is reported to interact with *N*-acetylneuraminic acid (sialic acid) containing sugar chains overexpressed on the surface of cancer cells [102, 155]. On the other hand, RGD peptide having Arg-Gly-Asp sequence is known to be an antagonist to integrin $\alpha_v\beta_3$ on cancer cells [47, 93, 156]. DND-PG($^{10}B_{12}H_{11}{}^{2-}$)-COOH was conjugated with 3-aminophenylboronic acid of natural abundance boron through an amide linkage using a condensing agent 1-(3-dimethylaminopropyl)-3-ethylcarbodiimide hydrochloride (EDC) to give DND-PG($^{10}B_{12}H_{11}{}^{2-}$)-PBA. The DND-PG($^{10}B_{12}H_{11}{}^{2-}$)-COOH with the COOH content of 0.74 mmol/g was reacted with about 0.56 mmol/g (0.76 eq. to –COOH) of 3-aminophenylboronic acid. This resulted in the PBA of 0.40 mmol/g in DND-PG($^{10}B_{12}H_{11}{}^{2-}$)-PBA, or 0.42 mmol/g of DND-PG($^{10}B_{12}H_{11}{}^{2-}$)-COOH (Table 5-1, Table S5-6 and S5-2-4 in Appendix III), which corresponds to 75% yield based on 3-aminophenylboronic acid. The ^{10}B content was estimated to be 7.59%. For characterization of DND-PG($^{10}B_{12}H_{11}{}^{2-}$)-PBA, broad signals between 7 – 8 ppm are assigned to aromatic protons in PBA moiety in ^1H NMR (Figure 5-4a), and the amide linkage was confirmed by stretching vibration of carbonyl group at 1543 cm^{-1} in FT-IR (Figure 5-2d).

The RGD peptide was conjugated with DND-PG($^{10}B_{12}H_{11}{}^{2-}$)-COOH through amide linkage at ε-amino group of lysine in a cyclic pentapeptide, cyclo(L-Arg-Gly-L-Asp-D-Tyr-L-Lys) (c(RGDyK)), with EDC and *N*-hydroxysccinimide (HOSu). Introduction of c(RGDyK) was confirmed by ^1H NMR with a pair of small doublet signals of aromatic ring in Tyr at 6.56 and 6.95 ppm (Figure 5-4b). From the integration value, the loading amount is estimated to be 0.014 mmol/g (Table S5-7 and S5-2-5 in Appendix III) that is very small as compared with the amount of c(RGDyK)•2TFA (0.46 mmol/g, or 0.62 eq. to –COOH) used for the reaction. As summarized in Table 5-1, assuming the diameter of DND core to be 5.12 nm, it can be calculated that 8.4 molecules of c(RGDyK) in average are attached in a particle of DND-PG($^{10}B_{12}H_{11}{}^{2-}$)-c(RGDyK) while ca. 5×10^3 of glycerol and glyceric acid units are contained [129]. The nanomaterials (nanodrugs) without $^{10}B_{12}H_{11}{}^{2-}$ moiety, DND-PG-PBA and DND-PG-c(RGDyK), were also prepared by the same procedures shown in Scheme 5-1b from DND-PG-COOH (data not shown).

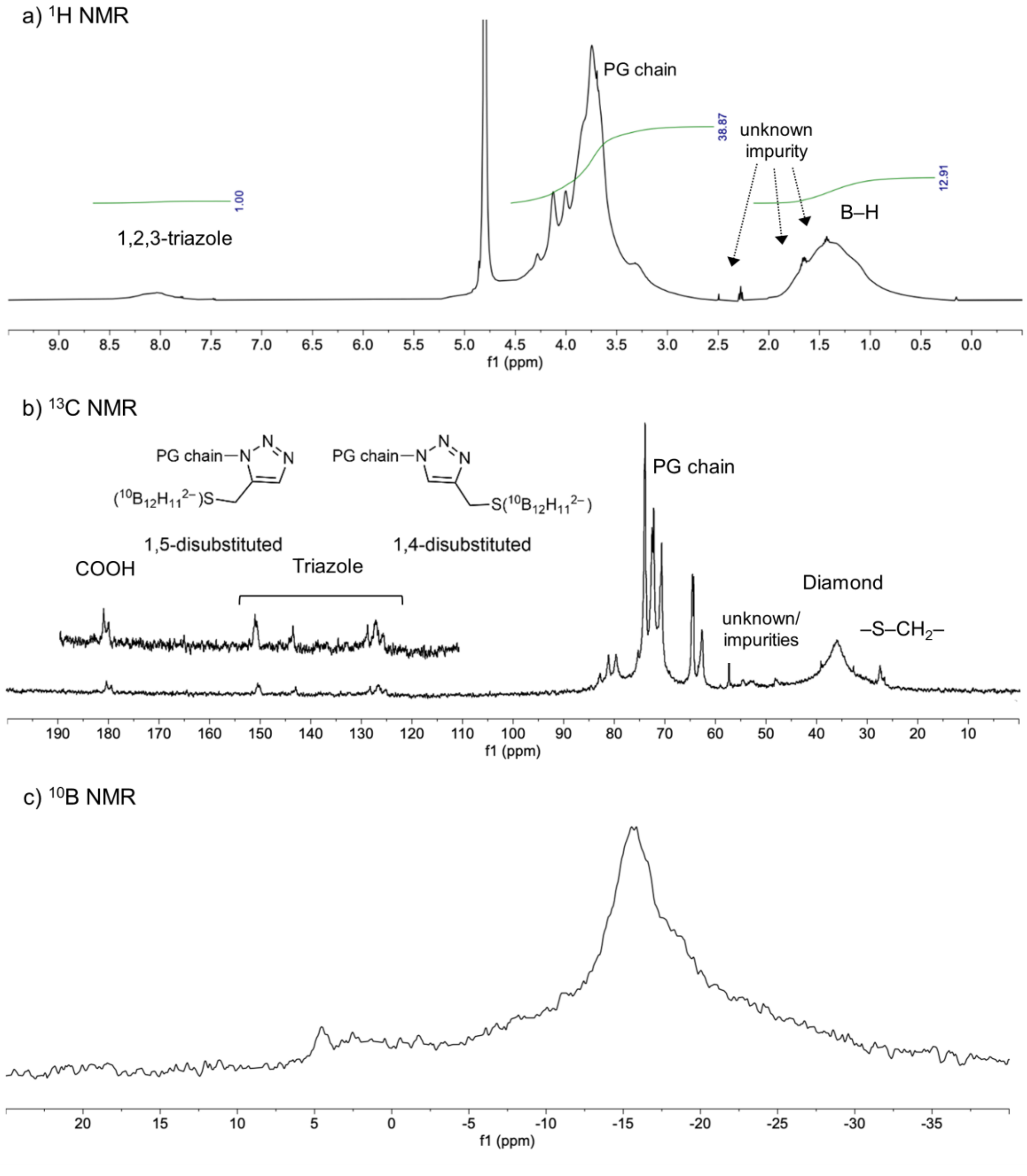

Figure 5-3. a) ^{1}H NMR, b) ^{13}C NMR by complete decoupling and c) ^{10}B NMR spectra of DND-PG($^{10}B_{12}H_{11}^{2-}$)-COOH in D_2O. The references are set at a) 4.80 ppm (the signal of HOD), b) 36.3 ppm (that of diamond core) and c) 19.49 ppm (that of $^{10}B(OH)_3$ as an external standard).

Table 5-1. Contents of $^{10}B_{12}H_{11}^{2-}$ and active targeting moieties in nanodrugs.

	$^{10}B_{12}H_{11}^{2-}$ moiety			Active targeting moiety	
	Content (mmol/g)	^{10}B content (%)	Numbers in one particle [a]	Content (mmol/g)	Numbers in one particle [a]
DND-PG($^{10}B_{12}H_{11}^{2-}$)-COOH	0.664	7.97	411	0.74 [b]	455
DND-PG($^{10}B_{12}H_{11}^{2-}$)-PBA	0.633	7.59	391	0.40	259
DND-PG($^{10}B_{12}H_{11}^{2-}$)-c(RGDyK)	0.664	7.97	410	0.0136	8.36

[a] Assuming that PG/DND ratio is 2.49 (see Supporting Information S2-1(ii)) and the diameter of DND core is 5.12 nm.

[b] Content of COOH group.

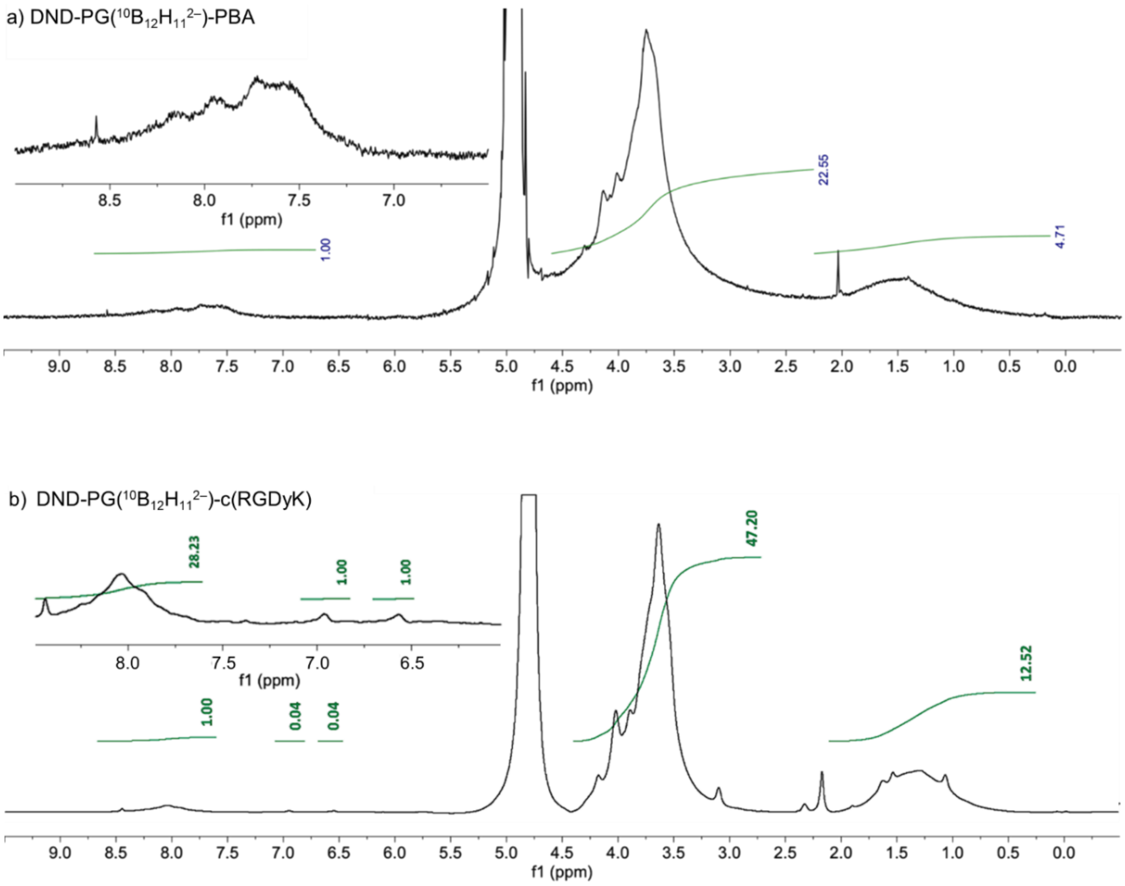

Figure 5-4. ^{1}H NMR spectra of a) DND-PG($^{10}B_{12}H_{11}^{2-}$)-PBA and b) DND-PG($^{10}B_{12}H_{11}^{2-}$)-c(RGDyK) in D_2O. The signal of HOD at 4.80 ppm is set as a reference.

5-2-2. *In vitro* evaluation of BNCT nanodrugs by cell viability assay

Cell viability assay was conducted with the following nanodrugs; DND-PG-COOH, -PBA and -c(RGDyK) with and without $^{10}B_{12}H_{11}^{2-}$ moiety as shown in Figure 5-5. In this work, we chose B16 murine melanoma cells, because they are reported to interact with PBA and RGD peptide [102, 156], and melanoma is one kind of tumors to which BNCT has been applied in clinical trials [157].

The cells were incubated in nanodrug-containing culture medium supplemented with and without fetal bovine serum (FBS) for 1 d (FBS(+) and FBS(–), respectively). The nanodrug concentrations were 125, 250 and 500 μg/mL for FBS(+), and 63, 125 and 250 μg/mL for FBS(–). Sample concentrations in FBS(–) was lowered by half of that in FBS(+) since the toxicity in FBS(–) was estimated to be higher than that in FBS(+) [158].

In the presence of FBS (Figure 5-5a), the nanodrugs with $^{10}B_{12}H_{11}^{2-}$ moiety exhibited toxicity depending on the concentration (500 > 250 > 125 μg/mL) and functionality (c(RGDyK) > PBA ≈ COOH), while the samples without $^{10}B_{12}H_{11}^{2-}$ moiety showed little or no toxicity. The nanodrugs are more toxic under FBS(–) conditions than FBS(+) ones as shown in Figure 5-5b; in particular, the difference is more significant in the cases of DND-PG-c(RGDyK), DND-PG($^{10}B_{12}H_{11}^{2-}$)-PBA and DND-PG($^{10}B_{12}H_{11}^{2-}$)-c(RGDyK) (Figure 5-5c). These results will be discussed below based on TEM analysis (Figure 5-8).

a)

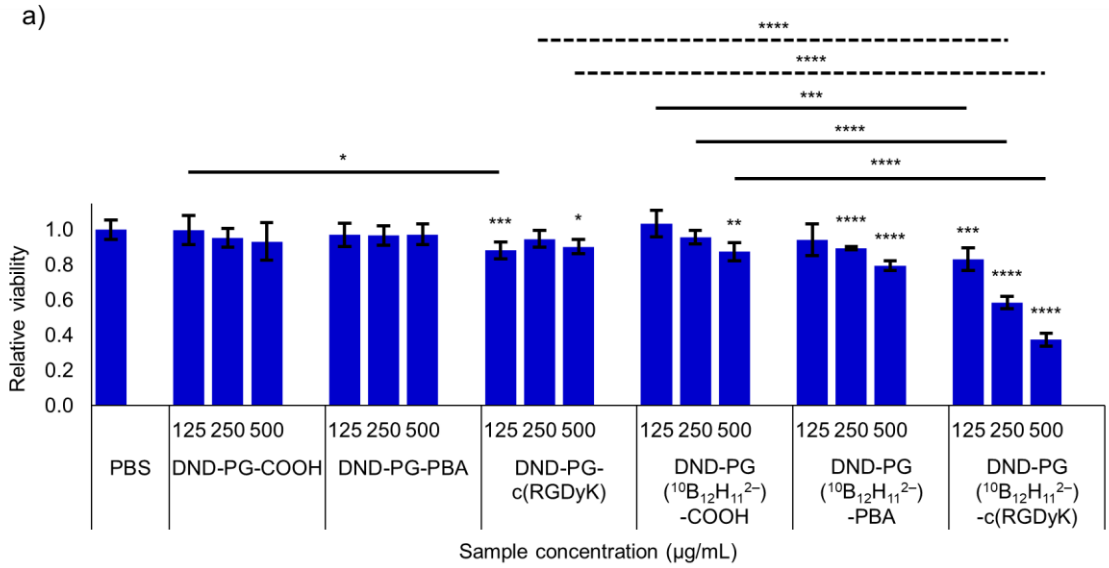

Relative viability
1.0
0.8
0.6
0.4
0.2
0.0
125 250 500
PBS
DND-PG-COOH
DND-PG-PBA
DND-PG-c(RGDyK)
DND-PG ($^{10}B_{12}H_{11}^{2-}$) -COOH
DND-PG ($^{10}B_{12}H_{11}^{2-}$) -PBA
DND-PG ($^{10}B_{12}H_{11}^{2-}$) -c(RGDyK)
Sample concentration (µg/mL)
*
**
***
****

b)

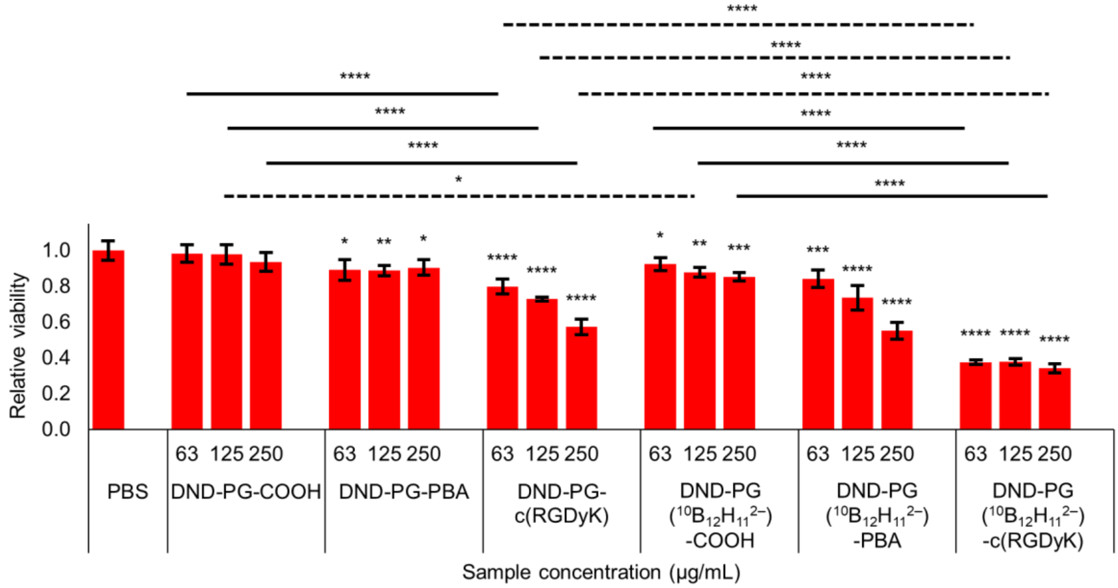

Relative viability
1.0
0.8
0.6
0.4
0.2
0.0
63 125 250
PBS
DND-PG-COOH
DND-PG-PBA
DND-PG-c(RGDyK)
DND-PG ($^{10}B_{12}H_{11}^{2-}$) -COOH
DND-PG ($^{10}B_{12}H_{11}^{2-}$) -PBA
DND-PG ($^{10}B_{12}H_{11}^{2-}$) -c(RGDyK)
Sample concentration (µg/mL)
*
**
***
****

c)

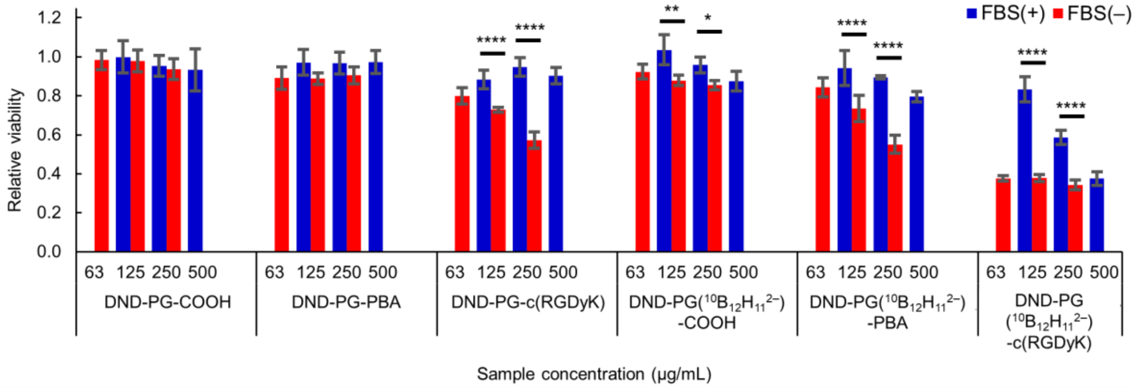

FBS(+)
FBS(–)
Relative viability
1.2
1.0
0.8
0.6
0.4
0.2
0.0
63 125 250 500
DND-PG-COOH
DND-PG-PBA
DND-PG-c(RGDyK)
DND-PG($^{10}B_{12}H_{11}^{2-}$) -COOH
DND-PG($^{10}B_{12}H_{11}^{2-}$) -PBA
DND-PG ($^{10}B_{12}H_{11}^{2-}$) -c(RGDyK)
Sample concentration (µg/mL)
*
**
****

Figure 5-5. a), b)**:** Cell viability of B16 murine melanoma cells with and without FBS (FBS(+) in a) and FBS(–) in b), respectively) at various nanodrug concentrations, and c): comparison of cell viability at the same sample concentrations between FBS(+) and (–).

Asterisks on each bar indicate the significancy to control (PBS) in a) and b). Lines with asterisks on each panel in a) and b) indicate the significancy between with and without c(RGDyK) moiety (solid lines) or ${}^{10}B_{12}H_{11}{}^{2-}$ moiety (dashed lines), and in c), the bars with asterisks indicate the significancy between FBS(+) and (–) at the same concentration ($n = 6$, Student's t-test in comparison with PBS, and 2-way ANOVA and Tukey's HSD test for comparison between nanodrugs: *$p < 0.05$, **$p < 0.01$, ***$p < 0.001$, ***$p < 0.0001$).

5-2-3. *In vitro* evaluation of BNCT nanodrugs by colony forming assay

BNCT efficacies of nanodrugs were examined on thermal neutron irradiation. After the treatment with nanodrug, detached cells were irradiated with thermal neutron. On the neutron irradiation at $1.19 \times 10^{12} - 3.47 \times 10^{12}$ neutrons/cm^2, no or only a few colonies were found at 500 μg/mL for DND-PG($^{10}B_{12}H_{11}^{2-}$)-COOH and -PBA, and 125 μg/mL for DND-PG($^{10}B_{12}H_{11}^{2-}$)-c(RGDyK) under FBS(+) conditions (Figure 5-6a and Table 5-2a), corresponding to 39.9, 38.0 and 9.9 μg/mL in ^{10}B concentrations, respectively, while the nanomaterials without $^{10}B_{12}H_{11}^{2-}$ moiety exhibited no BNCT efficacy. Therefore, the corresponding concentrations and fluences were reduced to 200 and 100 μg/mL (ca. 16 and 8 μg/mL of ^{10}B, respectively) and $4.09 \times 10^{11} - 1.17 \times 10^{12}$ neutrons/cm^2.

High BNCT efficacies along with the concentration and fluence relationship were observed as shown in Figure 5-6b and Table 5-2b. Similar BNCT efficacies were observed in the three nanodrugs with $^{10}B_{12}H_{11}^{2-}$ moiety. The significant difference ($p = 0.014$) is found only in the slopes between DND-PG($^{10}B_{12}H_{11}^{2-}$)-PBA and -c(RGDyK) at 200 μg/mL (blue and green dashed lines, respectively, in Figure 5-6b). The comparison between FBS(+) and (–) conditions in thermal neutron irradiation was additionally conducted at the ^{10}B concentration of ca. 12 μg/mL (200 μg/mL of nanodrug containing 5.8 – 6.1% of ^{10}B). As shown in Figure 5-6c and Table 5-2c, FBS(–) exhibited higher BNCT efficacy than FBS(+) in all three nanodrugs, DND-PG($^{10}B_{12}H_{11}^{2-}$)-COOH, -PBA and -c(RGDyK). Although DND-PG($^{10}B_{12}H_{11}^{2-}$)-c(RGDyK) and -COOH gave no colonies under FBS(–) conditions, DND-PG($^{10}B_{12}H_{11}^{2-}$)-PBA exhibited the significant difference in the slopes under FBS(+) and (–) conditions. These results will be interpreted by TEM observation in the next section.

a)

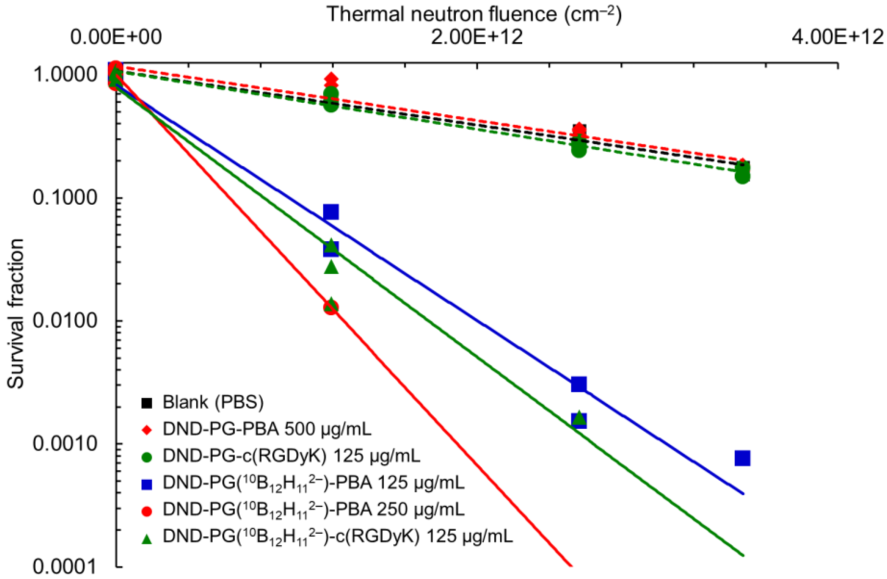
Thermal neutron fluence (cm^{-2})
0.00E+00
2.00E+12
4.00E+12
Survival fraction
1.0000
0.1000
0.0100
0.0010
0.0001
Blank (PBS)
DND-PG-PBA 500 μg/mL
DND-PG-c(RGDyK) 125 μg/mL
DND-PG($^{10}B_{12}H_{11}^{2-}$)-PBA 125 μg/mL
DND-PG($^{10}B_{12}H_{11}^{2-}$)-PBA 250 μg/mL
DND-PG($^{10}B_{12}H_{11}^{2-}$)-c(RGDyK) 125 μg/mL

b)

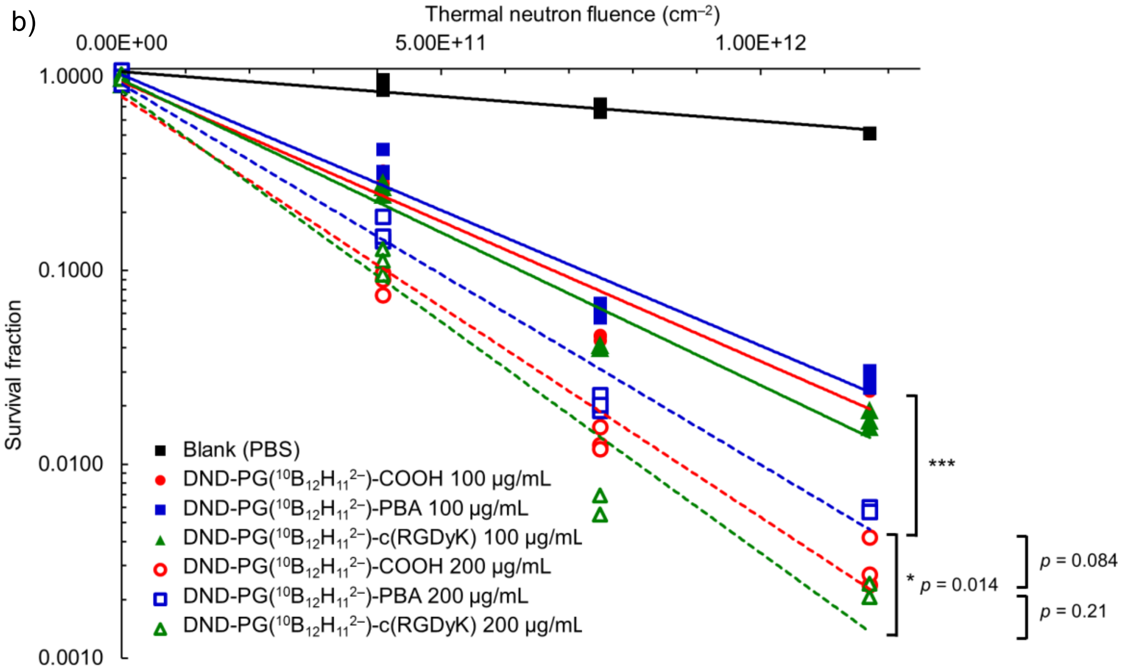
Thermal neutron fluence (cm^{-2})
0.00E+00
5.00E+11
1.00E+12
Survival fraction
1.0000
0.1000
0.0100
0.0010
Blank (PBS)
DND-PG($^{10}B_{12}H_{11}^{2-}$)-COOH 100 μg/mL
DND-PG($^{10}B_{12}H_{11}^{2-}$)-PBA 100 μg/mL
DND-PG($^{10}B_{12}H_{11}^{2-}$)-c(RGDyK) 100 μg/mL
DND-PG($^{10}B_{12}H_{11}^{2-}$)-COOH 200 μg/mL
DND-PG($^{10}B_{12}H_{11}^{2-}$)-PBA 200 μg/mL
DND-PG($^{10}B_{12}H_{11}^{2-}$)-c(RGDyK) 200 μg/mL
***
* p = 0.014
p = 0.084
p = 0.21

c)

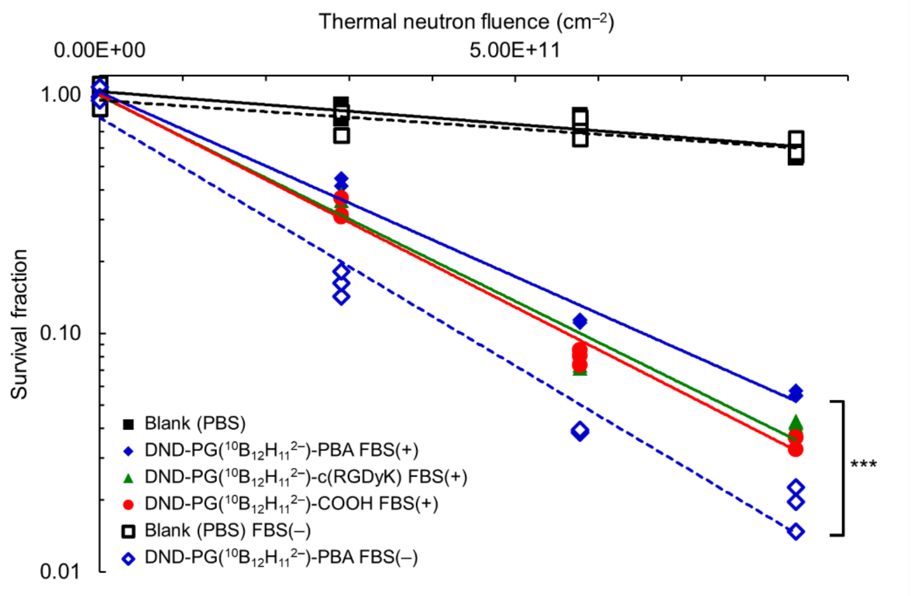

Figure 5-6. a) Result of colony forming assay on B16 cells exposed nanomaterials/nanodrugs with and without $^{10}B_{12}H_{11}{}^{2-}$ moiety on thermal neutron irradiation (first trial). Lines are the fitted curves in exponential approximation for the materials in the same colors.

b) Result on the exposure of $^{10}B_{12}H_{11}{}^{2-}$ functionalized nanodrugs and irradiation thermal neutron with reduced sample concentrations and irradiation doses. Result of colony forming assay on B16 cells exposed $^{10}B_{12}H_{11}{}^{2-}$ functionalized nanodrugs and irradiated with thermal neutron. Concentration of nanodrug in all entries except for blank are 200 µg/mL.

c) Result of colony forming assay on B16 cells exposed $^{10}B_{12}H_{11}{}^{2-}$ functionalized nanodrugs and irradiated with thermal neutron. Each nanodrug was exposed in the culture medium supplemented with or without FBS (FBS(+) or FBS(–), respectively). Concentration of nanodrug in all entries except for blank are 200 µg/mL.

(Significance in the difference of slopes after the logarithmic conversion: $^{*}p < 0.05$, $^{**}p < 0.01$, $^{***}p < 0.001$)

Table 5-2. Numbers of colonies in colony forming assay corresponding to a): Figure 5-6a, b): Figure 5-6b, and c): Figure 5-6c.

a)

Thermal neutron fluence/cm^{-2} (Number of seeded cells)	0 (300)			1.19×10^{12} (300)			2.57×10^{12} (2500)			2.57×10^{12} (500)			3.47×10^{12} (5000)			3.47×10^{12} (1000)		
	n=1	*n*=2	*n*=3	*n*=1	*n*=2	*n*=3	*n*=1	*n*=2	*n*=3	*n*=1	*n*=2	*n*=3	*n*=1	*n*=2	*n*=3	*n*=1	*n*=2	*n*=3
Blank (PBS)	89	83	73	52	50	51	233	204	238	57	60	58	240	210	228	62	58	67
DND-PG-PBA 500 µg/mL	56	55	54	45	35	51	160	149	166	40	43	38	164	168	152	47	37	46
DND-PG-c(RGDyK) 125 µg/mL	58	50	56	38	31	33	110	129	120	35	33	37	159	137	135	31	35	43
DND-PG($^{10}B_{12}H_{11}^{2-}$)-PBA 125 µg /mL	86	75	76	3	6	3	1	0	2	0	0	0	0	0	1	0	0	0
DND-PG($^{10}B_{12}H_{11}^{2-}$)-PBA 250 µg/mL	88	66	81	1	0	0	0	0	0	0	0	0	0	0	0	0	0	0
DND-PG($^{10}B_{12}H_{11}^{2-}$)-PBA 500 µg/mL	54	61	57	0	0	0	0	0	0	0	0	0	0	0	0	0	0	0
DND-PG($^{10}B_{12}H_{11}^{2-}$)-c(RGDyK) 125 µg/mL	74	66	78	2	3	1	1	1	0	0	0	0	0	0	0	0	0	0
DND-PG($^{10}B_{12}H_{11}^{2-}$)-COOH 500 µg/mL	53	51	49	0	0	0	0	0	0	0	0	0	0	0	0	0	0	0

b)

Thermal neutron fluence/cm^{-2} (Number of seeded cells)	0 (400)			4.09×10^{11} (400)			7.48×10^{11} (5000)			7.48×10^{11} (500)			1.17×10^{12} (10000)			1.17×10^{12} (1000)		
	n=1	*n*=2	*n*=3	*n*=1	*n*=2	*n*=3	*n*=1	*n*=2	*n*=3	*n*=1	*n*=2	*n*=3	*n*=1	*n*=2	*n*=3	*n*=1	*n*=2	*n*=3
Blank (PBS)	126	143	128	128	113	120				118	120	109				168	170	169
DND-PG($^{10}B_{12}H_{11}^{2-}$)-PBA 100 µg/mL	150	141	134	60	45	46	101	120	115	12	16	19	88	98	108	10	12	14
DND-PG($^{10}B_{12}H_{11}^{2-}$)-c(RGDyK) 100 µg/mL	124	139	115	34	31	36	63	65	65	13	13	12	60	53	49	7	10	6
DND-PG($^{10}B_{12}H_{11}^{2-}$)-COOH 100 µg/mL	111	105	115	36	31	33	60	63	64	11	10	10	68	66	77	8	7	8
DND-PG($^{10}B_{12}H_{11}^{2-}$)-PBA 200 µg/mL	137	116	127	18	24	19	30	36	32	8	4	4	19	18	18	5	8	2
DND-PG($^{10}B_{12}H_{11}^{2-}$)-c(RGDyK) 200 µg/mL	119	116	113	11	15	13	8	10	8	1	4	2	7	6	6	2	1	0
DND-PG($^{10}B_{12}H_{11}^{2-}$)-COOH 200 µg/mL	144	123	134	12	10	13	21	20	26	4	3	3	14	8	9	1	0	1

Table 5-2 (continued).

c)

Thermal neutron fluence/cm^{-2} (Number of seeded cells)	0 (400)			4.09 × 10^{11} (500)			7.48 × 10^{11} (5000)			7.48 × 10^{11} (500)			1.17 × 10^{12} (10000)			1.17 × 10^{12} (1000)		
	n=1	*n*=2	*n*=3	*n*=1	*n*=2	*n*=3	*n*=1	*n*=2	*n*=3	*n*=1	*n*=2	*n*=3	*n*=1	*n*=2	*n*=3	*n*=1	*n*=2	*n*=3
Blank (PBS)	145	156	144	158	147	169				152	146	153				202	214	208
DND-PG($^{10}\mathrm{B}_{12}\mathrm{H}_{11}^{2-}$)-PBA FBS(+)	170	173	178	90	97	79	248	240	246	46	41	36	239	249	237	47	47	44
DND-PG($^{10}\mathrm{B}_{12}\mathrm{H}_{11}^{2-}$)-c(RGDyK) FBS(+)	144	140	136	57	63	67	129	125	138	26	18	16	150	148	143	22	22	25
DND-PG($^{10}\mathrm{B}_{12}\mathrm{H}_{11}^{2-}$)-COOH FBS(+)	180	157	170	65	78	66	155	180	170	21	22	25	155	154	138	18	18	20
Blank (PBS) FBS(–)	101	112	88	85	106	85				96	82	101				165	140	143
DND-PG($^{10}\mathrm{B}_{12}\mathrm{H}_{11}^{2-}$)-PBA FBS(–)	175	159	154	29	33	37	78	79	80	4	13	8	60	80	92	3	4	7
DND-PG($^{10}\mathrm{B}_{12}\mathrm{H}_{11}^{2-}$)-c(RGDyK) FBS(–)	106	109	114	0	0	0	0	0	0	0	0	0	0	0	0	0	0	0
DND-PG($^{10}\mathrm{B}_{12}\mathrm{H}_{11}^{2-}$)-COOH FBS(–)	109	98	96	0	0	0	0	0	0	0	0	0	0	0	0	0	0	0

5-2-4. TEM analysis of cells after incubation with nanodrugs

To interpret the cytotoxicity and BNCT efficacy mentioned above, the cells treated with nanodrug under FBS(+) and FBS(–) conditions were analyzed by TEM. Concentrations of the nanodrugs were 100 and 750 μg/mL for the ones with and without $^{10}B_{12}H_{11}^{2-}$ moiety, respectively. Because no nanoparticles were observed in the TEM images of the nanodrugs without $^{10}B_{12}H_{11}^{2-}$ moiety at 200 μg/mL in our preliminary experiment (data not shown), much higher concentration (750 μg/mL) was applied. In addition, the nanodrugs should be taken up by the cells not through precipitation, but from the medium, because hydrodynamic diameters of the nanodrugs with and without FBS clearly indicate no significant aggregation (Figure 5-7) due to the high hydrophilicity and protein repellent property of PG mentioned above.

The black dots in vesicles in Figure 5-8, which are made to be clearer in the expanded images (Figure 5-9a – h) and images of different sights (Figure 5-9i – k), are assigned to be DND particles of nanodrugs, because they were not observed in control cells (Figure 5-8a or 5-9a) and loomed out in white (Figure 5-10) when TEM was defocused. In addition, boron was detected by energy dispersive X-ray spectroscopy with scanning electron microscopy (SEM-EDS) as shown in Figure 5-11, where a shoulder peak was observed at the energy of B*K* in some vesicles containing black dots (Figure 5-11b, c and d).

a) Hydrodynamic diameter of $^{10}B_{12}H_{11}^{2-}$ functionalized nanodrugs.

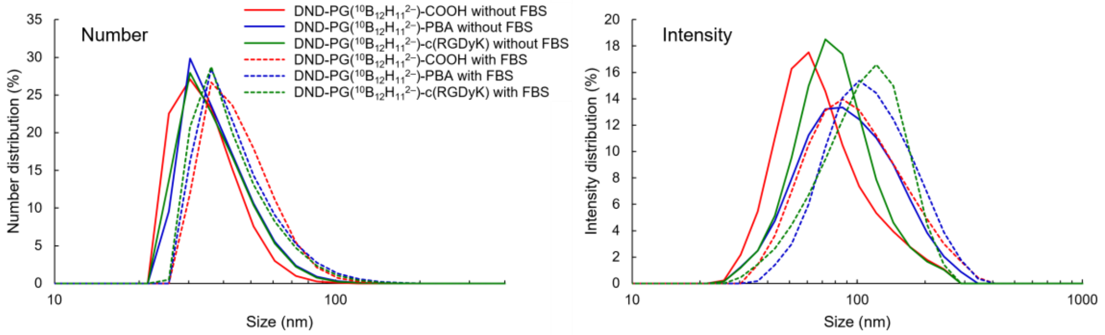

b) Hydrodynamic diameter of samples without $^{10}B_{12}H_{11}^{2-}$.

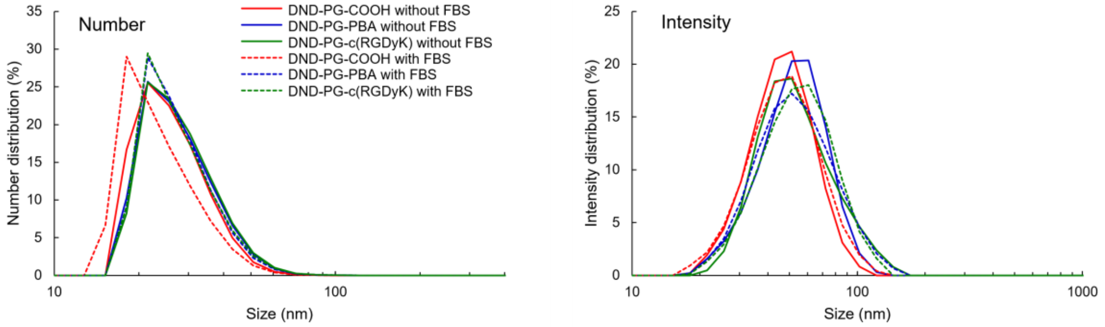

Figure 5-7. Hydrodynamic diameters of nanodrugs in PBS with and without FBS on number and scattered light intensity bases.

a) Control, FBS(+)

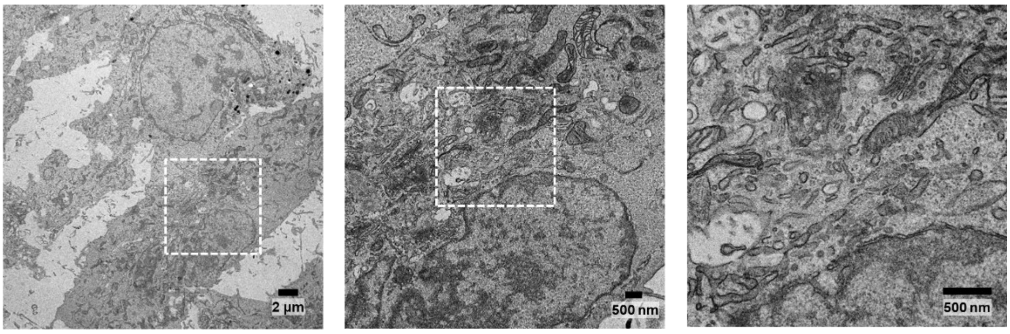

b) DND-PG(${}^{10}B_{12}H_{11}^{2-}$)-COOH, FBS(+)

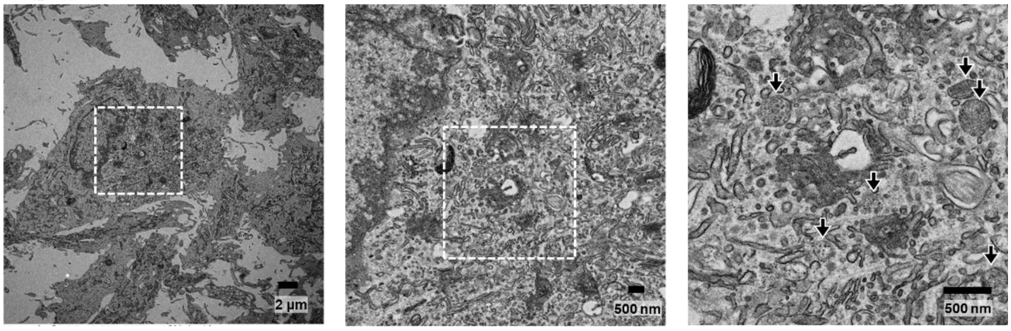

c) DND-PG(${}^{10}B_{12}H_{11}^{2-}$)-PBA, FBS(+)

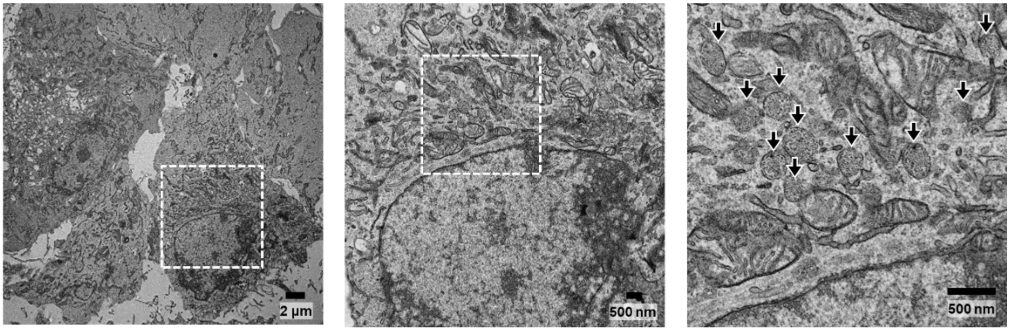

d) DND-PG(${}^{10}B_{12}H_{11}^{2-}$)-c(RGDyK), FBS(+)

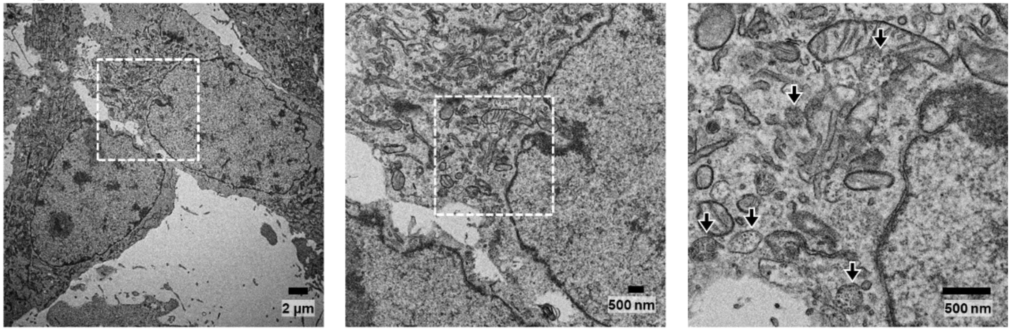

e) DND-PG-COOH, FBS(+)

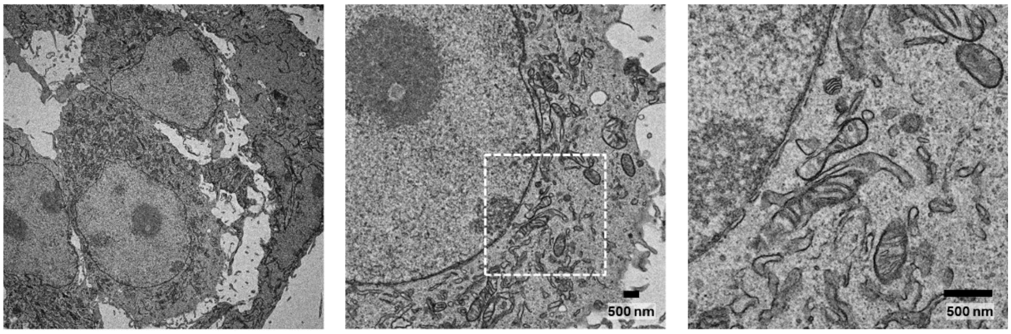

f) DND-PG-PBA, FBS(+)

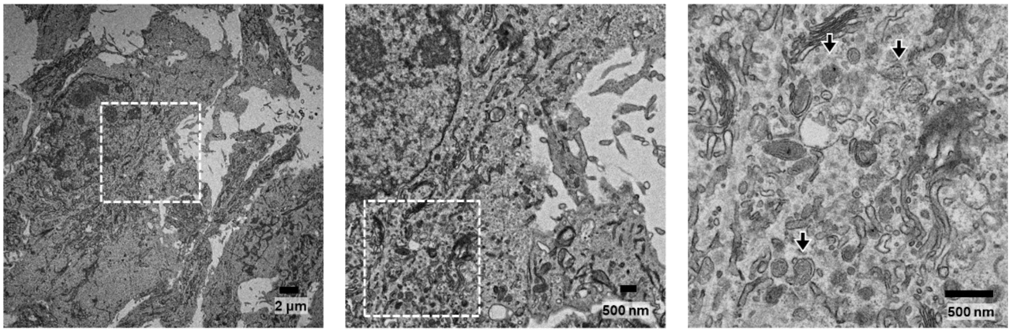

g) DND-PG-c(RGDyK), FBS(+)

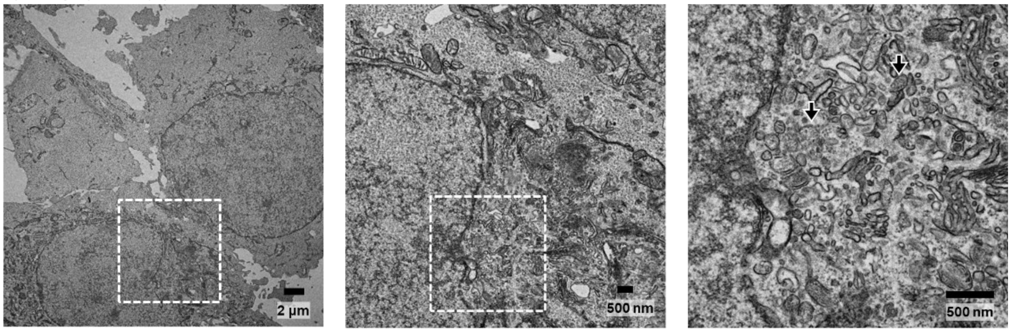

h) DND-PG($^{10}B_{12}H_{11}{}^{2-}$)-PBA, FBS(–)

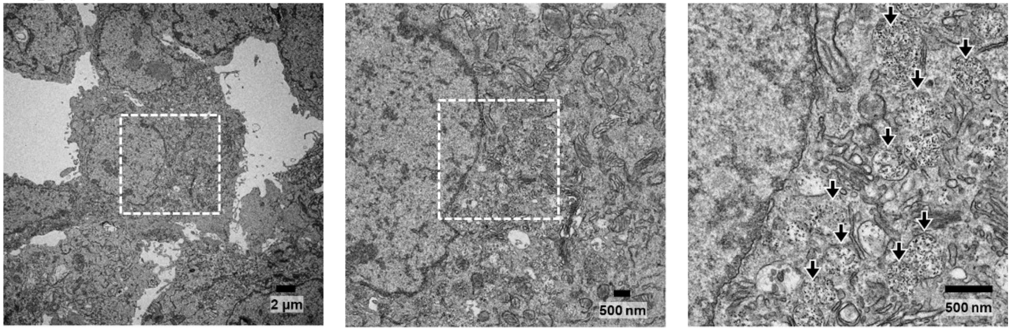

Figure 5-8. TEM images of B16 cells treated with nanodrugs under FBS(+) or FBS(–) conditions (accelerating voltage: 80 keV). Images of cells with each material consist of three images of different magnifications. Squares with white dashed lines indicate the areas of expansion that are shown on the right. Black arrows indicate the location of vesicles including dots of nanoparticles.

a) Expanded image of Figure 5-8a (right) for Blank in FBS(+).

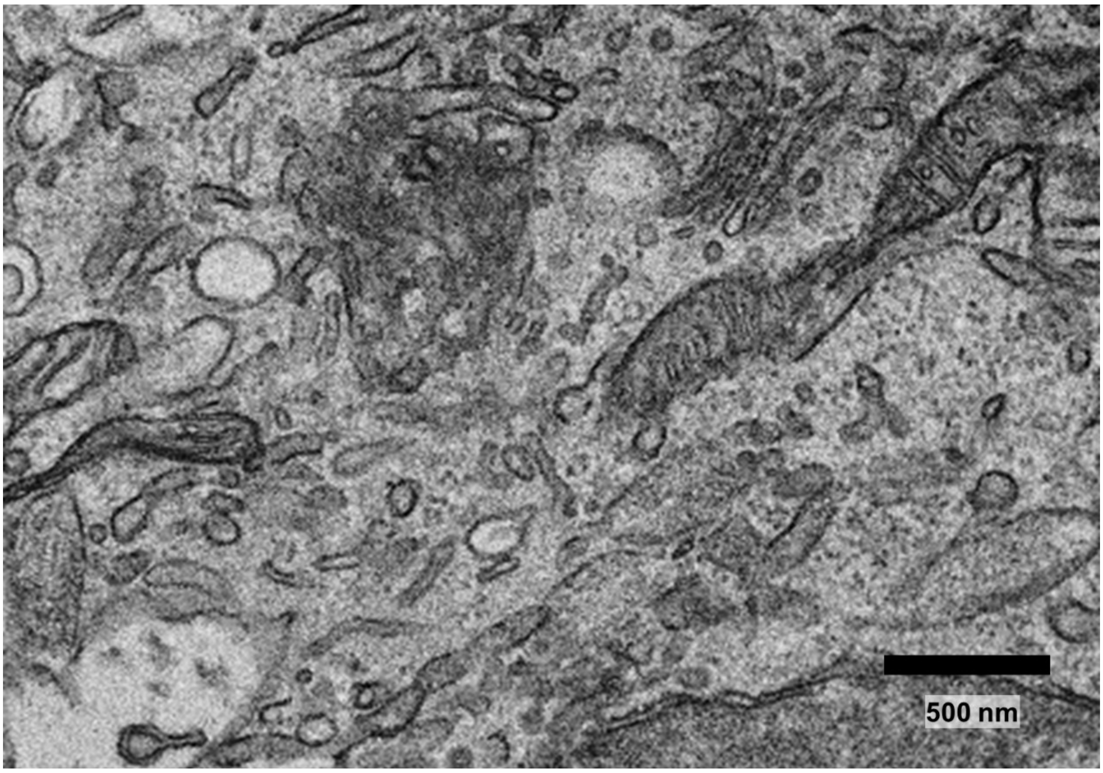

b) Expanded image of Figure 5-8b (right) for DND-PG($^{10}B_{12}H_{11}{}^{2-}$)-COOH in FBS(+).

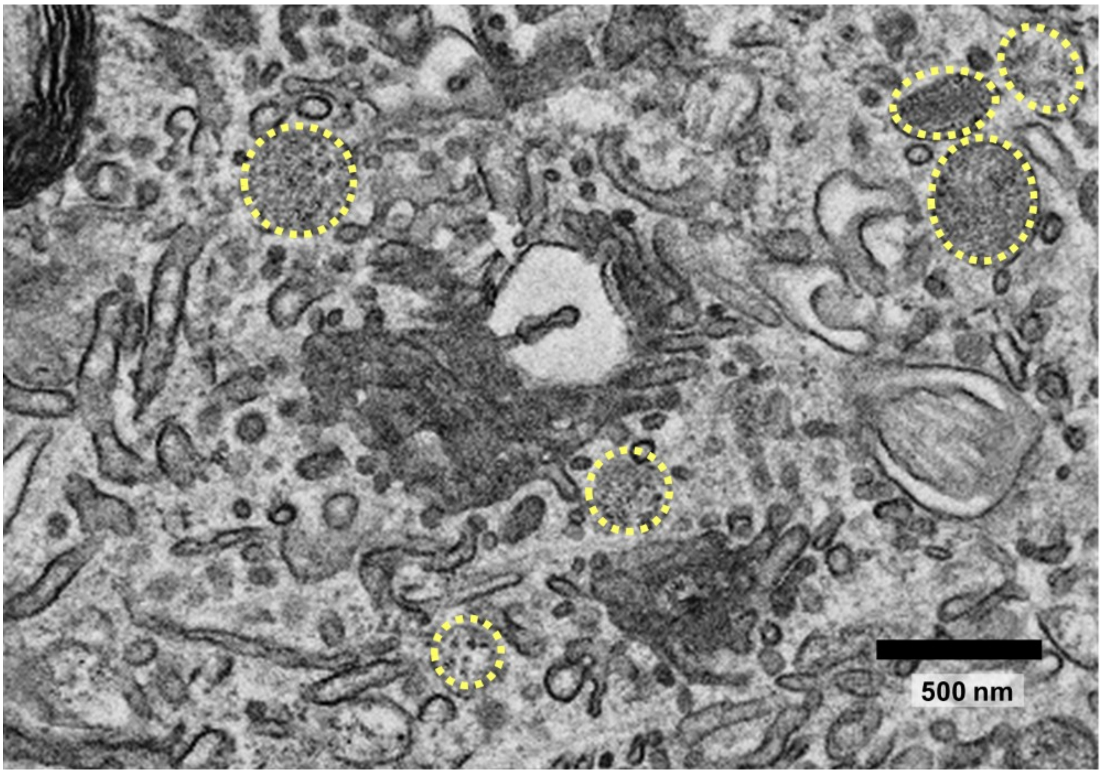

c) Expanded image of Figure 5-8c (right) for DND-PG($^{10}B_{12}H_{11}{}^{2-}$)-PBA in FBS(+).

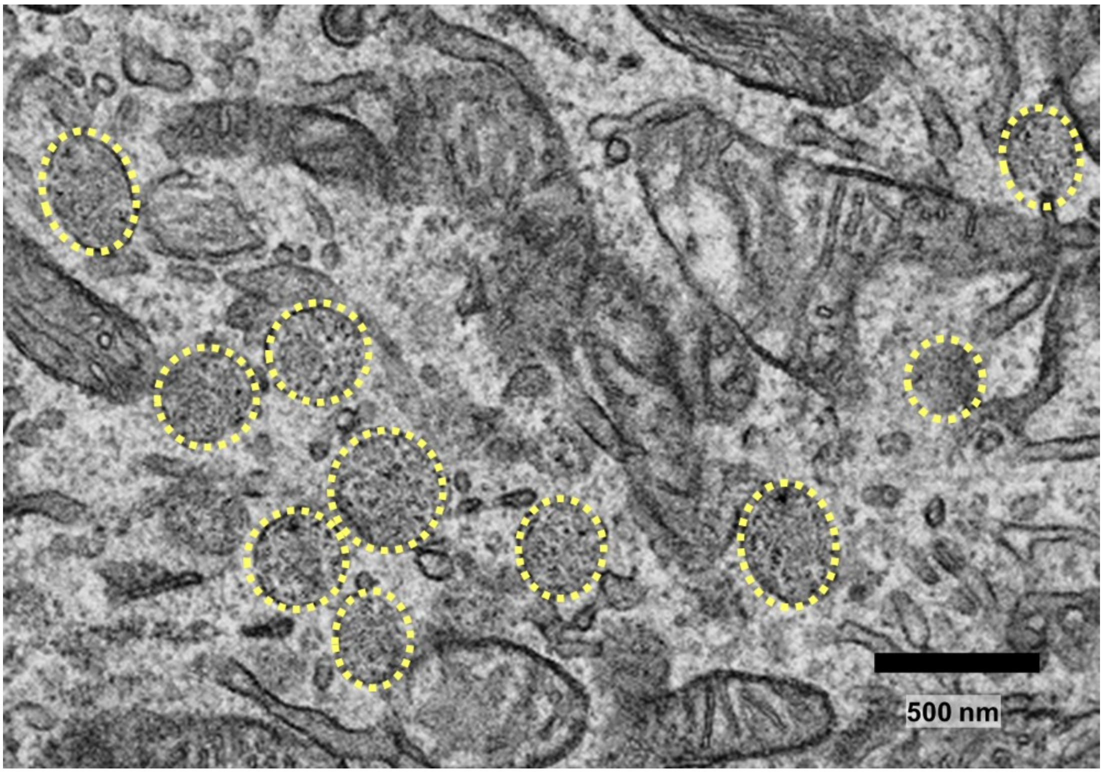

d) Expanded image of Figure 5-8d (right) for DND-PG($^{10}B_{12}H_{11}{}^{2-}$)-c(RGDyK) in FBS(+).

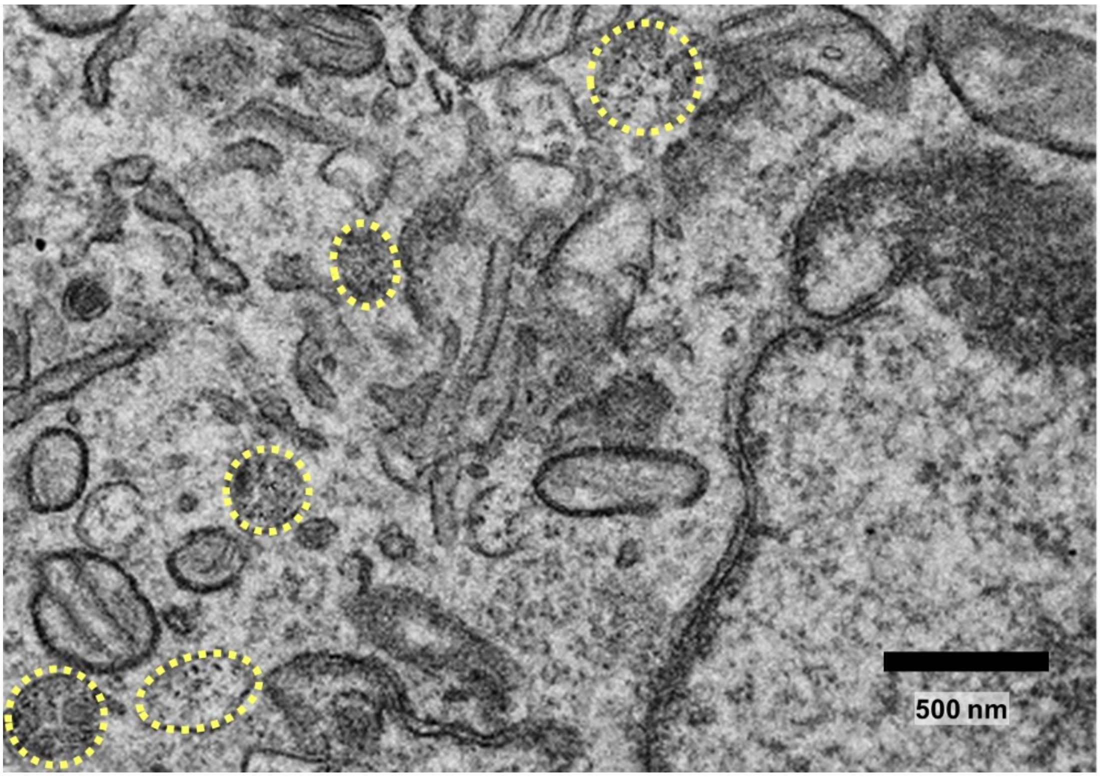

e) Expanded image of Figure 5-8e (right) for DND-PG-COOH in FBS(+).

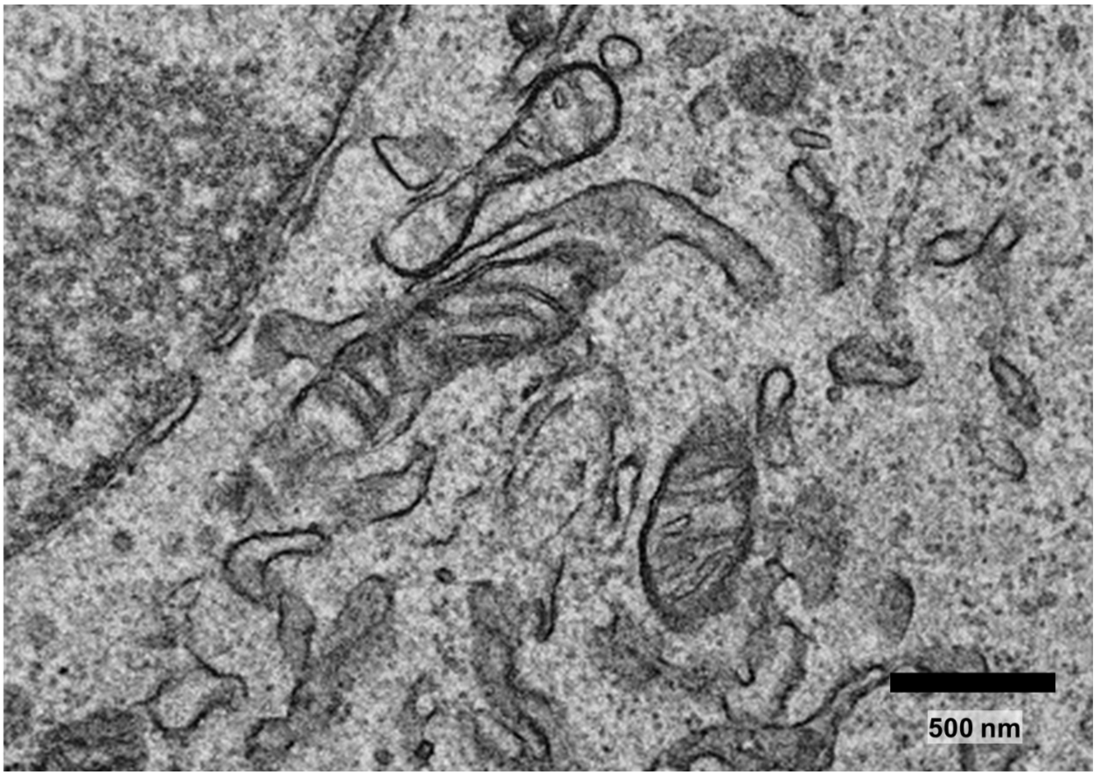

f) Expanded image of Figure 5-8f (right) for DND-PG-PBA in FBS(+).

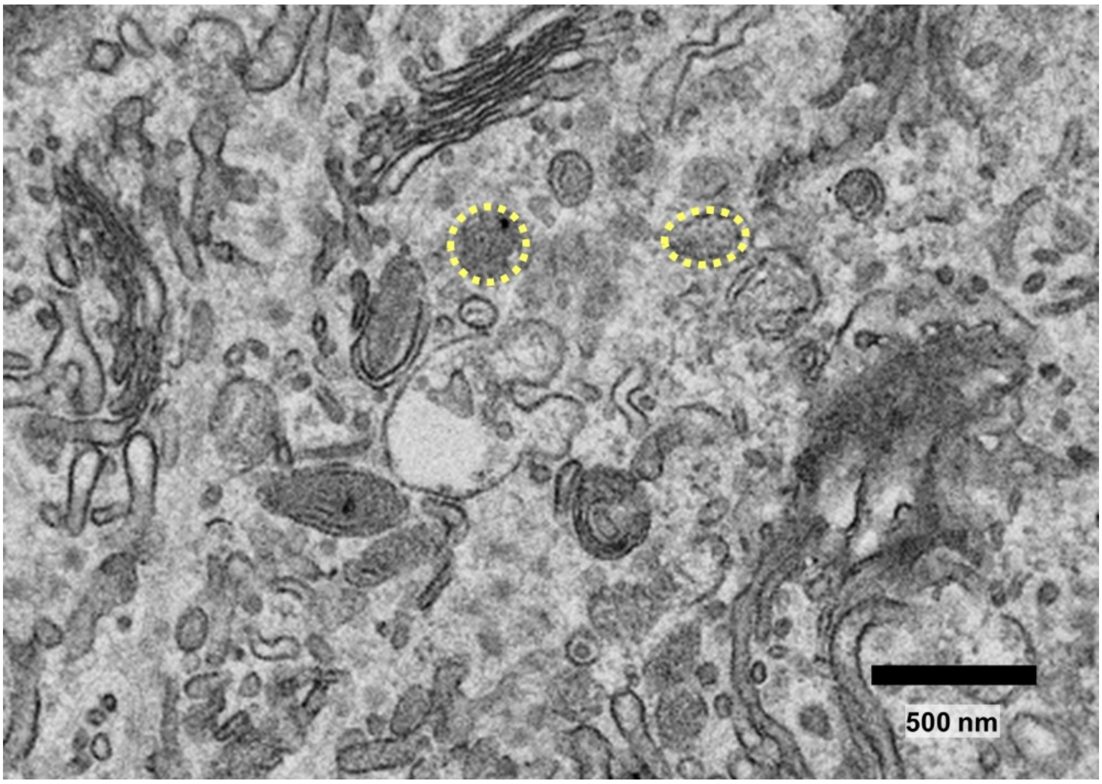

g) Expanded image of Figure 5-8g (right) for DND-PG-c(RGDyK) in FBS(+).

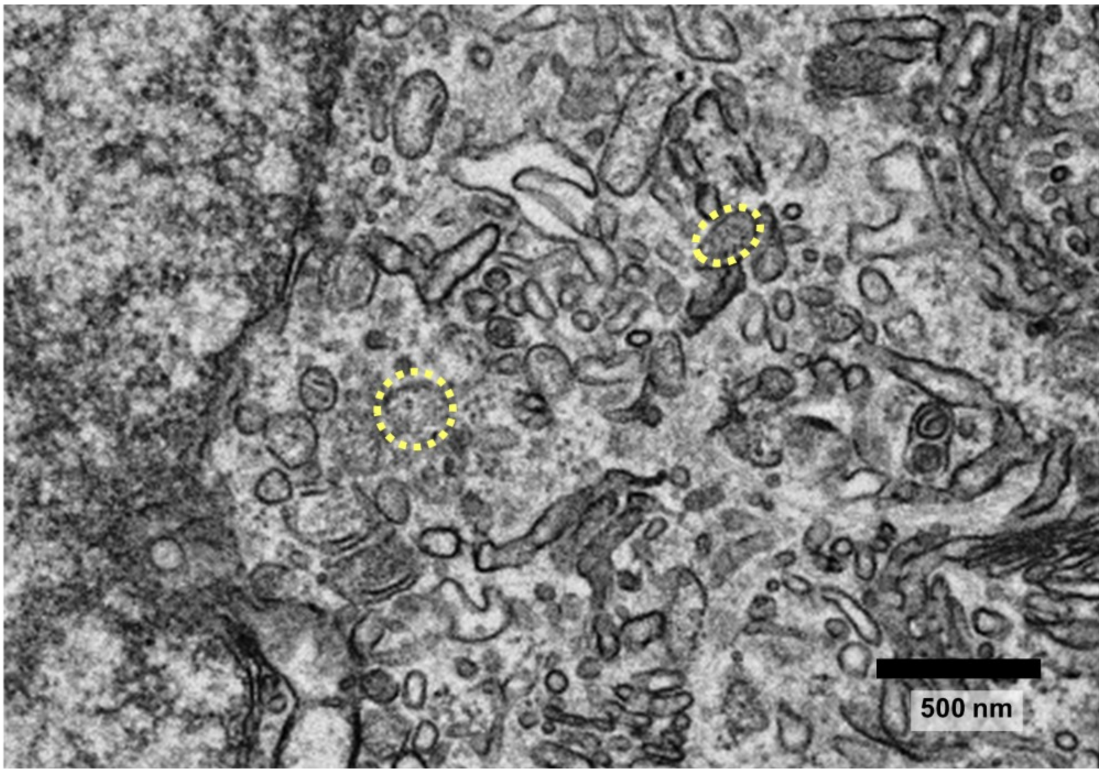

h) Expanded image of Figure 5-8h (right) for DND-PG($^{10}B_{12}H_{11}{}^{2-}$)-PBA in FBS(–).

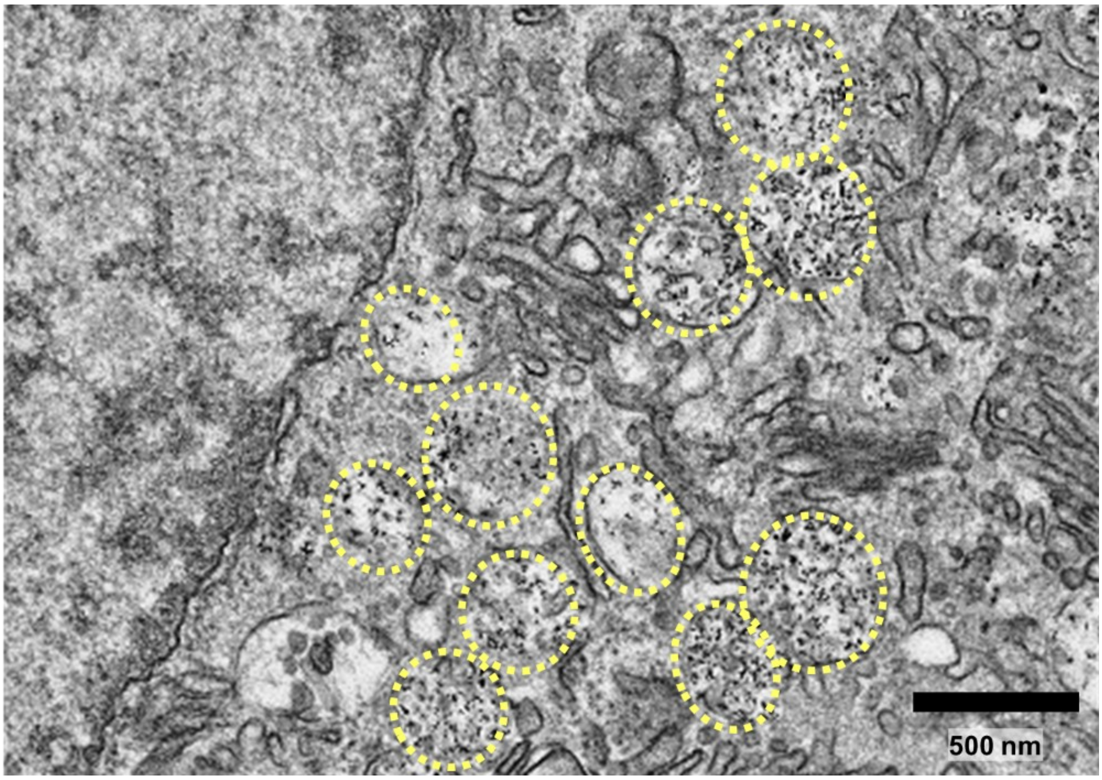

i) Different point of DND-PG($^{10}B_{12}H_{11}^{2-}$)-COOH in FBS(+).

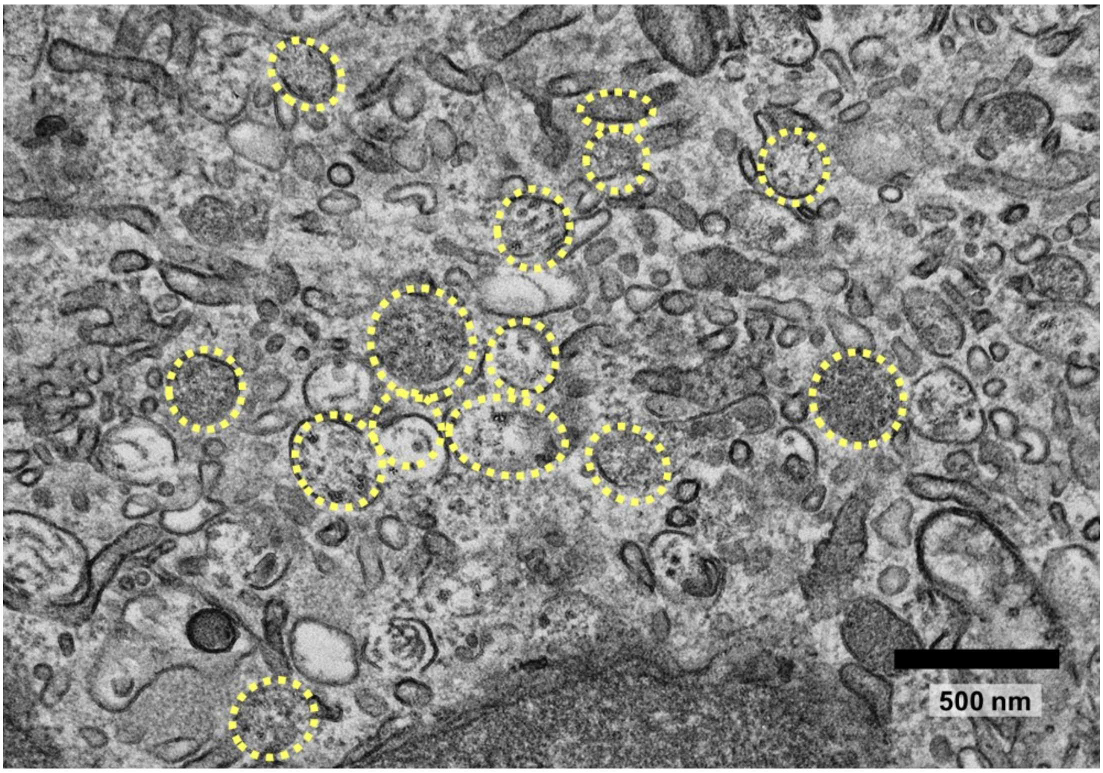

j) Different point of DND-PG($^{10}B_{12}H_{11}^{2-}$)-c(RGDyK) in FBS(+).

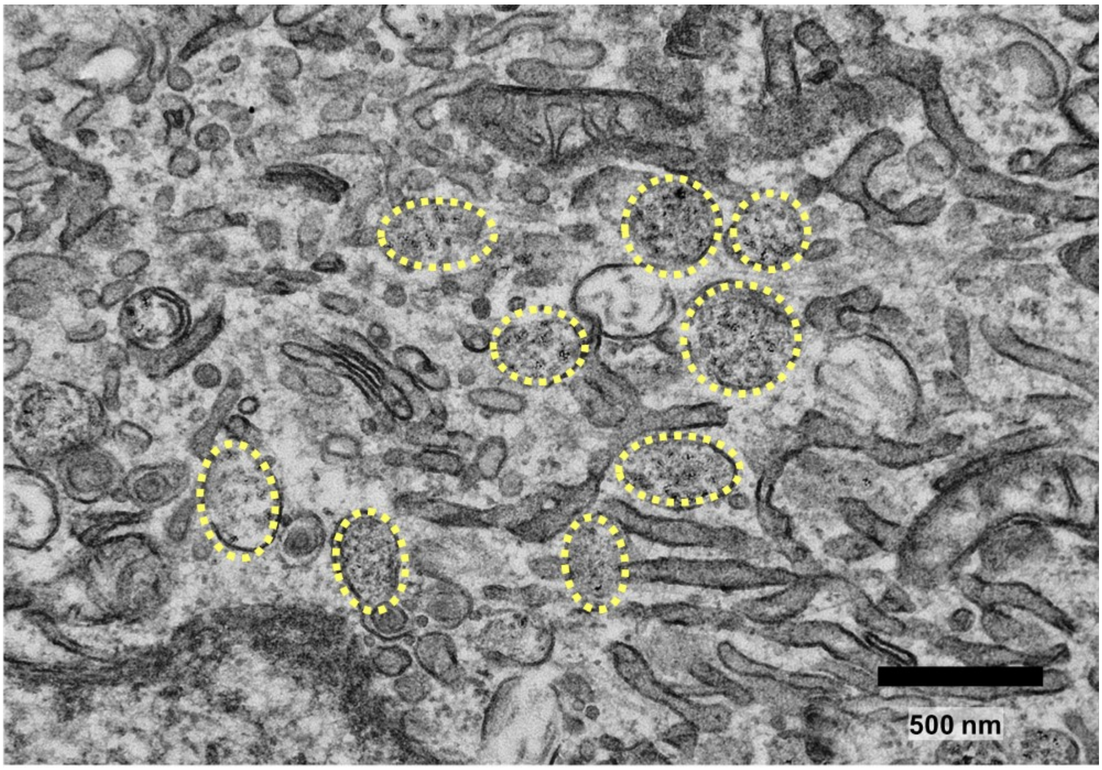

k) Different point of DND-PG($^{10}B_{12}H_{11}^{2-}$)-PBA in FBS(–). (Expanded image of Figure 5-12d)

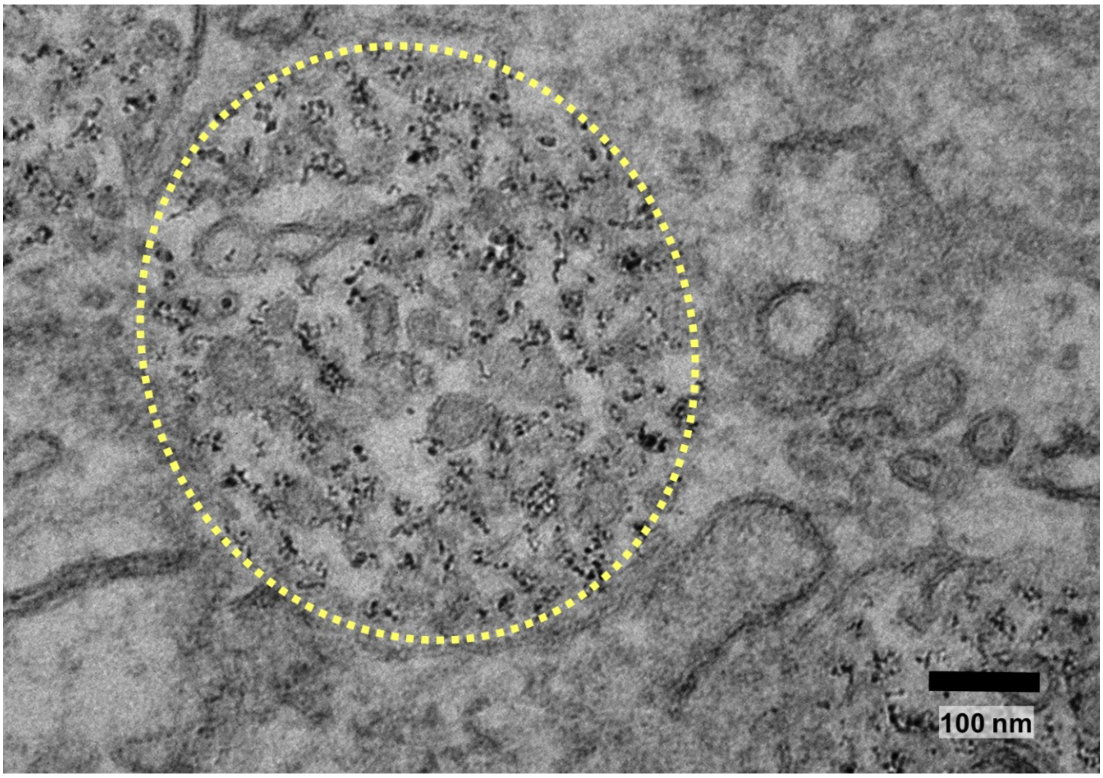

Figure 5-9. Enlarged TEM images of B16 cell treated with nanodrug. Vesicles with black dots (nanoparticles) are surrounded by yellow circles and ovals.

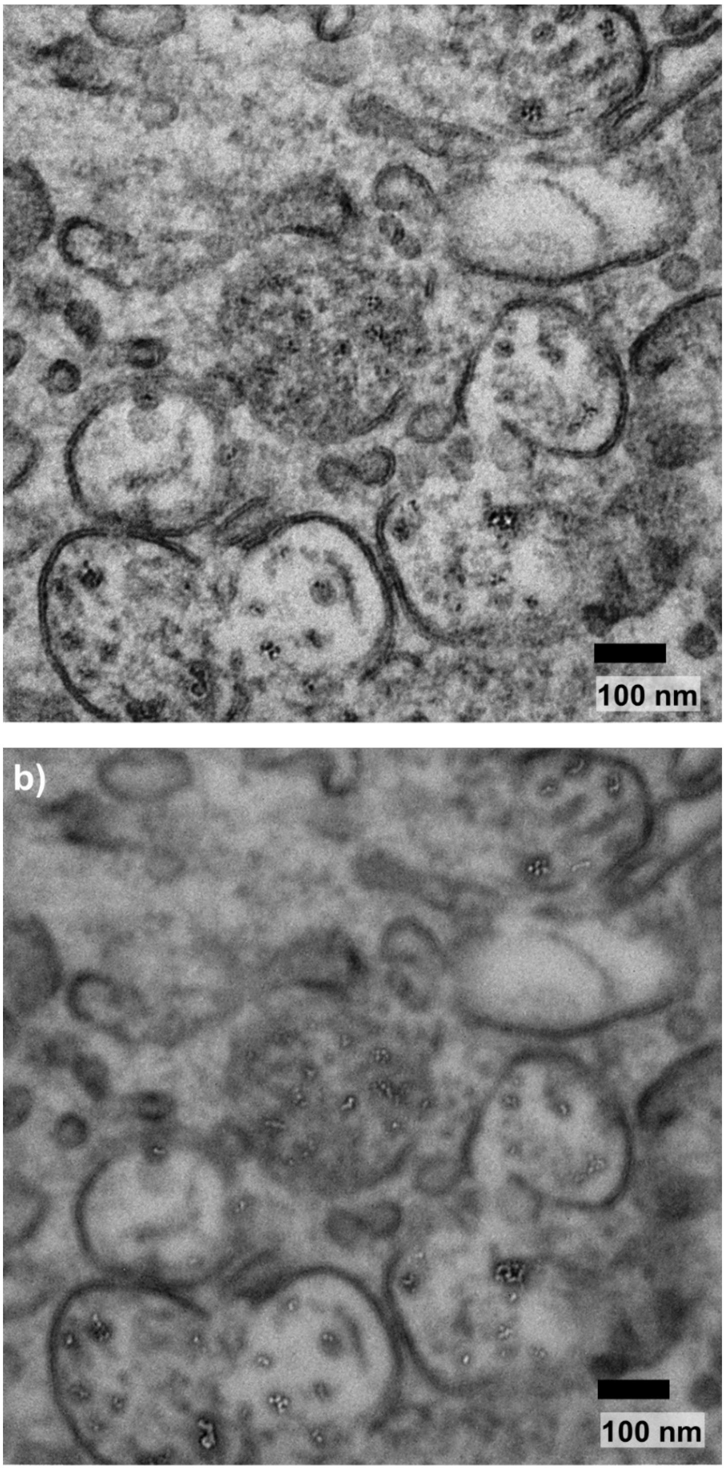

Figure 5-10 Appearance of nanoparticles in a vesicle in B16 cell plasma (DND-PG($^{10}B_{12}H_{11}{}^{2-}$)-PBA in FBS(+)). a) Nanoparticles look black dots in focused image, b) In the defocused image, they loom out in white.

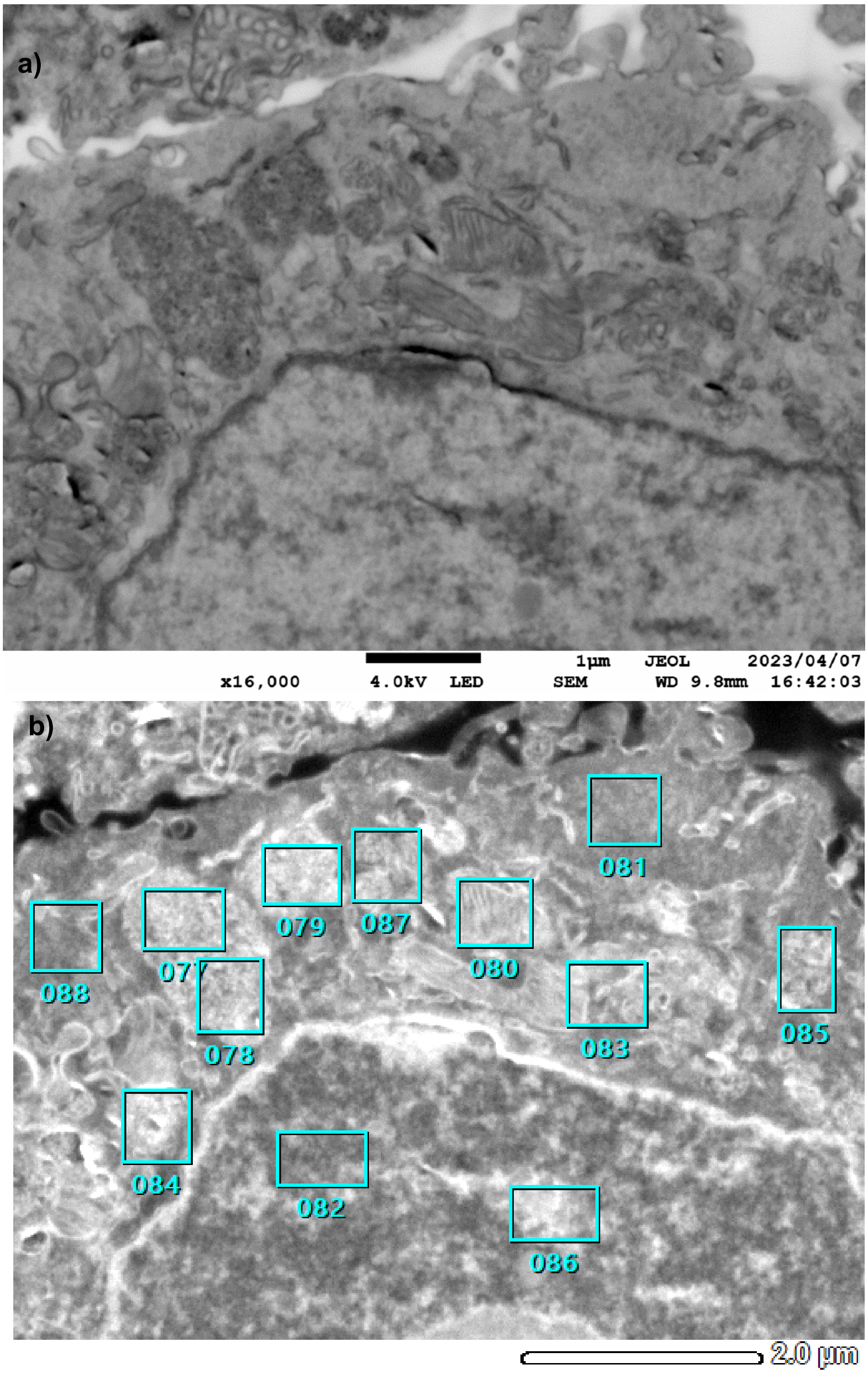
a)
1μm
JEOL
2023/04/07
x16,000
4.0kV
LED
SEM
WD 9.8mm
16:42:03
b)
081
079
087
088
07
080
078
083
085
084
082
086
2.0 μm

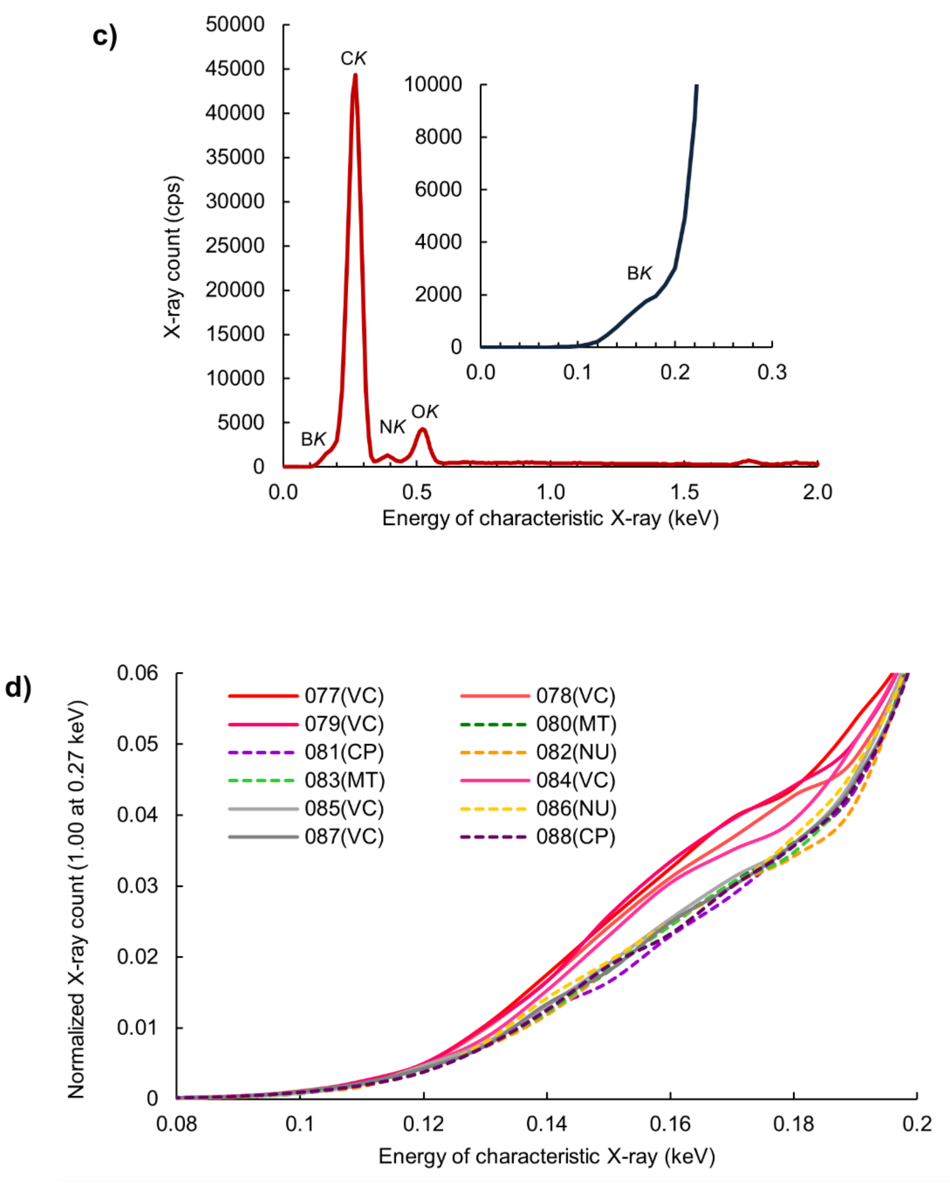

Figure 5-11. SEM-EDS of nanodrug incorporated cell (DND-PG($^{10}B_{12}H_{11}^{2-}$)-PBA). a) SEM image (inverted), b) areas of EDS analysis, c) typical chart of EDS analysis, the inset is a magnified chart of B*K* region, d) normalized EDS results of analyzed areas of B*K* region, VC: vesicle, MT: mitochondria, CP: cell plasma, NU: nucleus.

Similar numbers of the black dots in vesicles with 200 – 400 nm-size were observed in the cells treated with DND-PG($^{10}B_{12}H_{11}^{2-}$)-COOH, -PBA and -c(RGDyK) (100 μg/mL in culture medium) under FBS(+) conditions (Figure 5-8b, c and d, respectively). The above results of similar BNCT efficacies among the three nanodrugs can be interpreted by these TEM observations. Much less numbers of black dots were found in the cases of DND-PG-PBA and -c(RGDyK) (750 μg/mL in culture medium) under FBS(+) conditions (Figure 5-8f and g, respectively), while no black dots were observed in the cell treated with DND-PG-COOH at the same concentration (Figure 5-8e). Although active targeting capability of PBA and c(RGDyK) is observed in the absence of $^{10}B_{12}H_{11}^{2-}$ moiety, it seems to be hidden by $^{10}B_{12}H_{11}^{2-}$ moiety, which is considered to facilitate cellular uptake more than the active targeting moieties of PBA and c(RGDyK). This may be attributed to the dianionic nature of the boron cluster, which can interact electrostatically with the proteins in cell membrane and in serum to induce cellular uptake [123, 159, 160]. The higher toxicity of DND-PG($^{10}B_{12}H_{11}^{2-}$)-c(RGDyK) than PG($^{10}B_{12}H_{11}^{2-}$)-COOH and -PBA shown in Figure 5-5a and b implies that c(RGDyK) is much more toxic than COOH and PBA by taking into consideration the large difference in their numbers in one particle as shown in Table 5-1.

On the other hand, the sizes of vesicles containing DND-PG($^{10}B_{12}H_{11}^{2-}$)-COOH, -PBA and -c(RGDyK) under FBS(–) conditions are larger than those under FBS(+) conditions as shown in Figure 5-12. This indicates that the numbers of nanoparticles taken up by the cells are larger under FBS(–) conditions than FBS(+) ones, leading to the higher BNCT efficacies as described above (Figure 5-6c and Table 5-2c). This implies that the electrostatic interaction of $^{10}B_{12}H_{11}^{2-}$ moiety with the membrane proteins induces the cellular uptake more efficiently under FBS(–) conditions than FBS(+) ones, where the serum proteins adsorbed electrostatically by $^{10}B_{12}H_{11}^{2-}$ (Figure S5-3 and S5-4 in Appendix III) would reduce the cellular uptake efficiency [71, 72, 123, 158].

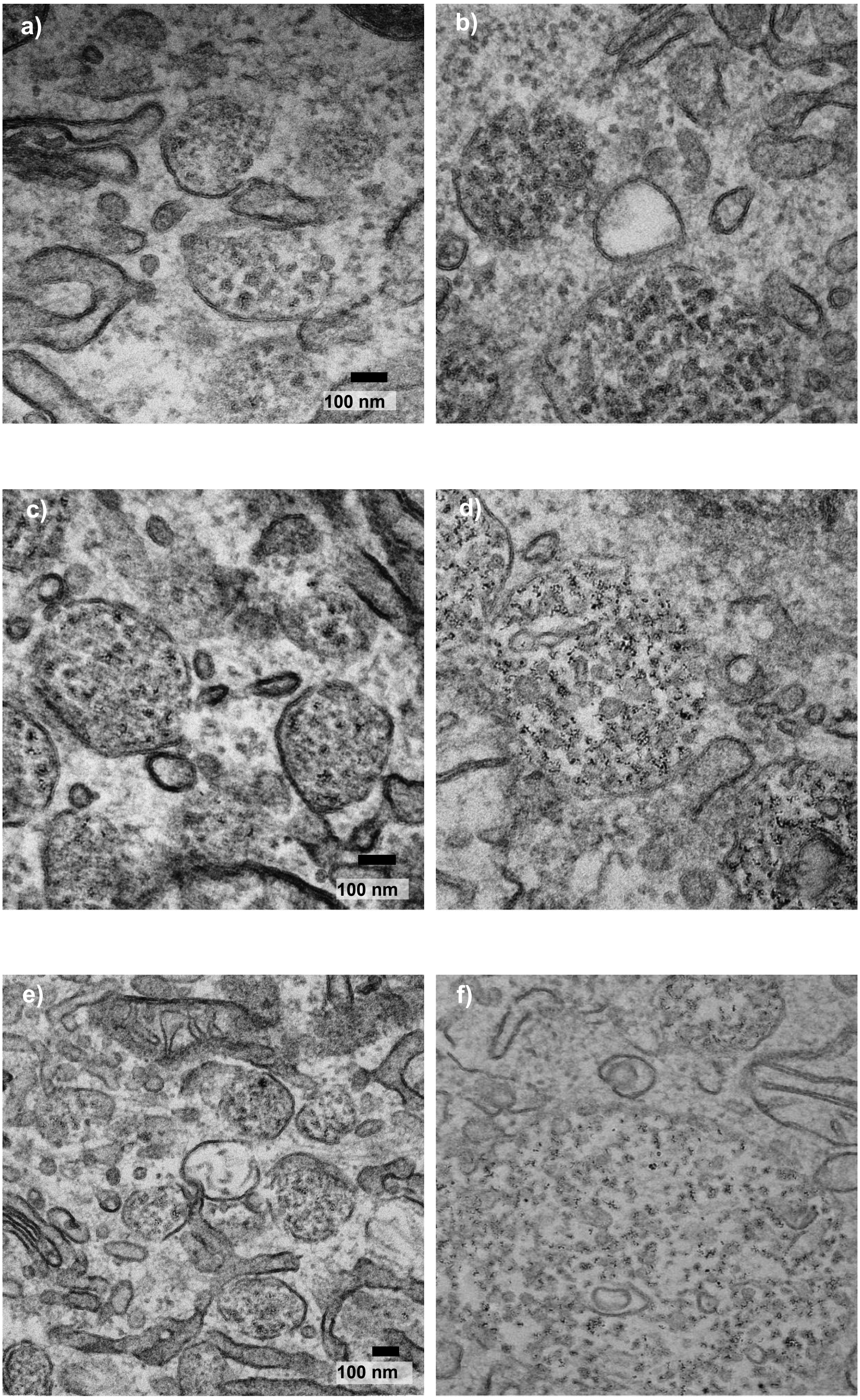
a)
100 nm
b)
c)
100 nm
d)
e)
100 nm
f)

Figure 5-12. Nanoparticles in the vesicles. (a, b) DND-PG($^{10}B_{12}H_{11}^{2-}$)-COOH under a) FBS(+) and b) FBS(–) conditions (x 50000), (c, d) DND-PG($^{10}B_{12}H_{11}^{2-}$)-PBA under c) FBS(+) and d) FBS(–) conditions (x 50000), (e, f) DND-PG($^{10}B_{12}H_{11}^{2-}$)-c(RGDyK) under e) FBS(+) and f) FBS(–) conditions (x 30000). The size of vesicles in FBS(–) seems to be larger than that in FBS(+).

5-3. Conclusion

We designed boron delivery agent for BNCT based on PG functionalized DND with a boron cluster and an active targeting moiety. To construct the nanodrug, $^{10}B_{12}H_{11}^{2-}$ moiety was first conjugated by click chemistry at the –OH groups of ND-PG-COOH, which is prepared by oxidation of DND-PG. Then, PBA or c(RGDyK) moiety for active targeting was introduced at the –COOH groups through amide linkage. The nanodrugs have ^{10}B content of 7.6 – 8.0% that is much higher than that of our previous BNCT nanodrug and exhibit good dispersibility under physiological conditions [113].

In vitro neutron irradiation experiments exhibited high BNCT efficacies in nanodrugs with $^{10}B_{12}H_{11}^{2-}$ moiety, showing small differences with and without targeting moieties. TEM observations of the cells treated with the nanodrugs indicate that $^{10}B_{12}H_{11}^{2-}$ moiety itself facilitates cellular uptake much more than the active targeting moieties of PBA and c(RGDyK), resulting in similar BNCT efficacies among these nanodrugs.

The nanodrug with $^{10}B_{12}H_{11}^{2-}$ moiety based on DND-PG-COOH would serve as a lead material of boron delivery agent for BNCT. However, we have to consider the improvement of active targeting efficiency. As well as applying more efficient active targeting moiety, possibility of effective spatial layout of active targeting moiety would be explored to enhance the interaction with tumor cells and suppress the influence of $^{10}B_{12}H_{11}^{2-}$ moiety. The multiple functionalization process we designed and achieved in this work is so flexible that it can be applied to nanodrugs with a variety of structural and functional features. Therefore, we are expecting to create more effective nanodrugs for BNCT in near future.

5-4. Experimental

Materials

Single-digit nanometer-sized water dispersion of DNDs was manufactured by Daicel Corporation (DINNOVARE^{TM}). For the modification of DNDs, the following reagents and solvents were purchased from FUJIFILM Wako Pure Chemical Corporation (Osaka Japan); sodium hypochlorite (NaClO) solution, sodium azide (NaN_3), acrylonitrile, ethylenediamine-*N,N,N',N'*-tetraacetic acid disodium salt (EDTA·2Na, produced by Dojindo Laboratories, Japan), hydrochloric acid (HCl), sodium hydroxide (NaOH), ethanolic solution of potassium hydroxide (KOH), acetic acid, sodium acetate, potassium dihydrogen phosphate, ethylene glycol, tetrahydrofuran (THF), *N,N*-dimethylformamide (DMF), acetonitrile (MeCN), ethyl acetate, 0.25% trypsin-EDTA·4Na solution, Dulbecco's phosphate-buffered saline (pH 7.4, PBS(–)), 10× PBS(–), sodium dodecyl sulfate (SDS) and Cell counting kit-8 (CCK-8, a formulation of 2-(2-methoxy-4-nitrophenyl)-3-(4-nitrophenyl)-5-(2,4-disulfophenyl)-2*H*-tetrazolium, monosodium salt (WST-8) and 1-Methoxy-5-methylphenazinium methylsulfate (1-methoxy PMS), produced by Dojindo Laboratories, Japan). 4-acetamido-2,2,6,6-tetramethylpiperidine-1-oxyl free radical (4-AcNH-TEMPO), *p*-toluenesulfonyl chloride (TsCl), tetramethylammonium hydroxide methanol solution (10%), propargyl bromide, sodium ascorbate, 3-aminophenylboronic acid monohydrate (natural abundance boron) and 2-(*N*-morpholino)ethanesulfonic acid (MES) were purchased from Tokyo Chemical Industry Co., Ltd. (Tokyo Japan). Sodium mercaptoundecahydro-*closo*-dodecaborate(^{10}B) (^{10}BSH) was purchased from Katchem spol. s r. o. (Czech). *N*-hydroxyscuuinimide (HOSu) from Peptide Institute, Inc. was used. 4% Paraformaldehyde in phosphate buffer produced by Muto Pure Chemicals Co., Ltd was used. Cyclo-(L-Arg-Gly-L-Asp-D-Tyr-L-Lys) trifluoroacetic acid salt (c(RGDyK)·2TFA) was purchased from Hanzhou Taijia Biotech Co., Ltd. Copper sulfate ($CuSO_4$, anhydrous) was purchased from Kishida Chemical Co., Ltd. (Osaka Japan). Sodium chlorite ($NaClO_2$) was purchased from Sigma-Aldrich Japan G. K. (Tokyo, Japan). 1-(3-Dimethylaminopropyl)-3-ethylcarbodiimide hydrochloride (EDC) is a product of Kokusan Chemical Co., Ltd. Antibiotics solution (penicillin-streptomycin-amphotericin B, 100×) was purchased from Thermo Fisher Scientific (MA USA). Dulbecco's modified Eagle Medium (DMEM, Glucose 4.5 g/L), PBS and 0.5% trypsin-EDTA·4Na solution, crystal violet, 25% glutaraldehyde (for electron microscopy), methanol and ethanol from Nacalai Tesque, Inc. (Kyoto Japan) were used. Fetal bovine serum (FBS) was supplied by Biosera Inc. (France). Bicinchoninic acid (BCA) assay was done with TaKaRa BCA protein assay kit (Takara Bio, Japan).

Equipment

^{1}H, ^{13}C and ^{10}B NMR spectra were measured with an ECX500 NMR spectrometer (JEOL). FT-IR spectra were recorded on an IR Tracer-100 FT-IR spectrometer (Shimadzu) equipped with DiffusIR DRIFT chamber (PIKE Technologies). Elemental analyses were conducted at Organic Elemental Microanalysis Centre of Kyoto University. ICP-AES analysis for boron content was done with an SPS3100 (SII Nanotechnology) at Nippon Steel Technology Co., Ltd. ESI-MS was measured with micrOTOF mass spectrometer (Bruker). TGA was performed with TG/DTA 6200 (SII). ζ-Potential was measured by ZetaSizer Nano (Malvern, UK). DLS measurement was done by Nanotrac Wave II particle size analyzer (MicrotracMRB). The absorbance of CCK-8 and BCA was measured with a microplate reader MTD-310 (Corona Electric Co., Japan). TEM observation of cells was performed on a H-7650 transmission electron microscope (Hitachi, Japan). Energy dispersive X-ray spectroscopy (SEM-EDS) was measured with JSM7900F scanning electron microscope (JEOL, Japan).

DND-PG(OTs)-COOH

To the water suspension of DND-PG-COOH (2.95% (w/w), 13.5 g, net 0.40 g, PG/DND 3.85, COOH content 1.01 mmol/g), water 2.45 mL and 8 M NaOH (3.0 mL, 24 mmol) were added, and the mixture was cooled in ice-bath. THF (3.6 mL) solution of TsCl (0.58 g, 3.0 mmol) was added in an intermittent manner for about 1 h with vigorously stirring. The reaction was stirred for more 2 h under ice-cooled condition, then added 6 M HCl (4.0 mL) to acidify and stirred for several hours. The mixture was centrifuged (3000 rpm, 30 min). The precipitate was washed three times by the addition of small amount of THF (2 – 3 mL) and water (10 – 15 mL) followed by centrifugation or ultracentrifugation (183400*g*, 30 min) according to the state of dispersion in supernatant to give the precipitate as much as possible. The precipitate was dispersed in DMF (20 mL) and ultracentrifuged. This operation was repeated once as solvent substitution, and DMF dispersion (18.5 g) of DND-PG(OTs)-COOH was obtained. The concentration was determined to be 1.48% (w/w) and net yield was 0.27 g. Elemental analysis: C; 56.85%, H: 6.53%, N; 0.51%, O; 29.08%, S; 4.08%.

DND-PG(N_3)-COOH

DMF suspension of DND-PG(OTs)-COOH (1.48% (w/w), 13.8 g, net 0.20 g) was added with NaN_3 (196 mg, 3.0 mmol), water (3.0 mL) and 1 M NaOH (0.30 mL, 0.30 mmol). The mixture was stirred at 60 °C for 0.5 h, then the temperature was raised to 90 °C for 18 h. Resulting cloudy suspension was ultracentrifuged (183400*g*, 2 h) and the precipitate was washed with water three times by the dilution and ultracentrifugation. The precipitate was dispersed in water (30.0 g). The concentration was determined to be 0.57% (w/w) and net yield was 0.17 g. Elemental analysis: C; 55.28%, H: 5.54%, N; 5.46%, O; 30.96%.

DND-PG($^{10}B_{12}H_{11}^{2-}$)-COOH

Aqueous dispersion of DND-PG(N_3)-COOH (0.57% (w/w), 8.84 g, net 50.1 mg) was added with MeCN (4.0 mL), 0.4 M phosphate buffer (pH 7.4, 2.5 mL), sodium ascorbate (42.2 mg, 0.21 mmol) and bis(tetramethylammonium) *S*-(propyn-3-yl)thioundecahydro-*closo*-dodecaborate(^{10}B) [($^{10}B_{12}H_{11}^{2-}$)S](Pgy)·2TMA, crude, 50.3 mg, starting from 21.1 mg of ^{10}BSH·2Na (0.10 mmol)), and the mixture was vacuum degassed with sonication. Aqueous solution of $CuSO_4$ (14.2 mg, 0.088 mmol in 0.50 mL water) was added slowly, then the reaction was stirred under nitrogen atmosphere at room temperature. The reaction was monitored by FT-IR (absorbances of azide and B–H at 2102 cm^{-1} and 2503 cm^{-1}, respectively) of sample taken from the reaction. As not negligible peak of azide remained, [($^{10}B_{12}H_{11}^{2-}$)S](Pgy)·2TMA (crude, 24.8 mg in total of three-time addition), sodium ascorbate (10.3 mg) and $CuSO_4$ (3.4 mg in small amount of water) were added after 22 – 30 h from the start. The reaction was stirred for more two days. Resulting dark-brown dispersion was ultracentrifuged (183400*g*, 30 min) and the precipitate was washed with water (10 mL), aqueous solution of EDTA·2Na (0.3 %, 10 mL, two times) and water (10 mL, three times) using centrifuge filter (Amicon® Ultra, 30 kDa). The concentrate on the filter was diluted with water to give dark-brown dispersion (10.1 g). The concentration was determined to be 0.50% (w/w) from the weight after lyophilization, and net yield was 50.5 mg. Elemental analysis: C; 48.22%, H: 5.33%, N; 3.78%. ^{10}B content (ICP-AES by alkaline fusion method for specimen preparation): 7.97%.

DND-PG($^{10}B_{12}H_{11}^{2-}$)-PBA

Aqueous dispersion of DND-PG($^{10}B_{12}H_{11}^{2-}$)-COOH (0.50% (w/w), 5.0 g, net 25.0 mg) was added with aqueous solution of MES (0.1 M, pH was adjusted to 4.5, 2.0 mL), 3-aminophenylboronic acid monohydrate (0.22 mL of 1.0 wt% DMF solution, 2.2 mg, 0.014 mmol) and EDC (0.50 mL of 1.0 wt% aqueous solution, 5.0 mg, 0.026 mmol). The mixture was stirred at room temperature for 15 h. After the reaction, pH was adjusted 10.0 with 1 M NaOH and the mixture was stirred for 45 min. The dispersion was ultrafiltered and then washed with water five times. The concentrate on the filter was diluted with water to give dark-brown dispersion (4.91 g). The concentration was determined to be 0.50% (w/w) from the weight after lyophilization, and net yield was 24.6 mg. Elemental analysis: C; 51.35%, H: 5.10%, N; 4.16%.

DND-PG($^{10}B_{12}H_{11}^{2-}$)-c(RGDyK)

Aqueous dispersion of DND-PG($^{10}B_{12}H_{11}^{2-}$)-COOH (0.50% (w/w), 3.4 g, net 16.9 mg) was added with phosphate buffer (0.4 M, pH 7.4, 2.0 mL), HOSu (0.47 mL of 1.0 wt% water solution, 4.7 mg, 0.041 mmol) and EDC (0.39 mL of 1.0 wt% aqueous solution, 3.9 mg, 0.020 mmol). The mixture was stirred at room temperature for 30 min. Then, c(RGDyK)·2TFA (7.4 mg, 0.0087 mmol) was added and the mixture was stirred at room temperature for 24 The dispersion was ultrafiltered and then washed with water six times. The concentrate on the filter was diluted with water to give dark-brown dispersion (1.70 g). The concentration was determined to be 0.85% (w/w) from the weight after lyophilization, and net yield was 14.5 mg.

Cell viability assay with CCK-8

B16 mouse melanoma cells were seeded on 96-well microplates by 3 × 10^3 cells/well in 100 μL of DMEM (Glucose 4.5 g/L) culture medium (supplemented with 10 % FBS and 1 % of 100× penicillin-streptomycin-amphotericin B solution) for each well. After incubation in CO_2 incubator at 37 °C for 3 d, culture medium (100 μL) was replaced once, PBS (as control) or PBS dispersion of nanoparticles (2500, 1250 and 625 μg/mL, 25 μL for each) were added, and the cells were further incubated for 24 h. Under FBS(–) conditions, replacement of culture medium was done with DMEM that was not supplemented with FBS, and the concentrations of nanoparticles were 1250, 625 and 312.5 μg/mL in PBS. The cells were washed with culture medium (two times) and PBS, CCK-8 in culture medium (10 μL of CCK-8 and 100 μL medium for each well) was added. After 0.5 h, the absorbance at 450 nm was measured for each well using the microplate reader.

Colony forming assay on thermal neutron irradiation

B16 cells (8.8×10^5 or 1.0×10^6 cells) in 10 mL DMEM culture medium (glucose 4.5 g/L, with 10% FBS and antibiotics/antimycotic) were seeded on 100 mmφ dishes, and incubated in CO_2 incubator at 37 °C for 2 d. The culture medium (10 mL, with or without FBS for FBS(+) or FBS(–) condition, respectively) was replaced once, PBS or PBS dispersion of nanoparticles (1.0 mL) were added to make predetermined sample concentrations in the medium. After incubated in CO_2 incubator at 37 °C for 22 – 24 h, the cells were washed with PBS and detached by treatment with trypsin (0.5%, 2.0 mL) at 37 °C for 5 min. After trypsinization was terminated with culture medium (with FBS), the number of cells was counted and adjusted the concentration to 100000 cells/mL, then the suspension of cells was dispensed into four plastic tubes by 1 mL/tube. Thermal neutron irradiation was conducted at KUR nuclear reactor (Kumatori campus, Kyoto University) at three levels of irradiation doses (for example, 5, 10 and 15 min of irradiation time in 1 MW output, corresponding to the fluence of 4.09×10^{11}, 7.48×10^{11} and 1.17×10^{12} neutrons/cm^2, respectively), and one tube for the control without the irradiation. The thermal neutron fluence was determined by averaging gold foils attached to the surface of the tube along the direction of incidence of the thermal neutrons. The cells were seeded on 60 mmφ dishes placed 5 mL culture medium (with FBS) by predetermined numbers (300 – 10000 cells/dish, see Table 5-2). After incubation in CO_2 incubator at 37 °C for 9 – 11 days, resulting colonies were fixed with 70%

ethanol and stained with 0.1% crystal violet solution. The numbers of colonies were counted by visual examination (naked eyes).

Analysis of total adsorbed protein (protein corona) by BCA assay

Mixtures of PBS dispersion (900 μL) of nanodrugs (net 0.20–1.0 mg) and FBS (100 μL) were incubated at 37 °C for 1 h. The mixtures were ultracentrifuged (434000*g*, 20 min). The lower layers (ca. 100 μL including pellet) were washed with water 3 times by repeating re-dispersion (total volume 1.0 mL) – ultracentrifugation procedures. SDS solution (20%, 100 μL) was added to each lower layer (ca. 100 μL) and ultracentrifuged. Resulting supernatant was transferred to 96-well microplate (20 μL × 4 wells for each material), and then PBS (80 μL), the mixture of solutions (100 μL) of reagent A and B of BCA assay kit were added. After the incubation at 37 °C for 1 h, absorbance of 570 nm was measured by the microplate reader. Calibration curve was created using BSA (bovine serum albumin) standard solution. The results are shown in Figure S5-3 (Appendix III).

TEM observation of cellular uptake

B16 cells were seeded on 8-well chamber slide (Nagel Nunc 177445) by 2.5×10^4 cells/well (3.0×10^4 cells/cm^2) in 400 μL of DMEM (Glucose 4.5 g/L, with 10% FBS) culture medium. After incubation in CO_2 incubator at 37 °C for 3 d, culture medium (400 μL, with or without FBS for FBS(+) or FBS(–) condition, respectively) was replaced once, PBS (control) or PBS dispersion of nanoparticles were added at predetermined concentration of each nanodrug, and the cells were further incubated for 24 h. The cells were washed with culture medium (two times) and PBS, then fixed in the mixture of 25% glutaraldehyde and 4% paraformaldehyde in 0.1 M phosphate buffer (1/10 (v/v)) for a couple of days in the refrigerator. Then the fixed cells were incubated with 1.5% potassium ferrocyanide followed by 2% osmium tetroxide in deionized water (DW) at 4 °C. After 1 h, the cells were washed with distilled water (DW) and fixed with 2% osmium tetroxide in DW at room temperature for 1 h. The specimens were then stained en bloc in a solution of 4% uranyl acetate dissolved in DW overnight for contrast enhancement and then washed with DW. Subsequently, the specimens were further stained with Walton's lead aspartate solution for 2 h, dehydrated with a dilution series of ethanol (60%, 70%, 80%, 90%, 99%, and 100%) and embedded in Epon 812. Ultrathin sections were made using an ultramicrotome (Leica UC7). Sections were stained with uranyl acetate and lead citrate and observed under an H-7650 electron microscope (HITACHI).

Statistical analysis

The differences between the groups were evaluated using Student's t test for two groups and a two-way analysis of variance (ANOVA) followed by Tukey's HSD test for multiple groups. For BNCT efficacy, significancy between the slope of fitted curve was evaluated.

Appendix III to Section 5

S5-1. Preparation of DND-PG-COOH

DND-PG (DND(+)-PG(h))

An aqueous dispersion of DND(+) (ζ-positive) was evaporated to dryness. The solid residue was dried at 105 °C for 2 h. To a suspension of resulting DND(+) powder (0.50 g) in ethylene glycol (3.74 g), glycidol (26.3 g, 0.35 mol) was added dropwise for 135 min to keep the temperature in the range of 95 – 100 °C. The resulting black dispersion was stirred at the same temperature for 28 h. After the reaction was cooled about 70 °C, water (40 mL) was added to degrade the unreacted glycidol. The dispersion was diluted with water to ca. 400 mL and concentrated with ultrafiltration membrane (Ultracel® membrane, 30 kDa) to < 20 mL. The concentrate was diluted and concentrated again, which was repeated twice.

To remove free PG, water dispersion of above concentrate (60 mL) was ultracentrifuged at 183400*g* (50000 rpm) for 2 h. Supernatant was removed carefully and remained lower layer was diluted and re-dispersed with water, and ultracentrifuged again (90 min), which was repeated three times. The resulting lower layer was adjusted to 50.0 g with water. An aliquot of the dispersion was accurately weighed (2.0586 g) and dried on heated PTFE sheet. From the weight of the residue (0.0820 g), the sample concentration was determined to be 3.98 % (w/w). The net yield of DND-PG was 1.99 g. FT-IR (DRIFT with KBr, cm^{-1}): 3332, 2918, 2875, 1456, 1118, 1075 (C–O). ^1H NMR (500 MHz, D_2O): δ ppm 3.42, 3.50, 3.58, 3.75, 3.88. Elemental analysis: C; 56.65%, H: 6.75%, N; 0.53%, O; 35.90%. TGA (Air atmosphere, 20 °C/min, % weight loss): 50–527 °C; 79.6%, 527–650 °C; 20.8% (PG/DND ratio was estimated to be 3.83).

DND-PG-COOH (Oxy-radical oxidation with 4-AcNH-TEMPO and $NaClO_2$)

Aqueous dispersion of purified DND-PG (3.98 % (w/w), 30.2 g, net 1.20 g, PG/DND 3.83) were added with 0.4 M acetate buffer (pH 4.7, 28 mL), $NaClO_2$ (content 81%, 169 mg, 1.5 mmol) and 4-AcNH-TEMPO (37.3 mg, 0.18 mmol). NaClO solution (111 μL, 0.20 mmol) was added into the mixture and the flask was equipped with an air-cooled condenser capped with a universal glass plug, then the reaction was heated at 50 °C for 24 h. The resulting dispersion was diluted with water to ca. 400 mL and concentrated with ultrafiltration membrane (Ultracel® membrane, 30 kDa) to < 10 mL. The concentrate was washed with water once by dilution and concentration with ultrafiltration membrane, and pH was adjusted to ca. 2.0 with 6 M HCl. The mixture was concentrated and then washed with water three times, and the weight of resulting black water dispersion was adjusted to 30.0 g with water. An aliquot of the dispersion was accurately weighed and dried on heated PTFE sheet. From the weight of the residue, the concentration was determined to be 2.95 % (w/w). The net yield of DND-PG-COOH was 0.884 g. COOH concentration was determined by acid-base titration to be 1.01 mmol/g. Elemental analysis: C; 54.39%, H: 6.48%, N; 0.51%, O; 36.94%. TGA (Air atmosphere, 20 °C/min, % weight loss): 50–531 °C; 79.8%, 531–650 °C; 20.7% (PG/DND ratio was estimated to be 3.85).

S5-2. Composition of components in nanodrugs and intermediates

S5-2-1. DND-PG(OTs)-COOH

(i) Elemental composition of DND-PG-COOH raw material (see Experimental in the main article)

Table S5-1. Elemental compositions of each component in DND-PG-COOH.

PG/DND ratio (TGA)	***A***	3.85
PG layer content (g/1 g DND-PG-COOH)	***B*** = ***A*** / (***A*** + 1)	0.794
COOH content in DND-PG-COOH (mmol/g)	***C***	1.01
COOH content in PG layer (mmol/g)	***D***	1.27
Glyceric acid unit (g/1 g DND-PG-COOH)	***E*** = ***C*** × 88.06 / 1000	0.089
Glycerol unit (g/1 g DND-PG-COOH)	***F*** = ***B*** – ***E***	0.705
DND core (g/1 g DND-PG-COOH)	***G*** = 1 – ***E*** – ***F***	0.206

		H (%)	C (%)	N (%)	O (%)
Elemental analysis of DND-PG-COOH	***H***	6.68	56.54	0.55	35.87
Elemental composition of glycerol unit as glycidol	***I***	8.16	48.64		43.19
Elemental composition of glyceric acid unit as 2,3-epoxypropionic acid	***J***	4.58	40.92		54.50
Glycerol unit (glycidol, for $C_3H_6O_2$, 70.5%) in DND-PG-COOH	***K*** = ***I*** × ***F***	5.75	34.29		30.44
Glyceric acid (2,3-epoxypropionic acid, for $C_3H_4O_3$, 8.9%)	***L*** = ***J*** × ***E***	0.41	3.64		4.85
Elemental composition of PG layer in DND-PG-COOH	***M*** = ***K*** + ***L***	6.16	37.93		35.29
PG layer	***N*** = ***M*** / ***B***	7.76	47.78		44.46
Elemental composition of DND core in DND-PG-COOH	***O*** = ***H*** – ***M***	0.52	18.61	0.55	0.58
DND core	***P*** = ***O*** / ***G***	2.50	90.29	2.67	2.81

(ii) Composition of DND-PG(OTs)-COOH

Based on the elemental compositions in DND-PG-COOH as shown above, PG/DND ratio in DND-PG(OTs)-COOH is calculated since the loss in PG chain (cleavage of ether linkage) is speculated. From the elemental analysis result, proportion of –OTs, PG layer and DND core is calculated so that the sum of the squared deviations of H, C, N, O and S contents is to be the least value. As the result, calculated PG/DND ratio in DND-PG(OTs)-COOH is 2.49 (PG content 71.3%) whereas that of DND-PG-COOH is 3.85 (PG content 79.4%) that implies about 35.4% ((3.85 – 2.49) / 3.85) of PG chain has been lost in the tosylation. The –OTs content is calculated to be 1.22 mmol/g from the S content (1000 × 0.0392 / 32.07), which corresponds to 1.59 mmol on 1 g of DND-PG-COOH.

The COOH content is reduced due to the loss of PG chain. It is estimated to be 0.669 mmol/g (1.27 mmol/g × 54.72%) in DND-PG(OTs)-COOH that corresponds to 0.907 mmol/g in the DND-PG-COOH component.

Table S5-2. Estimation of composition ratio of DND-PG(OTs)-COOH.

		H (%)	C (%)	N (%)	O (%)	S (%)	Total
Elemental analysis of DND-PG(OTs)-COOH	$\boldsymbol{Q}$	5.46	56.85	0.51	29.08	4.08	95.98
Elemental composition of –OTs (calculated for $C_7H_6O_2S$) [a]	$\boldsymbol{R}$	3.92	54.53		20.75	20.80	100.00
PG layer	$\boldsymbol{M}$ [b]	7.76	47.78		44.46		99.99
DND core	$\boldsymbol{P}$	2.50	90.29	2.67	2.81		98.26
Fitted composition of –OTs	$\boldsymbol{R'}$ [c]	0.74	10.28		3.91	3.92	19.36
PG layer	$\boldsymbol{M'}$ [c]	4.25	26.14		24.33		54.72
DND core	$\boldsymbol{P'}$ [c]	0.56	20.22	0.60	0.63		22.01
Total (DND-PG(OTs)-COOH)	$\boldsymbol{S} = \boldsymbol{R'} + \boldsymbol{M'} + \boldsymbol{P'}$	5.55	56.65	0.60	28.87	3.92	95.96
Deviation	$\boldsymbol{T} = \boldsymbol{Q} - \boldsymbol{S}$	–0.99	0.20	–0.09	0.21	0.16	

[a] As TsOH (*p*-toluenesulfonic acid) – H_2O

[b] Assuming that the composition of glycerol and glyceric acid unit is not changed before and after the tosylation.

[c] Obtained by the calculation so that the sum of squared deviations ($\Sigma(\boldsymbol{T}^2)$) becomes the least.

For comparison, DND-PG (without carboxy group) was tosylated via Schotten-Baumann reaction under identical conditions. As a result, estimated PG/DND ratio in DND-PG-OTs is 2.89 (47.78/16.55) while that of DND-PG is 3.83. About 24.6% of PG chain has been lost in the tosylation indicating that the same phenomenon occurs regardless of the existence of –COOH.

Table S5-3. Estimation of composition ratio of DND-PG-OTs via Schotten-Baumann reaction.

	H (%)	C (%)	N (%)	O (%)	S (%)	Total
Elemental analysis of DND-PG-OTs	5.60	56.61	0.32	28.12	6.99	97.84
Elemental composition of –OTs (calculated for $C_7H_6O_2S$) [a]	3.92	54.53		20.75	20.80	100.00
PG layer [b]	8.16	48.64		43.19		99.99
DND core	2.50	90.29	2.67	2.81		98.26
Fitted composition of –OTs [c]	1.29	18.00		6.85	6.87	33.02
PG layer [c]	3.90	23.24		20.64		47.78
DND core [c]	0.42	15.20	0.45	0.47		16.55
Total (DND-PG-OTs)	5.61	56.45	0.45	27.98	6.87	97.34
Deviation	–0.01	0.16	–0.13	0.16	0.12	

[a] As TsOH (*p*-toluenesulfonic acid) – H_2O

[b] PG/DND of DND-PG is 3.83.

[c] Obtained by the calculation so that the sum of squared deviations ($\Sigma(\boldsymbol{T}^2)$) becomes the least.

S5-2-2. DND-PG(N_3)-COOH

The content of –N_3 is calculated based on the fitted elemental composition of DND-PG-COOH in DND-PG(OTs)-COOH. From the difference in N contents between DND-PG-COOH (fitted) and DND-PG(N_3)-COOH, –N_3 content is estimated to be 4.72% corresponding 1.12 mmol/g as shown in Table S5-4. That corresponds to 1.16 mmol on 1 g of DND-PG-COOH; the reaction (conversion) yield (–OTs to –N_3) is 72.5%. The COOH content is estimated to be 0.882 mmol/g.

Table S5-4. Estimation of composition ratio of DND-PG(N_3)-COOH.

		H (%)	C (%)	N (%)	O (%)
Elemental analysis result of DND-PG(N_3)-COOH	$\boldsymbol{U}$	5.54	55.28	5.46	30.86
Fitted elemental composition of DND-PG-COOH	$\boldsymbol{V} = \boldsymbol{M'} + \boldsymbol{P'}$	4.81	46.22	0.59	24.98
Normalized composition	$\boldsymbol{W} = \boldsymbol{V} / (54.72 + 22.02) \times 100$	6.28	60.34	0.77	32.61
Calculated amount of –N_3 based on the difference in N content		4.72% (1.12 mmol/g)			

$$W_{N_3}(\%) = \frac{N_{DND-PG(N_3)-COOH} - N_{DND-PG-COOH}}{N_{N_3} - N_{DND-PG-COOH}} \times 100$$

S5-2-3. DND-PG($^{10}B_{12}H_{11}^{2-}$)-COOH

The amount of $^{10}B_{12}H_{11}^{2-}$ moiety was calculated by the change in C content by elemental analysis to be 17.3% (0.70 mmol/g as $^{10}B_{12}H_{11}^{2-}$ moiety and 8.36% as ^{10}B) that is consistent to the ICP result (7.97%). From the ICP result, the amount of $^{10}B_{12}H_{11}^{2-}$ moiety is 16.5% and 0.664 mmol/g. The reaction yield is 70.8% (0.664 / (1 – 0.165) / 1.12). Calculation based on N contents gives larger number inconsistent to $-N_3$ content in DND-PG(N_3)-COOH. The COOH content is estimated to be 0.737 mmol/g.

Table S5-5. Estimation of the amount of $^{10}B_{12}H_{11}^{2-}$ moiety by elemental analysis.

	H (%)	C (%)	N (%)	O (%)	S (%)	^{10}B (%)	Na (%)
DND-PG(N_3)-COOH	5.54	55.28	5.46	30.86			
DND-PG($^{10}B_{12}H_{11}^{2-}$)-COOH	5.33	48.22	3.78				
[($^{10}B_{12}H_{11}^{2-}$)S](Pgy)·2Na (calculated for $C_3H_{14}{}^{10}B_{12}Na_2S$ = 248.19) [d]	5.69	14.52			12.92	48.35	18.53
Calculated amount of $^{10}B_{12}H_{11}^{2-}$ moiety based on the difference of C content [e]					17.3% (0.698 mmol/g)		

$$W_{[(^{10}B_{12}H_{11}{}^{2-})S](Pgy)}(\%) = \frac{C_{DND-PG(^{10}B_{12}H_{11}{}^{2-})-COOH} - C_{DND-PG(N_3)-COOH}}{C_{[(^{10}B_{12}H_{11}{}^{2-})S](Pgy)} - C_{DND-PG(N_3)-COOH}} \times 100$$

[d] Assuming the boron cluster takes 2Na salt since methyl group from tetramethylammonium group is not detected in ^1H NMR.

[e] Status of carboxylate moiety is not considered (–COOH or –COONa).

S5-2-4. DND-PG($^{10}B_{12}H_{11}^{2-}$)-PBA

The loading amount of PBA moiety was calculated by the change of N content before and after the amide formation. Calculation by C content was not conducted since the difference in C content between DND-PG($^{10}B_{12}H_{11}^{2-}$)-COOH and PBA was small. As shown in Table S5-6, PBA moiety is introduced in 4.74% (0.40 mmol/g). The ^{10}B content is calculated to be 7.59%. The reaction yield from –COOH to amide is 56.9%.

Table S5-6. Estimation of the amount of PBA moiety.

	H (%)	C (%)	N (%)
DND-PG($^{10}B_{12}H_{11}^{2-}$)-COOH	5.33	48.22	3.78
DND-PG($^{10}B_{12}H_{11}^{2-}$)-PBA	5.10	51.35	4.16
PBA ($C_6H_8BNO_2$ = 136.95)	5.89	52.62	10.23
PBA – H_2O (C_6H_6BNO = 118.93)	5.08	60.59	11.79
Calculated amount of PBA moiety (as PBA – H_2O) based on the difference in N content [g]	4.74% (0.40 mmol/g)		

$$W_{PBA-H2O}(\%) = \frac{N_{DND-PG(^{10}B_{12}H_{11}{}^{2-})-PBA} - N_{DND-PG(^{10}B_{12}H_{11}{}^{2-})-COOH}}{N_{PBA-H2O} - N_{DND-PG(^{10}B_{12}H_{11}{}^{2-})-COOH}} \times 100$$

[g] $^{10}B_{12}H_{11}^{2-}$ moiety is considered to exist as 2Na salt, and the status of unreacted carboxylate moiety is not considered (–COOH or –COONa).

5. DND-PG($^{10}B_{12}H_{11}^{2-}$)-c(RGDyK)

The loading amount of RGD peptide is estimated by integration value of tyrosine (Tyr) as shown in Table S5-7. The amount of c(RGDyK) is very small probably due to the unoptimized reaction condition.

Table S5-7. Estimation of the amount of RGD peptide.

Proportion of DND-PG-COOH in DND-PG($^{10}B_{12}H_{11}^{2-}$)-COOH (see S5-2-3, 100% – 16.5%)	83.5%
PG/DND ratio (see S5-2-1(ii))	71.3%
Proportion of glycerol unit	88.8%
Proportion of glyceric acid unit	11.2%
Molar amount of monomer unit in 1 g of PG layer	12.7 mmol
in DND-PG($^{10}B_{12}H_{11}^{2-}$)-COOH	7.53 mmol
Average number of aliphatic protons in 1 monomer unit	4.80
Ratio of integration value of Tyr (aromatic, 4H) to PG layer in ^{1}H NMR	0.0015
Molar ratio of Tyr to PG (monomer unit)	0.0018
Molecular weight of c(RGDyK) (free form)	605.65
Loading amount of c(RGDyK) on 1 g of DND-PG($^{10}B_{12}H_{11}^{2-}$)-COOH in mole	0.0136 mmol
by weight	8.22 mg
content in DND-PG($^{10}B_{12}H_{11}^{2-}$)-c(RGDyK)	0.82%
^{10}B content	7.91%

S5-3. Synthesis of [$^{10}B_{12}H_{11}S^{2-}$](Pgy)

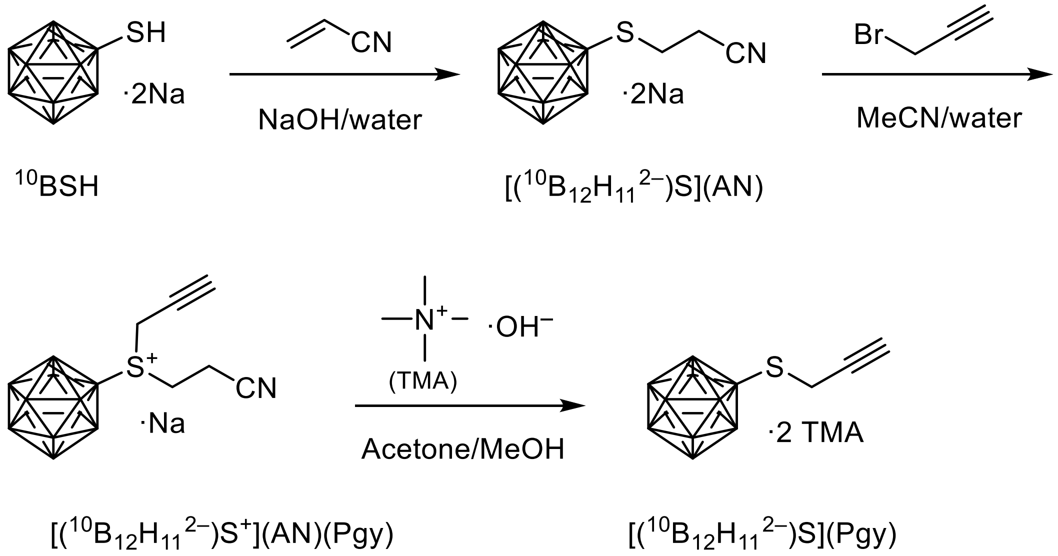

Scheme S5-1. Synthetic scheme of [$^{10}B_{12}H_{11}S^{2-}$](Pgy).

Bis(tetramethylammonium) *S*-(2-propynyl)thioundecahydro-*closo*-dodecaborate(^{10}B) ([($^{10}B_{12}H_{11}{}^{2-}$)S](Pgy)·2TMA)

Aqueous NaOH solution (10 wt%, 192 μL, net 19.2 mg, 0.48 mmol) was added in water (4.0 mL) and the mixture was vacuum degassed with sonication. Sodium mercaptoundecahydro-*closo*-dodecaborate(^{10}B) (^{10}BSH, 100.9 mg, 0.48 mmol) was dissolved, then acrylonitrile (60 μL, 0.92 mmol) was added. The mixture was stirred at room temperature under nitrogen atmosphere for 5 h. The aqueous solution was washed with ethyl acetate (ca. 10 mL) three times and the aqueous layer was evaporated to give colorless oil (204 mg) of *S*-(2-cyanoethyl)thioundecahydro-*closo*-dodecaborate(^{10}B) ([($^{10}B_{12}H_{11}{}^{2-}$)S](AN)). ESI-MS (negative, m/z): Anal. 108.6245 (M^{2-}); Calc. for $(C_3H_{15}{}^{10}B_{12}NS)^{2-}$ 217.2478.

The oil of [($^{10}B_{12}H_{11}{}^{2-}$)S](AN) was dissolved in the mixture of acetonitrile (MeCN, 20.0 mL) and water (5.0 mL), and added a solution of propargyl bromide (199 μL, 314 mg, 2.64 mmol) in MeCN (2.0 mL) and water (0.50 mL) slowly, then the mixture was stirred at room temperature overnight. The reaction was evaporated to dryness, and the residue was added with MeCN and evaporated again to remove remained water. MeCN (~10 mL) was added to the residue and insoluble salt was filtered off. The filtrate was evaporated to give a crude product of *S,S*-[(2-cyanoethyl)-(2-propynyl)]sulfonioundecahydro-*closo*-dodecaborate(^{10}B) ([($^{10}B_{12}H_{11}{}^{2-}$)S^{+}](AN)(Pgy)) as pale-yellow oil (170 mg). ESI-MS (negative, m/z): Anal. m/z 256.2669 (M^{-}); Calc. for $(C_6H_{18}{}^{10}B_{12}NS)^{-}$ 256.2712.

The crude [($^{10}B_{12}H_{11}{}^{2-}$)S^{+}](AN)(Pgy) was dissolved in acetone (2.0 mL) and added with methanol solution of tetramethylammonium hydroxide (10 wt%, 1.04 mL, 0.96 mmol) resulting in white precipitate. The precipitate was collected by filtration. The residue was washed with small amount of acetone then dried *in vacuo* at room temperature to give bis(tetramethylammonium) *S*-(2-propynyl)thioundecahydro-*closo*-dodecaborate(^{10}B) ([($^{10}B_{12}H_{11}{}^{2-}$)S](Pgy)·2TMA) as off-white to pale yellow powder. Yield 151 mg (theoretical yield 167 mg). The product was used for the click reaction without further purification although it might contain inorganic salt (NaBr) as an impurity. The filtrate was once evaporated to dryness and suspended in acetone to obtain pale yellow powder material (36.2 mg). ESI-MS (negative, m/z): Anal. m/z 101.1172 (M^{2-}); Calc. for $(C_3H_{14}{}^{10}B_{12}S)^{2-}$ 202.2369.

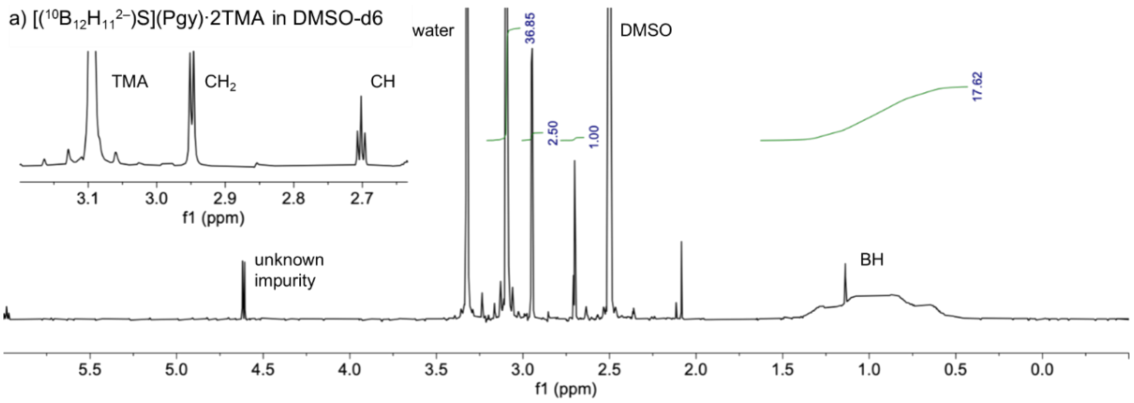
a) [($^{10}B_{12}H_{11}^{2-}$)S](Pgy)·2TMA in DMSO-d6

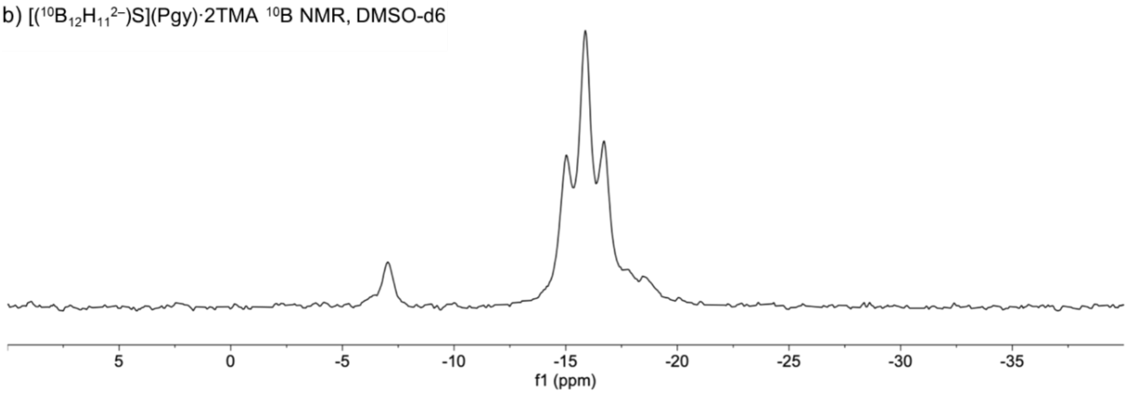
b) [($^{10}B_{12}H_{11}^{2-}$)S](Pgy)·2TMA ^{10}B NMR, DMSO-d6

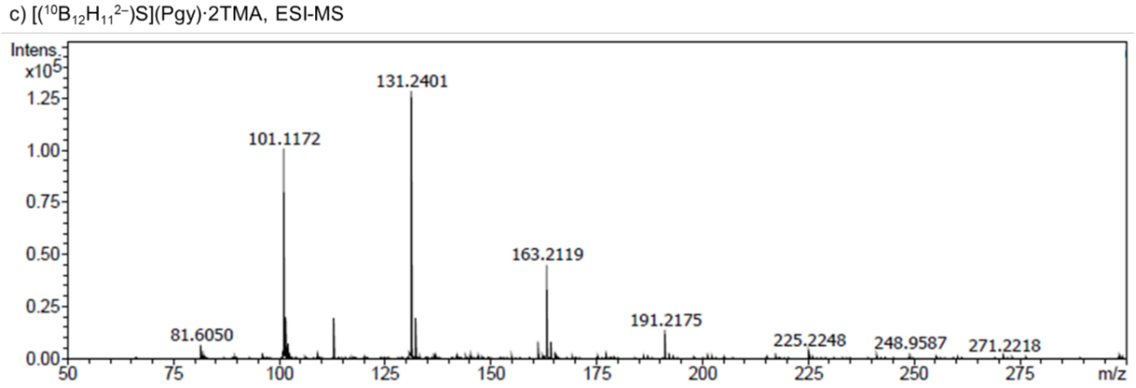
c) [($^{10}B_{12}H_{11}^{2-}$)S](Pgy)·2TMA, ESI-MS

Figure S5-1. a) ^{1}H NMR and b) ^{10}B NMR spectra of [($^{10}B_{12}H_{11}^{2-}$)S](Pgy) in DMSO-d$_6$, and c) ESI-MS spectrum of [($^{10}B_{12}H_{11}^{2-}$)S](Pgy). In NMR spectra, signal of DMSO at 2.50 ppm in ^{1}H NMR and ^{10}B(OH)$_3$ at 19.49 ppm in ^{10}B NMR are set as references.

S5-4. ζ-Potential of nanodrugs and protein corona formation

ζ-potential of nanodrugs were measured in PBS as shown in Figure S5-2. The samples with $^{10}B_{12}H_{11}^{2-}$ moiety exhibited lower ζ-potential than the samples without $^{10}B_{12}H_{11}^{2-}$ moiety. It may be because the boron cluster takes a divalent anion form making a 26 (4n + 2) delocalized electron system, and this negative charge is thought to be stable (strong).

Then, the amount of adsorbed serum protein on each material was evaluated. Aqueous dispersion of nanodrug samples with and without $^{10}B_{12}H_{11}^{2-}$ and targeting moieties, and unmodified DND core and DND-PG as references, were incubated in phosphate buffered saline (PBS) with 10% FBS. After washing with water, adsorbed proteins were detached and subjected to the bicinchoninic acid assay (BCA assay) to quantify as total protein. As the result, nanodrugs with $^{10}B_{12}H_{11}^{2-}$ moiety exhibited protein corona formation in 88.7–133.4 μg on 1.0 mg of nanodrug (purple bars in Figure S5-3), whereas almost no protein was adsorbed without $^{10}B_{12}H_{11}^{2-}$ moiety as the surface should have negative charge by mild acidic –COOH (red bars). The stronger negative charge of $^{10}B_{12}H_{11}^{2-}$ should have taken part in the electrostatic interaction with serum proteins. moiety Compared with DND core (blue bars), the amount of adsorbed protein on $^{10}B_{12}H_{11}^{2-}$ functionalized materials (purple bars) is moderate that does not make sedimentations in the presence of FBS, but it is larger than unmodified DND-PG (green bars) indicating some influences should have occurred by the protein corona formation.

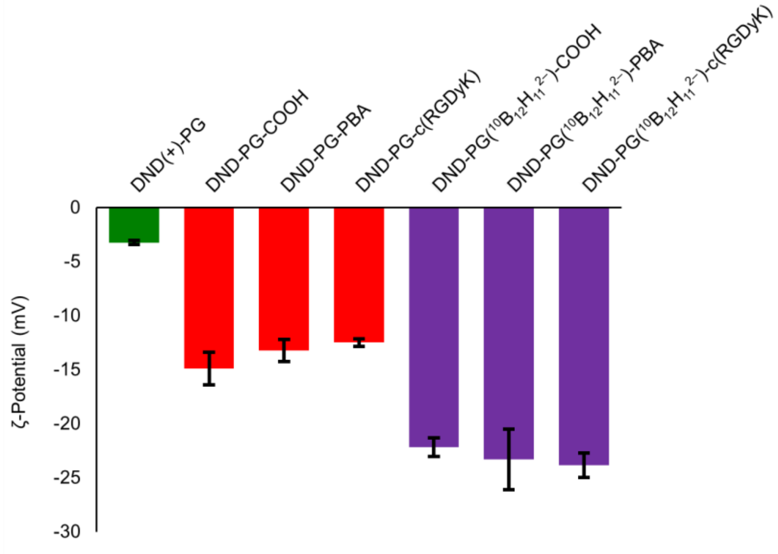

Figure S5-2. ζ-Potential of nanodrugs in PBS (sample concentration: 0.1 wt%).

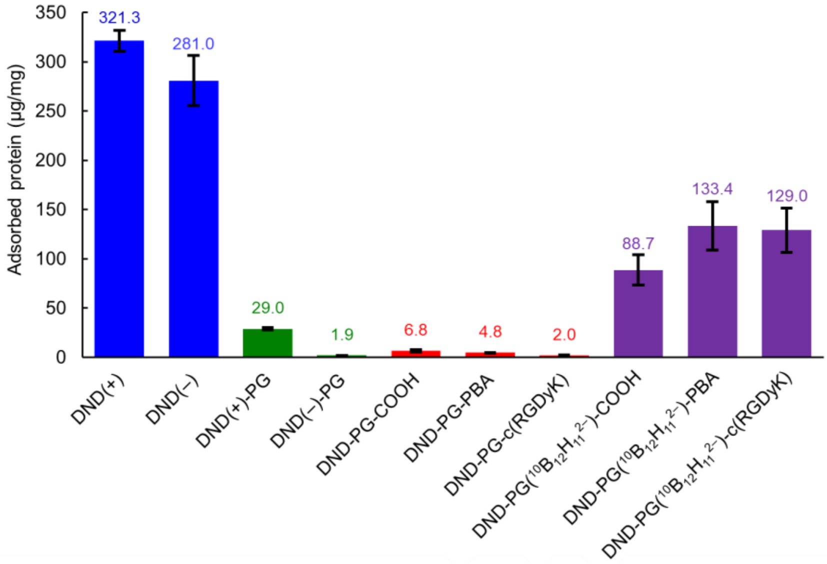

Figure S5-3. The amount of adsorbed protein on the surface of unmodified DNDs (blue bars), DND-PGs (green) and DND-PG-COOH relevant nanodrugs with and without $^{10}B_{12}H_{11}{}^{2-}$ moiety (red and purple, respectively). DND(+) and DND(–) represent DNDs of positive and negative -1-potentials, respectively. All DND-PG-COOH relevant nanodrugs in red and purple are made of DND(+). The contents of PG layer in DND(+)-PG and DND(–)-PG are 66.3% and 62.5%, respectively.

Chapter 6: Conclusion

In this thesis, the author first worked for precise and quantitative elucidations of the structure of PG functionalized NDs (DNDs and HPHT-NDs) with the development of the scalable and safe process that can control the amount of PG loadings (PG/ND ratio) precisely. Based on the results, further modification on DND-PG, quantitative characterization and biological evaluation were conducted for boron-10 carriers as BNCT agents.

In the PG functionalization process, EG was used as a solvent along with dropwise-addition of GD, which would prevent unexpected runaway reactions to make the ring-opening polymerization of GD safer. It was found that PG/ND ratios in ND-PGs can be theoretically predicted and controlled by the properties of ND core, the diameter, the oxygen content, and the reaction conditions; the amounts (weights) of GD, ND and EG. In ^{13}C NMR analysis of the resulting ND-PGs, the substructure abundances of monomer (glycerol) units were estimated, by which the amount of primary –OH group is quantified in combination with TGA result. In addition, behaviors in DLS measurement by the sample concentration and ionic strength in the dispersion were investigated to find the conditions to give reliable data. From DLS results under the conditions, the thickness of PG layer in aqueous dispersion, or the length of PG chain, was determined. The differences in the sizes determined by DLS and calculated by TGA indicate that the PG chain in DND-PG might be flexible to swell with water in aqueous dispersion probably due to the higher curvature of DND.

Novel –COOH containing PG functionalized DNDs was developed via the oxidation of primary alcohol in PG chain to carboxy group with nitroxyl radical catalysts known as TEMPO. The reaction can be performed under aqueous conditions with inexpensive fundamental inorganic oxidant like $NaClO_2$ with small amounts of NaClO. Behavior of the reaction was investigated to find that the amount of COOH can be precisely controlled in an almost stoichiometric manner for a range of COOH content ≤ 1 mmol/g while the cleavage of PG chain occurs with the large amount of oxidant for the larger COOH content. The product with controlled COOH content can be applied to further functionalization for various applications.

As for the biomedical application based on DND-PGs, PBA functionalized DND-PG for a BNCT agent was synthesized via multistep chemical transformation. ^{10}B-enriched PBA moiety was introduced to contain the percent order of boron-10 atoms via reductive amination of the corresponding aldehyde with DND-PG-NH_2 to give DND-PG-PBA. To grant the good dispersibility under physiological conditions, PBA with boronic acid moiety at the *o*-position of the aldehyde, corresponding to aminomethyl group after the reductive amination, was employed to form the Wulff-type coordination. To address the aggregation problem in the presence of serum protein, the amino groups of DND-PG-PBA were succinylated and methylated. The resulting nanodrug was confirmed to be accumulated in the tumor tissue and exert BNCT efficacy upon the neutron irradiation.

Since BNCT efficacy of the above nanodrug was thought to be insufficient, another boron delivery agent with a boron cluster, $^{10}B_{12}H_{11}^{2-}$ moiety, and an active targeting moiety, PBA or RGD peptide, was designed and synthesized. To construct the nanodrug, $^{10}B_{12}H_{11}^{2-}$ moiety was first conjugated by click chemistry at the –OH groups of ND-PG-COOH, which was prepared by the oxidation of DND-PG described above. Then, PBA or c(RGDyK) moiety was introduced at the –COOH groups through amide linkage. The nanodrugs have ^{10}B content of 7.6 – 8.0% that is much higher than the previous one and exhibit good dispersibility under physiological conditions. *In vitro* neutron irradiation experiments exhibited high BNCT efficacies in nanodrugs with $^{10}B_{12}H_{11}^{2-}$ moiety, showing small differences with and without targeting moieties. TEM observations of the cells treated with the nanodrugs indicate that $^{10}B_{12}H_{11}^{2-}$ moiety itself facilitates cellular uptake much more than the active targeting moieties of PBA and c(RGDyK) due to the negative charge of the boron cluster, resulting in similar BNCT efficacies among these nanodrugs.

The results in this thesis should provide useful information for the precise and quantitative design and preparation of ND-PGs including DND-PGs, and further chemical transformation of ND-PGs especially for biomedical application ranging from the laboratory scale to clinical and industrial purposes. In addition, through the precise control of ND-PGs and their related materials, the door to new insights in the behaviors of ND-PGs *in vivo* might be opened. The BNCT nanodrug based on ND-PG and ND-PG-COOH would serve as lead materials of BNCT agent, especially by combining with the prominent properties of ND core such as fluorescent property. The multiple functionalization process in this thesis can be applied to nanodrugs with a variety of structural and functional features. The author expects to create more effective nanodrugs for BNCT in near future.

References

1. E. Osawa and D. Ho, Nanodiamond and its application to drug delivery, *J. Med. Allied Sci.* **2012**, *2*, 31–40.
   https://jmas.in/?mno=210538
2. V. N. Mochalin, O. Shenderova, D. Ho and Y. Gogotsi, The properties and applications of nanodiamonds, *Nat. Nanotechnol.* **2012**, *7*, 11–23.
   https://doi.org/10.1038/nnano.2011.209
3. A. Y. Vul', A. T. Dideikin, A. E. Aleksenskii and M. V. Baidakova, "Detonation Nanodiamonds: Synthesis, Properties and Applications", Nanodiamond. O. A. Wiiliams, ed. Royal Society of Chemistry, 27–48, 2014.
   ISBN: 978-1-84973-639-8
4. V. V. Danilenko, Specific features of synthesis of detonation nanodiamonds, *Combust. Explos. Shock Waves* **2005**, *41*, 577–588.
   https://doi.org/10.1007/s10573-005-0072-5
5. V. Y. Dolmatov, V. Myllymaki and A. Vehanen, A possible mechanism of nanodiamond formation during detonation synthesis, *J. Superhard Mater.* **2013**, *35*, 143–150.
   https://doi.org/10.3103/S1063457613030039
6. E. Osawa, Monodisperse single nanodiamond particulates, *Pure Appl. Chem.* **2008**, *80*, 1365–1379.
   https://doi.org/10.1351/pac200880071365
7. A. Krueger, F. Kataoka, M. Ozawa, T. Fujino, Y. Suzuki, A.E. Aleksenskii, A. Y. Vul' and E. Osawa, Unusually tight aggregation in detonation nanodiamond: Identification and disintegration, *Carbon* **2005**, *43*, 1722–1730.

https://doi.org/10.1016/j.carbon.2005.02.020

8. K. Turcheniuk and V. N. Mochalin, Biomedical applications of nanodiamond (Review), *Nanotechnology* **2017**, *28*, 252001.
https://doi.org/10.1088/1361-6528/aa6ae4

9. K. P. Loh, D. Ho, G. N. C. Chiu, D. T. Leong, G. Pastorin and E. K. H. Chow, Clinical applications of carbon nanomaterials in diagnostics and therapy, *Adv. Mater.* **2018**, *30*, 1802368.
https://doi.org/10.1002/adma.201802368

10. A. M. Schrand, H. Huang, C. Carlson, J. J. Schlager, E. Ōsawa, S. M. Hussain and L. Dai, Are diamond nanoparticles cytotoxic?, *J. Phys. Chem. B.* **2007**, *3*, 2–7.
https://doi.org/10.1021/jp066387v

11. L. Moore, J. Yang, T. T. Ha Lan, E. Osawa, D.-K. Lee, W. D. Johnson, J. Xi, E. K.-H. Chow and D. Ho, Biocompatibility assessment of detonation nanodiamond in non-human primates and rats using histological, hematologic, and urine analysis, *ACS Nano* **2016**, *10*, 7385–7400.
https://doi.org/10.1021/acsnano.6b00839

12. K. J. van der Laan, M. Hasani, T. Zheng and R. Schirhagl, Nanodiamonds for *in vivo* applications, *Small* **2018**, *14*, 1703838.
https://doi.org/10.1002/smll.201703838

13. Y. Zhu, J. Li, W. Li, Y. Zhang, X. Yang, N. Chen, Y. Sun, Y. Zhao, C. Fan and Q. Huang, The biocompatibility of nanodiamonds and their application in drug delivery systems, *Theranostics* **2012**, *2*, 302–312.
https://doi.org/10.7150%2Fthno.3627

14. D. Terada, T. Genjo, T. F. Segawa, R. Igarashi and M. Shirakawa, Nanodiamonds for bioapplications–specific targeting strategies, *BBA-Gen. Subjects* **2020**, *1864*, 129354.

https://doi.org/10.1016/j.bbagen.2019.04.019

15. D. Terada, T. F. Segawa, A. I. Shames, S, Onoda, T. Ohshima, E. Osawa, R. Igarashi and M. Shirakawa, Monodisperse five-nanometer-sized detonation nanodiamonds enriched in nitrogen-vacancy centers, *ACS Nano* **2019**, *13*, 6461–6468.
https://doi.org/10.1021/acsnano.8b09383

16. L. P. McGuinness, Y. Yan, A. Stacey, D. A. Simpson, L. T. Hall, D. Maclaurin, S. Prawer, P. Mulvaney, J. Wrachtrup, F.Caruso, R. E. Scholten and L. C. L. Hollenberg, Quantum measurement and orientation tracking of fluorescent nanodiamonds inside living cells, *Nat. Nanotechnol.* **2011**, *6*, 358–363.
https://doi.org/10.1038/nnano.2011.64

17. A. Krueger and D. Lang, Functionality is key: Recent progress in the surface modification of nanodiamond, *Adv. Funct. Mater.* **2012**, *22*, 890–906.
https://doi.org/10.1002/adfm.201102670

18. G. Reina, L. Zhao, A. Bianco and N. Komatsu, Chemical functionalization of nanodiamonds: Opportunities and challenges ahead, *Angew. Chem. Int. Ed.* **2019**, *131*, 18084–18095.
https://doi.org/10.1002/anie.201905997

19. E. K. Chow, X.-Q. Zhang, M. Chen, R. Lam, E. Robinson, H. Huang, D. Schaffer, E. Osawa, A. Goga and D. Ho, Nanodiamond therapeutic delivery agents mediate enhanced chemoresistant tumor treatment, *Sci. Transl. Med.* **2011**, *3*, 73ra21.
https://doi.org/10.1126/scitranslmed.3001713

20. Y. Yu, M. Nishikawa, M. Liu, T. Tei, S. C. Kaul, R. Wadhawa, M. Zhang, J. Takahashi and E. Miyako, Self-assembled nanodiamond supraparticles for anticancer chemotherapy, *Nanoscale* **2018**, *10*, 8969–8978.
https://doi.org/10.1039/C8NR00641E

21. Y. Yu, X. Yang, M. Liu, M. Nishikawa, T. Tei and E. Miyako, Amphipathic nanodiamond supraparticles for anticancer drug loading and delivery, *ACS Appl. Mater. Interfaces* **2019**, *11*, 18978–18987. https://doi.org/10.1021/acsami.9b04792
22. D.-K. Lee, S. V. Kim, A. N. Limansubroto, A. Yen, A. Soundia, C.-Y. Wang, W. Shi, C. Hong, S. Tetradis, Y. Kim, N.-H. Park, M. K. Kang and D. Ho, Nanodiamond–gutta percha composite biomaterials for root canal therapy, *ACS Nano* **2015**, *9*, 11490–11501. https://doi.org/10.1021/acsnano.5b05718
23. Z. Xing, T. O. Pedersen, X. Wu, Y. Xue, Y. Sun, A. Finne-Wistrand, F. R. Kloss, T. Waag, A. Krueger, D. Steinmuller-Nethl and K. Mustafa, Biological effects of functionalizing copolymer scaffolds with nanodiamond particles, *Tissue Eng. Part A* **2013**, *19*, 1783–1791. https://doi.org/10.1089/ten.tea.2012.0336
24. J.-R. Bertrand, C. Pioche-Durieu, J. Ayala, T. Petit, H. A. Girard, C. P. Malvy, E. L. Cam, F. Treussart and J.-C. Arnault, Plasma hydrogenated cationic detonation nanodiamonds efficiently deliver to human cells in culture functional siRNA targeting the Ewing sarcoma junction oncogene, *Biomaterials* **2015**, *45*, 93–98. https://doi.org/10.1016/j.biomaterials.2014.12.007
25. X.-Q. Zhang, M. Chen, R. Lam, X. Xu, E. Osawa and D. Ho, Polymer-functionalized nanodiamond platforms as vehicles for gene delivery, *ACS Nano* **2009**, *3*, 2609–2616. https://doi.org/10.1021/nn900865g
26. Y. Yu, X. Yang, M. Liu, M. Nishikawa, T. Tei and E. Miyako, Multifunctional cancer phototherapy using fluorophore-functionalized nanodiamond supraparticles, *ACS Appl. Bio Mater.* **2019**, *2*, 3693–3705. https://doi.org/10.1021/acsabm.9b00603
27. R. Grall, H. Girard, L. Saad, T. Petit, C. Gesset, M. Combis-Schlumberger, V. Paget, J.

Delic, J.-C. Arnault and S. Chevillard, Impairing the radioresistance of cancer cells by hydrogenated nanodiamonds, *Biomaterials* **2015**, *61*, 290–298. https://doi.org/10.1016/j.biomaterials.2015.05.034

28. M. Kurzyp, H. A. Girard, Y. Cheref, E. Brun, C. Sicard-Roselli, S. Saada and J.-C Arnault, Hydroxyl radical production induced by plasma hydrogenated nanodiamonds under X-ray irradiation, *Chem. Commun.* **2017**, *53*, 1237–1240. https://doi.org/10.1039/C6CC08895C

29. M. D. Torelli, N. A. Nunn and O. A. Shenderova, A perspective on fluorescent nanodiamond bioimaging, *Small* **2019**, *15*, 1902151. https://doi.org/10.1002/smll.201902151

30. P. Reineck, M. Capelli, D. W. M. Lau, J. Jeske, M. R. Field, T. Ohshima, A. D. Greentree and B. C. Gibson, Bright and photostable nitrogen-vacancy fluorescence from unprocessed detonation nanodiamond, Nanoscale **2017**, *9*, 497–502. https://doi.org/10.1039/C6NR07834F

31. B. R. Smith, D. W. Inglis, B. Sandnes, J. R. Rabeau, A. V. Zvyagin, D. Gruber, C. J. Noble, R. Vogel, E. Osawa and T. Plakhotnik, Five-nanometer diamond with luminescent nitrogen-vacancy defect centers, *Small* **2009**, *5*, 1649–1653. https://doi.org/10.1002/smll.200801802

32. S. Sotoma, D. Terada, T. F. Segawa, R. Igarashi, Y. Harada and M. Shirakawa, Enrichment of ODMR-active nitrogen-vacancy centres in five-nanometre-sized detonation-synthesized nanodiamonds: Nanoprobes for temperature, angle and position, *Sci. Rep.* **2018**, *8*, 5463. https://doi.org/10.1038/s41598-018-23635-5

33. F. T.-K. So, A. I. Shames, D. Terada, T. Genjo, H. Morishita, I. Ohki, T. Ohshima, S. Onoda, H. Takashima, S. Takeuchi, N. Mizuochi, R. Igarashi, M. Shirakawa and T. F.

Segawa, Anomalous formation of irradiation-induced nitrogen-vacancy centers in 5 nm-sized detonation nanodiamonds, *J. Phys. Chem. C* **2022**, *126*, 5206–5217. https://doi.org/10.1021/acs.jpcc.1c10466

34. V. Y. Osipov, S. A. Zargaleh, F. Treussart, K. Takai, N. M. Romanov, F. M. Shakhov and A. Baldycheva, Nitrogen impurities and fluorescent nitrogen-vacancy centers in detonation nanodiamonds: identification and distinct features, *J. Opt. Technol.* **2019**, *86*, 1–8. https://doi.org/10.1364/JOT.86.000001

35. T. D. Merson, S. Castelletto, I. Aharonovich, A. Turbic, T. J. Kilpatrick and A. M. Turnley, Nanodiamonds with silicon vacancy defects for nontoxic photostable fluorescent labeling of neural precursor cells, *Opt. Lett.* **2013**, *38*, 4170–4173. https://doi.org/10.1364/OL.38.004170

36. Y. Makino, T. Mahiko, M. Liu, A. Tsurui, T. Yoshikawa, S. Nagamachi, S. Tanaka, K. Hokamoto, M. Ashida, M. Fujiwara, N. Mizuoch and M. Nishikawa, Straightforward synthesis of silicon vacancy (SiV) center-containing single-digit nanometer nanodiamonds via detonation process, *Diam. Relat. Mater.* **2021**, *112*, 108248. https://doi.org/10.1016/j.diamond.2021.108248

37. Y. Makino, Y. Saito, H. Takehara, A. Tsurui, N. Okuyama and M. Ashida, Effect of particle size on the optical properties of silicon-vacancy centers in nanodiamonds fabricated by a detonation process, *Phys. Status Solidi A* **2022**, *219*, 2200342. https://doi.org/10.1002/pssa.202200342

38. Y. Makino, T. Yoshikawa, A. Tsurui, M. Liu, G. Yamagishi, M. Nishikawa, T. Mahiko, M. Ohno, M. Ashida and N. Okuyama, Direct synthesis of group IV-vacancy center-containing nanodiamonds via detonation process using aromatic compound as group IV element source, *Diam. Relat. Mater.* **2022**, *130*, 109493. https://doi.org/10.1016/j.diamond.2022.109493

39. T. Yoshikawa, M. Liu, S. L. Y. Chang, I. C. Kuschnerus, Y. Makino, A. Tsurui, T. Mahiko and M. Nishikawa, Steric interaction of polyglycerol-functionalized detonation nanodiamonds, *Langmuir* **2022**, *38*, 661–669.
https://doi.org/10.1021/acs.langmuir.1c02283

40. S. Sotoma, K. Akagi, S. Hosokawa, R. Igarashi, H. Tochio, Y. Harada and M. Shirakawa, Comprehensive and quantitative analysis for controlling the physical/chemical states and particle properties of nanodiamonds for biological applications, *RSC Adv.* **2015**, *5*, 13818–13827.
https://doi.org/10.1039/C4RA16482B

41. T. Yoshikawa, V. Zuerbig, F. Gao, R. Hoffmann, C. E. Nebel, O. Ambacher and V. Lebedev, Appropriate salt concentration of nanodiamond colloids for electrostatic self-assembly seeding of monosized individual diamond nanoparticles on silicon dioxide surfaces, *Langmuir* **2015**, *31*, 5319–5325.
https://doi.org/10.1021/acs.langmuir.5b01060.

42. L. Zhao, T. Takimoto, M. Ito, N. Kitagawa, T. Kimura and N. Komatsu, Chromatographic separation of highly soluble diamond nanoparticles prepared by polyglycerol grafting, *Angew. Chem. Int. Ed.* **2011**, *50*, 1388–1392.
https://doi.org/10.1002/anie.201006310

43. T. Jafari, A. Simchim and N. Khakpash, Synthesis and cytotoxicity assessment of superparamagnetic iron–gold core–shell nanoparticles coated with polyglycerol, *J. Colloid Interface Sci.* **2010**, *345*, 64–71.
https://doi.org/10.1016/j.jcis.2010.01.038

44. L. Zhou, C. Gao and W. Xu, Efficient grafting of hyperbranched polyglycerol from hydroxyl-functionalized multiwalled carbon nanotubes by surface-initiated anionic ring-opening polymerization, *Macromol. Chem. Phys.* **2009**, *210*, 1011–1018.

https://doi.org/10.1002/macp.200900134

45. L. Zhou, C. Gao, W. Xu, X. Wang and Y. Xu, Enhanced biocompatibility and biostability of CdTe quantum dots by facile surface-initiated dendritic polymerization, *Biomacromolecules* **2009**, *10*, 1865–1874. https://doi.org/10.1021/bm9002877

46. Y. Zou, M. Nishikawa and N. Komatsu, Organic chemistry for nanodiamond: Controlled functionalization, quantitative characterization and structure-property relationships, *Carbon Reports* **2022**, *1*, 70–78. https://doi.org/10.7209/carbon.010204

47. L. Zhao, T. Chano, S. Morikawa, Y. Saito, A. Shiino, S. Shimizu, T. Maeda, T. Irie, S. Aonuma, H. Okabe, T. Kimura, T. Inubushi and N. Komatsu, Hyperbranched polyglycerol-grafted superparamagnetic iron oxide nanoparticles: Synthesis, characterization, functionalization, size separation, magnetic properties, and biological applications, *Adv. Funct. Mater.* **2012**, *22*, 5107–5117. https://doi.org/10.1002/adfm.201201060

48. H. Qin, K. Maruyama, T. Amano, T. Murakami and N. Komatsu, Hyperbranched polyglycerol-grafted titanium oxide nanoparticles: synthesis, derivatization, characterization, size separation, and toxicology, *Mater. Res. Express* **2016**, *3*, 105049. https://doi.org/10.1088/2053-1591/3/10/105049

49. Y. Wang, G. Reina, H. G. Kang, X. Chen, Y. Zou, Y. Ishikawa, M. Suzuki and N. Komatsu, Polyglycerol functionalized ^{10}B enriched boron carbide nanoparticle as an effective bimodal anticancer nanosensitizer for boron neutron capture and photothermal therapies, *Small* **2022**, *18*, 2204044. https://doi.org/10.1002/smll.202204044

50. B. S. Miller, L. Bezinge, H. D. Gliddon, D. Huang, G. Dold, E. R. Gray, J. Heaney, P. J.

Dobson, E. Nasatouli, J. J. L. Morton and R. A. McKendry, Spin-enhanced nanodiamond biosensing for ultrasensitive diagnostics, *Nature* **2020**, *587*, 588–593.
https://doi.org/10.1038/s41586-020-2917-1

51. L. P. Suarez-Kelly, S. H. Sun, C. Ren, I. V. Rampersaud, D. Albertson, M. C. Duggan, T. C. Noel, N. Courtney, N. J. Buteyn, C. Moritz, L. Yu, V. O. Yildiz, J. P. Butchar, S. Tridandapani, A. A. Rampersaud and W. E. Carson, Antibody conjugation of fluorescent nanodiamonds for targeted innate immune cell activation, *ACS Appl. Nano Mater.* **2021**, *4*, 3122–3139.
https://doi.org/10.1021/acsanm.1c00256

52. S. Sotoma, R. Igarashi, J. Iimura, Y. Kumiya, H. Tochio, Y. Harada and M. Shirakawa, Suppression of nonspecific protein-nanodiamond adsorption enabling specific targeting of nanodiamonds to biomolecules of interest, *Chem. Lett.* **2015**, *44*, 354–356.
https://doi.org/10.1246/cl.141036

53. D. Terada, S. Sotoma, Y. Harada, R. Igarashi and M. Shirakawa, One-pot synthesis of highly dispersible fluorescent nanodiamonds for bioconjugation. *Bioconjugate Chem.* **2018**, *29*, 2786–2792.
https://doi.org/10.1021/acs.bioconjchem.8b00412

54. M. Fujiwara, S. Sun, A. Dohms, Y. Nishimura, K. Suto, Y. Takezawa, K. Oshimi, L. Zhao, N. Sadzak, Y. Umehara, Y. Teki, N. Komatsu, O. Benson, Y. Shikano and E. Kage-Nakadai, Real-time nanodiamond thermometry probing *in vivo* thermogenic responses, *Sci. Adv.* **2020**, *6*, eaba9636.
https://doi.org/10.1126/sciadv.aba9636

55. M. Fujiwara, G. Uchida, I. Ohki, M. Liu, A. Tsurui, T. Yoshikawa, M. Nishikawa and N. Mizuochi, All-optical nanoscale thermometry based on silicon-vacancy centers in detonation nanodiamonds, *Carbon* **2022**, *198*, 57–62.

https://doi.org/10.1016/j.carbon.2022.06.076

56. F. Yoshino, T. Amano, Y. Zou, J. Xu, F. Kimura, Y. Furusho, T. Chano, T. Murakami, L. Zhao and N. Komatsu, Preferential tumor accumulation of polyglycerol functionalized nanodiamond conjugated with cyanine dye leading to near-infrared fluorescence in vivo tumor imaging, *Small* **2015**, *15*, 1901930.
https://doi.org/10.1002/smll.201901930

57. F.-J. Hsieh, S. Sotoma, H.-H. Lin, C.-Y. Cheng, T.-Y. Yu, C.-L. Hsieh, C.-H. Lin and H.-C. Chang, Bioorthogonal Fluorescent nanodiamonds for continuous long-term imaging and tracking of membrane proteins, *ACS Appl. Mater. Interfaces* **2019**, *11*, 19774–19781.
https://doi.org/10.1021/acsami.9b03640

58. K. Kvakova, M. Ondra, J. Schimer, M. Petrik, Z. Novy, H. Raabova, M. Hajduch and P. Cigler, Visualization of sentinel lymph nodes with mannosylated fluorescent nanodiamonds, *Adv. Funct. Mater.* **2022**, *32*, 2109960.
https://doi.org/10.1002/adfm.202109960

59. J. Barton, M. Gulka, J. Tarabek, Y. Mindarava, Z. Wang, J. Schimer, H. Raabova, J. Bednar, M.B. Plenio, F. Jelezko, M. Nesladek and P. Cigler, Nanoscale dynamic readout of a chemical redox process using radicals coupled with nitrogen-vacancy centers in nanodiamonds, *ACS Nano* **2020**, *14*, 12938–12950.
https://doi.org/10.1021/acsnano.0c04010

60. J.-P. Boudou, M.-O. David, V. Joshi, H. Eidi and P.A. Curmi, Hyperbranched polyglycerol modified fluorescent nanodiamond for biomedical research, *Diam. Relat. Mater.* **2013**, *38*, 131–138.
https://doi.org/10.1016/j.diamond.2013.06.019

61. L. Zhao, A. Shiino, H. Qin, T. Kimura and N. Komatsu, Synthesis, characterization, and magnetic resonance evaluation of polyglycerol-functionalized detonation nanodiamond

conjugated with gadolinium(III) complex, *J. Nanosci. Nanotechnol.* **2015**, *15*, 1076–1082. https://doi.org/10.1166/jnn.2015.9738

62. L. Zhao, Y. Nakae, H. Qin, T. Ito, T. Kimura, H. Kojima, L. Chan and N. Komatsu, Polyglycerol-functionalized nanodiamond as a platform for gene delivery: Derivatization, characterization, and hybridization with DNA, *Beilstein J. Org. Chem.* **2014**, *10*, 707–713. https://doi.org/10.1002/adfm.201304298

63. L. Zhao, Y. H. Xu, H. Qin, S. Abe, T. Akasaka, T. Chano, F. Watari, T. Kimura, N. Komatsu and X. Chen, Platinum on nanodiamond: A promising prodrug conjugated with stealth polyglycerol, targeting peptide and acid-responsive antitumor drug, *Adv. Funct. Mater.* **2014**, *24*, 5348–5357. https://doi.org/10.1002/adfm.201304298

64. N. Komatsu, Poly(glycerol)-based biomedical nanodevices constructed by functional programming on inorganic nanoparticles for cancer nanomedicine, *Acc. Chem. Res.* **2023**, *56*, 106–116. https://doi.org/10.1021/acs.accounts.2c00615

65. S. Sotoma, Polyglycerol/Polydopamine-coated nanoparticles for biomedical applications, *Front. Mater.* **2022**, *9*, 878455. https://doi.org/10.3389/fmats.2022.878455

66. Z. Rafiee and S. Omidi, Modification of carbon-based nanomaterials by polyglycerol: recent advances and applications, *RSC Adv.* **2022**, *12*, 181–192. https://doi.org/10.1039/D1RA07554C

67. Y. Wu and T. Weil, Recent developments of nanodiamond quantum sensors for biological applications, *Adv. Sci.* **2022**, *9*, 2200059. https://doi.org/10.1002/advs.202200059

68. A. Mzyk, Y. Ong, A. R. O. Moreno, S. K. Padamati, Y. Zhang, C. A. Reyes-San-Martin

and R. Schirhagl, Diamond color centers in diamonds for chemical and biochemical analysis and visualization, *Anal. Chem.* **2022**, *94*, 225–249. https://doi.org/10.1021/acs.analchem.1c04536

69. M. B. A. Olia, P. S. Donnelly, L. C. L. Hollenberg, P. Mulvaney and D. A. Simpson, Advances in the surface functionalization of nanodiamonds for biological applications: a review, *ACS Appl. Nano Mater.* **2021**, 4, 9985–10005. https://doi.org/10.1021/acsanm.1c02698

70. H.-S. Jung and K. C. Neuman, Surface modification of fluorescent nanodiamonds for biological applications, *Nanomaterials* **2021**, *11*, 153. https://doi.org/10.3390/nano11010153

71. Y. Zou and N. Komatsu, Quantitative investigation of the interaction between proteins and charged functional groups on the polyglycerol-grafted nanodiamond surface, *Carbon* **2020**, *163*, 395–401. https://doi.org/10.1016/j.carbon.2020.02.089

72. Y. Zou, S. Ito, F. Yoshino, Y. Suzuki, L. Zhao and N. Komatsu, Polyglycerol grafting shields nanoparticle from protein corona formation to avoid macrophage uptake, *ACS Nano* **2020**, *14*, 7216–7226. https://doi.org/10.1021/acsnano.0c02289

73. P. Das and N. R. Jana, Highly colloidally stable hyperbranched polyglycerol grafted red fluorescent silicon nanoparticle as bioimaging probe, *ACS Appl. Mater. Interfaces* **2014**, *6*, 4301–4309. https://doi.org/10.1021/am406061x

74. X. Yang, L. Zhao, L. Zheng, M. Xu and X. Cai, Polyglycerol grafting and RGD peptide conjugation on MnO nanoclusters for enhanced colloidal stability, selective cellular uptake and cytotoxicity, *Colloids Surf. B*, **2018**, *163*, 167–174.

https://doi.org/10.1016/j.colsurfb.2017.12.034

75. L. Zhao. Y.-H. Xu, T. Akasaka, S. Abe, N. Komatsu, F. Watari and X. Chen, Polyglycerol-coated nanodiamond as a macrophage-evading platform for selective drug delivery in cancer cells, *Biomaterials* **2014**, *35*, 5393–5406.
https://doi.org/10.1016/j.biomaterials.2014.03.041

76. M. Suzuki, Boron neutron capture therapy (BNCT): a unique role in radiotherapy with a view to entering the accelerator-based BNCT era, *Int. J. Clin. Oncol.* **2020**, *25*, 43–50.
https://doi.org/10.1007/s10147-019-01480-4

77. W. A. G. Sauerwein, "Principles and Roots of Neutron Capture Therapy", Neutron Capture Therapy: Principles and Applications, W. A. G. Sauerwein, A. Wittig, R. Moss and Y. Nakagawa ed. Springer, 1–16, 2012.
ISBN 978-3-642-31333-2
https://doi.org/10.1007/978-3-642-31334-9_1

78. M. A. Dymova, S. Y. Taskaev, V. A. Richter and E. V. Kuligina, Boron neutron capture therapy: Current status and future perspectives, *Cancer Commun.* **2020**, *40*, 406–421.
https://doi.org/10.1002/cac2.12089

79. R. F. Barth and J. C. Grecula, Boron neutron capture therapy at the crossroads - Where do we go from here?, *Appl. Radiat. Isot.* **2020**, *160*, 109029.
https://doi.org/10.1016/j.apradiso.2019.109029

80. Y. Kiyanagi, Y. Sakurai, H. Kumada and H. Tanaka, Status of accelerator-based BNCT projects worldwide, *AIP. Conf. Proc.* **2019**, *2160*, 050012-1–9.
https://doi.org/10.1063/1.5127704

81. S. Kawabata, M. Suzuki, K. Hirose, H. Tanaka, T. Kato, H. Goto, Y. Narita and S. Miyatake, Accelerator-based BNCT for patients with recurrent glioblastoma: a multicenter phase II study, *Neurooncol. Adv.* **2021**, *3*, vdab067.

https://doi.org/10.1093/noajnl/vdab067

82. D. E. Cartelli, M. E. Capoulat, M. Baldo, J. C. Suarez Sandin, M. Igarzabal, M. F. del Grosso, A. A. Valda, N. Canepa, M. Gun, D. M. Minsky, G. Conti, J. Erhardt, H. R. Somacal, A. A. Bertolo, J. Bergueiro, P. A. Gaviola and A. J. Kreiner, Status of low-energy accelerator-based BNCT worldwide and in Argentina, *Appl. Radiat. Isot.* **2020**, *166*, 109315.

   https://doi.org/10.1016/j.apradiso.2020.109315

83. W. A. G. Sauerwein, P. M. Bet and A. Wittig, "Drugs for BNCT: BSH and BPA", Neutron Capture Therapy: Principles and Applications, W. A. G. Sauerwein, A. Wittig, R. Moss and Y. Nakagawa ed. Springer, 117–160, 2012.

   ISBN 978-3-642-31333-2

   https://doi.org/10.1007/978-3-642-31334-9_8

84. P. Wongthai, K. Hagiwara, Y. Miyoshi, P. Wiriyasermkul, L. Wei, R. Ohgaki, I. Kato, K. Hamase, S. Nagamori and Y. Kanai, Boronophenylalanine, a boron delivery agent for boron neutron capture therapy, is transported by ATB$^{0,+}$, LAT1 and LAT2, *Cancer Sci.* **2015**, *106*, 279–286.

   https://doi.org/10.1111/cas.12602

85. K. Ishiwata, 4-Borono-2-^{18}F-fluoro-l-phenylalanine PET for boron neutron capture therapy-oriented diagnosis: overview of a quarter century of research, *Ann. Nucl. Med.* **2019**, *33*, 223–236.

   https://doi.org/10.1007/s12149-019-01347-8

86. A. Doi, S. Kawabata, K. Iida, K. Yokoyama, Y. Kajimoto, T. Kuroiwa, T. Shirakawa, M. Kirihata, S. Kasaoka, K. Maruyama, H. Kumada, Y. Sakurai, S. Masunaga, K. Ono and S. Miyatake, Tumor-specific targeting of sodium borocaptate (BSH) to malignant glioma by transferrin-PEG liposomes: a modality for boron neutron capture therapy, *J. Neurooncol.*

2008, *87*, 287–294.

https://doi.org/10.1007/s11060-008-9522-8

87. T. Kageji, Y. Mizobuchi, S. Nagahiro, Y. Nakagawa and H. Kumada, Clinical results of boron neutron capture therapy (BNCT) for glioblastoma, *Appl. Radiat. Isot.* **2011**, *69*, 1823–1825.

https://doi.org/10.1016/j.apradiso.2011.05.029

88. A. H. Soloway, W. Tjarks, B. A. Barnum, F.-G. Rong, R. F. Barth, I. M. Codogni and J. G. Wilson, The chemistry of neutron capture therapy, *Chem. Rev.* **1998**, *98*, 1515–1562.

https://doi.org/10.1021/cr941195u

89. P. Coghi, J. Li, N. S. Hosmane and Y. Zhu, Next generation of boron neutron capture therapy (BNCT) agents for cancer treatment, *Med. Res. Rev.* **2023**, 1–22.

https://doi.org/10.1002/med.21964

90. A. Pitto-Barry, Polymers and boron neutron capture therapy (BNCT): a potent combination, *Polym. Chem.* **2021**, *12*, 2035–2044.

https://doi.org/10.1039/D0PY01392G

91. M. Lamba, A. Goswami and A. Bandyopadhyay, A periodic development of BPA and BSH based derivatives in boron neutron capture therapy (BNCT), *Chem. Commun.* **2021**, *57*, 827–839.

https://doi.org/10.1039/D0CC06557A

92. T. Nomoto, Y. Inoue, Y. Yao, M. Suzuki, K. Kanamori, H. Takemoto, M. Matsui, K. Tomoda and N. Nishiyama, Poly(vinyl alcohol) boosting therapeutic potential of *p*-boronophenylalanine in neutron capture therapy by modulating metabolism, *Sci. Adv.* **2020**, *6*, eaaz1722.

https://doi.org/10.1126/sciadv.aaz1722

93. K. Kawai, K. Nishimura, S. Okada, S. Sato, M. Suzuki, T. Takata and H. Nakamura, Cyclic

RGD-functionalized *closo*-dodecaborate albumin conjugates as integrin targeting boron carriers for neutron capture therapy, *Mol. Pharmaceutics* **2020**, *17,* 3740–3747. https://doi.org/10.1021/acs.molpharmaceut.0c00478

94. J.-D. Lee, M. Ueno, Y. Miyajima and H. Nakamura, Synthesis of boron cluster lipids: *closo*-dodecaborate as an alternative hydrophilic function of boronated liposomes for neutron capture therapy, *Org. Lett.* **2007**, *9*, 323–326. https://doi.org/10.1021/ol062840+

95. M. E. El-Zaria and H. Nakamura, New strategy for synthesis of mercaptoundecahydrododecaborate derivatives via click chemistry: possible boron carriers and visualization in cells for neutron capture therapy, *Inorg. Chem.* **2009**, *48*, 11896–11902. https://doi.org/10.1021/ic902033c

96. S. Kusaka, Y. Hattori, K. Uehara, T. Asano, S. Tanimori and M. Kirihata, Synthesis of optically active dodecaborate-containing L-amino acids for BNCT, *Appl. Radiat Isot.* **2011**, *69*, 1768–1770. https://doi.org/10.1016/j.apradiso.2011.03.042

97. A. R. Genady, J. A. Ioppolo, M. M. Azaam and M. E. El-Zaria, New functionalized mercaptoundecahydrododecaborate derivatives for potential application in boron neutron capture therapy: Synthesis, characterization and dynamic visualization in cells, *Eur. J. Med. Chem.* **2015**, *93*, 574–583. https://doi.org/10.1016/j.ejmech.2015.02.033

98. H. Koganei, S. Tachikawa, M. E. El-Zariaac and H. Nakamura, Synthesis of oligo-*closo*-dodecaborates by Hüisgen click reaction as encapsulated agents for the preparation of high-boron-content liposomes for neutron capture therapy, *New. J. Chem.* **2015**, *39*, 6388–6394. https://doi.org/10.1039/C5NJ00856E

99. A. Isono, M. Tsuji, Y. Sanada, A. Matsushita, S. Masunaga, T. Hirayama and H. Nagasawa,

Design, synthesis, and evaluation of lipopeptide conjugates of mercaptoundecahydrododecaborate for boron neutron capture therapy, *ChemMedChem* **2019**, *14*, 823–832.

https://doi.org/10.1002/cmdc.201800793

100. I. Nakase, A. Aoki, Y. Sakai, S. Hirase, M. Ishimura, T. Takatani-Nakase, Y. Hattori and M. Kirihata, Antibody-based receptor targeting using an Fc-binding peptide-dodecaborate conjugate and macropinocytosis induction for boron neutron capture therapy, *ACS Omega* **2020**, *5*, 22731–22738.

https://doi.org/10.1021/acsomega.0c01377

101. S. Hirase, A. Aoki, Y. Hattori, K. Morimoto, K. Noguchi, I. Fujii, T. Takatani-Nakase, S. Futaki, M. Kirihata and I. Nakase, Dodecaborate-encapsulated extracellular vesicles with modification of cell-penetrating peptides for enhancing macropinocytotic cellular uptake and biological activity in boron neutron capture therapy, *Mol. Pharmaceutics* **2022**, *19*, 1135–1145.

https://doi.org/10.1021/acs.molpharmaceut.1c00882

102. A. Kim, M. Suzuki, Y. Matsumoto, N. Fukumitsu and Yukio Nagasaki, Non-isotope enriched phenylboronic acid-decorated dual-functional nano-assembles for an actively targeting BNCT drug, *Biomaterials* **2021**, *268*, 120551.

https://doi.org/10.1016/j.biomaterials.2020.120551

103. A. Kim, Y. Suzuki and Y. Nagasaki, Molecular design of a high-performance polymeric carrier for delivery of a variety of boronic acid-containing drugs, *Acta Biomater.* **2021**, *121*, 554.–565.

https://doi.org/10.1016/j.actbio.2020.12.015

104. N. Kuthala, R. Vankayala, Y.-N. Li, C.-S. Chiang and K. C. Hwang, Engineering novel targeted boron-10-enriched theranostic nanomedicine to combat against murine brain

tumors via MR imaging-guided boron neutron capture therapy, *Adv. Mater.* **2017**, *29*, 1700850.

https://doi.org/10.1002/adma.201700850

105. L. Li, J. Li, Y. Shi, P. Du, Z. Zhang, T. Liu, R. Zhang and Z. Liu, On-demand biodegradable boron nitride nanoparticles for treating triple negative breast cancer with boron neutron capture therapy, *ACS Nano* **2019**, *13*, 13843–13852.

https://doi.org/10.1021/acsnano.9b04303

106. H. Nakamura, H. Koganei, T. Miyoshi, Y. Sakurai, K. Ono and M. Suzuki, Antitumor effect of boron nitride nanotubes in combination with thermal neutron irradiation on BNCT, *Bioorg. Med. Chem. Lett.* **2015**, *25*, 172–174.

https://doi.org/10.1016/j.bmcl.2014.12.005

107. A. Sunder, R. Hanselmann, H. Frey and R. Mu, Controlled synthesis of hyperbranched polyglycerols by ring-opening multibranching polymerization. *Macromolecules* 1999, *32*, 4240–4246.

https://doi.org/10.1021/ma990090w

108. D. Wilms, J. Nieberle, J. Klos, H. Löwe and H. Frey, Synthesis of hyperbranched polyglycerol in a continuous flow microreactor, *Chem. Eng. Technol.* **2007**, *30*, 1519–1524.

https://doi.org/10.1002/ceat.200700277

109. S. Xiaoying, Y. Xiaohui, L. Yunhang and W. Xinling, Synthesis and characterization of a multiarm star polymer, *J. Polym. Sci. A Polym. Chem.* **2004**, *42*, 2356–2364.

https://doi.org/10.1002/pola.20083

110. E. Mohammadifar, A. Bodaghi, A. Dadkhahtehrani, A. N. Kharat, M. Adeli and R. Haag, Green synthesis of hyperbranched polyglycerol at room temperature. *ACS Macro Lett.* **2017**, *6*, 35–40.

https://doi.org/10.1021/acsmacrolett.6b00804

111. S. Osswald, G. Yushin, V. Mochalin, S. O. Kucheyev and Y. Gogotsi, Control of sp^2/sp^3 carbon ratio and surface chemistry of nanodiamond powders by selective oxidation in air, *J. Am. Chem. Soc.* **2006**, *128*, 11635–11642. https://doi.org/10.1021/ja063303n

112. C. H. Klute and W. Viehmann, Heat of polymerization of phenyl glycidyl ether and of an epoxy resin, *J. Appl. Polym. Sci.* **1961**, *5*, 86–95. https://doi.org/10.1002/app.1961.070051313

113. M. Nishikawa, H. G. Kang, Y. Zou, H. Takeuchi, N. Matsuno, M. Suzuki and N. Komatsu, Conjugation of phenylboronic acid moiety through multistep organic transformations on nanodiamond surface for an anticancer nanodrug for boron neutron capture therapy, *Bull. Chem. Soc. Jpn.* **2021**, *94*, 2302–2312. https://doi.org/10.1246/bcsj.20210200

114. A. M. Panich, A. I. Shames, N. A. Sergeev, M. Olszewski, J. K. McDonough, V. N. Mochalin and Y. Gogotsi, Nanodiamond graphitization: A magnetic resonance study, *J. Phys. Condens. Matter* **2013**, *25*, 245303. https://doi.org/10.1088/0953-8984/25/24/245303

115. X. W. Fang, J. D. Mao, E. M. Levin and K. Schmidt-Rohr, Nonaromatic Core-shell structure of nanodiamond from solid-state NMR spectroscopy, *J. Am. Chem. Soc.* **2009**, *131*, 1426–1435. https://doi.org/10.1021/ja8054063

116. C. Bradac, T. Gaebel, N. Naidoo, M. J. Sellars, J. Twamley, L. J. Brown, A. S. Barnard, T. Plakhotnik, A. V. Zvyagin and J. R. Rabeau, Observation and control of blinking nitrogen-vacancy centres in discrete nanodiamonds, *Nature Nanotech.* **2010**, *5*, 345–349. https://doi.org/10.1038/nnano.2010.56

117. W. Radke, G. Litvinenko and A. H. E. Müller, Effect of core-forming molecules on

molecular weight distribution and degree of branching in the synthesis of hyperbranched polymers, *Macromolecules* **1998**, *31*, 239–248. https://doi.org/10.1021/ma970952y

118. M. Tomšič, M. Bešter-Rogač, A. Jamnik, W. Kunz, D. Touraud, A. Bergmann and O. Glatter, Nonionic surfactant Brij 35 in water and in various simple alcohols: Structural investigations by small-angle X-ray scattering and dynamic light scattering, *J. Phys. Chem. B* **2004**, *108*, 7021–7032. https://doi.org/10.1021/jp049941e
119. ISO 22412:2017, Particle size analysis – dynamic light scattering (DLS).
120. S. Sotoma, R. Igarashi and M. Shirakawa, Moderate plasma treatment enhances the quality of optically detected magnetic resonance signals of nitrogen-vacancy centers in nanodiamonds, *Appl. Phys. A* **2016**, *122*, 522. https://doi.org/10.1007/s00339-016-0030-y
121. I. Rehora and P. Cigler, Precise estimation of HPHT nanodiamond size distribution based on transmission electron microscopy image analysis, *Diam. Relat. Mater.* **2014**, *46*, 21–24. https://doi.org/10.1016/j.diamond.2014.04.002
122. P. Reineck, L. F. Trindade, J. Havlik, J. Stursa, A. Heffernan, A. Elbourne, A. Orth, M. Capelli, P. Cigler, D. A. Simpson and B. C. Gibson, Not all fluorescent nanodiamonds are created equal: A comparative study, *Part. Part. Syst. Charact.* **2019**, *36*, 1900009. https://doi.org/10.1002/ppsc.201900009
123. Y. Zou, S. Ito, M. Fujiwara and N. Komatsu, Probing the role of charged functional groups on nanoparticles grafted with polyglycerol in protein adsorption and cellular uptake, *Adv. Funct. Mater.* **2022**, *32*, 2111077. https://doi.org/10.1002/adfm.202111077
124. R. A. Sheldon and I. W. C. E. Arends, Organocatalytic oxidations mediated by nitroxyl

radicals, *Adv. Synth. Catal.* **2004**, *346*, 1051–1071. https://doi.org/10.1002/adsc.200404110

125. A. Isogai, T. Hänninen, S. Fujisawa and T. Saitoa, Review: Catalytic oxidation of cellulose with nitroxyl radicals under aqueous conditions, *Prog. Polym. Sci.* **2018**, *86*, 122–148. https://doi.org/10.1016/j.progpolymsci.2018.07.007

126. R. Doi, M. Shibuya, T. Murayama, Y. Yamamoto and Y. Iwabuchi, Development of an azanoradamantane-type nitroxyl radical catalyst for class-selective oxidation of alcohols, *J. Org. Chem.* **2015**, 80, 401–413. https://doi.org/10.1021/jo502426p

127. M. Shibuya, M. Tomizawa, I. Suzuki and Y. Iwabuchi, 2-Azaadamantane *N*-oxyl (AZADO) and 1-Me-AZADO: highly efficient organocatalysts for oxidation of alcohols, *J. Am. Chem. Soc.* **2006**, *128*, 8412–8413. https://doi.org/10.1021/ja0620336

128. Y. Iwabuchi, Discovery and exploitation of AZADO: the highly active catalyst for alcohol oxidation, *Chem. Pharm. Bull.* **2013**, *61*, 1197–1213. https://doi.org/10.1248/cpb.c13-00456

129. M. Nishikawa, M. Liu, T. Yoshikawa, H. Takeuchi, N. Matsuno and N. Komatsu, Thorough elucidation of synthesis and structure of poly(glycerol) functionalized nanodiamonds, *Carbon* **2023**, *205*, 463–474. https://doi.org/10.1016/j.carbon.2023.01.025

130. C. Tahiri and M. R. Vignon, TEMPO-oxidation of cellulose: Synthesis and characterisation of polyglucuronans, *Cellulose* **2000**, *7*, 177–188. https://doi.org/10.1023/A:1009276009711

131. R. Tanaka, T. Saito and A. Isogai, Cellulose nanofibrils prepared from softwood cellulose by TEMPO/NaClO/$NaClO_2$ systems in water at pH 4.8 or 6.8, *Int. J. Biol. Macromol.* **2012**,

51, 228–234.

https://doi.org/10.1016/j.ijbiomac.2012.05.016

132. M. M. Zhao, J. Li, E. Mano, Z. J. Song and D. M. Tschaen, Oxidation of primary alcohols to carboxylic acids with sodium chlorite catalyzed by TEMPO and bleach: 4-methoxyphenylacetic acid, *Org. Synth.* **2005**, *81*, 195–203.

https://doi.org/10.1002/0471264229.os081.21

133. T. Takimoto, T. Chano, S. Shimizu, H. Okabe, M. Ito, M. Morita, T. Kimura, T. Inubushi and N. Komatsu, Preparation of fluorescent diamond nanoparticles stably dispersed under a physiological environment through multistep organic transformations, *Chem. Mater.* **2010**, *22*, 3462–3471.

https://doi.org/10.1021/cm100566v

134. H. Nakamura and M. Kirihata, "Boron Compounds: New Candidates for Boron Carriers in BNCT", Neutron Capture Therapy: Principles and Applications, W. A. G. Sauerwein, A. Wittig, R. Moss and Y. Nakagawa ed. Springer, 99–116, 2012.

ISBN: 978-3-642-31333-2

135. T. Khan, K. Igarashi, A. Tanabe, T. Miyazawa, S. Fukushima, Y. Miura, Y. Matsumoto, T. Yamasoba, A. Matsumoto, H. Cabral. and K. Kataoka, Structural control of boronic acid ligands enhances intratumoral targeting of sialic acid to eradicate cancer stem-like cells, *ACS Appl. Bio Mater.* **2020**, *3*, 5030–5039.

https://doi.org/10.1021/acsabm.0c00530

136. L. Zhao, T. Takimoto, T. Kimura and N. Komatsu, Polyglycerol functionalization of ZnO nanoparticles for stable hydrosol in physiological media, *J. Indian Chem. Soc.* **2011**, *88*, 1787–1790.

137. L. Zhao, A. Shiino, H. Qin, T. Kimura and N. Komatsu, Synthesis, characterization, and magnetic resonance evaluation of polyglycerol-functionalized detonation nanodiamond

conjugated with gadolinium(III) complex, *J. Nanosci. Nanotechnol.* **2015**, *15*, 1076–1082. https://doi.org/10.1166/jnn.2015.9738

138. S. Roller, H. Zhou and R. Haag, High-loading polyglycerol supported reagents for Mitsunobu- and acylation-reactions and other useful polyglycerol derivatives, *Mol. Divers.* **2005**, *9*, 305–316. https://doi.org/10.1007/s11030-005-8117-y

139. S. Toyota, M. Asakura and T. Sakaue, Intramolecular C=O···B Interactions in *o*-boron substituted benzaldehyde, acetophenone, and benzophenone, *Bull. Chem. Soc. Jpn.* **2002**, *75*, 2667–2671. https://doi.org/10.1246/bcsj.75.2667

140. M. Lauer and G. Wulff, Arylboronic acids with intramolecular B–N interaction: convenient synthesis through ortho-lithiation of substituted benzylamines, *J. Organomet. Chem.* **1983**, *256*, 1–9. https://doi.org/10.1016/S0022-328X(00)99290-8

141. A. Stubelius, S. Lee and A. Almutairi, The chemistry of boronic acids in nanomaterials for drug delivery, *Acc. Chem. Res.* **2019**, *52*, 3108–3119. https://doi.org/10.1021/acs.accounts.9b00292

142. G. E. Negri and T. J. Deming, Protein complexation and pH dependent release using boronic acid containing PEG-polypeptide copolymers, *Macromol. Biosci.* 2017, *17*, 1600136. https://doi.org/10.1002/mabi.201600136

143. S. L. Wiskur, J. J. Lavigne, H. Ait-Haddou, V. Lynch, Y. H. Chiu, J. W. Canary and E. V. Anslyn, p*K*a Values and geometries of secondary and tertiary amines complexed to boronic acids – Implications for sensor design, *Org. Lett.* **2001**, *3*, 1311–1314. https://doi.org/10.1021/ol0156805

144. L. I. Bosch, T. M. Fylesb and T. D. James, Binary and ternary phenylboronic acid complexes with saccharides and Lewis bases, *Tetrahedron* **2004**, *60*, 11175–11190. https://doi.org/10.1016/j.tet.2004.08.046

145. T. Kobayashi and K. Kanda, Microanalysis system of ppm-order ^{10}B concentrations in tissue for neutron capture therapy by prompt gamma-ray spectrometry, *Nucl. Instrum. Methods.* **1983**, *204*, 525–531. https://doi.org/10.1016/0167-5087(83)90082-0

146. L. Zhao, Y.-H. Xu, H. Qin, S. Abe, T. Akasaka, T. Chano, F. Watari, T. Kimura, N. Komatsu and X. Chen, Platinum on nanodiamond: A promising prodrug conjugated with stealth polyglycerol, targeting peptide and acid-responsive antitumor drug, *Adv. Funct. Mater.* **2014**, *24*, 5348–5357. https://doi.org/10.1002/adfm.201304298

147. A. Doi, S. Kawabata, K. Iida, K. Yokoyama, Y. Kajimoto, T. Kuroiwa, T. Shirakawa, M. Kirihata, S. Kasaoka, K. Maruyama, H. Kumada, Y. Sakurai, S. Masunaga, K. Ono and S. Miyatake, Tumor-specific targeting of sodium borocaptate (BSH) to malignant glioma by transferrin-PEG liposomes: a modality for boron neutron capture therapy, *J. Neurooncol.* **2008**, *87*, 287–294. https://doi.org/10.1007/s11060-008-9522-8

148. T. Kageji, Y. Mizobuchi, S. Nagahiro, Y. Nakagawa and H. Kumada, Clinical results of boron neutron capture therapy (BNCT) for glioblastoma, *Appl. Radiat. Isot.* **2011**, *69*, 1823–1825. https://doi.org/10.1016/j.apradiso.2011.05.029

149. M. Nishikawa, H. Yagasaki, S. He and N. Komatsu, Poly(glycerol-*co*-glyceric acid) functionalized nanodiamonds by nitroxyl radical-catalyzed oxidation of primary alcohols in poly(glycerol) as scaffolds for further conjugation, *ChemNanoMat* **2023**, *9*, e202300204.

https://doi.org/10.1002/cnma.202300204

150. M. Sassi, L. Mascheroni, R. Ruffo, M. M. Salamone, G. A. Pagani, C. M. Mari, G. D’Orazio, B. La Ferla and L. Beverina, Exomethylene-3,4-ethylenedioxythiophene (emEDOT): A new versatile building block for functionalized electropolymerized poly(3,4-ethylenedioxythiophenes) (PEDOTs), *Org. Lett.* **2013**, *15*, 3502–3505. https://doi.org/10.1021/ol401008s

151. J. Totobenazara and A. J. Burke, New click-chemistry methods for 1,2,3-triazoles synthesis: recent advances and applications, *Tetrahedron Lett.* **2015**, *56*, 2853–2859. https://doi.org/10.1016/j.tetlet.2015.03.136

152. P. Thirumurugan, D. Matosiuk and K. Jozwiak, Click chemistry for drug development and diverse chemical–biology applications, *Chem. Rev.* **2013**, *113*, 4905–4979. https://doi.org/10.1021/cr200409f

153. H. Nulwala, K. Takizawa, A. Odukale, A. Khan, R. J. Thibault, B. R. Taft, B. H. Lipshutz and C. J. Hawker, Synthesis and characterization of isomeric vinyl-1,2,3-triazole materials by azide-alkyne click chemistry, *Macromolecules* **2009**, *42*, 6068–6074. https://doi.org/10.1021/ma900892h

154. P. Bendel, Biomedical applications of ^{10}B and ^{11}B NMR, *NMR Biomed.* **2005**, *18*, 74–82. https://doi.org/10.1002/nbm.886

155. H. Otsuka, E. Uchimura, H. Koshino, T. Okano and K. Kataoka, Anomalous binding profile of phenylboronic acid with *N*-acetylneuraminic acid (Neu5Ac) in aqueous solution with varying pH, *J. Am. Chem. Soc.* **2003**, *125*, 3493–3502. https://doi.org/10.1021/ja021303r

156. Z. Guo, B. He, H. Jin, H. Zhang, W. Dai, L. Zhang, H. Zhang, X. Wang, J. Wang, X. Zhang and Q. Zhang, Targeting efficiency of RGD-modified nanocarriers with different ligand intervals in response to integrin αvβ3 clustering, *Biomaterials* **2014**, *35*, 6106–6117.

https://doi.org/10.1016/j.biomaterials.2014.04.031

157. J. Hiratsuka, N. Kamitani, R. Tanaka, R. Tokiya, E. Yoden, Y. Sakurai and M. Suzuki, Long-term outcome of cutaneous melanoma patients treated with boron neutron capture therapy (BNCT), *J. Radiat. Res.* **2020**, *61*, 945–951. https://doi.org/10.1093/jrr/rraa068

158. Y. Zou, M. Nishikawa, H. G. Kang, G. Cheng, W. Wang, Y. Wang and N. Komatsu, Effect of protein corona on mitochondrial targeting ability and cytotoxicity of triphenylphosphonium conjugated with polyglycerol-functionalized nanodiamond, *Mol. Pharmaceutics* **2021**, *18*, 2823–2832. https://doi.org/10.1021/acs.molpharmaceut.1c00188

159. P.-P. P. Zhu Tang, M. P. Schweizer, K. M. Bradshaw and W. F. Bauer, ^{11}B nuclear magnetic resonance studies of the interaction of borocaptate sodium with serum albumin, *Biochem. Pharmacol.* **1995**, *49*, 625–632. https://doi.org/10.1016/0006-2952(94)00529-U

160. L. Kou, J. Sun, Y. Zhai and Z. He, The endocytosis and intracellular fate of nanomedicines: Implication for rational design, *Asian J. Pharm. Sci.* **2013**, *8*, 1–10. https://doi.org/10.1016/j.ajps.2013.07.001

List of abbreviations

^{10}BSH, mercaptoundecahydro-closo-dodecaborate(^{10}B); AN, acrylonitrile: ANOVA, analysis of variance; API, active pharmaceutical ingredient; AZADOL, 2-hydroxy-2-azaadamantane; B16, murine melanoma cell line; BALB/c, Bagg albino/c (mouse); BCA, bicinchoninic acid; BET-SSA, BET(Brunauer–Emmett–Teller) specific surface area; BNCT, boron neutron capture therapy; BSA, bovine serum albumin; c(RGDyK), cyclo(L-Arg-Gly-L-Asp-D-Tyr-L-Lys); CCK-8, cell counting kit; cryo-TEM, cryogenic transmission electron microscopy; CT26, a murine colorectal carcinoma cell line; CVD, chemical vapor deposition; DB, degree of branching; DDS, drug discovery system; DEPT, distortionless enhancement by polarization transfer; DLS, dynamic light scattering; DLVO theory, Boris Derjaguin, Lev Landau, Evert Verwey and Theodoor Overbeek theory; DMAP, *N,N*-dimethylaminopyridine; DMEM, Dulbecco's modified Eagle medium; DMF, *N,N*-dimethylformamide; DND, detonation nanodiamond; DRIFT, diffuse reflectance infrared Fourier transform; DW, distilled water; EDC, 1-(3-dimethylaminopropyl)-3-ethylcarbodiimide hydrochloride; EDTA, ethylenediamine-*N,N,N′,N′*-tetraacetic acid; EG, ethylene glycol; EMS, electro-magnetically spinning sphere; EPR, enhanced permeability and retention; EPR, electron spin resonance; ESI-MS, electrospray ionization mass spectroscopy; FBS, fetal bovine serum; FT-IR, Fourier transform infrared (spectroscopy); GD, glycidol; GeV, germanium vacancy; HMBC, heteronuclear multiple bond correlation; HMQC, heteronuclear multiple quantum correlation; HOSu, *N*-hydroxysccinimide; HPHT, high-pressure high-temperature; HSD, honestly significant difference; ICP-AES, inductively coupled plasma atomic emission spectroscopy; LAT1, L-amino acid transporter; L-BPA, L-boronophenylalanine; L-FBPA, *o*-fluoro-L-boronophenylalanine; Me, methyl; MeCN, acetonitrile; MES, 2-(*N*-morpholino)ethanesulfonic acid; ND, nanodiamond; NMR, nuclear magnetic resonance; NP, nanoparticle; NV, nitrogen vacancy; PBA, phenylboronic acid; PBS, phosphate buffered saline;

PEG, poly(ethylene glycol); PET, positron-emission tomography; PG, poly(glycerol); PGA, neutron-induced prompt gamma-ray analysis; Pgy, propargyl moiety; RDX, hexahydro-1,3,5-trinitro-1,3,5-triazine (Research Department eXplosive); RGD, Arginine-glycine-aspartic acid (amino acid sequence); RI, refractive index; ROS, reactive oxygen species; RPMI, Roswell Park Memorial Institute; SDS, sodium dodecyl sulfate; SEC, size exclusion chromatography; SEM-EDS, energy dispersive X-ray spectroscopy with scanning electron microscopy; SiV, silicon vacancy; SP, supraparticle; SPION, superparamagnetic iron oxide; Suc, succinic or succinyl moiety, succinate; T/B ratio, tumor/blood ratio; TEM, transmission electron microscopy; TEMPO, 2,2,6,6-tetramethylpiperidine-1-oxyl; TFA, trifluoroacetic acid, trifluoroacetate; TGA, thermogravimetric analysis; THF, tetrahydrofuran; TMA, tetramethylammonium; TNT, 2,4,6-trinitrotoluene; Ts, *p*-Toluenesulfonate; TsCl, *p*-Toluenesulfonyl chloride.

List of publications

Publications included in this thesis

(Chapter 2)

1) M. Nishikawa, M. Liu, T. Yoshikawa, H. Takeuchi, N. Matsuno and N. Komatsu, Thorough elucidation of synthesis and structure of poly(glycerol) functionalized nanodiamonds, *Carbon* **2023**, *205*, 463–474.

   https://doi.org/10.1016/j.carbon.2023.01.025

(Chapter 3)

2) M. Nishikawa, H. Yagasaki, S. He and N. Komatsu, Poly(glycerol-*co*-glyceric acid) functionalized nanodiamonds by nitroxyl radical-catalyzed oxidation of primary alcohols in poly(glycerol) as scaffolds for further conjugation, *ChemNanoMat* **2023**, *9*, e202300204.

   https://doi.org/10.1002/cnma.202300204

(Chapter 4)

3) M. Nishikawa, H. G. Kang, Y. Zou, H. Takeuchi, N. Matsuno, M. Suzuki and N. Komatsu, Conjugation of phenylboronic acid moiety through multistep organic transformations on nanodiamond surface for an anticancer nanodrug for boron neutron capture therapy, *Bull. Chem. Soc. Jpn.* **2021**, *94*, 2302–2312.

   https://doi.org/10.1246/bcsj.20210200

(Chapter 5)

4) M. Nishikawa, J. Yu, H. G. Kang, M. Suzuki and N. Komatsu, Rational design, multistep synthesis and *in vitro* evaluation of poly(glycerol) functionalized nanodiamond conjugated with boron-10 cluster and active targeting moiety for boron neutron capture therapy, *Chem. Eur. J.* **2023**, *29*, e202302073.

   https://doi.org/10.1002/chem.202302073

Publications not included in this thesis

(Credited as an affiliate of Kyoto University)

1) Y. Zou, M. Nishikawa and N. Komatsu, Organic chemistry for nanodiamond: Controlled functionalization, quantitative characterization and structure-property relationships, *Carbon Reports* **2022**, *1*, 70–78.

   https://doi.org/10.7209/carbon.010204

2) Y. Zou, M. Nishikawa, H. G. Kang, G. Cheng, W. Wang, Y. Wang and N. Komatsu, Effect of protein corona on mitochondrial targeting ability and cytotoxicity of triphenylphosphonium conjugated with polyglycerol-functionalized nanodiamond, *Mol. Pharmaceutics* **2021**, *18*, 2823–2832.

   https://doi.org/10.1021/acs.molpharmaceut.1c00188

(Credited as a member of Daicel Corporation regarding nanodiamonds)

3) Y. Makino, T. Mahiko, M. Liu, A. Tsurui, T. Yoshikawa, S. Nagamachi, S. Tanaka, K. Hokamoto, M. Ashida, M. Fujiwara, N. Mizuoch and M. Nishikawa, Straightforward synthesis of silicon vacancy (SiV) center-containing single-digit nanometer nanodiamonds via detonation process, *Diam. Relat. Mater.* **2021**, *112*, 108248.

   https://doi.org/10.1016/j.diamond.2021.108248

4) Y. Makino, T. Yoshikawa, A. Tsurui, M. Liu, G. Yamagishi, M. Nishikawa, T. Mahiko, M. Ohno, M. Ashida and N. Okuyama, Direct synthesis of group IV-vacancy center-containing nanodiamonds via detonation process using aromatic compound as group IV element source, *Diam. Relat. Mater.* **2022**, *130*, 109493.

   https://doi.org/10.1016/j.diamond.2022.109493

5) T. Yoshikawa, M. Liu, S. L. Y. Chang, I. C. Kuschnerus, Y. Makino, A. Tsurui, T. Mahiko and M. Nishikawa, Steric interaction of polyglycerol-functionalized detonation nanodiamonds, *Langmuir* **2022**, *38*, 661–669.
https://doi.org/10.1021/acs.langmuir.1c02283

6) M. Fujiwara, G. Uchida, I. Ohki, M. Liu, A. Tsurui, T. Yoshikawa, M. Nishikawa and N. Mizuochi, All-optical nanoscale thermometry based on silicon-vacancy centers in detonation nanodiamonds, *Carbon* **2022**, *198*, 57–62.
https://doi.org/10.1016/j.carbon.2022.06.076

7) Y. Yu, M. Nishikawa, M. Liu, T. Tei, S. C. Kaul, R. Wadhawa, M. Zhang, J. Takahashi and E. Miyako, Self-assembled nanodiamond supraparticles for anticancer chemotherapy, *Nanoscale* **2018**, *10*, 8969–8978.
https://doi.org/10.1039/C8NR00641E

8) Y. Yu, X. Yang, M. Liu, M. Nishikawa, T. Tei and E. Miyako, Amphipathic nanodiamond supraparticles for anticancer drug loading and delivery, *ACS Appl. Mater. Interfaces* **2019**, *11*, 18978–18987.
https://doi.org/10.1021/acsami.9b04792

9) Y. Yu, X. Yang, M. Liu, M. Nishikawa, T. Tei and E. Miyako, Multifunctional cancer phototherapy using fluorophore-functionalized nanodiamond supraparticles, *ACS Appl. Bio Mater.* **2019**, *2*, 3693–3705.
https://doi.org/10.1021/acsabm.9b00603

10) K. Miyashita, T. Kondo, S. Sugai, T. Tei, M. Nishikawa, T. Tojo and M. Yuasa, Boron-doped nanodiamond as an electrode material for aqueous electric double-layer capacitors, *Sci. Rep.* **2019**, *9*, 17846.
https://doi.org/10.1038/s41598-019-54197-9

11) I. C. Kuschnerus, H. Wen, X. Zeng, Y. Y. Khine, J. Ruan, C. -J. Su, U-S. Jeng, H. A. Girard, J. -C. Arnault, E. Ōsawa, O. Shenderova, V. N. Mochalin, M. Liu, M. Nishikawa and S. L. Y. Chang, Fabrication process independent and robust aggregation of detonation nanodiamonds in aqueous media, *Diam. Relat. Mater.* **2023**, *139*, 100199.
https://doi.org/10.1016/j.diamond.2023.110199

12) I. C. Kuschnerus, H. Wen, J. Ruan, X. Zeng, C. -J. Su, U-S. Jeng, G. Opletal, A. S. Barnard, M. Liu, M. Nishikawa and S. L. Y. Chang, Complex dispersion of detonation nanodiamond revealed by machine learning assisted cryo-TEM and coarse-grained molecular dynamics simulations, *ACS Nanosci. Au* **2023**, *3*, 211–221.
https://doi.org/10.1021/acsnanoscienceau.2c00055

13) T. Yoshikawa, N. Tokuda, Y. Makino, A. Tsurui, R. Ieki, R. Kojima, M. Liu, T. Mahiko and M. Nishikawa, Electrostatic layer-by-layer deposition of diamond nanoparticles onto substrate surfaces, *Carbon Trends* **2022**, *9*, 100202.
https://doi.org/10.1016/j.cartre.2022.100202

14) H. Itasaka , M. Liu, R. Kojima, T. Yoshikawa, M. Nishikawa, M. Nishi and K. Hamamoto, Single-particle observation of detonation nanodiamonds by tip-enhanced Raman

spectroscopy, *Chem. Lett.* **2021**, *50*, 1188–1190.

https://doi.org/10.1246/cl.210042

List of presentations

1) Masahiro Nishikawa, Minoru Suzuki and Naoki Komatsu, Anticancer nanodrug of boron neutron capture therapy by surface modification of nanodiamonds（ナノダイヤモンドの表面修飾によるホウ素中性子捕捉療法薬剤の創出）, 第 11 回ナノカーボンバイオシンポ ジウム, Japan, August 31, 2021, Oral (online).
2) Masahiro Nishikawa, Anticancer nanodrug of boron neutron capture therapy by surface modification of nanodiamond（ナノダイヤモンドの表面修飾によるホウ素中性子捕捉療法薬剤）, 第 35 回ダイヤモンドシンポジウム, Japan, November 19, 2021, Oral (online).
3) Masahiro Nishikawa, Ming Liu, Yuto Makino, Taro Yoshikawa, Akihiko Tsurui and Tomoaki Mahiko, Activities toward biomedical applications of detonation nanodiamonds (Invited), MRS spring meeting and exhibits, USA, May 22, 2022, Oral (international, online).
4) Masahiro Nishikawa, Poly(glycerol) functionalized nanodiamonds: control of the loading amount, structural analysis and applications（ポリグリセロール修飾ナノダイヤモンド修飾量制御と構造解析、およびその応用）, 量子生命科学会第 5 回大会, Japan, May 18, 2023, Oral.
5) Masahiro Nishikawa, Jie Yu, Heon Gyu Kang, Minoru Suzuki and Naoki Komatsu, Boron Neutron Capture Therapy with ^{10}B Cluster-Conjugated Poly(glycerol) Functionalized Nanodiamond（^{10}B クラスターを担持したポリグリセロール修飾ナノダイヤモンドによるホウ素中性子捕捉療法）, 第 13 回ナノカーボンバイオシンポ ジウム, Japan, September 3, 2023, Oral.
6) Masahiro Nishikawa, Ming Liu, Shinji Nagamachi and Motoi Nakao, Production of highly concentrated SiV center in polycrystalline diamond thin film, Poland, September 16, 2019, Poster.

7) Masahiro Nishikawa, Ming Liu, Akihiko Tsurui, Shinji Nagamachi, Naoki Komatsu and Motoi Nakao, Enrichment of fluorescent SiV center in silicon-doped diamond by post-treatment, 14th International Conference on New Diamond and Nano Carbons, Japan, June 8, 2021, Poster (international, online).

List of patents

1) Surface functionalized nanoparticles（表面修飾ナノ粒子）, Masahiro Nishikawa and Naoki Komatsu, JP2022-023332 (June 9, 2022), Priority: JP2021-098083 (June 11, 2021).
2) Surface functionalized minute particles and manufacturing method thereof（表面修飾微粒子、及びその製造方法）, Masahiro Nishikawa and Naoki Komatsu, JP2022-028954 (February 28, 2022).
3) Surface functionalized nanodiamonds（表面修飾ナノダイヤモンド）, Masahiro Nishikawa and Naoki Komatsu, JP2022-083332 (May 20, 2022).

Acknowledgements

It was one of my long-held dreams to be involved in research which would deserve to Ph D degree and simultaneously contribute to my company’s business. Hence, it was a God-given opportunity that I got acquainted with Prof. Komatsu as an adviser for my company in the development of detonation nanodiamonds. I had always felt delightful to talk with him about manipulation of surface chemistry, chemical modification and application of nanodiamonds including fluorescent nanodiamonds, then I joined his laboratory.

Now, in the end of this thesis, I would like to express my best gratitude before everything to Prof. Naoki Komatsu, Graduate School of Human and Environmental Studies, Kyoto University, who generously allowed me to be a student of his laboratory along with being a company employee. Of course, I appreciate him very much for his valuable and insightful suggestions, and right arrangements and decisions based on his great deal of knowledges and experiences as prominent chemist and (nano)material scientist. Also, I am extremely grateful to Prof. Hirohito Tsue and Prof. Ken-ichi Fujita in the same graduate school, and Prof. Li Zhao (Soochow University) for helpful discussions and suggestions to complete this thesis.

I extend my appreciation to Prof. Minoru Suzuki (Institute for Integrated Radiation and Nuclear Science, Kyoto University), who instructed me the procedures of biological experiments at Kyoto University Research Reactor (KUR) in Kumatori for neutron irradiation, and accommodated experiment schedules. I also thank Prof. Yoshinori Sakurai, Dr. Takushi Takata and other KUR members for their help to conduct the neutron irradiation surely and safely.

I would like to appreciate Mr. Haruyasu Kohda, Ms. Keiko Okamoto-Furuta and Mr. Tatsuya Katsuno (Division of Electron Microscopic Study, Center for Anatomical Studies, Graduate School of Medicine, Kyoto University) for technical assistance and discussions in TEM and SEM-EDS, and Ms. Fumie Sakata (Center for Organic Elemental Microanalysis, Graduate School of

Pharmaceutical Science, Kyoto University), and members for elemental analyses.

I am grateful very much to the members in Daicel Corporation; especially my past and present colleagues in the nanodiamond team; Dr. Ming Liu, Dr. Taro Yoshikawa, Mr. Hidekazu Takeuchi and Mr. Naoyoshi Matsuno for working on DND-PG together, and Dr. Tomoaki Mahiko, Mr. Akihiko Tsurui, Mr. Yoshiki Kishino, Mr. Takashi Kouuchi, Mr. Yusaku Takeuchi, Mr. Shingo Himeda, Dr. Yuto Makino, Mr. Norihiro Kimoto, Mr. Akira Kaga and other members for their great deal of cooperation. I also thank the members in the analytical department for their help with various kinds of analytical works.

As well, I would like to express my sincere thanks to the past and present members of Komatsu lab. including guest researchers for letting me have precious time as a student. Especially, I deeply appreciate my senior Ph D student Dr. Yajuan Zou (Okayama University) for her teaching biological assays and discussing PG functionalized NDs. Also, I thank Mr. Heon Gyu Kang for his help especially for the experiments at KUR and RI center (Kyoto University), Ms. Jie Yu who currently works on ND-PG for her help and discussions, and Mr. Shun Kimiya (Mitsubishi Material) for constructive discussions that helped me understand about PG deeper.

I would like to report on this thesis to late Prof. Tetsuo Shiba (Osaka University when I was a student in his laboratory) with my respect and gratitude. Also, I want to report to my late parents Masao Nishikawa and Chieko Nishikawa.

Finally, please allow me to express my best gratitude to my beloved wife Haruko Nishikawa, and our daughter Shoko Nishikawa and son Tetsuri Nishikawa. I really feel happy just for they are my family. I am always encouraged with the efforts of Shoko and Tetsuri. Again, I sincerely thank Haruko with love for her understanding and cooperation with everything to achieve the work for this thesis.

Thorough elucidation of synthesis and structure of poly(glycerol) functionalized nanodiamonds, *Carbon* **2023**, *205*, 463–474. (https://doi.org/10.1016/j.carbon.2023.01.025)

Poly(glycerol-*co*-glyceric acid) functionalized nanodiamonds by nitroxyl radical-catalyzed oxidation of primary alcohols in poly(glycerol) as scaffolds for further conjugation, *ChemNanoMat* **2023**, *9*, e202300204. (https://doi.org/10.1002/cnma.202300204)

Conjugation of phenylboronic acid moiety through multistep organic transformations on nanodiamond surface for an anticancer nanodrug for boron neutron capture therapy, *Bull. Chem. Soc. Jpn.* **2021**, *94*, 2302–2312. (https://doi.org/10.1246/bcsj.20210200)

Rational design, multistep synthesis and *in vitro* evaluation of poly(glycerol) functionalized nanodiamond conjugated with boron-10 cluster and active targeting moiety for boron neutron capture therapy, *Chem. Eur. J.* **2023**, *29*, e202302073. (https://doi.org/10.1002/chem.202302073)